

**Mechanochemical activation assisted solid state  
synthesis, self-propagating high-temperature  
synthesis, and characterisation of Ti-containing  
solid solutions with spinel-, pseudobrookite- and  
 $\text{Mn}_5\text{Si}_3$ -type structures**

Dissertation  
zur Erlangung des Doktorgrades  
der Naturwissenschaften

vorgelegt beim Fachbereich Geowissenschaften/Geographie  
der Johann Wolfgang Goethe-Universität  
in Frankfurt am Main

von  
Man He  
aus Henan, China

Frankfurt 2016  
(D 30)

vom Fachbereich Geowissenschaften/Geographie der  
Johann Wolfgang Goethe-Universität als Dissertation angenommen.

Dekan: Prof. Dr. Ulrich Achatz

1. Gutachter: Prof. Dr. Björn Winkler
2. Gutachter: PD Dr. Eiken Haussühl

Datum der Disputation: 24/10/2016

# Contents

<b>Abstract</b>	<b>IX</b>
<b>Zusammenfassung</b>	<b>XI</b>
<b>1 Introduction</b>	<b>1</b>
1.1 Spinel . . . . .	1
1.1.1 Crystal structure . . . . .	2
1.1.2 Synthesis . . . . .	4
1.1.3 Physical properties and applications . . . . .	5
1.2 Pseudobrookites . . . . .	7
1.2.1 Crystal structure . . . . .	7
1.2.2 Synthesis . . . . .	9
1.2.3 Physical properties and applications . . . . .	11
1.3 Task and outline . . . . .	12
<b>2 Experimental methods and principles</b>	<b>15</b>
2.1 Mechanochemical activation assisted synthesis . . . . .	15
2.1.1 High-speed ball milling . . . . .	15
2.1.2 Solid state synthesis . . . . .	16
2.1.3 Self-propagating high-temperature synthesis . . . . .	17
2.2 X-ray diffraction and neutron diffraction . . . . .	18
2.3 Raman and infrared spectroscopy . . . . .	20
2.4 Low-temperature heat capacity . . . . .	21
2.5 Density functional theory . . . . .	22
2.6 Other methods . . . . .	22
<b>3 <math>\text{Cu}_x\text{Zn}_{2-x}\text{TiO}_4</math> with <math>0 \leq x &lt; 1</math></b>	<b>25</b>
3.1 Introduction . . . . .	25
3.2 Materials and methods . . . . .	26
3.2.1 Sample preparation . . . . .	26
3.2.2 X-ray diffraction . . . . .	26
3.2.3 Neutron diffraction . . . . .	27
3.2.4 Characterisations of the bulk sample with $x = 0.4$ . . . . .	27
3.3 Results and discussion . . . . .	28
3.3.1 Rietveld refinement for the sample with $x = 0.4$ . . . . .	30
3.3.2 Rietveld refinements for the endmember $\text{Zn}_2\text{TiO}_4$ . . . . .	32

3.3.3	Rietveld refinement for the sample with $x = 0.5$ . . . . .	34
3.3.4	Rietveld refinement results of $\text{Cu}_x\text{Zn}_{2-x}\text{TiO}_4$ . . . . .	37
3.3.5	Structural changes in the $\text{Cu}_x\text{Zn}_{2-x}\text{TiO}_4$ solid solution . . . . .	40
3.3.6	Physical properties of the bulk sample with $x = 0.4$ . . . . .	42
3.4	Conclusion . . . . .	45
<b>4</b>	<b><math>\text{MgTi}_2\text{O}_5</math></b> . . . . .	<b>47</b>
4.1	Introduction . . . . .	47
4.2	Experimental and computational approaches . . . . .	48
4.2.1	Sample preparation . . . . .	48
4.2.2	X-ray diffraction . . . . .	49
4.2.3	Raman spectroscopy . . . . .	49
4.2.4	Low-temperature heat capacity . . . . .	50
4.2.5	Density functional theory . . . . .	50
4.3	Results and discussion . . . . .	50
4.3.1	Mg/Ti disorder . . . . .	50
4.3.2	Vibrational properties . . . . .	53
4.3.3	Elasticity . . . . .	58
4.3.4	Low-temperature thermodynamic properties . . . . .	59
4.4	Conclusion . . . . .	62
<b>5</b>	<b><math>\text{Zn}_x\text{Mg}_{1-x}\text{Ti}_2\text{O}_5</math> (<math>0 \leq x \leq 1</math>) and <math>\text{Cu}_x\text{Mg}_{1-x}\text{Ti}_2\text{O}_5</math> (<math>0 \leq x \leq 0.5</math>)</b> . . . . .	<b>63</b>
5.1	Introduction . . . . .	63
5.2	Experimental section . . . . .	64
5.2.1	Sample preparation . . . . .	64
5.2.2	X-ray diffraction . . . . .	64
5.2.3	Neutron diffraction . . . . .	65
5.2.4	Raman spectroscopy . . . . .	66
5.3	Results and discussion . . . . .	67
5.3.1	Phase compositions . . . . .	67
5.3.2	Rietveld refinements for $\text{MgTi}_2\text{O}_5$ . . . . .	68
5.3.3	Rietveld refinement results for $\text{Zn}_x\text{Mg}_{1-x}\text{Ti}_2\text{O}_5$ . . . . .	71
5.3.4	Structural changes in the $\text{Zn}_x\text{Mg}_{1-x}\text{Ti}_2\text{O}_5$ solid solution . . . . .	78
5.3.5	Raman spectra of $\text{Zn}_x\text{Mg}_{1-x}\text{Ti}_2\text{O}_5$ . . . . .	82
5.3.6	Le Bail refinement results for $\text{Cu}_x\text{Mg}_{1-x}\text{Ti}_2\text{O}_5$ . . . . .	85
5.3.7	Raman spectra of $\text{Cu}_x\text{Mg}_{1-x}\text{Ti}_2\text{O}_5$ . . . . .	88
5.4	Conclusion . . . . .	90
<b>6</b>	<b><math>\text{Ti}_5\text{Si}_3\text{Z}_x</math> with <math>\text{Z} = \text{B}</math> or <math>\text{O}</math></b> . . . . .	<b>91</b>
6.1	Introduction . . . . .	91
6.2	Experimental details . . . . .	92
6.2.1	Sample preparation . . . . .	92
6.2.2	X-ray diffraction . . . . .	92
6.3	Results and discussion . . . . .	92
6.4	Conclusion . . . . .	96

<b>7 Summary and outlook</b>	<b>97</b>
<b>A <math>\text{Cu}_x\text{Zn}_{2-x}\text{TiO}_4</math> cubic spinels</b>	<b>99</b>
<b>B Pseudobrookite-type <math>\text{MgTi}_2\text{O}_5</math></b>	<b>109</b>
<b>C Pseudobrookite-type <math>\text{Zn}_x\text{Mg}_{1-x}\text{Ti}_2\text{O}_5</math> and <math>\text{Cu}_x\text{Mg}_{1-x}\text{Ti}_2\text{O}_5</math></b>	<b>115</b>
<b>References</b>	<b>127</b>
<b>Acknowledgements</b>	<b>143</b>
<b>Curriculum Vitae</b>	<b>145</b>
<b>Declaration</b>	<b>147</b>

## List of figures

1.1	Crystal structure of $AB_2O_4$ cubic spinel . . . . .	3
1.2	Crystal structure of orthorhombic pseudobrookite-type $MgTi_2O_5$ . . . . .	8
2.1	Photograph and schematic drawing of the planetary ball mill . . . . .	16
2.2	Photograph and schematic drawing of the SHS set-up . . . . .	17
2.3	X-ray and neutron scattering factors of the ions . . . . .	18
2.4	X-ray and neutron diffraction instruments . . . . .	19
2.5	Instrument and energy levels for Raman spectroscopy . . . . .	20
2.6	The physical property measurement system . . . . .	21
2.7	SEM and the buoyancy density set-up . . . . .	23
2.8	The plane-wave ultrasound spectroscopy and dilatometer . . . . .	23
3.1	Photograph of the spinels $Cu_xZn_{2-x}TiO_4$ . . . . .	28
3.2	XRD patterns of the samples before and after soaking . . . . .	29
3.3	ND patterns of $Cu_xZn_{2-x}TiO_4$ solid solution . . . . .	30
3.4	Rietveld refinement of XRD for the sample with $x = 0.4$ . . . . .	31
3.5	Rietveld refinement results for $Zn_2TiO_4$ . . . . .	33
3.6	Rietveld refinement results of the sample with $x = 0.5$ . . . . .	36
3.7	Lattice parameter $a$ plotted against $x$ in $Cu_xZn_{2-x}TiO_4$ . . . . .	40
3.8	Positional and thermal displacement parameters for $O^{2-}$ . . . . .	41
3.9	Evolution of the mean bond lengths $d_{T-O}$ and $d_{M-O}$ . . . . .	42
3.10	UV-vis spectrum of the sample with $x = 0.4$ . . . . .	43
3.11	SEM images of the bulk sample with $x = 0.4$ . . . . .	43
3.12	Thermal expansion and elastic properties of the sample with $x = 0.4$ . . . . .	44
4.1	Photographs of the $MgTi_2O_5$ cylinders and pellets . . . . .	49
4.2	Rietveld refinement results of $MgTi_2O_5$ synthesised at 1173 K . . . . .	51
4.3	Dependence of the Mg/Ti disorder $X$ on the synthesis condition . . . . .	51
4.4	Raman spectra of disordered $MgTi_2O_5$ . . . . .	53
4.5	Assignments of the Raman bands based on fully ordered $MgTi_2O_5$ . . . . .	54
4.6	$B_{1g}(5)$ Raman frequencies versus the disorder parameter $X$ . . . . .	56
4.7	Oxygen O1 motions corresponding to the $B_{1g}(5)$ Raman mode . . . . .	57
4.8	Theoretical infrared absorption of fully ordered $MgTi_2O_5$ . . . . .	57
4.9	Representation surface of the longitudinal elastic stiffness . . . . .	59
4.10	Theoretical and experimental $C_p$ . . . . .	60
4.11	Evolution of $S_{config}^0$ with the disorder parameter $X$ . . . . .	60
4.12	$\Delta H$ and $\Delta S$ between $MgTi_2O_5$ with $X = 0.37$ and $X = 0.14$ . . . . .	61

5.1	Samples of $\text{Cu}_x\text{Mg}_{1-x}\text{Ti}_2\text{O}_5$ and $\text{Zn}_x\text{Mg}_{1-x}\text{Ti}_2\text{O}_5$ . . . . .	65
5.2	The SHS product for the synthesis of $\text{ZnTi}_2\text{O}_5$ . . . . .	68
5.3	Rietveld refinement result for the SHS product . . . . .	69
5.4	Rietveld refinement of neutron diffraction for $\text{MgTi}_2\text{O}_5$ . . . . .	70
5.5	Rietveld results for $\text{Zn}_x\text{Mg}_{1-x}\text{Ti}_2\text{O}_5$ with $x = 0.4$ . . . . .	73
5.6	Rietveld results of XRD for $x = 0.8$ . . . . .	75
5.7	Rietveld refinement of ND for $x = 0.8$ . . . . .	77
5.8	Lattice parameters of $\text{Zn}_x\text{Mg}_{1-x}\text{Ti}_2\text{O}_5$ with $0 \leq x \leq 1$ . . . . .	78
5.9	Site occupancy in $M1$ ( $4c$ ) of $\text{Zn}_x\text{Mg}_{1-x}\text{Ti}_2\text{O}_5$ . . . . .	79
5.10	Bond lengths of $d_{M-O}$ in $\text{Zn}_x\text{Mg}_{1-x}\text{Ti}_2\text{O}_5$ . . . . .	80
5.11	Bond angles of $M-O1-M$ in $\text{Zn}_x\text{Mg}_{1-x}\text{Ti}_2\text{O}_5$ . . . . .	81
5.12	Normalised Raman spectra of $\text{Zn}_x\text{Mg}_{1-x}\text{Ti}_2\text{O}_5$ . . . . .	82
5.13	Raman spectra of $\text{Zn}_x\text{Mg}_{1-x}\text{Ti}_2\text{O}_5$ with $x = 0.9$ and $\text{ZnTi}_2\text{O}_5$ . . . . .	83
5.14	Raman shifts for $\text{Zn}_x\text{Mg}_{1-x}\text{Ti}_2\text{O}_5$ . . . . .	84
5.15	Raman shift of the overtone for $\text{Zn}_x\text{Mg}_{1-x}\text{Ti}_2\text{O}_5$ . . . . .	85
5.16	Le Bail refinement of XRD for $\text{Cu}_x\text{Mg}_{1-x}\text{Ti}_2\text{O}_5$ with $x = 0.5$ . . . . .	86
5.17	Lattice parameters of $\text{Cu}_x\text{Mg}_{1-x}\text{Ti}_2\text{O}_5$ . . . . .	87
5.18	Normalised Raman spectra of $\text{Cu}_x\text{Mg}_{1-x}\text{Ti}_2\text{O}_5$ . . . . .	88
5.19	Raman shifts for $\text{Cu}_x\text{Mg}_{1-x}\text{Ti}_2\text{O}_5$ . . . . .	89
6.1	Crystal structure of $\text{Ti}_5\text{Si}_3$ with space group $P6_3/mcm$ . . . . .	91
6.2	Rietveld refinements of $\text{Ti}_5\text{Si}_3$ using one or two unit cells . . . . .	93
6.3	Rietveld refinements of $\text{Ti}_5\text{Si}_3$ with different dilutions . . . . .	94
6.4	Lattice parameters of $\text{Ti}_5\text{Si}_3$ plotted against dilution . . . . .	95
6.5	Le Bail refinement of the sample containing 4 wt.% $\text{NaBH}_4$ . . . . .	96
6.6	Lattice parameters of $\text{Ti}_5\text{Si}_3\text{Z}_x$ in the samples containing $\text{NaBH}_4$ . . . . .	96
A.1	Picture of soaking the samples in the acetic acid solution . . . . .	99
A.2	Rietveld refinement results of the sample with $x = 0.1$ . . . . .	100
A.3	Rietveld refinement results of the sample with $x = 0.2$ . . . . .	101
A.4	Rietveld refinement results of the sample with $x = 0.3$ . . . . .	102
A.5	Rietveld refinement results of the sample with $x = 0.4$ . . . . .	103
A.6	Rietveld refinement results of the sample with $x = 0.6$ . . . . .	104
A.7	Rietveld refinement results of the sample with $x = 0.7$ . . . . .	105
A.8	Rietveld refinement results of the sample with $x$ around 0.75 . . . . .	106
A.9	Rietveld refinement results of the sample with $x$ around 0.86 . . . . .	107
B.1	Polynomial fits of the measured $C_p$ with $X = 0.14(1)$ and $0.37(1)$ . . . . .	109
B.2	Rietveld refinement results of $\text{MgTi}_2\text{O}_5$ with $X = 0.14$ . . . . .	110
B.3	Rietveld refinement results of $\text{MgTi}_2\text{O}_5$ with $X = 0.30$ . . . . .	111
B.4	Rietveld refinement results of $\text{MgTi}_2\text{O}_5$ with $X = 0.33$ . . . . .	112
B.5	Rietveld refinement results of $\text{MgTi}_2\text{O}_5$ with $X = 0.34$ . . . . .	113
B.6	Rietveld refinement results of $\text{MgTi}_2\text{O}_5$ with $X = 0.37$ . . . . .	114
C.1	Mixtures of $\text{Zn}_x\text{Mg}_{1-x}\text{Ti}_2\text{O}_5$ after ball milling . . . . .	115
C.2	Mixtures of $\text{Cu}_x\text{Mg}_{1-x}\text{Ti}_2\text{O}_5$ after ball milling . . . . .	115

C.3	Rietveld refinement results of $Zn_xMg_{1-x}Ti_2O_5$ with $x = 0.1$	116
C.4	Rietveld refinement results of $Zn_xMg_{1-x}Ti_2O_5$ with $x = 0.2$	117
C.5	Rietveld refinement results of $Zn_xMg_{1-x}Ti_2O_5$ with $x = 0.3$	118
C.6	Rietveld refinement results of $Zn_xMg_{1-x}Ti_2O_5$ with $x = 0.5$	119
C.7	Rietveld refinement results of $Zn_xMg_{1-x}Ti_2O_5$ with $x = 0.6$	120
C.8	Rietveld refinement results of $Zn_xMg_{1-x}Ti_2O_5$ with $x = 0.7$	121
C.9	Rietveld refinement results of $Cu_xMg_{1-x}Ti_2O_5$ with $x = 0$	122
C.10	Le Bail refinement of $Cu_xMg_{1-x}Ti_2O_5$ with $x = 0.1$	123
C.11	Le Bail refinement of $Cu_xMg_{1-x}Ti_2O_5$ with $x = 0.2$	124
C.12	Le Bail refinement of $Cu_xMg_{1-x}Ti_2O_5$ with $x = 0.3$	125
C.13	Le Bail refinement of $Cu_xMg_{1-x}Ti_2O_5$ with $x = 0.4$	126



## List of tables

1.1	Structural parameters of the Ti/Ge/Sn-containing 4-2 spinels . . . . .	4
1.2	Physical properties of common pseudobrookites . . . . .	12
2.1	Mechanochemical activation conditions of the solid solutions . . . . .	16
3.1	A list of the refined parameters for ND data analysis . . . . .	28
3.2	Rietveld refinement of XRD for the sample with $x = 0.4$ . . . . .	30
3.3	Rietveld refinement results for the endmember $Zn_2TiO_4$ . . . . .	32
3.4	Refinement sequences of ND for the sample with $x = 0.5$ . . . . .	34
3.5	Rietveld refinement results for the sample with $x = 0.5$ . . . . .	37
3.6	Rietveld refinement results for $Cu_xZn_{2-x}TiO_4$ solid solution . . . . .	38
3.7	Rietveld refinement results by using fixed cation $U_{iso}$ . . . . .	39
4.1	Synthesis condition and Rietveld results of $MgTi_2O_5$ . . . . .	52
4.2	Theoretical and experimental Raman modes of $MgTi_2O_5$ . . . . .	55
4.3	Theoretical infrared modes of fully ordered $MgTi_2O_5$ . . . . .	58
4.4	Theoretical elastic stiffness coefficients of fully ordered $MgTi_2O_5$ . . . . .	58
4.5	Standard enthalpies and entropies of $MgTi_2O_5$ . . . . .	61
5.1	Synthesis conditions and purities of $Zn_xMg_{1-x}Ti_2O_5$ and $Cu_xMg_{1-x}Ti_2O_5$ . . . . .	67
5.2	Rietveld refinement results for $MgTi_2O_5$ . . . . .	71
5.3	Rietveld refinement results of XRD for $Zn_xMg_{1-x}Ti_2O_5$ . . . . .	74
5.4	Refinement strategies and results for $x = 0.7$ and $0.8$ . . . . .	76
5.5	Variation of $d_{M-O}$ with increasing amount of $Zn^{2+}$ from 0 to 0.8 . . . . .	79
5.6	Bond lengths of $d_{M-M}$ in $Zn_xMg_{1-x}Ti_2O_5$ . . . . .	80
5.7	Le Bail refinement results of XRD for $Cu_xMg_{1-x}Ti_2O_5$ . . . . .	87
5.8	Assignment of Raman modes for $Cu_xMg_{1-x}Ti_2O_5$ . . . . .	88
6.1	Phase composition of $Ti_5Si_3$ with 0–40 wt.% dilution . . . . .	93
6.2	Synthesis condition and phases of $Ti_5Si_3$ with 1–4 wt.% $NaBH_4$ . . . . .	95
A.1	Structural parameters of CuO in $Cu_xZn_{2-x}TiO_4$ with $x = 0.86$ . . . . .	99



## Abstract

Many natural minerals exist in the form of a solid solution. The systematic changes in structural and physical properties of oxide solid solutions are of geological importance and allow for wide applications. In order to understand the composition-structure-property relations, substitutional solid solutions of  $\text{Cu}_x\text{Zn}_{2-x}\text{TiO}_4$ ,  $\text{Zn}_x\text{Mg}_{1-x}\text{Ti}_2\text{O}_5$  and  $\text{Cu}_x\text{Mg}_{1-x}\text{Ti}_2\text{O}_5$  have been synthesised by mechanochemical activation assisted solid state synthesis. Self-propagating high-temperature synthesis has been employed to achieve the interstitial solid solutions of  $\text{Ti}_5\text{Si}_3\text{Z}_x$  ( $Z$  refers to the element boron or oxygen). The changes in the crystal structure and physical properties due to the formation of solid solutions are investigated by employing X-ray diffraction, neutron diffraction, Raman spectroscopy, low-temperature heat capacity, thermal expansion, scanning electron microscopy, UV-vis spectroscopy, plane-wave ultrasound spectroscopy and density functional theory calculations.

Oxide spinels,  $\text{AB}_2\text{O}_4$ , and those doped with transition metal cations, have emerged as interesting semiconductors, efficient photocatalysts, pigments and dyes, substrates for integrated electronics, as well as transparent windows and shield materials. Replacing  $\text{Zn}^{2+}$  by  $\text{Cu}^{2+}$  leads to changes in the vibrational properties and band gap energy of  $\text{Zn}_2\text{TiO}_4$  spinel. Cation distribution in  $\text{Cu}_x\text{Zn}_{2-x}\text{TiO}_4$  cubic spinels is determined by neutron diffraction. The results indicate  $\text{Zn}^{2+}$ ,  $<0.04 \text{ Cu}^{2+}$  and  $<0.04 \text{ Ti}^{4+}$  occupying the tetrahedral sites of  $\text{Cu}_x\text{Zn}_{2-x}\text{TiO}_4$ . With the increase of copper concentration, the lattice parameter decreases linearly for  $0 \leq x \leq 0.6$  but contracts more strongly at a higher  $x$ . The positional parameter and isotropic thermal displacement parameter both increase and are described by a second-order and a first-order polynomial, respectively. Incorporation of  $\text{Cu}^{2+}$  leads to a decrease of the average octahedral bond length but no change of the average tetrahedral bond length. The coefficient of linear thermal expansion for the bulk sample with  $x = 0.4$  shows 10% of the expected value. This is due to the inhomogeneous microstructure and a low density of only 90% of the theoretical density.

Pseudobrookite-type minerals,  $\text{AB}_2\text{O}_5$ , may have a critical role in the petrogenesis of the mare basalts and lunar picritic glasses as a source of titanium, and may be present in other planetary bodies as well. A low bulk thermal expansion coefficient, a high refractive index, a wide bandgap of 3.4 eV and the ability to host transition metal ions, make karrooite,  $\text{MgTi}_2\text{O}_5$ , attractive for multiple applications, such as ceramic pigments, filters, UV photocatalysts, and as anode materials for batteries. Disordered  $\text{MgTi}_2\text{O}_5$  are characterised by X-ray diffraction and Raman spectroscopy. *Ab initio* calculations are performed based on a fully ordered  $\text{MgTi}_2\text{O}_5$  structure model. A good agreement of the experimental and theoretical results is achieved. The complete prediction of 24 Raman and 21 infrared normal modes allows assignments of the experimental Raman spectra for disordered  $\text{MgTi}_2\text{O}_5$ . The exchange of  $\text{Mg}^{2+}$  by  $\text{Ti}^{4+}$  in M1 octahedral sites leads to a linear blueshift of  $B_{1g}(5)$  Raman mode, which is due to an increased displacement

of the cornersharing oxygens O1 parallel to [001] direction. The theoretical bulk modulus and standard entropy of  $\text{MgTi}_2\text{O}_5$  are determined to be 161(1) GPa and 134.24 J K<sup>-1</sup>, respectively.

Effect of divalent cation substitution on the structural and vibrational properties of karrooite is investigated by using X-ray diffraction, neutron diffraction and Raman spectroscopy. The complete solid solution of  $\text{Zn}_x\text{Mg}_{1-x}\text{Ti}_2\text{O}_5$  obeys Vegard's law. With the increasing substitution of  $\text{Mg}^{2+}$  by  $\text{Zn}^{2+}$ , the unit cell of  $\text{MgTi}_2\text{O}_5$  expands. The smallest lattice parameter  $a$  decreases while the larger parameters  $b$  and  $c$  increase.  $\text{Zn}^{2+}$  preferably replaces  $\text{Mg}^{2+}$  in the  $M1$  sites at  $x \geq 0.6$  and incorporates into both  $M1$  and  $M2$  sites at a higher zinc concentration. The replacement of  $\text{Mg}^{2+}$  by  $\text{Zn}^{2+}$  leads to redshifts of the  $B_{1g}(3)$  and  $B_{1g}(5)$  Raman modes and a blueshift of the  $B_{1g}(1)$  Raman mode. At maximum half of  $\text{Mg}^{2+}$  in  $\text{MgTi}_2\text{O}_5$  can be replaced by  $\text{Cu}^{2+}$  and copper causes no change of the unit cell volume. The  $B_{1g}(3)$  and  $B_{1g}(5)$  Raman modes of  $\text{Cu}_x\text{Mg}_{1-x}\text{Ti}_2\text{O}_5$  redshift at  $x \leq 0.3$  and blueshift at a higher copper fraction, indicating a movement of  $\text{Ti}^{4+}$  from the  $M2$  to the  $M1$  octahedral sites at  $x \geq 0.3$ .

The  $\text{Ti}_5\text{Si}_3$  intermetallic compound has potential application as high temperature structural materials due to the high melting point, low density and excellent oxidation resistance. Incorporating the interstitial atoms into the  $\text{Mn}_5\text{Si}_3$ -type structure is expected to improve the ductility and fracture toughness performance of  $\text{Ti}_5\text{Si}_3$ . By employing self-propagating high-temperature synthesis,  $\text{Ti}_5\text{Si}_3\text{O}_x$  is achieved by adding 5–40 wt.% product of  $\text{Ti}_5\text{Si}_3$  into its stoichiometric starting materials while  $\text{Ti}_5\text{Si}_3\text{B}_x$  is formed by adding 1–4 wt.%  $\text{NaBH}_4$ . The migration of the elements B and O into the cavity of  $\text{Ti}_5\text{Si}_3$  leads to a contraction and an expansion of the unit cell, respectively.

## Zusammenfassung

Viele natürliche Minerale sind Mischkristalle. Die Bildung von Mischkristallen durch Austausch von Kationen eines Minerals führt zu systematischen Änderungen der strukturellen, thermodynamischen und physikalischen Eigenschaften. Es ist von fundamentalem Interesse, die Zusammensetzung – Struktur – Eigenschaftsbeziehungen zu verstehen. Titan ist eine wesentliche Komponente von feuerfesten gesteinsbildenden Mineralen und ist eins der 18 häufigsten Elemente in unserem Sonnensystem. Die Synthese, Untersuchungen zur Struktur und die Charakterisierung von titanhaltigen Mischkristallen trägt zu unserem kristallographischen Wissen bei.

Oxidspinelle,  $AB_2O_4$ , mit Übergangsmetallkationen sind als interessante Halbleiter, effiziente Photokatalysatoren, Pigmente und Farbstoffe, Substrate für integrierte Elektronikschaltungen sowie als transparentes Fenster- und Abschirmmaterial bekannt geworden. Die  $Ti^{4+}$ -enthaltenden Spinelle, unter anderem  $Mg_2TiO_4$ ,  $Mn_2TiO_4$ ,  $Fe_2TiO_4$ ,  $Co_2TiO_4$ ,  $Zn_2TiO_4$  und  $LiFeTiO_4$ , kristallisieren in der kubischen inversen Spinellstruktur in der Raumgruppe  $Fd\bar{3}m$  unter Normalbedingungen. Die Hälfte der divalenten Kationen,  $B^{2+}$ , besetzen die Tetraederlücken während  $Ti^{4+}$  und die Hälfte der  $B^{2+}$  Kationen Oktaederlücken besetzen.  $Zn^{2+}$  in  $Zn_2TiO_4$  kann durch andere divalente Kationen mit ähnlichem Ionenradius ersetzt werden, ohne die dichteste Kugelpackung des flächenzentrierten isometrischen Subgitters der Anionen aufzubrechen. Die Mischkristallreihe  $Cu_xZn_{2-x}TiO_4$  ist nicht vollständig und zeigt ein positives Überschußvolumen. Die Untersuchung der Kationenverteilung von  $Cu_xZn_{2-x}TiO_4$  kubischen Spinellsystem spielt eine signifikante Rolle bei dem Verständnis der physikalischen Eigenschaften.

Kubische  $Cu_xZn_{2-x}TiO_4$  Mischkristalle mit Konzentrationen  $x$ ,  $0 \leq x < 1$ , sind in hoher Reinheit aus den binären Oxiden durch Festkörpersynthesen mit mechanochemischer Aktivierung synthetisiert worden. Wolframcarbidmahlbehälter sind anstelle von Achatbehältern mit einer zusätzlichen Säurebadbehandlung verwendet worden. Die Kristallinität der Proben wurde durch Röntgenbeugungsexperimente kontrolliert. Rietveld-Verfeinerung der Röntgenbeugungsdaten für die Probe mit  $x = 0.4$  haben keinen strukturellen Unterschied durch die Säurebadbehandlung gezeigt.

Hochauflösende Neutronenbeugungsdaten von  $Cu_xZn_{2-x}TiO_4$  wurden unter Normalbedingungen am D2B Diffraktometer am Institut Laue-Langevin in Grenoble durchgeführt. Rietveld-Verfeinerungen für die Strukturanalysen der Mischkristalle wurden unter Verwendung der Programme GSAS, EXPGUI und gsalanguage ausgeführt. Die verfeinerten Strukturparameter für das Endglied  $Zn_2TiO_4$  sind konsistent mit Literaturwerten. Die Positions- und thermischen Verschiebungsparameter der Anionen sind von den constraints für die Kationen abhängig. Diese Parameter nehmen mit dem Austausch von  $Zn^{2+}$  durch  $Cu^{2+}$  zu und wurden durch Polynome zweiter (Positionsparameter) und erster Ordnung (thermische Verschiebungsparameter) beschrieben. Die Ergebnisse zeigen, dass  $Zn^{2+}$ ,  $< 0.04 Cu^{2+}$  und  $< 0.04 Ti^{4+}$  die Tetraederlücken von ku-

bischen  $\text{Cu}_x\text{Zn}_{2-x}\text{TiO}_4$  Spinellmischkristallen besetzen. Mit dem Anstieg der Kupferkonzentration nimmt der Gitterparameter linear für Konzentrationen  $0 \leq x \leq 0.6$  ab und kontrahiert stärker für höhere Konzentrationen  $x$ . Die durchschnittliche Bindungslänge in den Tetraedern von  $\text{Cu}_x\text{Zn}_{2-x}\text{TiO}_4$  bleibt bei einem Wert von 1.986(2) Å. Der Einbau von  $\text{Cu}^{2+}$  führt zu einer Abnahme der durchschnittlichen Bindungslänge in den Oktaedern um 0.012(2) Å von 2.034(2) Å für  $x=0$  zu 2.022(2) Å für  $x=0.86(5)$ .

Bedingt durch den elektronischen  $d-d$  Übergang des oktaedrischen  $\text{Cu}^{2+}$  ( $3d^9$ ) wird eine Absorptionsbande im Sichtbaren (um 750 nm) im UV-vis Spektrum von kubischen  $\text{Cu}_x\text{Zn}_{2-x}\text{TiO}_4$  Spinellen erwartet. Der Koeffizient der linearen thermischen Ausdehnung für eine bulk Probe mit einer Konzentration  $x=0.4$  wurde bestimmt und lag bei nur 10% des erwarteten Wertes. Dies ist durch eine inhomogene Mikrostruktur und eine niedrige Dichte von 90% der theoretischen Dichte bedingt.

Ähnlich wie bei Spinellen besitzt die Pseudobrookit-Gruppe  $\text{AB}_2\text{O}_5$  zwei kristallographisch unterschiedliche Kationenplätze. Die  $\text{AB}_2\text{O}_5$  Gruppe kristallisiert in einer orthorhombischen Struktur in Raumgruppe  $Cmcm$ . Die  $A$  Kationen besetzen die  $M1$  Oktaederplätze und die  $B$  Kationen besetzen die  $M2$  Oktaederplätze für eine vollständig geordnete Struktur. Beide Plätze sind stark verzerrt und der  $M2$  Platz ist kleiner als der  $M1$  Platz. Die Kationen können zwischen beiden Plätzen wechseln, was zu einer Kationenunordnung und einem Anstieg der Entropie führt. Durch die Ordnungs-Unordnungsphänomene ist die Pseudobrookit-Gruppe durch thermodynamische Instabilitäten charakterisiert und wird als entropiestabilisierte Phase angesehen. Minerale der Pseudobrookit-Gruppe können eine kritische Rolle in der Petrogenese von Mare Basalten und pikritischen Mondgläsern als Titanquelle gespielt haben. Sie mögen in anderen Planeten ebenfalls vorhanden sein. Natürlicher Pseudobrookit hat eine  $\text{Fe}_2\text{TiO}_5$ - $\text{FeTi}_2\text{O}_5$  Mischkristallzusammensetzung und enthält eine nennenswerte Menge von Mg und weiteren Elementen. Es ist möglich, die thermische Geschichte von natürlichem Pseudobrookit über die Kationenverteilung zu identifizieren.

Karrooit,  $\text{MgTi}_2\text{O}_5$ , ist ein Endglied der Pseudobrookit-Gruppe. Die Synthese, strukturelle Charakterisierung und Bestimmung der thermodynamischen Stabilität dieses Endgliedes sind von fundamentaler Wichtigkeit für das Verständnis der Strukturen und Eigenschaften der isostrukturellen Pseudobrookit-Mischkristalle.  $\text{MgTi}_2\text{O}_5$  mit verschiedenartiger Mg/Ti Fehlordnung können in einem weiten Temperaturbereich gebildet und genutzt werden, da sie eine große positive Entropie bei hohen Temperaturen und eine langsame Kinetik des Mg/Ti Austausches bei Temperaturen unter 973 K haben. Ein kleiner thermischer Expansionskoeffizient für den bulk, ein hoher Brechungsindex, eine große Bandlücke von 3.4 eV und die Eignung zur Aufnahme von Übergangsmetallionen machen ihn attraktiv für viele Anwendungen wie keramische Pigmente, Filter, UV Photokatalysatoren und als Anodenmaterial für Batterien.

$\text{MgTi}_2\text{O}_5$  wurde mit unterschiedlichen Mg/Ti Unordnungsparametern  $X$  aus MgO und  $\text{TiO}_2$  Anatas in einem Temperaturbereich von 1173–1473 K synthetisiert. Die Proben wurden von der Synthesetemperatur in einer Eis/Wassermischung abgeschreckt. Ein zusätzlicher Temperschritt bei 873 K für 60 Tage wurde bei einer Probe mit einem  $X = 0.37$  angewandt und führte zu einem kleineren Wert von  $X = 0.14$ . Messungen der Tieftemperatur-Wärmekapazität von  $\text{MgTi}_2\text{O}_5$  mit einem Mg/Ti Unordnungsparameter von 0.14 und 0.37 wurden im Temperaturbereich von 2 K to 325 K

---

gemessen. Ungeordnetes  $\text{MgTi}_2\text{O}_5$  wurde mit Röntgenbeugung und Raman Spektroskopie charakterisiert. Rietveld Verfeinerungen der Röntgenbeugungsdaten wurden zur Bestimmung der Strukturparameter von  $\text{MgTi}_2\text{O}_5$  durchgeführt. DFT Rechnungen wurden auf der Basis eines vollständig geordneten  $\text{MgTi}_2\text{O}_5$  Strukturmodells ausgeführt. Schwingungsfrequenzen und Intensitäten, elastische Festigkeitskonstanten und Tieftemperatur Wärmekapazität wurden berechnet.

Die Synthesetemperatur von orthorhombischem Pseudobrookit-Typ  $\text{MgTi}_2\text{O}_5$  konnte verlässlich von 1373 K auf 1173 K durch die Anwendung mechanochemischer Aktivierung gesenkt werden. Die Mg/Ti Unordnung hängt von den Synthesebedingungen ab.  $\text{MgTi}_2\text{O}_5$  entsteht bei höherer Synthesetemperatur mit höherer Unordnung. Bei gleicher Synthesetemperatur führt die Bearbeitung in der Kugelmühle zu höherer Mg/Ti Unordnung. Außerdem wirkt sich eine Änderung der Mg/Ti Unordnung auf die Frequenzen der Raman Moden aus. Durch DFT Rechnungen konnte eine vollständige Vorhersage von 24 Raman und 21 IR Moden für vollständig geordnetes  $\text{MgTi}_2\text{O}_5$  erreicht werden. Dies hat eine Zuordnung der Moden aus experimentellen Raman Spektren für ungeordnetes  $\text{MgTi}_2\text{O}_5$  ermöglicht. Interessanterweise bewirkt der Austausch von  $\text{Mg}^{2+}$  durch  $\text{Ti}^{4+}$  auf M1 Plätzen (vergleichbar einem Anstieg des Unordnungsparameters) eine signifikante Blauverschiebung der  $B_{1g}(5)$  Raman Mode. Diese Blauverschiebung resultiert aus einer vergrößerten Verschiebung der eckenverknüpften Sauerstoffe O1 parallel zur [001] Richtung, welche zwei O1–M1–O1 Winkeländerungsbewegungen und einer antiphasen Streckbewegung von zwei M2–O1 Bindungen zugeordnet werden können. Raman Frequenzen der  $B_{1g}(5)$  Mode zeigen eine lineare Abhängigkeit von  $X$  und deuten die Möglichkeit einer schnellen Bestimmung der Mg/Ti Ordnung in  $\text{MgTi}_2\text{O}_5$  durch Raman Spektroskopie an.

Der theoretische bulk Modulus und die Standardentropie von vollständig geordnetem  $\text{MgTi}_2\text{O}_5$  wurden zu 161(1) GPa und  $134.24 \text{ J K}^{-1}$  bestimmt. Die Werte stimmen gut mit experimentellen Daten aus der Literatur überein. Die Anisotropie der Elastizität von vollständig geordnetem  $\text{MgTi}_2\text{O}_5$  ist nicht sehr groß, wie aus der Darstellung der longitudinalen Festigkeit abgeleitet worden ist. Die Kompressibilität ist am größten entlang der [100] Richtung und am kleinsten entlang [001] und ist damit umgekehrt proportional zur thermischen Ausdehnung. Die gemessenen Wärmekapazitäten der beiden ungeordneten  $\text{MgTi}_2\text{O}_5$  Proben wurden mit Polynomen höherer Ordnung in drei Temperaturbereichen angepasst. Mit einem Anstieg der Mg/Ti Unordnung nehmen die Schwingungs- und die Konfigurationsentropie von  $\text{MgTi}_2\text{O}_5$  zu. Die Standardexcess-Schwingungsentropie und die Konfigurationsentropie bei 298 K haben die gleiche Größe.

Mg kann in  $\text{MgTi}_2\text{O}_5$  durch zweiwertige Elemente Zn, Co, Ni, Mn oder Ca ersetzt werden, um Pseudobrookittyp Mischkristalle zu bilden. Der Einbau von 5% Übergangsmetallionen in  $\text{MgTi}_2\text{O}_5$  verbessert wirksam die Färbung von Karrooit. Die Löslichkeit eines Übergangsmetalls ist laut der Literatur nicht vollständig.  $\text{NiTi}_2\text{O}_5$ – $\text{MgTi}_2\text{O}_5$  Mischkristalle sind exzellente gelb-orange Pigmente, der Einbau von  $\text{Ni}^{2+}$  ist auf 60% molaren Anteil begrenzt. Da  $\text{Ni}^{2+}$  bevorzugt in der Oktaederlücke eingebaut wird wurde  $\text{Zn}^{2+}$ , welches den Einbau in der Tetraederlücke bevorzugt, als Vergleich gewählt.  $\text{Cu}^{2+}$ , das die OKtaederlücke bevorzugt und einen vergleichbaren Radius wie  $\text{Mg}^{2+}$ ,  $\text{Ni}^{2+}$  und  $\text{Zn}^{2+}$  hat, wurde ebenfalls als Ersatz von  $\text{Mg}^{2+}$  in  $\text{MgTi}_2\text{O}_5$

verwendet.

Vollständige Mischkristalle von  $\text{Zn}_x\text{Mg}_{1-x}\text{Ti}_2\text{O}_5$  wurden mit Unterstützung durch mechanochemische Aktivierung synthetisiert. Festkörpersynthesen mit einer Abschrecktemperatur von 1473–1573 K wurden aus den binären Oxiden durchgeführt.  $\text{TiO}_2$  als Ausgangsmaterial wurde teilweise durch metallisches  $\alpha$ -Ti ersetzt, um das Endglied  $\text{ZnTi}_2\text{O}_5$  zu synthetisieren. Diese Synthese wurde als self-propagating high-temperature Synthese (SHS) unter Argonatmosphäre gezündet. Röntgenbeugung wurde genutzt, um den Phasenbestand zu kontrollieren und Rietveld Verfeinerungen wurden für die Analysen der Struktur verwendet. Neutronenbeugung für die Proben mit  $x = 0$  und 0.8 wurde am D2B Diffraktometer durchgeführt und die Daten mit Rietveldverfeinerungen analysiert. Von  $\text{Zn}_x\text{Mg}_{1-x}\text{Ti}_2\text{O}_5$  wurden Raman Spektren aufgenommen.

Die Ergebnisse der Rietveld Verfeinerungen zeigen, dass der Ersatz von  $\text{Mg}^{2+}$  durch  $\text{Zn}^{2+}$  die orthorhombische Symmetrie der Pseudobrookit-Struktur ändert. Die Reinheit von  $\text{Zn}_x\text{Mg}_{1-x}\text{Ti}_2\text{O}_5$  hängt von der Synthesetemperatur ab. Bei weniger als 60% Zink ist die Reinheit über 99 wt.% für Proben mit einer Synthesetemperatur von 1473 K. Für Molfraktionen von 0.7 und 0.8 von  $\text{Zn}^{2+}$  wurde die Synthesetemperatur auf 1573 K erhöht, während sich die Reinheit leicht auf 96 wt.% reduziert hat. Jedoch konnten nur  $\sim 30$  wt.% Pseudobrookit-Typ  $\text{Zn}_x\text{Mg}_{1-x}\text{Ti}_2\text{O}_5$  bei einer Erhöhung der Molfraktion von  $\text{Zn}^{2+}$  auf 90% erhalten werden. Eine neue kristalline Phase wurde in Röntgenbeugungsdaten bei Verwendung des SHS-Aufbaus beobachtet. Sie wurde als Endglied  $\text{ZnTi}_2\text{O}_5$  identifiziert und betrug 19 wt.% in der Synthese.

Mit zunehmendem  $\text{Zn}^{2+}$  Einbau verändern sich die Gitterparameter  $a$ ,  $b$  und  $c$  von  $\text{Zn}_x\text{Mg}_{1-x}\text{Ti}_2\text{O}_5$  linear. Eine Extrapolation der Daten mit  $0 \leq x \leq 0.8$  führt zu idealen Gitterparametern für  $\text{ZnTi}_2\text{O}_5$ , welche mit den experimentell bestimmten Werten nach Verwendung des SHS Aufbaus verglichen wurden. Die Unterschiede sind sehr klein,  $\pm 0.1\%$ , und zeigen keine Abweichung von der Vegard'schen Regel für  $\text{Zn}_x\text{Mg}_{1-x}\text{Ti}_2\text{O}_5$  Mischkristalle an.

Rietveld Verfeinerungen von Röntgen- und Neutronenbeugungsdaten zeigten, dass  $\text{Zn}^{2+}$  bevorzugt  $\text{Mg}^{2+}$  auf den  $M1$  Plätzen bis zu einem Anteil von 60% ersetzt. Bei höherem Zinkgehalt besetzt 60%  $\text{Zn}^{2+}$  den  $M1$  Platz während der Extrateil von  $\text{Zn}^{2+}$  auf den  $M2$  Plätzen eingebaut wird. Durch den Austausch von  $\text{Mg}^{2+}$  durch  $\text{Zn}^{2+}$  ändern sich die Gitterparameter  $a$ ,  $b$  und  $c$  um  $-0.7\%$ ,  $+0.4\%$  and  $+1.3\%$ . Der Einbau von Zink in  $\text{MgTi}_2\text{O}_5$  führt zu einer Expansion des Einheitszellvolumens von 0.9%, was auf eine Vergrößerung der durchschnittlichen  $M1$ -O und  $M2$ -O Bindungslängen zurückgeführt wird. Mit zunehmendem Zinkanteil verzerren sich die  $M1$  und  $M2$  Oktaeder. Die Winkel zwischen eckenverknüpften  $M2$  Oktaedern und eckenverknüpften  $B1$  Oktaedern nehmen um rund 3% ab. Die strukturellen Änderungen sind wahrscheinlich Folge einer zunehmenden Abstoßung zwischen den eckenverknüpften  $M2$  Oktaedern.

Die Raman Spektren von  $\text{Zn}_x\text{Mg}_{1-x}\text{Ti}_2\text{O}_5$  mit Linienverbreiterung waren signifikant durch den Kationenaustausch verändert. Beobachtet wurden Frequenzverschiebungen und Intensitätsänderungen der Raman Bänder. Basierend auf den Ergebnissen der theoretischen Rechnungen für vollständig geordnetes  $\text{MgTi}_2\text{O}_5$  wurden die Moden in Raman Spektren von  $\text{Zn}_x\text{Mg}_{1-x}\text{Ti}_2\text{O}_5$  unter Berücksichtigung von Frequenz und Intensität zugeordnet. Die Rotverschiebungen der  $B_{1g}(3)$  and  $B_{1g}(5)$  Raman Moden



---

mit zunehmendem Zinkanteil zeigen eine zunehmende Verschiebung der eckenverknüpften Sauerstoffe parallel zu den [010] and [001] Richtungen an. Zusätzlich nimmt die  $B_{1g}(3)$  Mode von  $Zn_xMg_{1-x}Ti_2O_5$  in ihrer Intensität ab und geht im Untergrund für  $x$  größer 0.6 unter. Die Raman Verschiebungen und Intensitätsänderungen werden einer zunehmenden Unordnung auf den M1 Plätzen zugeschrieben. Eine besonders signifikante Frequenzänderung von identifizierten Raman Moden tritt bei der  $B_{1g}(1)$  Mode auf, die eine Blauverschiebung mit zunehmendem  $Zn^{2+}$  zeigt.

$Cu_xMg_{1-x}Ti_2O_5$  Mischkristalle,  $0 \leq x \leq 0.5$ , wurden bei einer Temperatur von 1273 K synthetisiert und bleiben in der orthorhombischen Pseudobrookit-Struktur. Kupfereinbau führt zu keiner Änderung im Zellvolumen von  $MgTi_2O_5$ . Frequenzen und Intensitäten der Raman Moden verändern sich mit dem Anteil von  $Cu^{2+}$ . Mit dem Anstieg von  $Cu^{2+}$  werden die  $B_{1g}(3)$  and  $B_{1g}(5)$  Raman Moden nach Rot verschoben für  $x$  unter 0.3 und nach Blau für größere Werte von  $x$ . Die Intensitäten der  $B_{1g}(3)$  Mode nehmen für  $x \leq 0.3$  ab und sind stabil für  $0.3 \leq x \leq 0.5$ . Diese Raman Moden zeigen, dass bis zu 30%  $Cu^{2+}$   $Mg^{2+}$  in den M1 Plätzen substituiert und ein weiterer Anstieg des  $Cu^{2+}$  Gehalts M2 Plätze besetzt. Die  $B_{1g}(1)$  Raman Mode verschiebt nach Blau durch den Kupfereinbau.

Neben den Austausch-Mischkristallreihen vom kubischen Spinelltyp ( $Cu_xZn_{2-x}TiO_4$ ), orthorhombischem Pseudobrookit-Typ ( $Zn_xMg_{1-x}Ti_2O_5$  und  $Cu_xMg_{1-x}Ti_2O_5$ ) wurden Einbau-Mischkristalle mit dem Endglied  $Ti_5Si_3$  durch SHS Reaktionen unter Argonatmosphäre synthetisiert. Die intermetallische Verbindung  $Ti_5Si_3$  hat ein Potential für Anwendung als Hochtemperatur-Strukturmaterial durch den hohen Schmelzpunkt, die geringe Dichte und den ausgezeichneten Widerstand gegen Oxidation.  $Ti_5Si_3$  zeigt eine hexagonale  $Mn_5Si_3$ -Typ Struktur mit Raumgruppe  $P6_3/mcm$ .  $Ti_5Si_3$  hat eine niedrige Duktilität und niedrige Bruchhärte. Der Einbau von Atomen in Mischkristallen läßt erwarten, die Duktilität und die Bruchhärte von  $Ti_5Si_3$  zu verbessern.  $Ti_5Si_3O_x$  wurde durch Zusatz von weniger als 40 wt.%  $Ti_5Si_3$  zum stöchiometrischen Ausgangsmaterial gewonnen, während  $Ti_5Si_3B_x$  durch Zusatz von 1–4 wt.%  $NaBH_4$  gewonnen wurde. Die Migration von Bor und Sauerstoff in die Hohlräume von  $Ti_5Si_3$  hat zu einer Kontraktion bzw. Ausdehnung der Einheitszelle geführt.



# 1 Introduction

## 1.1 Spinel

The spinel family refers to a group of compounds which are formed by a cubic close packing sublattice of the anions with 1/8 of the tetrahedral and 1/2 of the octahedral interstices occupied by the cations<sup>[1,2]</sup>. Generally, spinels have a formula of  $AB_2X_4$ , where  $A$  and  $B$  represent the cations while  $X$  denotes the anions. Though various cations with a valence from 1 to 6 can be accommodated into the spinel structure, the anions are limited to the elements O, S, Se, Te and, less commonly, Cl<sup>[3,4]</sup>.

There are many different classifications of the spinels. According to the incorporated anions, the spinels are categorised into the oxide spinels, the sulfospinel, the chloride spinels, the selenospinel and the tellurospinel. On the basis of the valences of the constituent cations, the spinels are classified as the 2-1 spinels ( $A^{2+}B_2^{1+}X_4^{1-}$  with  $B = \text{Li, Na}$  and  $X = \text{Cl, Br, F}$ )<sup>[5-7]</sup>, the 2-3 spinels ( $A^{2+}B_2^{3+}X_4^{2-}$ ), the 4-2 spinels ( $A^{4+}B_2^{2+}X_4^{2-}$ ), the 6-1 spinels ( $A^{6+}B_2^{1+}X_4^{2-}$  with  $A = \text{Mo, W}$  and  $B = \text{Na}$ )<sup>[8,9]</sup>, where the 2-3 and the 4-2 spinels are the most common types<sup>[10]</sup>. Depending on the  $B$  cations, the spinels are grouped into the aluminium spinels, the iron spinels, the chromium spinels, the vanadium spinels, the silicate spinels, the germanate spinels and other series. Based on the site occupancies of the cations in the structures, the spinels can be divided into three broad types of the normal, the inverse and the intermediate spinels (see details in page 3)<sup>[2]</sup>. There are still some other categories which are made on the basis of colour, stoichiometry and physical properties.

The natural spinel minerals host various cations and co-exist with impurity phases. Biagioni and Pasero<sup>[4]</sup> have overviewed the known 43 mineral species with a spinel-type structure including 24 oxide spinels, 18 sulfospinel and 3 selenospinel. Information of the type locality, the origin of the name, the chemical formula, the structural and spectroscopic data are summarised<sup>[4]</sup>. Due to the small size of the natural grains and formation of solid solution, the crystal structure and physical properties of some species can only be determined in the synthetic samples rather than the natural minerals<sup>[4]</sup>. Endmembers and solid solutions of the oxide spinels are significant minerals in geology, earth science, crystal chemistry and solid-state physics<sup>[11,12]</sup>. For instance,  $\text{Mg}_2\text{SiO}_4$  spinel (ringwoodite) is a high-pressure polymorph (6–18 GPa) of the major rock-forming mineral olivine and 8% denser than the olivine polymorph<sup>[13]</sup>. The solid solution with its analogous  $\text{Fe}_2\text{SiO}_4$  spinel (ahrensite) are probably the major minerals of the seismic discontinuity at 670 km depth<sup>[13]</sup>. The crystal structure, phase transition and cation ordering behaviour of the  $(\text{Mg,Fe})_2\text{SiO}_4$  spinels at deep earth conditions have been studied<sup>[14,15]</sup>. Hazen<sup>[13]</sup> demonstrates that the spinel minerals deep in the lower mantle are relatively disordered as evidenced by the increased tetrahedral bond length of the  $(\text{Mg,Fe})_2\text{SiO}_4$  spinel solid solutions with respect to the endmember  $\text{Mg}_2\text{SiO}_4$ .

Research of the oxide spinels has been carried out on the phase transition and cation disordering under non-ambient conditions as well as the structure-property relations. The cubic spinels break down to  $BO$  and  $ABO_3$  or transform to a reduced-symmetry modification at low temperatures<sup>[16]</sup>. After being annealed at low temperatures, the spinels  $Mg_2TiO_4$ ,  $Zn_2TiO_4$  and  $Mn_2TiO_4$  maintain the tetragonal structure due to ordering of the octahedral cations<sup>[16]</sup>. According to the calorimetric studies of the cubic-tetragonal transition, considerable short-range order probably exist in the spinels<sup>[16]</sup>. O'Neill et al.<sup>[17]</sup> have studied the cation disorder of  $Mg_2TiO_4$  at high temperatures using *in situ* neutron diffraction and found that 4 mol% of  $Ti^{4+}$  occupies the tetrahedral site at 1689 K. As demonstrated by Hazen and Yang<sup>[18]</sup>, the state of cation order-disorder of spinels has a dramatic effect on the bulk modulus and the thermal expansion. Compressibilities for normal (with fully ordered octahedral cations) versus inverse (with disordered octahedral cations) variants differ by as much as 17%, while the thermal expansion differs by as much as 15%<sup>[18,19]</sup>.

### 1.1.1 Crystal structure

$AB_2X_4$  spinel is built by a close-packed face-centred isometric sublattice of the anions  $X$  (typically O, S, Se, Te). The structure of  $AB_2O_4$  spinel crystals has been determined in 1915 by Bragg and Nishikawa<sup>[20]</sup>. The majority of the spinels crystallise in the cubic crystal system with space group  $Fd\bar{3}m$  ( $O_h^7$ , no. 227)<sup>[2-4,21]</sup>. The spinel structure contains 8 formula units per unit cell ( $Z = 8$ ) which includes 32 anion atoms, 64 tetrahedral interstices and 32 octahedral interstices, while the primitive unit cell consists of two formula units with a total of 14 atoms<sup>[21]</sup>. In the spinel structure, only 1/8 of the tetrahedral ( $A$ -site) and 1/2 of the octahedral ( $B$ -site) interstices are occupied by the cations<sup>[2]</sup>.

Figure 1.1 shows the polyhedral structure of the oxide spinel  $AB_2O_4$  as well as the surroundings of the  $TO_4$  tetrahedron and the  $MO_6$  octahedron. As shown in figure 1.1 (a), the octahedra are linked through edges whereas the tetrahedra are separated from each other. Each tetrahedron shares 4 vertices with 12 octahedra and one of such corner-sharings is presented in figure 1.1 (b). Figure 1.1 (c) depicts the corner- and edge-sharings of a  $MO_6$  octahedron with the adjacent 6  $TO_4$  tetrahedra and 6  $MO_6$  octahedra.

Three parameters are needed to describe the spinel structure, namely the lattice parameter  $a$ , the anion positional parameter  $u$  and the degree of inversion  $i$ <sup>[2]</sup>. Since there are 4 equivalent choices of setting for the origin of the unit cell in the spinel structure, the coordination of atoms is dependent on the choice of the origins<sup>[2]</sup>. The conventional origin is either a tetrahedrally coordinated cation with point symmetry  $\bar{4}3m$  or an octahedrally coordinated vacancy with point symmetry  $\bar{3}m$ <sup>[2]</sup>. In the latter choice, the anions occupy the Wyckoff position  $32e$  ( $u, u, u$ ), while the cations distribute between the tetrahedral Wyckoff positions  $8a$  ( $1/8, 1/8, 1/8$ ) and the octahedral Wyckoff positions  $16d$  ( $1/2, 1/2, 1/2$ )<sup>[2]</sup>.

For a perfect cubic close packed anion arrangement, which originates at  $(0, 0, 0)$  with point symmetry  $\bar{3}m$ , the anion packing density equals to 68% whereas  $u$  equals to 0.25<sup>[2]</sup>. However, the anion sublattice of the spinels is not ideally face centred. The

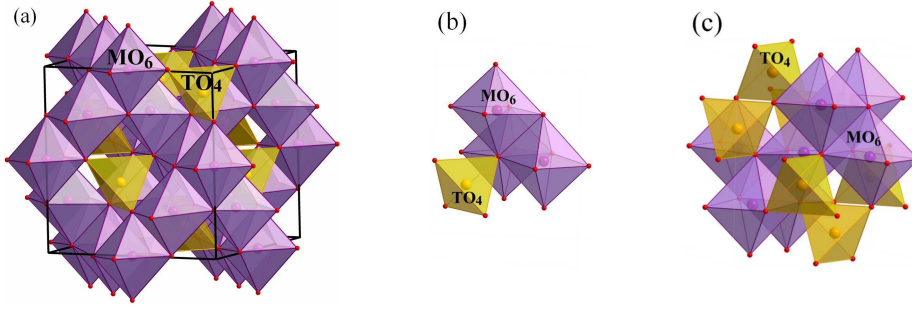


Figure 1.1: (a) Crystal structure of the oxide spinel  $AB_2O_4$  with space group  $Fd\bar{3}m$  consisting of  $TO_4$  tetrahedra and  $MO_6$  octahedra. The black rectangles show the unit cell dimensions. (b) Corner-sharing of one of the vertices of a  $TO_4$  tetrahedron with 3  $MO_6$  octahedra. (c) Surrounding of the central  $MO_6$  octahedron by 6  $TO_4$  tetrahedra and the other 6  $MO_6$  octahedra. The red spheres denote the oxygen atoms while the yellow and purple polyhedra represent the  $TO_4$  tetrahedra and the  $MO_6$  octahedra, respectively.

experimentally observed  $a$  ranges from  $\sim 9.16 \text{ \AA}$  to  $\sim 7.9 \text{ \AA}$ , which corresponds to an anion packing density of 48–74%<sup>[22]</sup>. The range of  $u$  at ambient conditions is relatively small ranging from 0.25 to 0.267<sup>[23]</sup>. With the increase of  $u$  from its ideal value, anions move away from the tetrahedrally coordinated  $A$ -sites along the  $[111]$  direction, which leads to an expansion of the  $A$ -site tetrahedron while the octahedral  $B$ -sites become correspondingly smaller<sup>[2]</sup>. Interestingly, the dependence of  $u$  on pressure varies with the specific spinel. It decreases with the increasing pressure in normal spinel  $MgAl_2O_4$  up to 4 GPa, increases with pressure in  $Ni_2SiO_4$  and keeps unchanged in  $Fe_3O_4$  even at a high pressure of 4.5 GPa<sup>[24]</sup>.

The atomic fraction of cation  $A$  in the octahedral sites is defined as the degree of inversion  $i$ <sup>[2]</sup>. The value of  $i$  is between 0 for the completely normal spinels and 1 for the completely inverse spinels. In the normal spinel structure  $A$  is in tetrahedral coordination and  $B$  is in octahedral coordination, whereas in the inverse structure half  $B$  is in tetrahedral coordination and the octahedral sites are  $A$  and half  $B$ . Spinel with an intermediate cation distribution are between the two extremes<sup>[2]</sup>. It is noticed that  $i = 2/3$  refers to a random cation arrangement throughout all cationic sites. The parameter  $i$  is influenced by several principal factors, such as the temperature, the electrostatic contribution to the lattice energy, the cationic radii, the cationic charge, and the crystal-field effects<sup>[2]</sup>.

The parameters  $a$  and  $u$  are highly dependent on the cations and adjust with the change of cation distributions<sup>[2]</sup>. For a given binary spinel compound, the spinel unit cell expands or contracts by varying  $u$ , until the  $A$ - and  $B$ -site volumes match the radii of the constituent cations<sup>[2]</sup>. According to the geometry of the spinel structure,  $a$  and  $u$  depend on the cation-anion bond lengths. For the spinels with an origin of point symmetry  $\bar{3}m$ , the average distance between the tetrahedral cation and the anion  $d_{T-O}$  and the average distance between the octahedral cation and the anion  $d_{M-O}$  are associated with the structural parameters  $a$  and  $u$  ( $\sim 0.25$ ) by the equations 1.1 and 1.2<sup>[1,2,10]</sup>.

$$d_{T-O} = \sqrt{3}a(u - 1/8) \quad (1.1)$$

$$d_{M-O} = a\sqrt{3u^2 - 2u + 3/8} \quad (1.2)$$

Based on the equations 1.1 and 1.2<sup>[1,10]</sup>, Hazen and Yang<sup>[18]</sup> give the unit cell parameter  $a$  by the expression 1.3.

$$a = \frac{40d_{T-O} + 8\sqrt{33d_{M-O}^2 - 8d_{T-O}^2}}{11\sqrt{3}} \quad (1.3)$$

Table 1.1: Structural parameters of the Ti/Ge/Sn-containing 4-2 spinels at ambient conditions. Origin of the spinel structures is (0, 0, 0) with point symmetry  $\bar{3}m$ .

Compound	$a$ [Å]	$u$	$i$	Literature
Mg <sub>2</sub> TiO <sub>4</sub>	8.4419(1), 8.4376(5)	0.2594(1), 0.2605(1)	1.0	[16,17]
Mn <sub>2</sub> TiO <sub>4</sub>	8.6806(1)	0.2611	1.0	[25]
Fe <sub>2</sub> TiO <sub>4</sub>	8.530	0.261(1)	1.0	[1,26]
Co <sub>2</sub> TiO <sub>4</sub>	8.4350(5), 8.45(5)	0.260(8)	1.0	[27,28]
Zn <sub>2</sub> TiO <sub>4</sub>	8.456, 8.467	0.2602(5), 0.255	1.0	[1,29,30]
Mg <sub>2</sub> GeO <sub>4</sub>	8.2496(6)	0.2508(5)	0.0	[31]
Fe <sub>2</sub> GeO <sub>4</sub>	8.4127(7)	0.2466(1)	0.0	[32]
Co <sub>2</sub> GeO <sub>4</sub>	8.3175(5)		0.0	[33]
Ni <sub>2</sub> GeO <sub>4</sub>	8.223(1)	0.2504(6)	0.0	[34]
Mg <sub>2</sub> SnO <sub>4</sub>	8.600	0.25	1.0	[1]
Mn <sub>2</sub> SnO <sub>4</sub>	8.865	0.258	1.0	[1]
Co <sub>2</sub> SnO <sub>4</sub>	8.62(1), 8.644	0.25	1.0	[1,35]
Zn <sub>2</sub> SnO <sub>4</sub>	8.6574	0.265	1.0	[1]
Cd <sub>2</sub> SnO <sub>4</sub>	9.143	0.267	1.0	[1]

Theoretical investigations have been made to predict the cation distribution of spinels from crystal field theory<sup>[36,37]</sup>, normalised ion energies<sup>[20]</sup> and first principles<sup>[3]</sup>. Zhang and Zunger<sup>[3]</sup> have carried out quantum mechanical calculations of 230 spinels and a success rate of 96% is achieved. The results show that the anion type plays a very minor role in determining normal versus inverse spinels<sup>[3]</sup>.

### 1.1.2 Synthesis

The solid state synthesis starting from stoichiometric mixtures of binary oxides at ambient pressure is a conventional and widely used method for the synthesis of oxide spinels. The synthesis temperature was relatively high (normally above 1473 K) and could be effectively reduced by the application of a mechanochemical activation process prior to the heat treatments<sup>[38]</sup>. In addition, nanocrystalline Zn<sub>2</sub>TiO<sub>4</sub> inverse spinel

was synthesised by ball milling the mixture of ZnO and TiO<sub>2</sub> (anatase) (2 : 1 in molar ratio) in a high energy planetary ball mill at 300 rpm for 8 h<sup>[39]</sup>. Nanocrystalline spinel solid solutions (Co,Ni)Al<sub>2</sub>O<sub>4</sub>, (Cu,Fe)Al<sub>2</sub>O<sub>4</sub> and (Cu,Cr,Fe)Al<sub>2</sub>O<sub>4</sub> were synthesised by mechanical milling and annealing at a temperature of 873 K from Al–Ni–Co and Al–Ni–Fe quasicrystalline materials<sup>[40,41]</sup>.

The synthesis condition is the key to the valence state of the transition metal cations of spinels<sup>[10]</sup>. Robertson and Pointon<sup>[42]</sup> synthesised NiFe<sub>2</sub>O<sub>4</sub> at various temperatures in the range 1373–1773 K in air and found that the magnetic moment of samples being quenched in water was larger than of samples being cooled slowly, implying a structural change due to the cooling rates. Subramanyam and Khare<sup>[43]</sup> revealed that Fe<sup>3+</sup> in NiFe<sub>2</sub>O<sub>4</sub> partly transformed to Fe<sup>2+</sup> during the sintering in air at 1373–1773 K, as indicated by an increase of the lattice parameter. Besides, the stoichiometry of spinels containing the transition metal cation is highly sensitive to the oxygen fugacity<sup>[44]</sup>. Tare et al.<sup>[45]</sup> replaced one of the starting materials, CuO, with metallic copper to synthesise ZnCuTiO<sub>4</sub>, ZnCuSnO<sub>4</sub> and ZnCuGeO<sub>4</sub> by a solid state method at 1373 K. However, hexagonal ZnCuGeO<sub>4</sub> was obtained instead of the expected cubic structure<sup>[45]</sup>. Though ZnCuTiO<sub>4</sub> cubic spinel was obtained, copper had two oxidation states of +1 and +2, as estimated from the structure factors using the XRD data<sup>[45]</sup>.

Besides the solid state synthesis, wet chemical methods are used for the synthesis of spinels<sup>[46]</sup>. Inagaki et al.<sup>[47]</sup> prepared Co<sub>2</sub>TiO<sub>4</sub> using alkoxide hydrolysis in a solution of the ammonium complex and found that the positional parameter  $u$  varied from 0.258 to 0.266, and the lattice parameter ranged from 8.421 Å to 8.448 Å. Tribochemical reaction of LiCl with ZnCl<sub>2</sub> was proved to be an easy method for synthesising the stable spinel-type ambient-temperature modification of Li<sub>2</sub>ZnCl<sub>4</sub><sup>[6]</sup>. In addition, ternary halides such as Li<sub>2</sub>MnCl<sub>4</sub> and Li<sub>2</sub>ZnCl<sub>4</sub> were synthesised by dehydration of the appropriate hydrates<sup>[6]</sup>. Nanocrystalline MAl<sub>2</sub>O<sub>4</sub> spinels ( $M = \text{Co, Ni or Co}$ ) were prepared in different particle sizes using single source heterometal alkoxides in a microemulsion assisted sol-gel process<sup>[48]</sup>. Ferdov<sup>[49]</sup> reported an one-step template-free, mild hydrothermal synthesis of highly crystalline, phase pure nanoparticles of Cu<sub>2</sub>GeO<sub>4</sub> at a low temperature of 503 K and autogenous pressure for several days using a Teflon-lined stainless steel autoclave by fast cooling.

### 1.1.3 Physical properties and applications

Recent studies show that the transparent MgAl<sub>2</sub>O<sub>4</sub> spinel ceramics with a low residual porosity of less than 0.1% and a small pore diameter of less than 20 nm, which allow both visible and infrared electromagnetic radiation to go through, can be fabricated by hot pressing<sup>[50]</sup> and spark plasma sintering<sup>[51]</sup>. Oxide spinels AB<sub>2</sub>O<sub>4</sub> and those doped with transition metal cations, have emerged as interesting semiconductors<sup>[52,53]</sup>, efficient photocatalysts<sup>[54]</sup>, pigments and dyes, substrates for integrated electronics<sup>[22]</sup>, as well as transparent windows and shield materials<sup>[50,55]</sup>.

Some of the oxide spinels have interesting conductivities and are suitable for applications as light emitting diodes and electronics due to the energy splitting of the transition metal cations in the octahedral sites<sup>[52]</sup>. The transparent spinel films containing at least two transition metal cations, typically NiCo<sub>2</sub>O<sub>4</sub>, were reported to be  $p$ -type semicon-

ductors<sup>[52]</sup>.  $ZnM_2O_4$  with  $M = Co, Rh, Ir$  were identified as potential  $p$ -type transparent semiconductors<sup>[53,56,57]</sup>. However, the density field theory calculations of the valence band showed that they are not  $p$ -type alternative to the industry standard  $n$ -type transparent conducting oxides<sup>[58]</sup>. Nevertheless, the semiconductor spinels are proven to be efficient photocatalysts in the degradation of pollutants and/or the production of photocatalytic hydrogen, such as  $MgAl_2O_4$  nanoparticles<sup>[54]</sup>.

Superconductivity of spinels has been observed. It is detected at 4.80 K in  $CuRh_2S_4$ , at 3.49 K for  $CuRh_2Se_4$  and at 4.45 K for  $CuV_2S_4$ <sup>[59]</sup>.  $LiTi_2O_4$  is the only known spinel oxide superconductor with a superconducting transition temperature of  $T_c = 11$  K<sup>[60–62]</sup>. It displays the highest  $T_c$  at ambient conditions in the spinel group<sup>[62]</sup>.  $T_c$  of  $CuRh_2Se_4$ ,  $CuRh_2S_4$  and  $LiTi_2O_4$  increased linearly under hydrostatic pressure up to 2.2 GPa<sup>[63]</sup>. Incorporation of  $Mg^{2+}$  into  $LiTi_2O_4$  caused a reduction of  $T_c$ <sup>[64]</sup>. The superconducting property of  $Li_{1+x}Ti_{2-x}O_4$  was homogeneous for  $x \leq 0.15$  and disappeared at higher  $x$  values. Cao et al.<sup>[65]</sup> studied the superconductivity of Zn-doped  $CuIr_2S_4$  and found that superconductivity appeared due to the substitution of  $Cu^{2+}$  for  $Zn^{2+}$ .  $T_c$  decreased from 3.3 K to 2.2 K with an increasing content of zinc from 25 mol% to 50 mol%<sup>[65]</sup>. Luo et al.<sup>[66]</sup> reported the observation of superconductivity in  $CuIr_2Se_4$  spinel induced by partial replacements of Ir with Pt, where an addition of 20 mol% Pt resulted in a highest  $T_c$  of 1.76 K.

Magnetic spinels have a wide range of applications such as microwave devices, solid oxide fuel cells and magnetic recording<sup>[67]</sup>.  $Co_2SnO_4$  shows ferromagnetic ordering below 41 K and is in the spin-glass state below 39.1 K<sup>[68,69]</sup>. The anomalous magnetic ordering of  $Co_2SnO_4$  are ascribed to the special cation distribution, different magnitudes of  $Co^{2+}$  moments on the  $A$  and  $B$ -sites and their different temperature dependences, and zero moment on  $Sn^{4+}$ <sup>[69]</sup>.  $Co_2TiO_4$  has a ferromagnetic order temperature of 55 K and a spin-glass temperature of 46 K<sup>[28]</sup>. In addition, the magnetic properties of ferrite spinels are particularly sensitive to their cation distribution<sup>[70]</sup>.

Thermal expansion behaviours of various oxide spinels (except ferrites) in the temperature region 293–1293 K have been measured by high-temperature X-ray diffraction, where powder samples were prepared by the solid state method<sup>[71]</sup>. Cation occupancy of the octahedral sites is the main influence on the magnitude of the thermal expansion coefficient  $\alpha$ <sup>[71]</sup>. Generally, a big valency difference between the octahedral and the tetrahedral cations leads to a high  $\alpha$  value<sup>[71]</sup>. For example, the 1-6 spinel  $Na_2WO_4$  has the highest  $\alpha$  of  $24.6 \pm 0.7 \times 10^{-6} K^{-1}$  while the 2-3 spinel  $CoCr_2O_4$  shows the lowest  $\alpha$  of  $6.6 \pm 0.3 \times 10^{-6} K^{-1}$ <sup>[71]</sup>. Meanwhile,  $\alpha$  of the spinel with an identical valence of the octahedral cations is smaller than that with mixed valencies<sup>[71]</sup>. Moreover, the formation of superstructures affects  $\alpha$  of the spinels.  $\alpha$  of the superstructures  $Li_2ZnGe_3O_8$  and  $Li_2ZnTi_3O_8$  is double the value of the spinels  $LiAl_5O_8$  and  $LiAl_5O_8-ZnAl_2O_4$ <sup>[71]</sup>.

The oxide spinels show similar bulk moduli and a similar global compressibility of around 200 GPa<sup>[23,72]</sup>. The bulk modulus of the solid solution  $(Mg,Fe)_2SiO_4$  only varies from 184 GPa for  $Mg_2SiO_4$  to 207 GPa for  $Fe_2SiO_4$ <sup>[13]</sup>. It is explained by an equal compression rate for the  $FeO_6$  octahedra, the  $MgO_6$  octahedra and the  $SiO_4$  tetrahedra along the solid solution<sup>[73]</sup>.



## 1.2 Pseudobrookites

Pseudobrookite originally refers to the mineral  $\text{Fe}_2\text{TiO}_5$ , which is observed naturally at the locality of Hunedoara county, Romania<sup>[74,75]</sup>. It occurs frequently in basalts and is a common accessory mineral in oxidised igneous rocks<sup>[76]</sup>. As determined by Pauling<sup>[77]</sup>, the crystal structure of  $\text{Fe}_2\text{TiO}_5$  has an orthorhombic symmetry and is built up of edge- and corner-sharing octahedra which occupy two crystallographically non-equivalent distorted 6-coordinated sites (Wyckoff positions  $4c$  and  $8f$ ). Natural pseudobrookite minerals have an intermediate composition between  $\text{Fe}_2\text{TiO}_5$  and the isomorphous  $\text{FeTi}_2\text{O}_5$ , and contain some appreciable Mg and some other minor elements (Cr, Al, V, Mn, Ca, Zr)<sup>[74]</sup>.

Minerals with the same orthorhombic pseudobrookite-type structure as  $\text{Fe}_2\text{TiO}_5$  are described by the pseudobrookite group  $A_2B\text{O}_5$  where  $A$  and  $B$  stand for the cations. It includes the natural endmember minerals  $\text{Fe}_2\text{TiO}_5$  (pseudobrookite),  $\text{FeTi}_2\text{O}_5$  (ferropseudobrookite),  $\text{MgTi}_2\text{O}_5$  (karooite) and  $\text{Mg}_{0.5}\text{Fe}_{0.5}\text{Ti}_2\text{O}_5$  (armalcolite), as well as several synthetic compounds, such as  $\text{Al}_2\text{TiO}_5$  (tielite),  $\text{Ti}_3\text{O}_5$  (anosovite),  $\text{Ga}_2\text{TiO}_5$ ,  $\text{CoTi}_2\text{O}_5$ ,  $\text{Sc}_2\text{TiO}_5$  and  $\text{Fe}_2\text{ZrO}_5$ <sup>[19,74]</sup>. Natural armalcolites are first discovered in the high-Ti basalts from Mare Tranquillitatis on the moon, which are essentially  $\text{FeTi}_2\text{O}_5$ – $\text{MgTi}_2\text{O}_5$  solid solutions bearing minor trivalent  $\text{Al}^{3+}$  and  $\text{Cr}^{3+}$ <sup>[78,79]</sup>. It is later identified on earth and in meteorites<sup>[74]</sup>. Notably, the mineral  $\text{Fe}_2\text{MgTi}_3\text{O}_{10}$  with the discarded name of Kennedyite is in fact an intermediate of the armalcolite solid solution<sup>[74]</sup>. No occurrence of tielite is naturally observed. However, the synthetic  $\text{Al}_2\text{TiO}_5$  has been developed as filter materials, ceramic pigments and excellent thermal shock resistances for insulating applications in engine components such as portliners, piston bottoms and turbochargers due to the low thermal expansion and high refractory<sup>[80,81]</sup>.

The stability of the pseudobrookite-type structure at ambient conditions is attributed to the large positive entropy of formation<sup>[82,83]</sup>. Being a sum of the vibrational and configurational effects, the entropy increases with increasing cation disorder<sup>[82]</sup>. It is possible to predict the thermal history of naturally occurring pseudobrookites based on cation distributions<sup>[84]</sup>. Pseudobrookite oxide solid solutions may have had a critical role in the petrogenesis of the mare basalts and lunar picritic glasses as a source of  $\text{TiO}_2$ , and be present in other planetary bodies as well<sup>[85]</sup>. They are of particular theoretical and practical interests because of the cation order-disordering phenomena and the participation in the  $\text{TiO}_2$ -slag smelting process. The site occupancies of the pseudobrookites affect their physical and mechanical properties.

### 1.2.1 Crystal structure

The pseudobrookite-type structure consists of edge- and corner-sharing distorted octahedra and has an orthorhombic symmetry<sup>[77]</sup>. It is commonly described in space group  $Cmcm$  ( $D_{2h}^{17}$ , no. 63)<sup>[22,86,87]</sup>. Alternative settings use space groups  $Bbmm$ <sup>[77,88,89]</sup> and  $Ccmm$ <sup>[90,91]</sup>. The lattice parameters  $a$ ,  $b$  and  $c$  in space group  $Cmcm$  correspond to  $c$ ,  $a$  and  $b$  in  $Bbmm$ , and  $b$ ,  $a$  and  $c$  in  $Ccmm$ , respectively. There are two crystallographically distinct cation sites in the pseudobrookite-type structure, namely Wyckoff  $4c$  ( $M1$ , point symmetry  $m2m$ ) and  $8f$  ( $M2$ , point symmetry  $m$ ) positions<sup>[87]</sup>. The  $M1$  octahedron is

larger than the  $M2$  octahedron and both sites are fully occupied by the cations<sup>[87]</sup>. Each unit cell contains four formula units ( $Z = 4$ ) with a total of 32 atoms, including 4 cations in the  $M1$  sites and 8 cations in the  $M2$  sites<sup>[87]</sup>.

Cation distribution of  $AB_2O_5$  can be described by the disorder parameter  $X$  or the order parameter  $s$ <sup>[92]</sup>.  $X$  is defined as the atomic concentration of cations  $A$  in  $M1$  sites ( $0 \leq X \leq 1$ ) and  $s$  relates with it by  $s = 1 - 2X$  ( $-1 \leq s \leq 1$ )<sup>[83,93]</sup>. The fully ordered structure of  $AB_2O_5$  has cations  $A$  in  $M1$  sites and cations  $B$  in  $M2$  sites. Thus,  $X = 0$  while  $s = 1$ <sup>[93]</sup>. The cations  $A$  can interchange with  $B$  to form a disordered structure<sup>[92]</sup>.  $X = 2/3$  or  $s = -1/3$  denotes a completely disordered structure where all cations are randomly distributed between the two octahedral sites<sup>[93]</sup>. The anti-ordered phase has all cations  $A$  in  $M2$  sites, corresponding to  $X = 1$  and  $s = -1$ <sup>[93]</sup>.

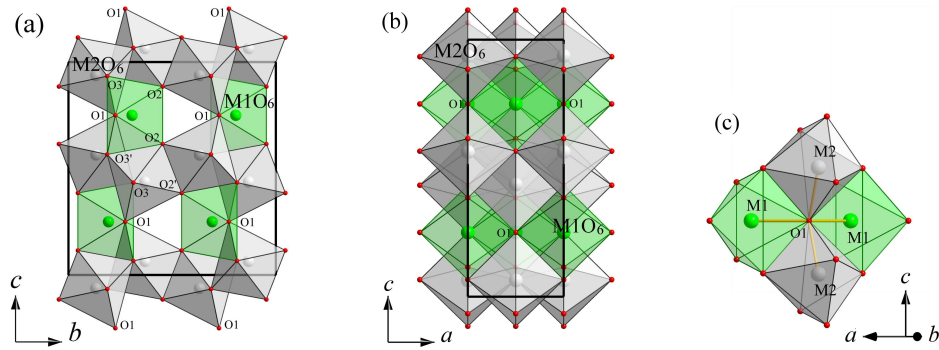


Figure 1.2: Crystal structure<sup>[88,89]</sup> of the orthorhombic pseudobrookite-type  $MgTi_2O_5$  with space group  $Cmcm$  consisting of  $MO_6$  octahedra ( $M = Mg/Ti$ ). (a) and (b) present views along  $[100]$  and  $[010]$ , respectively. (c) gives the corner-sharing of 2  $M1$  octahedra and 2  $M2$  octahedra via the bridging oxygen  $O1$ . The black rectangles show the unit cell dimensions. The red, green and gray spheres denote the oxygen atoms and the cations in the  $M1$  and  $M2$  sites, respectively.

Figure 1.2 shows crystal structure of the orthorhombic pseudobrookite-type  $MgTi_2O_5$  with space group  $Cmcm$ <sup>[88,89]</sup> and the linkage of the  $MO_6$  octahedra where  $M$  refers to  $Mg/Ti$  cations. As shown in figure 1.2 (a), the edge-sharing  $M2$  octahedra form double chains running along the  $[010]$  direction, which are connected through the oxygen bridges  $O1$  and the  $M1$  octahedra. Figure 1.2 (b) shows that the double chains extend in the  $[100]$  direction and the bridging oxygens  $O1$  link the octahedra forming corners. The corner-sharing of the  $M1$  and  $M2$  octahedra is depicted in figure 1.2 (c). In an ideal fully ordered structure of  $MgTi_2O_5$ , the larger  $M1$  sites are exclusively occupied by the  $Mg^{2+}$  ions (mean radius  $r_{Mg} = 0.72 \text{ \AA}$ )<sup>[94]</sup> while the  $Ti^{4+}$  ions ( $r_{Ti} = 0.605 \text{ \AA}$ )<sup>[94]</sup> would occupy the  $M2$  sites. However, part of  $Mg^{2+}$  in the  $M1$  sites can be exchanged by  $Ti^{4+}$ , giving rise to a lattice expansion. The  $Mg/Ti$  disorder parameter  $X$ , which is defined as the atomic concentration of  $Ti$  in  $M1$  sites, can be linearly correlated with the ambient temperature lattice parameter  $b$  (in space group  $Cmcm$ ) according to the equation:  $X = 8.6909b - 84.334$ <sup>[92]</sup>.

The  $Mg/Ti$  order is related to the thermal history of  $MgTi_2O_5$ <sup>[92]</sup>. Usually, quench-

ing from high temperatures leads to an increase of the cation disorder, while annealing at low temperatures or high pressures results in a decrease of the cation disorder<sup>[89,92,95]</sup>. The Mg/Ti disorder of MgTi<sub>2</sub>O<sub>5</sub> can be partly or fully retained at ambient conditions<sup>[83]</sup>. The high-temperature Mg<sup>2+</sup>-Ti<sup>4+</sup> configuration of MgTi<sub>2</sub>O<sub>5</sub> probably can be quenched between 1000 to 1300 K, whereas annealing in excess of 70 days is needed for temperatures below 1000 K<sup>[83]</sup>.

Crystal structure and cation distribution of the binary solid solution series such as Fe<sub>2</sub>TiO<sub>5</sub>-FeTi<sub>2</sub>O<sub>5</sub><sup>[96]</sup>, FeTi<sub>2</sub>O<sub>5</sub>-Ti<sub>3</sub>O<sub>5</sub><sup>[90]</sup>, FeTi<sub>2</sub>O<sub>5</sub>-MgTi<sub>2</sub>O<sub>5</sub>, MgTi<sub>2</sub>O<sub>5</sub>-Ti<sub>3</sub>O<sub>5</sub><sup>[91]</sup> and MgTi<sub>2</sub>O<sub>5</sub>-Al<sub>2</sub>TiO<sub>5</sub> have been extensively studied by employing X-ray diffraction, Mössbauer spectroscopy and neutron diffraction. Navrotsky<sup>[82]</sup> has summarised the thermodynamical data of the Ti-containing pseudobrookites A<sub>2</sub><sup>3+</sup>Ti<sup>4+</sup>O<sub>5</sub> (A = Fe, Al, Ga, Ti) and B<sup>2+</sup>Ti<sub>2</sub><sup>4+</sup>O<sub>5</sub> (B = Fe, Mg). Results show that Ti<sup>4+</sup> has a strong preference for the M2 (8f) sites<sup>[82]</sup>. The solid solution FeTi<sub>2</sub>O<sub>5</sub>-Ti<sub>3</sub>O<sub>5</sub> have been characterised by Mössbauer spectroscopy and X-ray diffraction, where Mössbauer spectra are sensitive to the monoclinic distortion of the structure<sup>[90]</sup>. With an iron concentration of above 35 mol% the pseudobrookite-type solid solution maintains the orthorhombic symmetry while with less iron it exhibits a monoclinic distortion<sup>[90]</sup>. Ferrous ions in the fourfold and eightfold sites give rise to separate quadrupole doublets in the Mössbauer spectra, and thus the site occupancy can be determined as a function of composition by a least-squares analysis of the spectra<sup>[90]</sup>.

### 1.2.2 Synthesis

Many of the pure pseudobrookites are only available in synthetic form including MgTi<sub>2</sub>O<sub>5</sub>, Al<sub>2</sub>TiO<sub>5</sub>, Ti<sub>3</sub>O<sub>5</sub>, Ga<sub>2</sub>TiO<sub>5</sub>, CoTi<sub>2</sub>O<sub>5</sub>, Sc<sub>2</sub>TiO<sub>5</sub>, Fe<sub>2</sub>ZrO<sub>5</sub>, MgFeNbO<sub>5</sub> and MgFeTaO<sub>5</sub><sup>[19,74]</sup>. Therefore, in this section the synthesis of the pseudobrookite-type endmembers and solid solutions (single crystals and polycrystalline samples) will be introduced.

MgTi<sub>2</sub>O<sub>5</sub> single crystals have been grown by melting a 1:2 mixture of MgO and TiO<sub>2</sub> in an Ir crucible in air with an induction furnace, annealing at about 1773 K for 12 h and then quenching to ambient temperature<sup>[88]</sup>. Yang and Hazen<sup>[89]</sup> synthesised white and transparent MgTi<sub>2</sub>O<sub>5</sub> crystals by the flux method in air derived from MgO and TiO<sub>2</sub> contained in a Pt crucible in a vertical tube furnace. K<sub>2</sub>WO<sub>4</sub> was used as a flux and a high temperature of 1673 K was employed<sup>[89]</sup>. The parent MgTi<sub>2</sub>O<sub>5</sub> crystals were obtained by quenching from 1473 K to ambient temperature and mainly elongated along the *a* axis (in space group *Cmcm*)<sup>[89]</sup>. A dimension of more than 1 mm was achieved in the largest crystal<sup>[89]</sup>. Finally, MgTi<sub>2</sub>O<sub>5</sub> crystals with the cation disorder parameter ranging from 0.070(5) to 0.485(5) were obtained by annealing at 873–1673 K for 5–1008 h followed by a quenching process<sup>[89,97,98]</sup>.

Black needle-like crystals of armalcolite, Mg<sub>0.5</sub>Fe<sub>0.5</sub>Ti<sub>2</sub>O<sub>5</sub>, up to several millimetres in length, have been grown from a glass initially having the composition of the lunar rock<sup>[88]</sup>. The glass was prepared by melting a mixture of pure oxides, Fe metal and synthetic anorthite with an induction furnace in a closed Fe crucible in an Ar atmosphere above the liquidus temperature and was quenched by turning off the power<sup>[88]</sup>. Then the glass was placed on a Mo strip heater of the furnace with flowing He and H<sub>2</sub> and

$\text{Mg}_{0.5}\text{Fe}_{0.5}\text{Ti}_2\text{O}_5$  crystallised during the rise of the temperature<sup>[88]</sup>. Finally, the crystals were gradually cooled to about 1273 K and then rapidly cooled to ambient temperature<sup>[88]</sup>. As a result, the armalcolite crystals grew as needles with their  $b$  axes oriented normal to the strip heater (space group  $Cmcm$ )<sup>[88]</sup>.

Polycrystalline pseudobrookites have been widely synthesised by solid state reactions of the oxides. The conventional synthesis temperature is in the range 1573–1773 K. In the  $\text{MgO-TiO}_2$  binary system, the mixture in any ratio preferably formed  $\text{MgTiO}_3$  and then  $\text{MgTi}_2\text{O}_5$  was produced from stoichiometric  $\text{MgTiO}_3$  and  $\text{TiO}_2$  (1 : 1 in molar ratio)<sup>[99,100]</sup>. Due to the addition of a LiF flux, a low temperature at 1273 K was achieved for the reactive sintering of  $\text{MgTi}_2\text{O}_5$ <sup>[99]</sup>.

Matteucci et al.<sup>[101]</sup> synthesised  $\text{Mg}_{1-x}\text{Ti}_{2-x}\text{M}_{2x}\text{O}_5$  with  $x = 0.02$  or  $0.05$  ( $M = \text{V, Cr, Mn, Fe, Co, Ni}$ ) from the oxides at 1573 K in air in an electric kiln and the samples were cooled naturally by shutting off the kiln. Huang and Shen<sup>[102]</sup> synthesised  $\text{Mg}_{0.95}\text{M}_{0.05}^{2+}\text{Ti}_2\text{O}_5$  from the oxides at 1623–1773 K using a cooling rate of  $10 \text{ K min}^{-1}$ . Llusar et al.<sup>[103]</sup> substituted  $\text{Mg}^{2+}$  in  $\text{MgTi}_2\text{O}_5$  for up to 0.6  $\text{Ni}^{2+}$  per formula by solid state synthesis, using  $\text{MgCO}_3$ ,  $\text{NiO}$  and  $\text{TiO}_2$  (anatase) as precursors. They demonstrated that the solid solubility of the divalent  $\text{Ni}^{2+}$  in  $\text{MgTi}_2\text{O}_5$  increased with the synthesis temperature<sup>[103]</sup>. The solubility of  $\text{Ni}^{2+}$  was below 10 mol% at 1273 K, around 40 mol% at 1473 K and around 60–70 mol% at 1673–1773 K<sup>[103]</sup>. By employing the natural cooling to ambient temperature and the fast quenching with liquid  $\text{N}_2$  at 1673 K, the maximum incorporation of  $\text{Ni}^{2+}$  was between 60 mol% and 70 mol%<sup>[103]</sup>.

$\text{MgFeNbO}_5$  and  $\text{MgFeTaO}_5$  were synthesised by Bayer<sup>[22]</sup> using solid state reactions of the corresponding oxides in an oxidising atmosphere at 1523 K. They were derived from  $\text{MgTi}_2\text{O}_5$  by substituting 2  $\text{Ti}^{4+}$  for  $\text{Fe}^{3+}$  and  $\text{Nb}^{5+}$  (or  $\text{Ta}^{5+}$ ). Bayer<sup>[22]</sup> made attempts to prepare other  $\text{Mg}^{2+}\text{A}^{3+}\text{B}^{5+}\text{O}_5$ -type compounds ( $\text{MgAlNbO}_5$ ,  $\text{MgAlTaO}_5$ ,  $\text{MgGaNbO}_5$ ,  $\text{MgGaTaO}_5$ ,  $\text{MgCrNbO}_5$ ,  $\text{MgCrTaO}_5$ ,  $\text{MgFeSbO}_5$ ,  $\text{MgFeVO}_5$ ) and the corresponding compositions with Zn, Ni, Co, and Cu instead of Mg. However, none of them was successful in the employed temperature range 1523–1773 K<sup>[22]</sup>. Bayer<sup>[22]</sup> speculated that some of these combinations might form pseudobrookite phases which were only stable at high temperatures. In addition, attempts to substitute a combination of trivalent and pentavalent cations for  $\text{Ti}^{4+}$  in  $\text{Al}_2\text{TiO}_5$  were not successful<sup>[22]</sup>. Moreover, substitution of  $\text{Ti}^{4+}$  by other tetravalent ions ( $\text{Ge}^{4+}$ ,  $\text{Sn}^{4+}$ ,  $\text{Zr}^{4+}$ ) at temperatures up to 1773 K in air was partly successful for  $\text{MgTi}_2\text{O}_5$  but not for  $\text{Al}_2\text{TiO}_5$ <sup>[22]</sup>. Pure  $\text{Ga}_2\text{TiO}_5$ , the least stable pseudobrookite, was prepared by annealing at 1773 K for 20 h and then quenching<sup>[22]</sup>.

Nanosized  $\text{MgTi}_2\text{O}_5$  powders have been prepared by various wet processes, including hydrolysis, co-precipitation, and sol-gel methods<sup>[100]</sup>. Kapoor et al.<sup>[104]</sup> attempted to synthesise nanocrystalline pseudobrookite-type  $\text{MTi}_2\text{O}_5$  ( $M = \text{Mg, Mn, Fe, Co, Zn}$  and  $\text{Sn}$ ) for photocatalysis applications by a modified aerogel process. The preparation method involved the formation of a single source precursor by the condensation reaction of  $\text{Ti}(\text{OPr}^n)_4$  with  $M(\text{OAc})_2$ , followed by  $(M[\text{O-Ti}(\text{OPr}^n)_3]_2)$  hydrolysis and drying under supercritical conditions. However, only  $\text{MgTi}_2\text{O}_5$  with a pseudobrookite-type structure was obtained<sup>[104]</sup>.

As a special member of the pseudobrookite group,  $\text{Ti}_3\text{O}_5$  is stabilised in the monoclinic structure at ambient conditions<sup>[105]</sup>. When it was heated from ambient tem-

perature,  $\text{Ti}_3\text{O}_5$  transformed into the orthorhombic pseudobrookite-type phase  $\alpha\text{-Ti}_3\text{O}_5$  above 500 K<sup>[105,106]</sup>. By doping with  $\text{Mg}^{2+}$ , the orthorhombic  $\text{Ti}_3\text{O}_5$  can be stabilised at ambient conditions<sup>[106]</sup>.

### 1.2.3 Physical properties and applications

Generally, the pseudobrookites with space group  $Cmcm$  are characterised by an unusually strong expansion anisotropy, where the thermal expansion is negative or very small in the  $a$  direction and quite large in the  $b$  and  $c$  directions<sup>[22]</sup>. Bayer<sup>[22]</sup> performed thermal expansion measurements of the pseudobrookites in two temperature ranges of 293–794 K and 293–1293 K where a strong expansion anisotropy was observed in each case. The smallest expansion was always found in the  $a$  direction, which were even negative for  $\text{Al}_2\text{TiO}_5$  and  $\text{Ga}_2\text{TiO}_5$ <sup>[22]</sup>. The highest expansion occurred in the  $c$  direction, whereas the expansion in the  $b$  direction (around  $8 \times 10^{-6} \text{ K}^{-1}$ ) was in the typical range observed for close-packed oxides such as  $\text{Al}_2\text{O}_3$ ,  $\text{TiO}_2$  and  $\text{MgO}$ <sup>[22]</sup>. The bridging oxygens (equivalent to O1 of  $\text{MgTi}_2\text{O}_5$  in figure 1.2) probably play a special role for the strong expansion in the  $c$  and also in the  $b$  direction<sup>[22]</sup>. Despite large anisotropic thermal expansions, the volume thermal expansion coefficients of pseudobrookites are not too different from those of other close-packed oxides<sup>[22]</sup>.

Due to the small bulk thermal expansion coefficient and high refractive index,  $\text{Al}_2\text{TiO}_5$  and  $\text{MgTi}_2\text{O}_5$  are expected to be used as high-temperature ceramics with good thermal shock resistance<sup>[100]</sup>. However, the expectation is not fulfilled<sup>[22]</sup>. In polycrystalline pseudobrookites, thermal expansion anisotropy leads to the formation of internal cracks by thermal stresses, which makes the bulk material mechanically weak<sup>[100,107]</sup>. Besides microcracking, the decomposition of pseudobrookites at high temperatures is another undesirable property for applications<sup>[87,92,108]</sup>. The decomposition is not only a function of time and temperature but also of the purity and size of the crystals<sup>[22,107]</sup>. Single crystals or larger crystals will be more stable than small crystals<sup>[22]</sup>. Moreover, the crystallite size affects thermal diffusivity of the polycrystalline pseudobrookite<sup>[109]</sup>. Siebeneck et al.<sup>[109]</sup> studied the effect of grain size on the thermal diffusivity of polycrystalline  $\text{MgTi}_2\text{O}_5$  from 298 K to 1073 K and observed that the decrease of the thermal diffusivity of the sample with a small grain size was much more pronounced than in the sample with a large grain size by a factor of two.

$\text{Al}_2\text{TiO}_5$  decomposes into the oxides (corundum and rutile) after prolonged heating in the temperature range 1023–1573 K<sup>[22]</sup>. Above 1573 K, the oxides combine again to form  $\text{Al}_2\text{TiO}_5$ <sup>[22]</sup>.  $\text{Ga}_2\text{TiO}_5$  is the least stable pseudobrookite<sup>[22]</sup> and it decomposes strongly exothermically into the components at 1253 K when being heated<sup>[22]</sup>.  $\text{Al}_2\text{TiO}_5$  needs a longer heating time (e.g. 100 h at 1273 K) to decompose completely<sup>[22]</sup>.  $\text{Fe}_2\text{TiO}_5$ ,  $\text{MgTi}_2\text{O}_5$  and  $\text{MgFeTaO}_5$  are the most stable pseudobrookites<sup>[22]</sup>. Table 1.2 tabulates physical properties of the most common pseudobrookites.

Huang and Shen<sup>[102]</sup> have studied microwave dielectric properties of the  $\text{MgTi}_2\text{O}_5$ -based ceramics by replacing 5 mol% Mg with the transition metals Co, Ni or Zn. Results show that cation substitution of  $\text{MgTi}_2\text{O}_5$  leads to an improvement of the microwave dielectric property<sup>[102]</sup>. The  $\text{Mg}_{0.95}\text{M}_{0.05}\text{Ti}_2\text{O}_5$  solid solution ( $M = \text{Co}, \text{Ni}, \text{Zn}$ ) has a much lower dielectric loss, a compatible dielectric constant and similar resonant frequency

Table 1.2: Melting temperature  $T_m$ , decomposition temperature  $T_{\text{decom}}$ , linear thermal expansion coefficient  $\alpha$  ( $\times 10^{-6} \text{K}^{-1}$ ) in the temperature range of 298–873 K of the most common pseudobrookites.

	$\text{Fe}_2\text{TiO}_5$	$\text{FeTi}_2\text{O}_5$	$\text{MgTi}_2\text{O}_5$	$\text{Al}_2\text{TiO}_5$
$T_m$ [K]			1923 <sup>[110]</sup>	2133 <sup>[111]</sup>
$T_{\text{decom}}$ [K]	838 <sup>[92]</sup>	1413 <sup>[92]</sup>	$\sim 403$ <sup>[100]</sup>	1023–1573 <sup>[22]</sup>
$\alpha_a/\alpha_b/\alpha_c$	0.7(1)/9.8(6)/14.6(7) <sup>[22]</sup>		2.3(2)/8.1(4)/13.2(7) <sup>[22]</sup>	–2.9(2)/10.3(6)/20(1) <sup>[22]</sup>

stability as compared to  $\text{MgTiO}_3$ - and  $\text{MgTi}_2\text{O}_4$ -based ceramics<sup>[102]</sup>.

A new field of application for the pseudobrookites is that of ceramic pigments for low-temperature glazes and glassy coatings with a firing temperature below 1323 K. Dondi et al.<sup>[112]</sup> synthesised pseudobrookite-type brown pigments, which had a 6–20 % excess of  $\text{TiO}_2$  in the chemical stoichiometry  $\text{Fe}_2\text{TiO}_5$ . The pigments were well dispersed in glazes and glassy coatings under industrial fast firing condition with a synthesis temperature of 1473 K<sup>[112]</sup>. However, the colouring performance depended on the ceramic matrices and varied from intense brown, light brown to light grey<sup>[112]</sup>. Pigments based on  $\text{MgTi}_2\text{O}_5$  and  $\text{Al}_2\text{TiO}_5$  were more widely studied<sup>[101,103]</sup>. With incorporation of 2–5 mol% transition metal ions,  $\text{MgTi}_2\text{O}_5$  ceramic pigments with colours ranging from orange, brown tan (Cr, Fe, Mn, V), green (Co) to yellow (Ni) were obtained<sup>[101]</sup>. They could be applied to low-temperature ceramic glazes and glassy coatings, which have a synthesis temperature of below 1323 K<sup>[101]</sup>. Llusar et al.<sup>[103]</sup> investigated yellow pigments by substituting up to 60 mol%  $\text{Mg}^{2+}$  in  $\text{MgTi}_2\text{O}_5$  with divalent  $\text{Ni}^{2+}$ . The  $(\text{Ni,Mg})\text{Ti}_2\text{O}_5$  pigments were only partially stable in the tested ceramic glazes with a synthesis temperature range of 1273–1323 K and were much less stable in a Ca- and Zn-enriched glaze<sup>[103]</sup>. Dondi et al.<sup>[81]</sup> synthesised  $\text{Al}_2\text{TiO}_5$ -based ceramic pigments at 1673 K and applied them to the glaze with a synthesis temperature of 1323 K. The colour of pigments was pink for  $(\text{Al,Co})\text{Ti}_2\text{O}_5$  and  $(\text{Al,Mg,Co})\text{Ti}_2\text{O}_5$ , green for  $(\text{Al,Cr})\text{Ti}_2\text{O}_5$  and brown for  $(\text{Al,Mn})\text{Ti}_2\text{O}_5$  and  $(\text{Al,Mg,Mn})\text{Ti}_2\text{O}_5$ <sup>[81]</sup>. Their crystal structure, optical properties, colouring performance and thermal stability were investigated<sup>[81]</sup>. The expected decomposition of  $\text{Al}_2\text{TiO}_5$  into a mixture of  $\text{Al}_2\text{O}_3$  and  $\text{TiO}_2$  on refiring at above 1173 K was inhibited by the doping of Cr, Mg/Co and Mg/Mn<sup>[81]</sup>. In summary, the ceramic glazes obtained from  $\text{Al}_2\text{TiO}_5$ -based pigments, except for those containing Co, showed satisfactory performances<sup>[81]</sup>.

### 1.3 Task and outline

The spinel group  $AB_2O_4$  and the pseudobrookite group  $A_2BO_5$ , where  $A$  and  $B$  denote the cations, are both dense oxide minerals containing two crystallographically distinct sites occupied by at least two different cations<sup>[19]</sup>. Despite the common structural character, the spinels have a cubic symmetry with space group  $Fd\bar{3}m$  showing isotropic physical properties whereas the pseudobrookites are described in the orthorhombic space group  $Cmcm$  resulting in anisotropic physical properties. The cations compete between the tetrahedral and octahedral sites in spinels while in pseudobrookites the

cations distribute between the two octahedral sites. Incorporation of various cations, including transition metals, into each type of the structures leads to a systematic change of the physical properties<sup>[103,113]</sup>, which enable applications as pigments, filters, semiconductors, dielectrics, catalysts, anodes for Li-ion batteries, etc.<sup>[52,53,81]</sup>. In addition, the cation distribution affects the unit cell volume, compressibility, thermal expansion and elasticity of the dense oxide minerals<sup>[11,18,97]</sup>. Therefore, the main goal of the thesis is to investigate the effect of cation substitution on the crystal structure and physical properties in the spinel and pseudobrookite systems. The experimental studies have been complemented by theoretical approaches, which were performed by Prof. Dr. Björn Winkler.

The substitutional solid solutions were chosen to contain tetravalent  $\text{Ti}^{4+}$  cations, which is one of the major refractory rock-forming elements. The endmember was cubic inverse spinel  $\text{Zn}_2\text{TiO}_4$  and orthorhombic pseudobrookite-type  $\text{MgTi}_2\text{O}_5$ . Solid state synthesis and self-propagating high-temperature synthesis (SHS), which were assisted by a mechanochemical activation process, were employed to obtain the substitutional solid solutions of  $\text{Cu}_x\text{Zn}_{2-x}\text{TiO}_4$ ,  $\text{Zn}_x\text{Mg}_{1-x}\text{Ti}_2\text{O}_5$  and  $\text{Cu}_x\text{Mg}_{1-x}\text{Ti}_2\text{O}_5$ . The samples were characterised by X-ray diffraction (XRD) using our laboratory X-ray diffractometer and neutron diffraction (ND) using the D2B neutron diffractometer at Institut Laue-Langevin (ILL, Grenoble). Rietveld refinements of the XRD and ND data were employed for the structural analyses. The microstructure of the bulk samples was characterised by scanning electron microscopy (SEM). Moreover, vibrational, elastic, UV-vis absorption, thermal expansion and low-temperature thermodynamic properties of the samples were analysed. Density functional theory (DFT) calculations were carried out to predict the theoretical properties, which were compared with the experimental results.

In addition to the investigation of the substitutional solid solutions, interstitial atoms were incorporated into the trigonal antiprisms of the hexagonal  $\text{Mn}_5\text{Si}_3$ -type  $\text{Ti}_5\text{Si}_3$  compound by self-propagating high-temperature synthesis. Structural changes of the interstitial solid solutions  $\text{Ti}_5\text{Si}_3\text{Z}_x$  ( $Z = \text{B/O}$ ) were investigated by employing Rietveld and Le Bail refinements of XRD data.





## 2 Experimental methods and principles

This chapter outlines the basic principles of the experimental methods, a description of the materials, experimental equipments and procedures, and the softwares for data analysis.

High-speed ball milling, solid state synthesis and self-propagating high-temperature synthesis were employed for the sample preparations. X-ray and neutron diffraction were employed to identify crystalline phases of the polycrystalline samples and solve the crystal structures based on Rietveld refinements. Vibrational and optical properties of the samples were characterised by Raman, infrared and UV-vis spectroscopy. Low-temperature thermodynamic properties were investigated by measuring the low-temperature heat capacities. In order to supplement the experimental results, quantum-mechanical calculations based on density functional theory were performed by Prof. Dr. Björn Winkler. The microstructure, density, elasticity and linear thermal expansion coefficients of the bulk sample were characterised by SEM, the bouyancy method, plane-wave ultrasound spectroscopy and a dilatometer, respectively.

### 2.1 Mechanochemical activation assisted synthesis

Mechanochemical processing refers to a powder processing technique involving deformation, fracturing and cold welding of the particles during repeated collisions with a ball during high-energy milling<sup>[114]</sup>. The process uses mechanical energy to activate chemical reactions, structural changes and particle size reduction<sup>[38,114]</sup>. In the thesis, mechanochemical activation of the solid mixture by high-energy ball milling was employed to assist the synthesis of samples.

#### 2.1.1 High-speed ball milling

High-speed ball milling was employed to mix the starting materials uniformly and increase the reactivity of the mixture.

Figure 2.1 (a) presents a photograph of our laboratory planetary ball mill (Fritsch P7). The grinding bowls and balls are available in several different materials: agate (density  $2.65 \text{ g cm}^{-3}$ ), stainless steel (density  $7.8 \text{ g cm}^{-3}$ ) and tungsten carbide (density  $14.7 \text{ g cm}^{-3}$ ). Bowls and balls of the same material are used in the mechanochemical activation process. The capacity of the equipped grinding bowls is 80 mL. The grinding balls have different diameter sizes: 10 mm and 15 mm. Gassing lids for all grinding bowls are equipped so that various grinding atmospheres are available: air, inert gas and reactive gas.

Figure 2.1 (b) shows a schematic drawing of the planetary ball mill<sup>[114]</sup>. The starting materials are crushed and ground by grinding balls in the bowls. The grinding bowls

and the support disc have opposite directions of rotation. The disk rotates at an angular velocity  $\omega$  whereas the grinding bowls rotate at an angular velocity  $\omega_1$ , where  $\omega_1 = -2\omega$ .

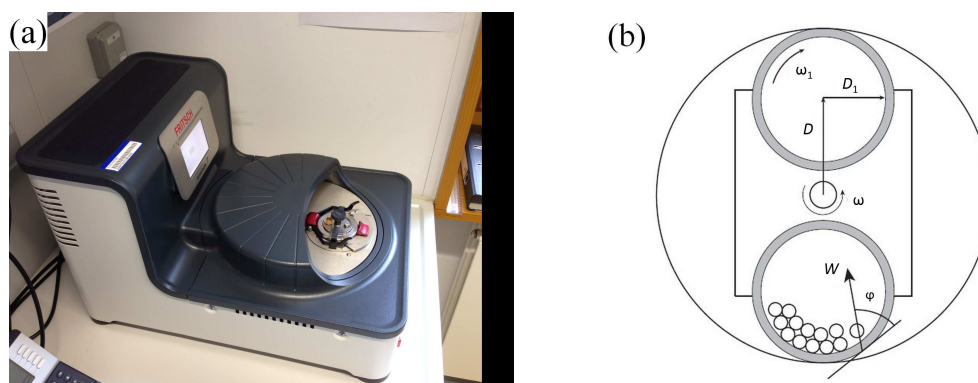


Figure 2.1: The planetary high-speed ball mill: (a) a photograph of the ball mill (Fritsch P7) and (b) a schematic drawing<sup>[114]</sup>.  $\omega_1 = -2\omega$ , where  $\omega_1$  is the angular velocity of the grinding bowl rotation and  $\omega$  is the angular velocity of the disk rotation.

The mechanochemical activation conditions have significant effects on kinetics of the phase transition<sup>[114]</sup>. Table 2.1 tabulates experimental parameters of the mechanochemical activation processes in various solid solutions. The chosen material of bowls and balls is tungsten carbide due to the high density.

Table 2.1: Mechanochemical activation conditions of the solid solutions.

	$\text{Cu}_x\text{Zn}_{2-x}\text{TiO}_4$	$\text{MgTi}_2\text{O}_5$	$\text{Zn}_x\text{Mg}_{1-x}\text{Ti}_2\text{O}_5$		$\text{Cu}_x\text{Mg}_{1-x}\text{Ti}_2\text{O}_5$
Starting materials	oxides	oxides	oxides	oxides, $\alpha$ -Ti	oxides
Speed of the disc rotation	300 rpm	300 rpm	300 rpm	750 rpm	300 rpm
Grinding atmosphere	air	air	air	Ar	air
Material of bowls and balls	tungsten carbide (93% WC + 6% Co, density $14.7 \text{ g cm}^{-3}$ )				
Volume of bowls	80 mL				
Diameter of balls	10 mm				
Mass ratio of balls to powder	10 : 1				

### 2.1.2 Solid state synthesis

Solid state synthesis is the most common and conventional method to synthesise compounds<sup>[115]</sup>. The compound crystallises at high temperatures and retains the crystal structure at ambient temperature<sup>[115]</sup>. In the solid state synthesis process, the starting materials were mixed, pressed into cylinders and then heat treated in a furnace (Nabertherm) at different temperatures. The green density of the cylinders, which refers to a bulk density of the ceramic compact prior to sintering, was controllable by varying the mass of the mixture. Solid state reactions of the explored compounds and solid solutions took place at a temperature range of 1073–1573 K. The samples were ei-

ther cooled down naturally to ambient temperature by switching off the electric power of the furnace or quenched from the synthesis temperature into a mixture of ice/water.

### 2.1.3 Self-propagating high-temperature synthesis

Self-propagating high-temperature synthesis describes a process in which, once being initiated, the reaction occurs in a very fast mode as combustion wave propagation<sup>[116,117]</sup>. It is discovered in 1967 and allows a near net-shape production of industrial components even ones with complex shapes<sup>[118]</sup>. A wide range of materials, such as refractory compounds, thermal unstable compounds, alloys and thermoelectrics, have been synthesised by using this method<sup>[117,119]</sup>.

Figure 2.2 presents a photograph and a schematic diagram of our SHS set-up. The reactions were initiated using the tungsten coil and five samples could be placed in the combustion chamber at maximum. The combustion chamber was pumped to be vacuum and then purged with Ar prior to the reaction. In order to exclude reactive gas in the chamber, the process was repeated twice. The SHS reaction took place under Ar flow and pressure of the inert gas inside the chamber was slightly higher than ambient pressure.

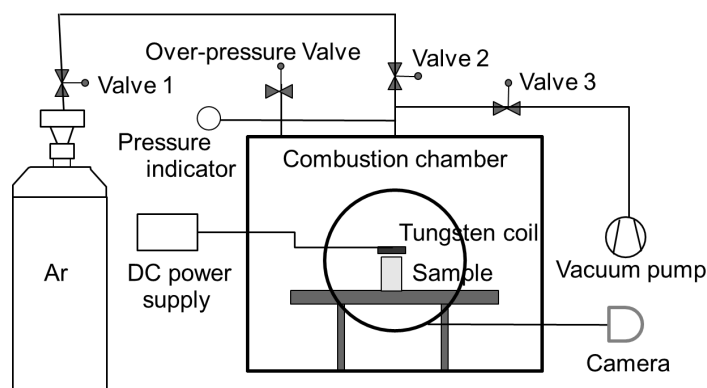


Figure 2.2: Photograph and schematic drawing of the SHS set-up.

## 2.2 X-ray diffraction and neutron diffraction

Crystal structures of the polycrystalline samples were determined by XRD and ND data. Rietveld refinement, which was developed by Hugo M. Rietveld<sup>[120,121]</sup>, was employed to analyse the XRD and ND data. The Rietveld refinements were carried out using the GSAS, EXPGUI and gsalanguage software packages<sup>[122–124]</sup>.

The Bragg equation 2.1<sup>[125]</sup> expresses the condition for diffraction when the electromagnetic waves or neutrons interact with crystals.

$$n\lambda = 2d \sin \theta \quad (2.1)$$

where  $n$  is an integer,  $\lambda$  refers to the wavelength of the radiation,  $d$  is the interplanar spacing between lattice layers and  $\theta$  is the angle between the incident beam and the family of lattice planes.

In the elastic scattering process, X-rays interact with the electron cloud whereas neutrons interact with the nuclei<sup>[126]</sup>. Figure 2.3 shows the change of the X-ray scattering factor and coherent neutron scattering length with  $\sin \theta / \lambda$  for some ions<sup>[127,128]</sup>. The scattering factor of X-rays decreases with the increasing scattering angles while the scattering length of neutrons is independent of the scattering angles.

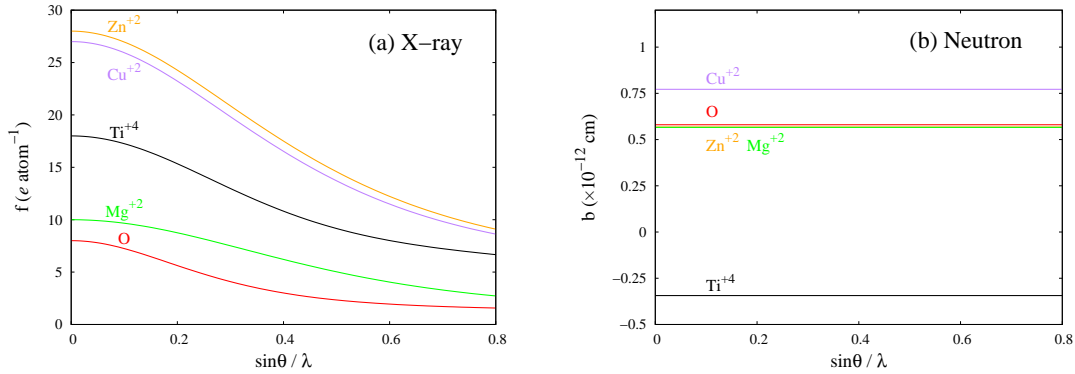


Figure 2.3: (a) X-ray scattering factor with  $\text{CuK}\alpha_1$  radiation and (b) coherent neutron scattering length vs.  $\sin \theta / \lambda$  for the ions<sup>[127,128]</sup>.

The XRD data were measured using our laboratory X-ray diffractometer (PANalytical X'Pert Pro) with Bragg-Brentano geometry and  $\text{CuK}\alpha_1$  radiation, as shown in figure 2.4 (a). A PIXcel detector is installed, which improves the resolution and greatly shortens the measuring time. The ND data were collected on the D2B diffractometer at ILL. Figure 2.4 (b) shows the layout of the instrument<sup>[129]</sup>.

The Rietveld method uses least-squares refinements to minimise residuals between the experimental data and the calculated data<sup>[130]</sup>. Equation 2.2 is the residual<sup>[130]</sup>.

$$S_y = \sum_i w_i (y_i - y_{ci})^2 \quad (2.2)$$

where  $w_i = 1/y_i$ ,  $y_i$  and  $y_{ci}$  is the observed and calculated intensity at the  $i^{\text{th}}$  step, respectively.

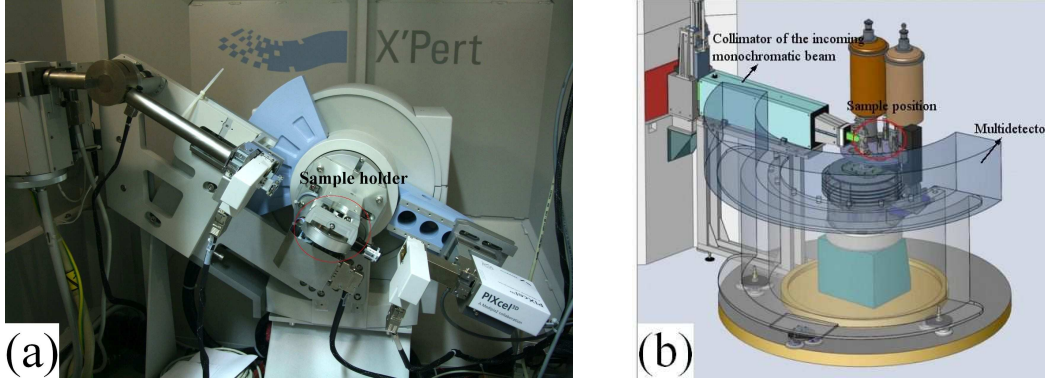


Figure 2.4: (a) Bragg-Brentano geometry in PANalytical X'Pert Pro X-ray diffractometer, (b) Instrument layout of D2B neutron diffractometer at ILL<sup>[129]</sup>.

Peak shapes and the background in the XRD and ND data were described by pseudo-Voigt functions and the polynomial function, respectively<sup>[130]</sup>. Background, zero shift, absorption correction, lattice parameters, and profile parameters (GU, GV, GW, LX, LY) were preliminarily refined using the Le Bail method<sup>[131]</sup>. It differed from the Rietveld method in that only background, lattice parameters and peak shape were refined and no structural parameter contributed to the calculated intensities<sup>[130]</sup>. Then Rietveld refinement was carried out to refine these parameters together with structural parameters, which included atom positional parameters ( $x, y, z$ ), site occupancies and isotropic thermal displacement parameters ( $U_{iso}$ ). Finally, convergence was achieved after some iterations and estimated standard deviations (esd's) of the refined parameters were obtained. Esd's provided by the programme GSAS indicated the accuracy of the least-squares fit<sup>[122]</sup>.

Rietveld agreement  $R$ -factors and the reduced  $\chi^2$  (goodness of fit) were used as indicators for the quality of the least-squares refinement. Weighted profile  $R$ -factor  $R_{wp}$ , weighted background corrected  $R$ -factor  $R_{wpb}$ , and the reduced  $\chi^2$  were described in equation 2.3, 2.4 and 2.5, respectively<sup>[122]</sup>.

$$R_{wp} = \sqrt{\frac{\sum w (I_o - I_c)^2}{\sum w I_o^2}} \quad (2.3)$$

$$R_{wpb} = \sqrt{\frac{\sum w \left( \frac{(I_o - I_c)(I_o - I_b)}{I_o} \right)^2}{\sum w (I_o - I_c)^2}} \quad (2.4)$$

$$\chi^2 = \frac{\sum w (I_o - I_c)^2}{N_{obs} - N_{var}} \quad (2.5)$$

where  $w$  is the weight,  $I_o$  and  $I_c$  denote the observed and computed reflection intensities, respectively<sup>[122]</sup>.  $I_b$  is the background contribution to the profile<sup>[122]</sup>.  $N_{obs}$  is the total number of observations in the diffractogram and  $N_{var}$  is the number of variables

in the least-squares refinement<sup>[122]</sup>.

## 2.3 Raman and infrared spectroscopy

Vibrational properties of the polycrystalline samples were characterised by Raman and IR spectroscopy in experiments and theory. The data complement each other and are able to provide information about the structures.

Raman scattering is the inelastic scattering generated by the interactions of photons with molecular vibrations, phonons in solids or other excitations<sup>[132]</sup>. Figure 2.5 gives a photograph of the Raman spectrometer (Renishaw) and an energy-level diagram showing the incident radiation  $E_i$  and the scattered radiation  $E_e$ <sup>[133]</sup>.

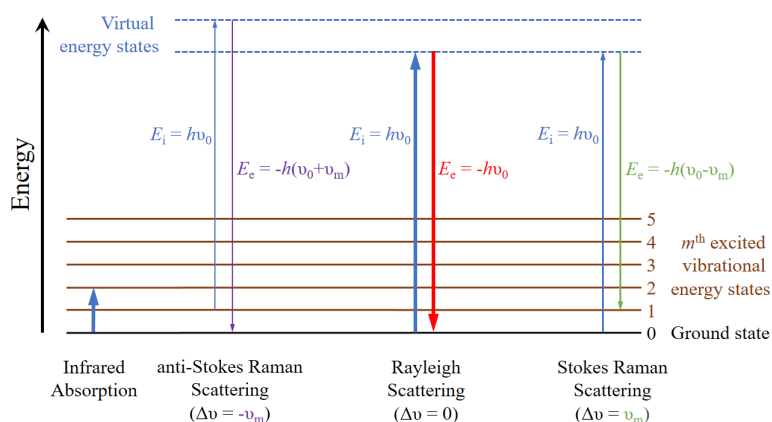


Figure 2.5: (a) Photograph of the Raman spectrometer (Renishaw), (b) Energy-level diagram showing the states and radiations involved in Raman scattering<sup>[133]</sup>.

The inelastic Stokes and anti-Stokes Raman scattering lines are on each side of the elastic Rayleigh line where energies of the scattered photons are the same with the incident energy of  $h\nu_0$ <sup>[133]</sup>. The Stokes scattered photon has an energy of  $h(\nu_0 + \nu_m)$  while the anti-Stokes scattered photon has an energy of  $h(\nu_0 - \nu_m)$ <sup>[132,134,135]</sup>. The energy shift of photons gives information about the phonon modes in the systems. A polarizability change of phonons is required for the systems to exhibit the Raman effect

and the amount of the polarizability change determines the Raman scattering intensity<sup>[132,134,135]</sup>.

IR spectrum, which plots the vibrational intensity with IR frequency, is generated by the changes of dipole moment or charge distribution caused by the vibrational excitation of bonds and groups upon absorption of the infrared radiations<sup>[135]</sup>. It provides a reflection of the vibrational motions<sup>[135]</sup>.

## 2.4 Low-temperature heat capacity

Low-temperature heat capacity  $C_p$  of solids is mainly contributed from electrons and phonons<sup>[136]</sup>. For nonmetal and nonalloy solids without magnetic transition at low temperatures, the electronic contribution is very small compared with the contribution of phonons (lattice vibrations)<sup>[136]</sup>. Hence,  $C_p$  equals to the lattice heat capacity, i.e. the contribution of phonons<sup>[136]</sup>.

The standard enthalpy  $H^0$  and entropy  $S^0$  at 298 K can be calculated by integrating  $C_p$  and  $\frac{C_p}{T}$  over temperature in the range of 0–298 K, respectively, as shown in equations 2.6 and 2.7<sup>[136]</sup>.

$$H^0 = \int_0^{298\text{K}} C_p dT \quad (2.6)$$

$$S^0 = \int_0^{298\text{K}} \frac{C_p}{T} dT \quad (2.7)$$

A physical property measurement system (PPMS, Quantum Design) with an available temperature range of 1.9–400 K was employed to measure heat capacities of the samples. Figure 2.6 shows a photograph of the equipment.



Figure 2.6: Photograph of the physical property measurement system (Quantum Design).

The PPMS probe consists of a superconducting magnet, a temperature control and

a sample puck connector<sup>[137]</sup>. The connector is at the bottom of the sample chamber and offers convenient access to electrical leads and sample mounting<sup>[137]</sup>. It allows you to plug in a removable sample insert<sup>[137]</sup>. Environment of the sealed sample chamber is controllable by operating the vacuum pump, heaters and thermometers<sup>[137]</sup>. The sample insert is first pumped to be vacuum and cooled down to 1.9 K by helium<sup>[137]</sup>. Then heaters warm the gas to the correct temperature<sup>[137]</sup>. At each temperature, the response to a heat pulse is measured three times<sup>[137]</sup>. Heat capacities of the empty holder containing adhesive, with which the sample is thermally coupled to the sample insert, are measured prior to the sample mounting and are automatically removed by the operation system<sup>[137]</sup>. The actual thermal coupling of the samples is recorded and compensated in order to determine the heat capacities of samples<sup>[137]</sup>.

### 2.5 Density functional theory

Density functional theory is presently one of the most successful approaches to compute the electronic structure of condensed matter<sup>[138]</sup>. Using this theory, the structure-property relations of a many-electron system can be investigated by using functionals of the electron density<sup>[139]</sup>. Perdew-Burke-Ernzerhof (PBE), the most popular GGA-type (generalised gradient approximation) functional, is able to give reliable results for the chemical bonds including the covalent, ionic, metallic and hydrogen bridge<sup>[138]</sup>.

In order to predict lattice dynamical properties of fully ordered MgTi<sub>2</sub>O<sub>5</sub>, *ab initio* simulation based on DFT using a plane-wave basis set and normconserving pseudopotentials<sup>[140,141]</sup> was carried out by Prof. Dr. Björn Winkler. The theoretical results complemented the experimental observations and provided fundamental understanding of the vibrational, elastic and low-temperature thermodynamic properties.

### 2.6 Other methods

A scanning electronic microscopy (PhenomProX) was employed to examine the microstructure homogeneity of the bulk samples for the elasticity and thermal expansion measurements. Figure 2.7 (a) shows the SEM photograph. Bouyancy density of the samples was obtained by using the set-up in figure 2.7 (b).

Elastic stiffness coefficients of the samples at ambient conditions were predicted by DFT calculations and determined by the plane-wave ultrasound spectroscopy (HP 4395A network analyzer). Figure 2.8 (a) gives a photograph of the set-up. The velocities of the ultrasonic wave,  $v$ , are obtained by equation 2.8<sup>[142,143]</sup>.

$$v = 2D\Delta f \quad (2.8)$$

where  $D$  is the thickness of the sample,  $\Delta f$  is the separation between neighboring resonant frequencies.

The elastic stiffness coefficients,  $c_{ij}$ , are related to the ultrasound velocity  $v$  and the sample density  $\rho$  by equation 2.9<sup>[142,143]</sup>.



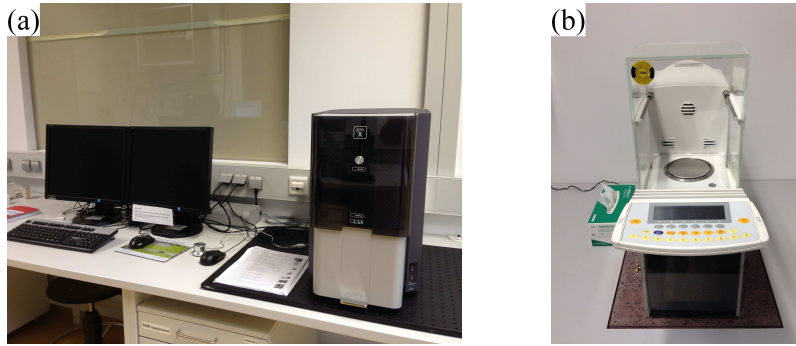


Figure 2.7: Photographs of (a) the SEM (PhenomProX) and (b) the buoyancy density set-up.

$$c_{ij} = \rho v^{-2} \quad (2.9)$$

Thermal expansions of the samples were measured in the temperature range of 297–1067 K in air atmosphere with a dilatometer (Netzsch4), as shown in figure 2.8 (b). The dilatometer was calibrated with a corundum pellet.

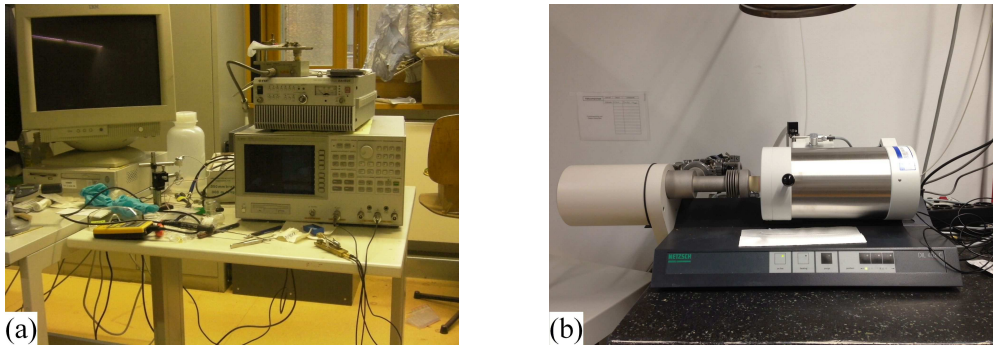


Figure 2.8: Photographs of (a) the plane-wave ultrasound spectroscopy (HP 4395A) and (b) the dilatometer (Netzsch4).

Optical properties of the samples were measured by UV-vis spectroscopy equipped with a tungsten lamp and a deuterium lamp. UV-vis absorption spectra demonstrate the absorbed wavelengths of light. The samples absorb UV and visible radiations and undergo electronic transitions. The absorbance of samples,  $A$ , is related to the intensity of light passing through the sample ( $I$ ) and the intensity of light passing through the blank reference ( $I_0$ ) according to equation 2.10.

$$A = \log \frac{I}{I_0} \quad (2.10)$$



## 3 $\text{Cu}_x\text{Zn}_{2-x}\text{TiO}_4$ with $0 \leq x < 1$

### 3.1 Introduction

Among the  $\text{Ti}^{4+}$ -containing spinels, all the known compounds  $\text{Mg}_2\text{TiO}_4$ ,  $\text{Mn}_2\text{TiO}_4$ ,  $\text{Fe}_2\text{TiO}_4$ ,  $\text{Co}_2\text{TiO}_4$ ,  $\text{Zn}_2\text{TiO}_4$  and  $\text{LiFeTiO}_4$  crystallise with an inversion parameter  $i = 1$  in space group  $Fd\bar{3}m$  at ambient conditions<sup>[144,145]</sup>. Solid solutions based on the  $\text{Zn}_2\text{TiO}_4$  cubic inverse spinel have attracted significant attention due to a wide range of applications, including their use as catalysts, semiconductors, pigments, photoluminescent materials and dielectrics<sup>[146,147]</sup>.

According to the XRD studies and colour of the spinels, replacing  $\text{Zn}^{2+}$  in cubic spinel  $\text{Zn}_2\text{TiO}_4$  with other divalent metal ions like  $\text{Mg}^{2+}$ ,  $\text{Co}^{2+}$  and  $\text{Ni}^{2+}$  led to an increasing loss of zinc in the octahedral site of the cubic spinels<sup>[21]</sup>. The divalent cations had similar Shannon ionic radii<sup>[94]</sup>:  $r_{\text{Zn}} = 0.74 \text{ \AA}$ ,  $r_{\text{Mg}} = 0.72 \text{ \AA}$ ,  $r_{\text{Ni}} = 0.69 \text{ \AA}$ ,  $r_{\text{Co}} = 0.65 \text{ \AA}$  for low spin state and  $0.745 \text{ \AA}$  for high spin state. For the  $\text{Mg}_x\text{Zn}_{2-x}\text{TiO}_4$  spinel solid solution with  $0 \leq x \leq 1$ , there was no change in the lattice parameter<sup>[21]</sup>. However, incorporation of the transition metal cations ( $\text{Co}^{2+}$ ,  $\text{Ni}^{2+}$ ) into spinel  $\text{Zn}_2\text{TiO}_4$  consistently resulted in a contraction of the unit cell<sup>[148]</sup>. With increasing replacement of  $\text{Zn}^{2+}$  by  $\text{Co}^{2+}$ , the lattice parameter of the  $\text{Co}_x\text{Zn}_{2-x}\text{TiO}_4$  spinel solid solution decreased linearly for  $x$  below 0.6 and remained the same for  $0.6 \leq x \leq 1$ <sup>[148]</sup>. In the other cubic spinel solid solution of  $\text{Ni}_x\text{Zn}_{2-x}\text{TiO}_4$ , the accessible incorporation of  $\text{Ni}^{2+}$  was limited to 0.635<sup>[148]</sup>. With the increase of nickel, the lattice parameter of  $\text{Ni}_x\text{Zn}_{2-x}\text{TiO}_4$  decreased linearly<sup>[148]</sup>.

A recent study showed that around 0.85 molar fraction of  $\text{Zn}^{2+}$  was substituted by  $\text{Cu}^{2+}$  ( $r_{\text{Cu}} = 0.73 \text{ \AA}$ ) at maximum<sup>[113]</sup>. The lattice parameter of the  $\text{Cu}_x\text{Zn}_{2-x}\text{TiO}_4$  cubic spinel solid solution ( $0 \leq x < 1$ ) decreased with increasing copper concentrations<sup>[113]</sup>. The results indicated that  $\text{Cu}^{2+}$  was probably incorporated into both the octahedral and tetrahedral sites of the spinel solid solution<sup>[113]</sup>. Since very few studies have been reported on  $\text{Cu}^{2+}$ -containing 4-2 oxide cubic spinels<sup>[45,113]</sup>, the accurate cation distribution of  $\text{Cu}_x\text{Zn}_{2-x}\text{TiO}_4$  cubic spinels are of fundamental interest. In addition, a complete substitution of  $\text{Zn}^{2+}$  for  $\text{Cu}^{2+}$  was reported in the  $\text{Cu}_x\text{Zn}_{1-x}\text{Al}_2\text{O}_4$  normal spinel solid solution<sup>[149]</sup>, which was different with the incomplete solid solubility of  $\text{Cu}_x\text{Zn}_{2-x}\text{TiO}_4$ <sup>[113]</sup>. It is worth comparing cation distribution of the two systems. Therefore, high-resolution powder neutron diffraction data of the cubic spinel solid solution  $\text{Cu}_x\text{Zn}_{2-x}\text{TiO}_4$  with  $0 \leq x < 1$  were collected and the Rietveld method was employed to provide detailed structural changes due to the replacement of  $\text{Zn}^{2+}$  by  $\text{Cu}^{2+}$ .

## 3.2 Materials and methods

### 3.2.1 Sample preparation

Ten samples with compositions of  $\text{Cu}_x\text{Zn}_{2-x}\text{TiO}_4$  ( $0 \leq x < 1$ ) were prepared starting from the binary oxides (purity 99%, Merck) ZnO, CuO and  $\text{TiO}_2$  (anatase). For  $x$  ranging from 0 to 0.7, the interval was 0.1 and molar ratio of the oxides was in stoichiometric amounts. Molar fractions of CuO:ZnO: $\text{TiO}_2$  in the other two samples were 0.75:1.25:1 and 1:1:1, which corresponded to the spinel  $\text{Cu}_x\text{Zn}_{2-x}\text{TiO}_4$  with  $x$  around 0.75 and 0.86, respectively.

The mixture of the oxides was ball milled at 300 rpm for 8 h using a planetary ball mill (Fritsch P7). The material of the grinding bowls and balls was tungsten carbide and the mass ratio of balls to powder was 10:1. Then the well-blended mixture was pressed into small cylinders (diameter 5 mm, height 9 mm), followed by a heat treatment at 1073 K for 8 h in air. Finally, the cylinders were ground into powder using an agate mortar.

The phase composition of the samples was checked by XRD using  $\text{CuK}\alpha_1$  radiation ( $\lambda = 1.5406 \text{ \AA}$ , 40 kV, 30 mA) at ambient conditions. The X-ray diffractometer was calibrated using silicon powders. The  $2\theta$  scan range, step size, and time per step were  $10\text{--}90^\circ$ ,  $0.01^\circ$  and 150 s, respectively. It took 1 h for the data collection of one sample. Results showed that the samples were mainly cubic spinel phases. However, a second phase ZnO appeared in the samples with a nominal composition of  $x < 0.5$  and an increasing amount of an impurity phase CuO emerged for  $x \geq 0.6$ .

Acetic acid was tested to reduce the impurity contamination in  $\text{Cu}_x\text{Zn}_{2-x}\text{TiO}_4$  spinels. Before treating the samples, the starting chemicals of ZnO and CuO were immersed in a dilute solution of acetic acid (75 vol.%  $\text{CH}_3\text{COOH}$  and 25 vol.%  $\text{H}_2\text{O}$ ), respectively. ZnO dissolved in the solution quickly while it took a longer time to remove CuO. The samples with a nominal composition of  $\text{Cu}_x\text{Zn}_{2-x}\text{TiO}_4$ ,  $0 \leq x \leq 0.7$ , were treated by soaking in the acetic acid solution for 4 days and then washed with distilled water 5 times. Afterwards, XRD measurements were repeated in a selected range of  $2\theta = 25\text{--}44^\circ$ . Due to the slow dissolution rate of CuO in the acetic acid solution and the apparent amount of co-existing CuO, the samples with  $x = 0.75$  and 0.86 were used without any treatment.

### 3.2.2 X-ray diffraction

XRD measurement with a  $\text{CuK}\alpha_1$  radiation was carried out for the sample with  $x = 0.4$  before and after the soaking treatment, respectively. A  $2\theta$  scan range of  $10\text{--}140^\circ$  and a step size ( $\sim 0.002^\circ$ ) were used. Each measurement took around 15 h.

Rietveld refinements<sup>[120,121]</sup> of the powder XRD data with pseudo-Voigt profile functions were carried out using the GSAS<sup>[122]</sup> and EXPGUI<sup>[123]</sup> software packages. The background was described by a Chebyshev polynomial with 8 terms. Absorption correction due to the rough surface of powder samples was made. All atoms were described with an isotropic thermal displacement parameter  $U_{\text{iso}}$ . Cations in the same set of sites were constrained to have the same value of  $U_{\text{iso}}$ . All sites were assumed to be fully occupied and copper was assumed to occupy the octahedral sites. The refinement

sequence was as follows: scale factor, background, absorption correction, zero shift, lattice parameter  $a$ , sample displacement, more background, profile parameters (GU, GV, GW, LX, LY), oxygen positional parameter  $u$ ,  $U_{\text{iso}}$  and cation occupancy. Titanium was allowed to be in both tetrahedral and octahedral coordinations.

### 3.2.3 Neutron diffraction

High-resolution powder neutron diffraction data of 10 samples were collected at ambient conditions on the D2B diffractometer of the Institut Laue-Langevin. The powder sample with a typical mass of 5 g was put into a cylindrical vanadium can for the measurement. A Ge 335 monochromator was employed to produce a neutron beam with a monochromatic wavelength of 1.5946(10) Å. The primary neutron beam was focused by putting a collimator with a vertical divergence of  $1/6^\circ$  and a horizontal slit of 30 mm between the monochromator and sample. Neutron reflection intensities were collected in a  $2\theta$  range of  $0\text{--}160^\circ$ . The diffractometer is equipped with 128 detectors which are spaced at  $1.25^\circ$  intervals. With a step size of  $0.05^\circ$ , every scan takes 25 steps. Each scan was repeated 10 times to obtain a complete diffraction pattern with improved statistics. One measurement took around 4 h.

Structural analyses by Rietveld refinements<sup>[120,121]</sup> of the neutron diffraction data were performed using the GSAS<sup>[122]</sup>, EXPGUI<sup>[123]</sup> and gsastrans<sup>[124]</sup> software packages. Data in the  $2\theta$  range of  $0\text{--}20^\circ$  ( $d > 3.68$  Å) were excluded from the analyses, since there were no reflections and the backgrounds were too complex to refine. The background was modeled by a Chebyshev polynomial with 24 terms. Neutron cross section for Ti, Zn, Cu and O was taken as  $-0.3438$ ,  $0.5680$ ,  $0.7718$  and  $0.5803 \times 10^{-12}$  cm<sup>-1</sup>, respectively<sup>[128]</sup>.

A starting model of Zn<sub>2</sub>TiO<sub>4</sub> with the fully inverse cubic spinel structure<sup>[150]</sup> was used to refine Cu <sub>$x$</sub> Zn <sub>$2-x$</sub> TiO<sub>4</sub> spinels. Fractions of Zn<sup>2+</sup>, Cu<sup>2+</sup> and Ti<sup>4+</sup> were allowed to vary in either the tetrahedral sites or the octahedral sites. All atoms were treated with an isotropic thermal displacement parameter  $U_{\text{iso}}$  and cations in the same set of sites were constrained to have the same  $U_{\text{iso}}$ . The refined parameters are tabulated in table 3.1. Convergence was achieved at the last step of refinement, where scale factor, background, crystal structural parameters and profile parameters were refined simultaneously. Moreover, charge balance, full site occupancy and chemistry of the spinels are satisfying in a successful Rietveld refinement.

### 3.2.4 Characterisations of the bulk sample with $x = 0.4$

A bulk sample of Cu <sub>$x$</sub> Zn <sub>$2-x$</sub> TiO<sub>4</sub> with  $x = 0.4$  was prepared in order to characterise the microstructure and physical properties at ambient conditions. The powder was pressed into a cylinder (diameter 10 mm). The cylinder was heat-treated at 1123 K for 12 h and at 1273 K for 2 h. Density of the bulk sample was measured by buoyancy method in water at ambient condition. The measurement was repeated 5 times to give an average bulk density.

SEM imaging of the bulk sample was performed on a Phenom ProX desktop SEM using an accelerating voltage of 10.0 kV. The surfaces of the sample were polished with 3–15 μm Al<sub>2</sub>O<sub>3</sub> powder and the two sides were parallel with each other. It had an

Table 3.1: A list of the refined parameters for Rietveld refinement of the neutron diffraction data.

Scale factor	
Zero shift	
Background	A Chebyshev polynomial with 24 terms
Lattice parameter	$a$
Oxygen positional parameter	$u$
Site occupancies	$\text{Zn}^{2+}$ ( $8a$ ), $\text{Cu}^{2+}$ ( $8a$ ), $\text{Ti}^{4+}$ ( $8a$ ), $\text{Zn}^{2+}$ ( $16d$ ), $\text{Cu}^{2+}$ ( $16d$ ), $\text{Ti}^{4+}$ ( $16d$ )
Thermal displacement parameters	Oxygen $U_{\text{iso}}$ , $U_{\text{iso}}$ ( $8a$ ), $U_{\text{iso}}$ ( $16d$ )
Profile parameters	Pseudo-Voigt functions with GU, GV, GW, LX, LY

initial height of 5.697(5) mm. Plane wave ultrasound spectroscopy was employed in order to determine the elastic stiffness coefficients. Thermal expansion was measured in the temperature range of 297–1067 K at a heating rate of 2 K min<sup>-1</sup>. The sample was measured two times in air. UV-vis absorption spectra of the sample with  $x = 0.4$  were collected in the wavelength range of 400–1000 nm.

The SEM data were collected with the help of Dr. Anja Thust and Dr. Nadine Schrod. The elasticity and dilatometry were performed with the help of Dr. Eiken Haussül. The UV-vis spectra were obtained with the help of Dr. Alexandra Friedrich and Dr. Javier Ruiz-Fuertes.

### 3.3 Results and discussion

The colour of the synthesised spinels varied with the change of copper concentrations, ranging from white, lightyellow, yellowgreen to darkolivegreen, as shown in figure 3.1.

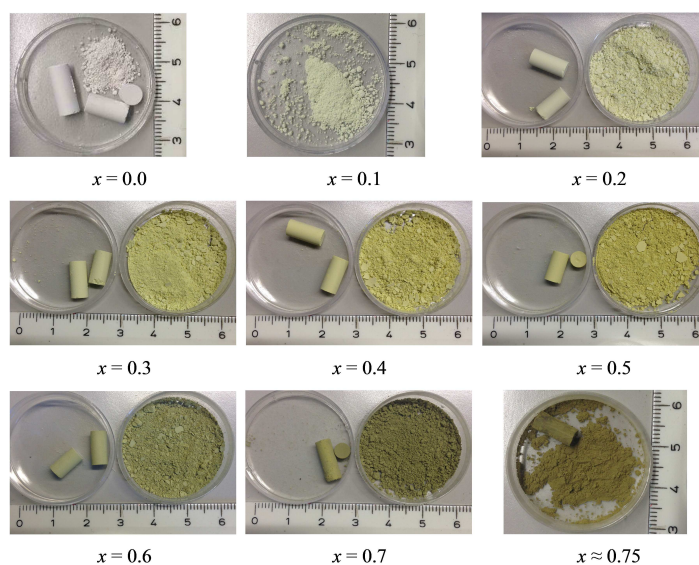
Figure 3.1: Photograph of the spinel solid solution  $\text{Cu}_x\text{Zn}_{2-x}\text{TiO}_4$ .

Figure 3.2 gives powder XRD patterns in the  $2\theta$  range of  $25\text{--}41^\circ$  for the samples  $\text{Cu}_x\text{Zn}_{2-x}\text{TiO}_4$  ( $0 \leq x \leq 0.7$ ) before and after being soaked. The reflections of the impurity phase (ZnO or CuO) were very weak and disappeared after the soaking treatments. It indicated that phase-pure spinels were synthesised.

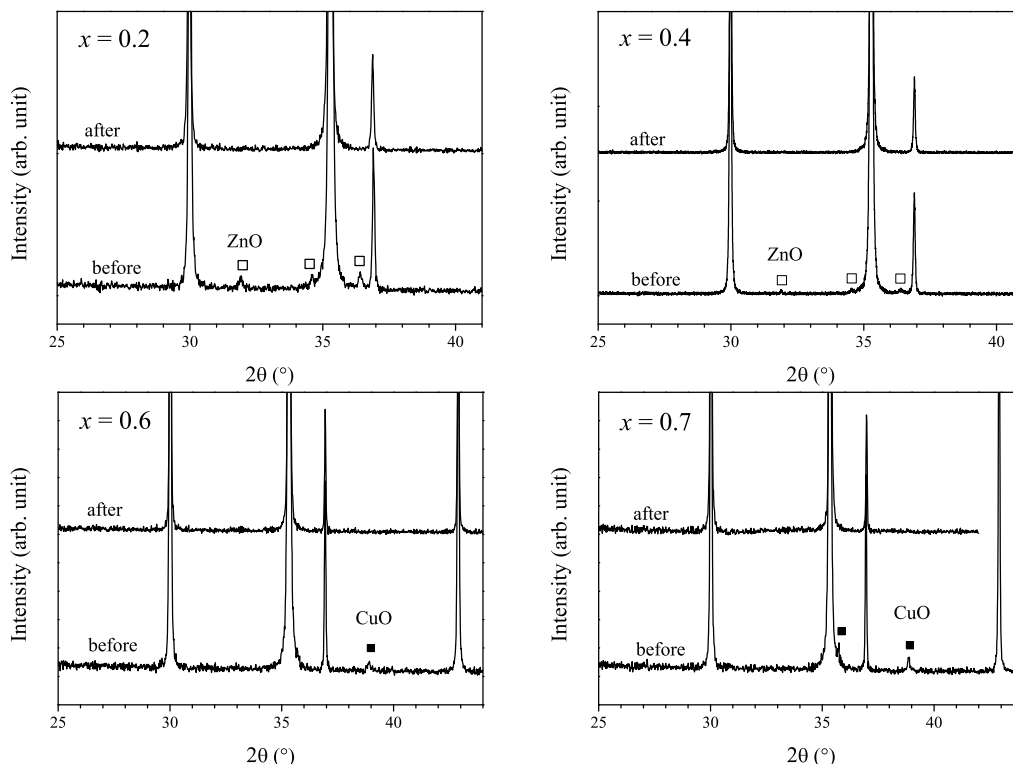


Figure 3.2: XRD patterns of the samples  $\text{Cu}_x\text{Zn}_{2-x}\text{TiO}_4$  before and after the soaking treatments. Reflections of the impurity phases ZnO and CuO are indicated by open and filled squares, respectively.

Figure 3.3 presents powder neutron diffraction patterns of 10 samples at ambient conditions. The data showed that the Jahn-Teller  $\text{Cu}^{2+}$  cations produced no long range distortion of the  $\text{Cu}_x\text{Zn}_{2-x}\text{TiO}_4$  spinels ( $0 \leq x < 1$ ), which confirmed the previously published XRD data<sup>[113]</sup>. This study differed with the literature<sup>[113]</sup> by replacing the agate milling bowls and balls by tungsten carbide ones in the mechanochemical activation process. The impurity phase  $\text{Zn}_2\text{SiO}_4$  was avoided and the phase purity was improved in this study. Nevertheless, both of them yielded cubic inverse spinels  $\text{Cu}_x\text{Zn}_{2-x}\text{TiO}_4$  with space group  $Fd\bar{3}m$ .

Owing to the small deviations from stoichiometry of the samples  $\text{Cu}_x\text{Zn}_{2-x}\text{TiO}_4$  ( $0 \leq x \leq 0.7$ ), the composition of the spinels is, in the following, assumed to be stoichiometric. However, CuO appeared in the samples with high copper contents of  $x$  around 0.75 and 0.86.

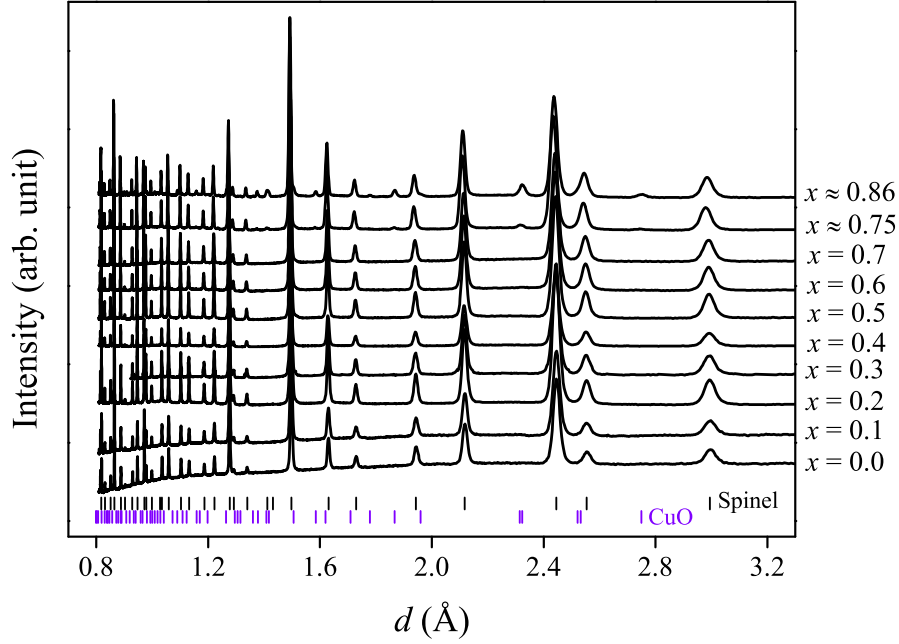


Figure 3.3: Neutron diffraction patterns of  $\text{Cu}_x\text{Zn}_{2-x}\text{TiO}_4$  ( $0 \leq x < 1$ ) solid solution at ambient conditions. Black tickmarks indicate the reflection positions of the  $\text{Zn}_2\text{TiO}_4$  spinel phase whereas the purple ones show the reflection positions of the second phase  $\text{CuO}$ .

### 3.3.1 Rietveld refinement for the sample with $x = 0.4$

Rietveld refinements of  $\text{Cu}_x\text{Zn}_{2-x}\text{TiO}_4$  with  $x = 0.4$  using the XRD data gave a lattice parameter of  $a = 8.46045(1) \text{ \AA}$  and a positional parameter of  $u = 0.2583(1)$ . No change was observed after the soaking process, as tabulated in table 3.2. The average  $U_{\text{iso}}$  values were  $0.0267(3) \text{ \AA}^2$ ,  $0.0186(1) \text{ \AA}^2$  and  $0.0193(1) \text{ \AA}^2$  for anions and cations in the tetrahedral  $8a$  and octahedral  $16d$  sites, respectively.

Figure 3.4 shows X-ray diffractograms for the sample with  $x = 0.4$  before and after the soaking treatment.

Table 3.2: Rietveld refinement result of XRD for the sample  $\text{Cu}_x\text{Zn}_{2-x}\text{TiO}_4$  with  $x = 0.4$  before and after the soaking treatment. Thermal displacement parameters  $U_{\text{iso}}$  have a unit of  $\times 0.01 \text{ \AA}^2$ .

	Before	After
$a$ [ $\text{\AA}$ ]	8.46045(1)	8.46045(1)
$u$	0.25826(5)	0.25831(5)
Oxygen $U_{\text{iso}}$	2.74(3)	2.61(3)
$U_{\text{iso}}(8a)$	1.89(1)	1.82(1)
$U_{\text{iso}}(16d)$	1.91(1)	1.95(1)
$R_{\text{wp}}$ [%]	16.59	16.75
$R_{\text{wpb}}$ [%]	25.29	23.77



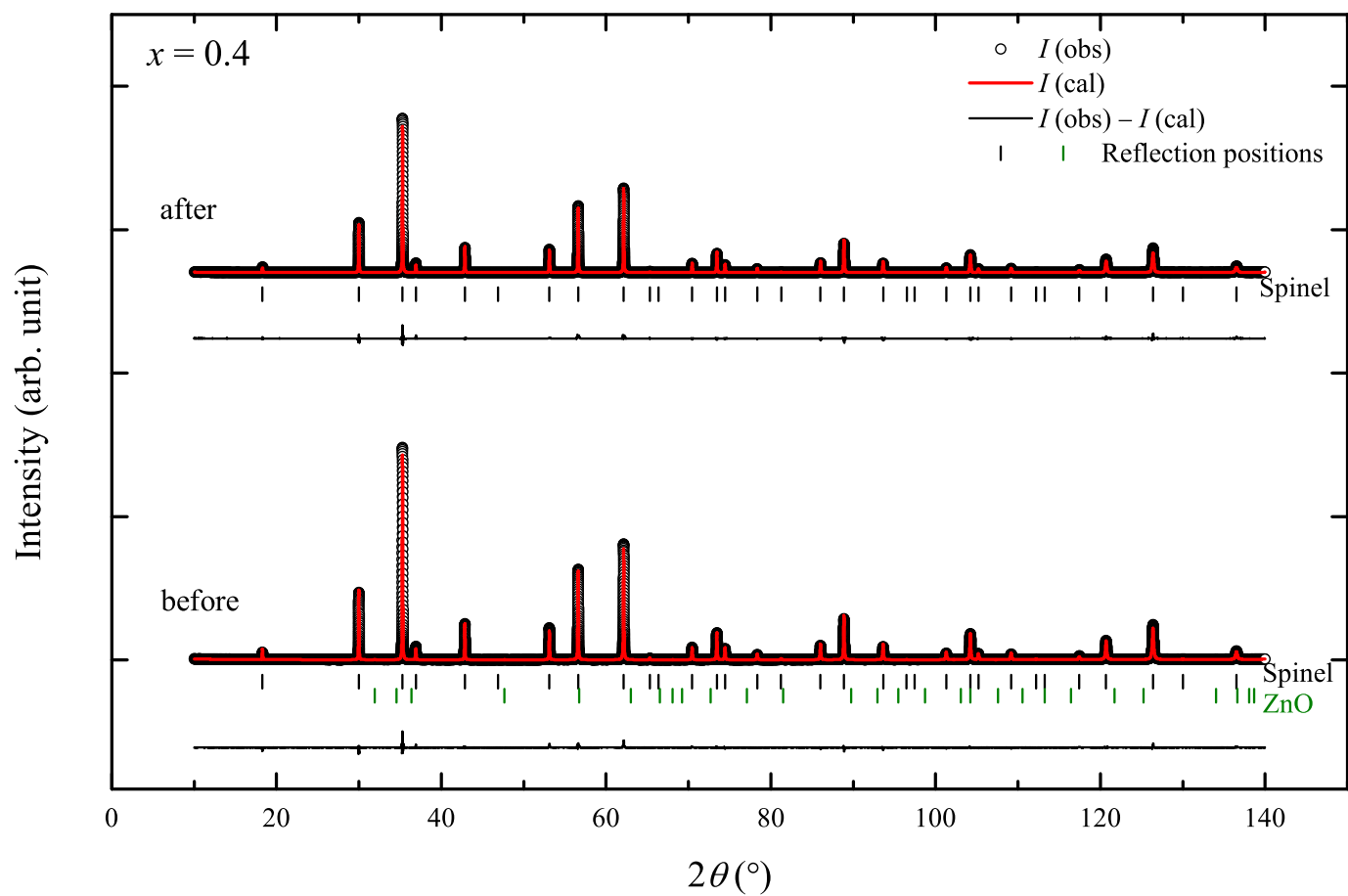


Figure 3.4: Rietveld refinement result of XRD for the sample  $\text{Cu}_x\text{Zn}_{2-x}\text{TiO}_4$  with  $x = 0.4$  before and after the soaking treatment. Observed (circles) and calculated data (red curves), a difference curve (bottom black curves), and reflection positions of the crystalline phases (tickmarks) are shown.

### 3.3.2 Rietveld refinements for the endmember $Zn_2TiO_4$

The endmember  $Zn_2TiO_4$  was refined with a fully inverse spinel structure, where initial  $a$  and  $u$  values from the literature<sup>[150]</sup> were used. Titanium was allowed to occupy the tetrahedral site in the refinement. Value of  $U_{iso}$  for the cations in the same site was constrained to be the same. No constraint was added on the site occupancy. Convergence was achieved by refining scale factor, background,  $a$ ,  $u$ , site occupancies,  $U_{iso}$  and profile parameters together. Due to the unrealistic value of  $U_{iso}$  ( $16d$ ) =  $2.27 \times 10^{-2} \text{ \AA}^2$ , the thermal displacement parameter for cations in the octahedral site was constrained to have a reasonable value of  $0.01 \text{ \AA}^2$ .

Figure 3.5 presents the final Rietveld refinement result of  $Zn_2TiO_4$ . The refinement parameters are tabulated in table 3.3. The results in this study are in very good agreement with the Rietveld refinement results of XRD data for  $Zn_2TiO_4$ <sup>[150]</sup> and of neutron diffraction data for  $Mg_2TiO_4$ <sup>[150]</sup>. No  $Ti^{4+}$  was found in the tetrahedral site, which was the same with the result by Millard et al.<sup>[150]</sup>. It was consistent with  $< 1\%$  titanium in the tetrahedral site of  $Mg_2TiO_4$  cubic spinel, as determined by X-ray and neutron diffraction<sup>[16,17,150]</sup>. The refinement of neutron diffraction data showed that the  $Zn_2TiO_4$  cubic spinel had a stoichiometric chemistry.

Table 3.3: Rietveld refinement results for the endmember spinel  $Zn_2TiO_4$  from neutron diffraction data of this study and data in the literature. Thermal displacement parameters  $U_{iso}$  have a unit of  $\times 0.01 \text{ \AA}^2$ .

Parameter	$Zn_2TiO_4$ (this study)	$Zn_2TiO_4$ (Lit. <sup>[150]</sup> )	$Mg_2TiO_4$ (Lit. <sup>[150]</sup> )
$a$ [ $\text{\AA}$ ]	8.47119(2) $\text{\AA}$	8.47056(3) $\text{\AA}$	8.4872(1) $\text{\AA}$
$u$	0.26037(3)	0.2599(2)	0.2610(1)
$Zn^{2+}$ ( $8a$ )	1.01(1)	1	1
$Zn^{2+}$ ( $16d$ )	0.51(1)	0.5	0.5
$Ti^{4+}$ ( $16d$ )	0.48(1)	0.5	0.5
Oxygen $U_{iso}$	1.07(1)	0.912(63)	1.02(3)
$U_{iso}$ ( $8a$ )	0.85(3)	0.481(25)	1.14(8)
$U_{iso}$ ( $16d$ )	1.00 †	0.887(25)	1.19(8)
Mean $d_{T-O}$	1.986(2) $\text{\AA}$	1.979(2) $\text{\AA}$	1.999(2) $\text{\AA}$
Mean $d_{M-O}$	2.034(2) $\text{\AA}$	2.037(2) $\text{\AA}$	2.033(2) $\text{\AA}$
$R_{wp}$ [%]	1.17	12.96	8.9

† The value was constrained in the refinement.

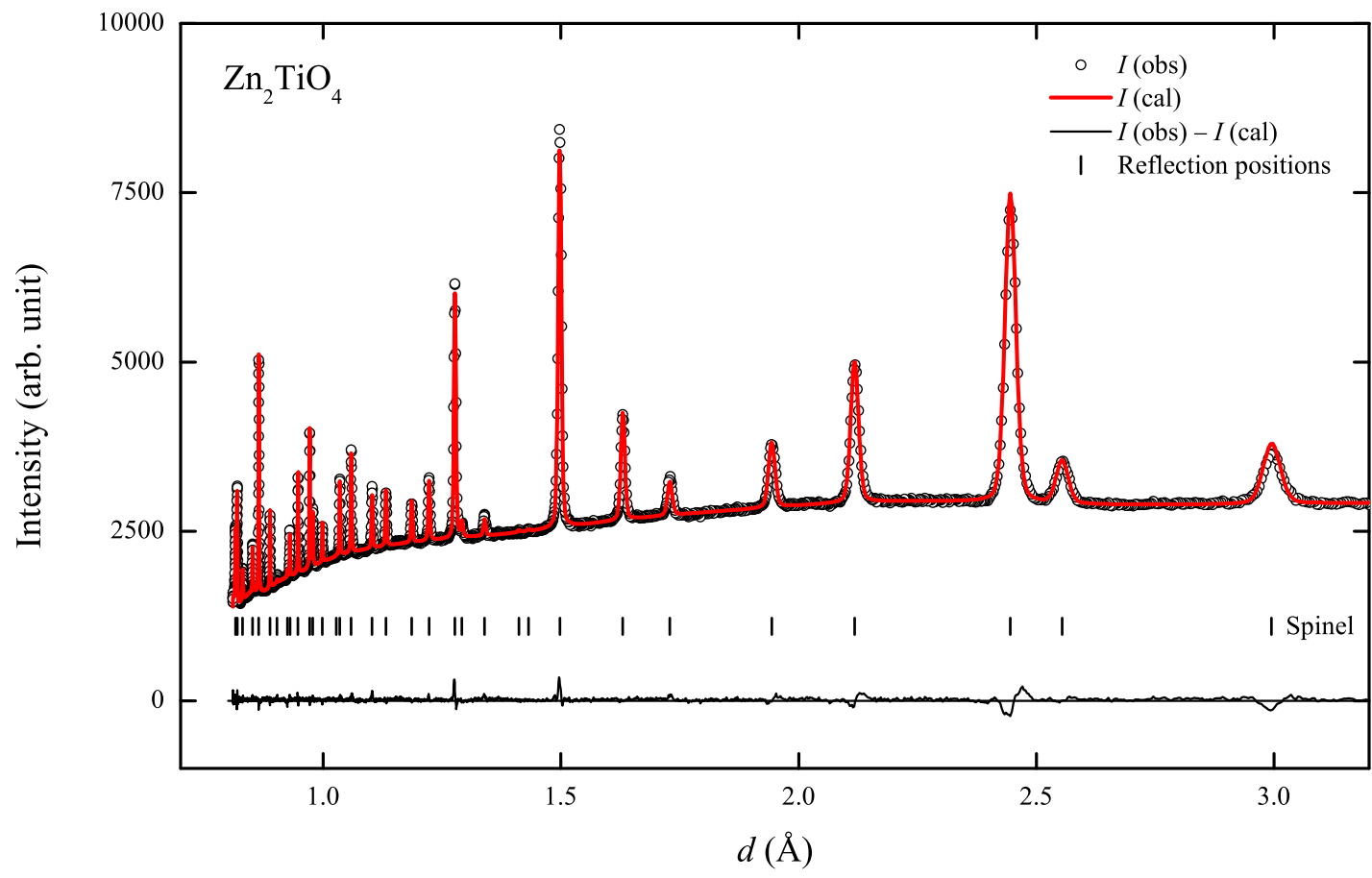


Figure 3.5: Rietveld refinement results of neutron diffraction data for  $\text{Zn}_2\text{TiO}_4$ . Observed (circles) and calculated data (red curve), a difference curve (bottom black curve) and reflection positions of the spinel (black tickmarks) are shown.

### 3.3.3 Rietveld refinement for the sample with $x = 0.5$

Basically, two requirements of the spinel structure have to meet during the refinement: (1) a full cation occupancy of each set of sites, (2) an overall mass balance of each atom and a charge balance. However, both aspects are highly correlated with each other and only one aspect of the constraints can be added in GSAS during the refinement process. Therefore, a free refinement of the cation distribution is not possible due to the complexity in three cations occupying two distinct sets of sites, which allows at least two independent cation occupancy parameters.

Rietveld refinements were employed to each data set using 4 strategies by assuming different cations in the tetrahedral  $8a$  sites: only  $Zn^{2+}$  (strategy 1),  $Zn^{2+}$  and  $Cu^{2+}$  (strategy 2),  $Zn^{2+}$  and  $Ti^{4+}$  (strategy 3),  $Zn^{2+}$ ,  $Cu^{2+}$  and  $Ti^{4+}$  (strategy 4). The refinement sequence for each strategy was not exactly the same. For the sample with  $x = 0.5$ , the refinement sequences are given in table 3.4 using 4 different strategies.

Table 3.4: Rietveld refinement sequences of neutron diffraction data for the sample with  $x = 0.5$  using 4 different strategies.

Sequence	Strategy 1: only $Zn^{2+}$ in the tetrahedral sites
To achieve convergence	scale factor, background, zero shift, $a$ , profile functions
To add new atoms	$Ti(16d) = Ti1(16d) + Ti2(16d)$
To add constraints of $U_{iso}$	$Cu(16d) = Zn(16d) = Ti1(16d) = Ti2(16d)$
To add constraints of site occupancies	$Cu(16d) + Ti1(16d) = 0.5$ $Zn(16d) + Ti2(16d) = 0.5$
To set damping factor of all parameters	5
To refine $u$ and $U_{iso}$	scale factor, $a$ , $u$ , $U_{iso}$ , profile parameters
To refine cation occupancies	scale factor, $a$ , $u$ , $U_{iso}$ , site occupancies (16d)
To achieve convergence	scale factor, background, zero shift, $a$ , $u$ , $U_{iso}$ of all atoms, site occupancies, profile parameters
To check the result	chemical stoichiometry and charge balance
Sequence	Strategy 2: $Zn^{2+}$ and $Cu^{2+}$ in the tetrahedral sites
To achieve convergence	scale factor, background, zero shift, $a$ , profile functions
To add new atoms	$Ti(16d) = Ti1(16d) + Ti2(16d)$
To add constraints of $U_{iso}$	$Cu(8a) = Zn(8a)$ $Cu(16d) = Zn(16d) = Ti1(16d) = Ti2(16d)$
To add constraints of site occupancies	$Cu(8a) + Zn(8a) = 1$ $Cu(16d) + Ti1(16d) = 0.5$ $Zn(16d) + Ti2(16d) = 0.5$
To set damping factor of all parameters	5
To refine $u$ and $U_{iso}$	scale factor, $a$ , $u$ , $U_{iso}$ , profile parameters
To refine cation occupancy in the $8a$ sites	scale factor, $a$ , $u$ , $U_{iso}$ , site occupancies (8a)
To reset cation occupancies (8a)	$Cu(8a) = 0$ and $Zn(8a) = 1$
To refine cation occupancy in the $16d$ sites	scale factor, $a$ , $u$ , $U_{iso}$ , site occupancies (16d)
To delete the constraint	$Cu(8a) + Zn(8a) = 1$
To refine cation occupancies (8a)	scale factor, $a$ , $u$ , site occupancies (8a)
To achieve convergence	scale factor, background, zero shift, $a$ , $u$ , $U_{iso}$ of all atoms, profile parameters
To check the result	chemical stoichiometry and charge balance

Continued on next page

Table 3.4: (continued)

Sequence	Strategy 3: Zn <sup>2+</sup> and Ti <sup>4+</sup> in the tetrahedral sites
To achieve convergence	scale factor, background, zero shift, $a$ , profile functions
To add new atoms	Ti (16d) = Ti1 (16d) + Ti2 (16d)
To add constraints of $U_{\text{iso}}$	Zn (8a) = Ti (8a) Cu (16d) = Zn (16d) = Ti1 (16d) = Ti2 (16d)
To add constraints of site occupancies	Cu (16d) + Ti1 (16d) = 0.5 Zn (16d) + Ti2 (16d) = 0.5
To set damping factor of all parameters	5
To refine $u$ and $U_{\text{iso}}$	scale factor, $a$ , $u$ , $U_{\text{iso}}$ , profile parameters
To refine cation occupancy in the 8a sites	scale factor, $a$ , $u$ , site occupancies (8a)
To refine cation occupancy in the 16d sites	scale factor, $a$ , $u$ , $U_{\text{iso}}$ , site occupancies (16d)
To achieve convergence	scale factor, background, zero shift, $a$ , $u$ , $U_{\text{iso}}$ of all atoms, profile parameters
To check the result	chemical stoichiometry and charge balance
Sequence	Strategy 4: Zn <sup>2+</sup> , Cu <sup>2+</sup> and Ti <sup>4+</sup> in the tetrahedral sites
To achieve convergence	scale factor, background, zero shift, $a$ , profile functions
To add new atoms	Zn (8a) = Zn1 (8a) + Zn2 (8a), Ti (16d) = Ti1 (16d) + Ti2 (16d)
To add constraints of $U_{\text{iso}}$	Cu (8a) = Ti (8a) = Zn1 (8a) = Zn2 (8a), Cu (16d) = Zn (16d) = Ti1 (16d) = Ti2 (16d)
To add constraints of site occupancies	Cu (8a) + Zn1 (8a) = 0.5, Ti (8a) + Zn2 (8a) = 0.5, Cu (16d) + Ti1 (16d) = 0.5, Zn (16d) + Ti2 (16d) = 0.5
To set damping factor of all parameters	5
To refine $u$ and $U_{\text{iso}}$	scale factor, $a$ , $u$ , $U_{\text{iso}}$ , profile parameters
To refine cation occupancy in the 8a sites	scale factor, $a$ , $u$ , site occupancies (8a)
To refine cation occupancy in the 16d sites	scale factor, $a$ , $u$ , $U_{\text{iso}}$ , site occupancies (16d)
To achieve convergence	scale factor, background, zero shift, $a$ , $u$ , $U_{\text{iso}}$ of all atoms, profile parameters
To check the result	chemical stoichiometry and charge balance

Convergent refinement with a reasonable chemical stoichiometry was achieved for each strategy. Table 3.5 lists the Rietveld refinement results of neutron diffraction data for the sample  $\text{Cu}_x\text{Zn}_{2-x}\text{TiO}_4$  with  $x = 0.5$ . Rietveld agreement factors showed no apparent difference. The thermal displacement parameter and site occupancies were within the experimental error. No copper was found in the tetrahedral sites while at maximum 0.01  $\text{Ti}^{4+}$  occupied the tetrahedral sites. Figure 3.6 presents a typical Rietveld refinement result for this sample (strategy 4).

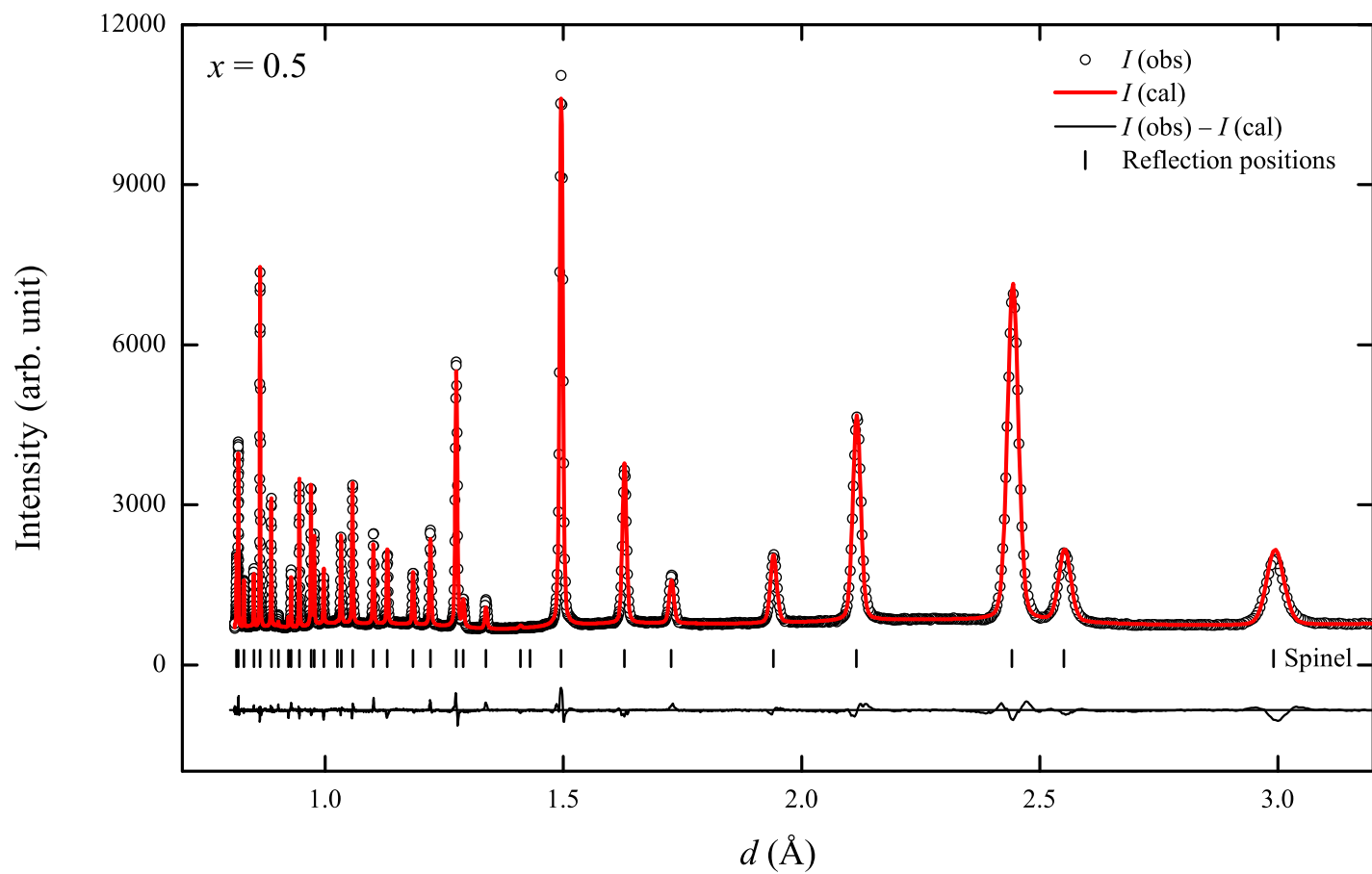


Figure 3.6: Rietveld refinement results of neutron diffraction data for the sample  $\text{Cu}_x\text{Zn}_{2-x}\text{TiO}_4$  with  $x=0.5$  assuming  $\text{Zn}^{2+}$ ,  $\text{Cu}^{2+}$  and  $\text{Ti}^{4+}$  in the tetrahedral sites (strategy 4). Observed (circles) and calculated data (red curve), a difference curve (bottom black curve) and reflection positions of the spinel (black tickmarks) are shown.

Table 3.5: Rietveld refinement results of neutron diffraction data for the sample  $\text{Cu}_x\text{Zn}_{2-x}\text{TiO}_4$  with  $x = 0.5$  using 4 different refinement strategies. Thermal displacement parameters  $U_{\text{iso}}$  have a unit of  $\times 0.01 \text{ \AA}^2$ .

Cations in $8a$	Strategy 1 $\text{Zn}^{2+}$	Strategy 2 $\text{Zn}^{2+}$ and $\text{Cu}^{2+}$	Strategy 3 $\text{Zn}^{2+}$ and $\text{Ti}^{4+}$	Strategy 4 $\text{Zn}^{2+}$ , $\text{Cu}^{2+}$ and $\text{Ti}^{4+}$
$a$ [ $\text{\AA}$ ]	8.45848(2)	8.45848(2)	8.45848(2)	8.45848(2)
$u$	0.26061(4)	0.26062(3)	0.26062(3)	0.26062(3)
$\text{Zn}^{2+}$ ( $8a$ )	0.99(1)	1.00(1)	0.99(1)	0.99(1)
$\text{Cu}^{2+}$ ( $8a$ )		0.00 ‡		0.00
$\text{Ti}^{4+}$ ( $8a$ )			0.01(1)	0.01(1)
$\text{Zn}^{2+}$ ( $16d$ )	0.25(1)	0.26(1)	0.25(1)	0.25(1)
$\text{Cu}^{2+}$ ( $16d$ )	0.25(1)	0.25(1)	0.25(1)	0.25(1)
$\text{Ti}^{4+}$ ( $16d$ )	0.50(1)	0.50(1)	0.50(1)	0.50(1)
Oxygen $U_{\text{iso}}$	1.13(1)	1.14(1)	1.14(1)	1.14(1)
$U_{\text{iso}}$ ( $8a$ )	0.55(1)	0.49(2)	0.49(2)	0.50(2)
$U_{\text{iso}}$ ( $16d$ )	0.66(1)	0.69(6)	0.69(6)	0.68(6)
$R_{\text{wp}}$ [%]	3.25	3.24	3.24	3.24
$R_{\text{wpb}}$ [%]	4.48	4.46	4.46	4.46
$\chi^2$	10.22	10.16	10.17	10.14

‡ The value was constrained in the refinement because it became slightly negative.

### 3.3.4 Rietveld refinement results of $\text{Cu}_x\text{Zn}_{2-x}\text{TiO}_4$

Rietveld refinements of neutron diffraction data for the other samples were carried out using the strategies as shown in table 3.4. For each sample, the lattice parameter  $a$ , oxygen positional parameter  $u$  and thermal displacement parameter  $U_{\text{iso}}$  were the same within experimental error. At maximum 0.01  $\text{Cu}^{2+}$  and 0.02  $\text{Ti}^{4+}$  were incorporated into the tetrahedral  $8a$  sites of the spinel solid solution. The results are presented in appendix A. Table 3.6 tabulates the Rietveld refinement results for  $\text{Cu}_x\text{Zn}_{2-x}\text{TiO}_4$  solid solution assuming  $\text{Zn}^{2+}$  and  $\text{Ti}^{4+}$  in the tetrahedral sites.

Considering the fluctuation of  $U_{\text{iso}}$  for the cations and the strong correlation of  $U_{\text{iso}}$  with the site occupancies, Rietveld refinements were carried out by using a fixed value of  $U_{\text{iso}}(8a) = U_{\text{iso}}(16d) = 0.005 \text{ \AA}^2$ .  $\text{Zn}^{2+}$ ,  $\text{Cu}^{2+}$  and  $\text{Ti}^{4+}$  were allowed in the tetrahedral sites. A full site occupancy on each set of sites was constrained. Convergent refinements were obtained. The results are tabulated in table 3.7. Chemical stoichiometry of the spinels in this table was not as good as the results in table 3.6. An excess of titanium was observed.

At maximum 0.04  $\text{Cu}^{2+}$  and 0.04  $\text{Ti}^{4+}$  incorporated into the tetrahedral ( $8a$ ) sites of  $\text{Cu}_x\text{Zn}_{2-x}\text{TiO}_4$  spinel solid solution. This phenomenon is in consistent with the preference of  $\text{Cu}^{2+}$  and  $\text{Ti}^{4+}$  for octahedral sites<sup>[151]</sup>. In another cubic spinel solid solution  $\text{Cu}_x\text{Zn}_{1-x}\text{Al}_2\text{O}_4$ , a complete replacement of  $\text{Zn}^{2+}$  by  $\text{Cu}^{2+}$  was achieved, and  $\text{Cu}^{2+}$  simultaneously occupied the tetrahedral and octahedral sites<sup>[149]</sup>. This discrepancy was related to different behaviors of the co-existing cations. With the increase of  $\text{Cu}^{2+}$ , part of  $\text{Al}^{3+}$  transferred from the octahedral to the tetrahedral sites of  $\text{Cu}_x\text{Zn}_{1-x}\text{Al}_2\text{O}_4$ <sup>[149]</sup>.  $\text{Cu}^{2+}$  competed with  $\text{Al}^{3+}$  to compensate the loss of  $\text{Zn}^{2+}$  in the tetrahedral sites<sup>[149]</sup>.

Table 3.6: Rietveld refinement results of neutron diffraction data for  $\text{Cu}_x\text{Zn}_{2-x}\text{TiO}_4$  ( $0 \leq x < 1$ ) assuming  $\text{Zn}^{2+}$  and  $\text{Ti}^{4+}$  in the tetrahedral sites. The spinel solid solution crystallises in space group  $Fd\bar{3}m$  ( $Z = 8$ ). All structural parameters including  $a$ ,  $V$ ,  $u$ ,  $U_{\text{iso}}$  for the atoms and site occupancies of cations, and profile parameters (GU, GV, GW, LX, LY) are presented. Thermal displacement parameters  $U_{\text{iso}}$  have a unit of  $\times 0.01 \text{ \AA}^2$ .

	$x=0$	$x=0.1$	$x=0.2$	$x=0.3$	$x=0.4$	$x=0.5$	$x=0.6$	$x=0.7$	$x \approx 0.75$	$x \approx 0.86$
$a$ [ $\text{\AA}$ ]	8.47119(2)	8.46896(4)	8.46614(4)	8.4631(1)	8.46089(4)	8.45850(3)	8.45549(4)	8.45262(3)	8.45092(4)	8.44132(4)
$V$ [ $\text{\AA}^3$ ]	607.901(4)	607.423(8)	606.814(8)	606.16(2)	605.688(8)	605.174(7)	604.529(9)	603.913(7)	603.549(8)	601.494(9)
$u$	0.26037(3)	0.26038(4)	0.26036(4)	0.26040(4)	0.26052(4)	0.26062(4)	0.26069(4)	0.26081(4)	0.26081(4)	0.26102(4)
Oxygen $U_{\text{iso}}$	1.07(1)	0.86(1)	1.11(1)	1.07(1)	1.47(1)	1.19(1)	1.45(1)	1.49(1)	1.47(1)	1.60(1)
$U_{\text{iso}}$ ( $8a$ )	0.85(3)	0.35(2)	0.57(2)	0.45(2)	0.83(2)	0.47(2)	0.77(2)	0.70(2)	0.68(2)	0.76(2)
$U_{\text{iso}}$ ( $16d$ )	1 (fixed)	1.12(5)	1.32(5)	0.49 (5)	1.21(5)	0.64(5)	0.81(5)	0.66(5)	0.70(5)	0.86(5)
Total $\text{Cu}^{2+}$	0	0.10(1)	0.20(1)	0.30(1)	0.40(1)	0.50(1)	0.60(1)	0.70(3)	0.73(3)	0.86(5)
$\text{Zn}^{2+}$ ( $8a$ )	1.01(1)	0.99(1)	0.99(1)	0.99(1)	0.98(1)	0.98(1)	0.98(1)	0.98(1)	0.98(1)	0.98(1)
$\text{Ti}^{4+}$ ( $8a$ )	0	0.01(1)	0.01(1)	0.01(1)	0.02(1)	0.02(1)	0.02(1)	0.02(1)	0.02(1)	0.02(1)
$\text{Zn}^{2+}$ ( $16d$ )	0.51(1)	0.43(1)	0.40(1)	0.33(1)	0.30(1)	0.25(1)	0.20(1)	0.14(1)	0.12(1)	0.04(1)
$\text{Cu}^{2+}$ ( $16d$ )	0	0.06(1)	0.10(1)	0.16(1)	0.20(1)	0.25(1)	0.30(1)	0.35(1)	0.37(1)	0.44(1)
$\text{Ti}^{4+}$ ( $16d$ )	0.48(1)	0.51(1)	0.50(1)	0.51(1)	0.50(1)	0.50(1)	0.52(1)	0.51(1)	0.51(1)	0.52(1)
GU	107(1)	110(1)	108(1)	149(5)	99(1)	93(1)	121(1)	89(1)	78(1)	107(1)
GV	-349(3)	-342(3)	-351(3)	-421(5)	-355(3)	-319(2)	-353(3)	-319(3)	-282(3)	-345(3)
GW	360(2)	365(2)	359(2)	363(3)	378(2)	351(2)	365(2)	347(2)	314(2)	360(2)
LX	10.3(1)	11.9(1)	11.9(1)	12.6(2)	10.4(1)	9.1(1)	10.0(2)	9.3(1)	9.7(1)	9.1(1)
LY	0.63(1)	0.84(1)	0.69(1)	0.84(2)	0.69(1)	0.76(1)	0.80(1)	0.79(1)	0.93(1)	0.74(1)
$R_{\text{wp}}$ [%]	1.17	1.36	3.98	3.36	3.68	3.28	3.56	2.77	3.98	4.17
$R_{\text{wpb}}$ [%]	2.51	2.43	4.81	3.96	4.65	4.53	4.55	3.92	5.01	5.50
$\chi^2$	3.15	3.70	11.85	12.93	6.08	10.26	10.12	7.89	11.43	12.23



Table 3.7: Rietveld refinement results of neutron diffraction data for  $\text{Cu}_x\text{Zn}_{2-x}\text{TiO}_4$  ( $0 \leq x < 1$ ) by using a fixed value of the thermal displacement parameter  $U_{\text{iso}}$  for the cations. The constraint was added in the refinement:  $U_{\text{iso}}(8a) = U_{\text{iso}}(16d) = 0.005 \text{ \AA}^2$ . Thermal displacement parameters  $U_{\text{iso}}$  have a unit of  $\times 0.01 \text{ \AA}^2$ .

	$x=0$	$x=0.1$	$x=0.2$	$x=0.3$	$x=0.4$	$x=0.5$	$x=0.6$	$x=0.7$	$x \approx 0.75$	$x \approx 0.86$
$a$ [ $\text{\AA}$ ]	8.47119(3)	8.46897(2)	8.46615(2)	8.4631(1)	8.46093(2)	8.45850(2)	8.45550(2)	8.45263(2)	8.45092(4)	8.44134(2)
$u$	0.26027(3)	0.26043(3)	0.26032(3)	0.26042(5)	0.26046(4)	0.26071(3)	0.26067(3)	0.26079(3)	0.26077(4)	0.26099(4)
Oxygen $U_{\text{iso}}$	1.11(1)	0.89(1)	1.10(1)	1.06(1)	1.45(1)	1.12(1)	1.38(1)	1.43(1)	1.49(1)	1.61(1)
$\text{Zn}^{2+}(8a)$	0.979(2)	0.990(2)	0.972(9)	0.978(4)	0.958(9)	0.975(6)	0.961(2)	0.936(2)	0.956(6)	0.955(1)
$\text{Cu}^{2+}(8a)$	0	0.008(1)	0.011(9)	0.012(4)	0.005(5)	0.014(1)	0.033(2)	0.027(1)	0.011(6)	0.008(1)
$\text{Ti}^{4+}(8a)$	0.021(1)	0.002(2)	0.017(2)	0.010(1)	0.037(5)	0.011(6)	0.006(1)	0.037(2)	0.033(1)	0.037(1)
$\text{Zn}^{2+}(16d)$	0.473(1)	0.476(1)	0.454(9)	0.332(1)	0.302(1)	0.256(1)	0.241(1)	0.144(1)	0.129(1)	0.035(1)
$\text{Cu}^{2+}(16d)$	0	0.017(1)	0.043(2)	0.160(1)	0.187(1)	0.243(1)	0.258(1)	0.343(1)	0.359(1)	0.437(1)
$\text{Ti}^{4+}(16d)$	0.527(1)	0.507(1)	0.503(9)	0.508(1)	0.511(1)	0.501(1)	0.501(1)	0.513(1)	0.512(1)	0.528(1)
Total $\text{Cu}^{2+}$	0	0.042	0.097	0.332	0.379	0.500	0.549	0.713	0.729	0.882
Total $\text{Zn}^{2+}$	1.925	1.942	1.880	1.642	1.562	1.487	1.443	1.224	1.214	1.025
Total $\text{Ti}^{4+}$	1.075	1.016	1.023	1.026	1.059	1.013	1.008	1.063	1.057	1.093
$R_{\text{wp}}$ [%]	1.23	1.38	4.05	3.35	3.93	3.27	3.71	2.87	4.08	4.28
$R_{\text{wpb}}$ [%]	2.88	2.55	5.03	3.93	5.12	4.43	4.73	4.05	5.08	5.65
$\chi^2$	3.46	3.83	12.33	12.87	6.91	10.17	10.88	8.43	11.97	12.75

### 3.3.5 Structural changes in the $\text{Cu}_x\text{Zn}_{2-x}\text{TiO}_4$ solid solution

According to the Rietveld refinement results of neutron diffraction data, structural changes in  $\text{Cu}_x\text{Zn}_{2-x}\text{TiO}_4$  spinel solid solution are analysed.

Figure 3.7 shows the lattice parameter against molar fraction of  $\text{Cu}^{2+}$  in the spinels. The agreement between ND data of this study and XRD data from the literature<sup>[113]</sup> is excellent. The maximum incorporation of copper in  $\text{Cu}_x\text{Zn}_{2-x}\text{TiO}_4$  was 0.86(5). Considering the whole composition of  $0 \leq x < 1$ , the variation of  $a$  does not obey the Vegard's law. The solid solution shows an excess volume which has been modeled by a two-parameter Margules equation<sup>[113]</sup>. However,  $a$  correlates linearly with  $x$  in the other spinel solid solutions  $\text{Co}_x\text{Zn}_{2-x}\text{TiO}_4$  and  $\text{Ni}_x\text{Zn}_{2-x}\text{TiO}_4$ , as shown in figure 3.7. A linear fitting of  $a$  for  $\text{Cu}_x\text{Zn}_{2-x}\text{TiO}_4$  was made using a combination of the ND and XRD data with  $0 \leq x \leq 0.6$ . The linear equation is  $a = 8.4716 - 0.027x$  where the unit of  $a$  is Å. At  $x$  above 0.6,  $a$  contracted more strongly and deviated from the line.

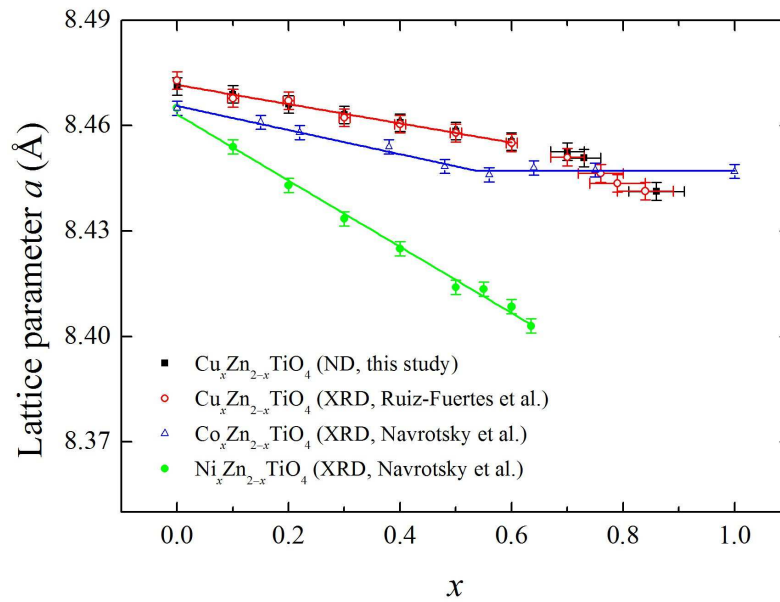


Figure 3.7: Lattice parameter  $a$  plotted against  $x$  in the spinel solid solutions from neutron diffraction data in this study and X-ray diffraction data in the literature<sup>[113,148]</sup>.  $x$  represents the molar fraction of  $\text{Cu}^{2+}$  in  $\text{Cu}_x\text{Zn}_{2-x}\text{TiO}_4$  spinels, or  $\text{Co}^{2+}$  in  $\text{Co}_x\text{Zn}_{2-x}\text{TiO}_4$  spinels, or  $\text{Ni}^{2+}$  in  $\text{Ni}_x\text{Zn}_{2-x}\text{TiO}_4$  spinels. Error bars for the copper content below 0.7 are smaller than the symbol size. Data of each solid solution are described by the linear fittings.

The positional parameters  $u$  and the thermal displacement parameters  $U_{\text{iso}}$  of the anions  $\text{O}^{2-}$  are plotted against the molar fraction of  $\text{Cu}^{2+}$  in  $\text{Cu}_x\text{Zn}_{2-x}\text{TiO}_4$  spinels, as shown in figure 3.8. Model 1 shows the Rietveld refinement results in table 3.6 while model 2 presents the results in table 3.7. The differences of values between the two models are within the experimental error. Data in model 1 were used for the second-order polynomial fitting of  $u$  and the linear fitting of oxygen  $U_{\text{iso}}$ .

Replacing  $\text{Zn}^{2+}$  by  $\text{Cu}^{2+}$  in  $\text{Cu}_x\text{Zn}_{2-x}\text{TiO}_4$  led to a slight increase of the positional

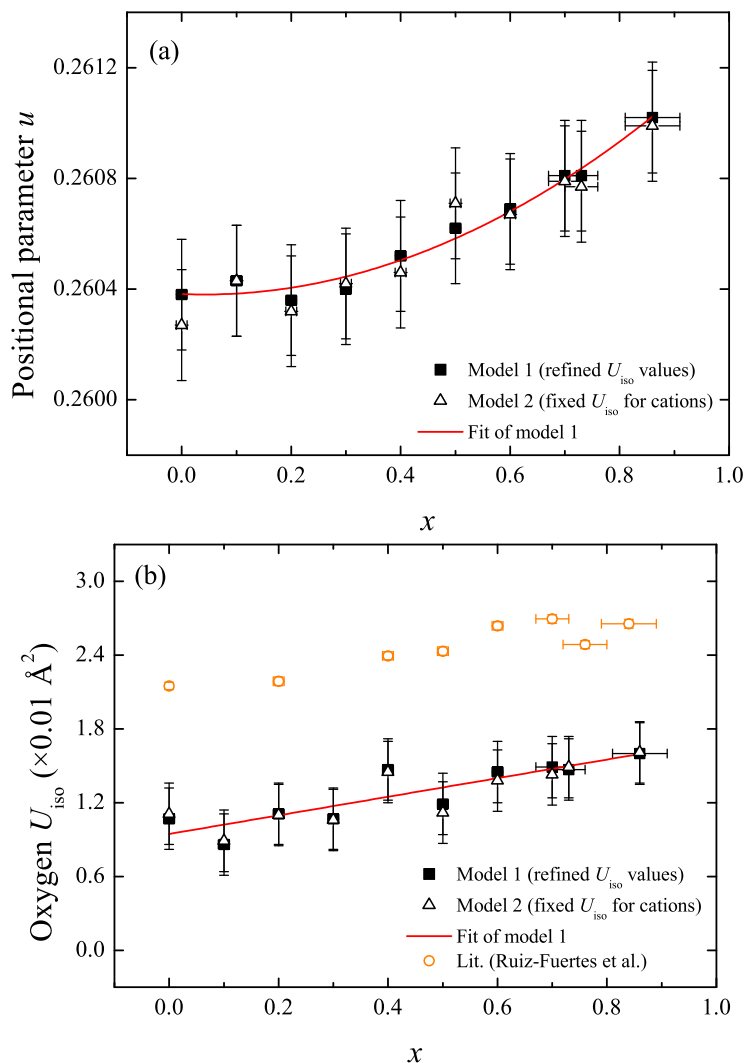


Figure 3.8: The positional parameter  $u$  (a) and the thermal displacement parameter  $U_{\text{iso}}$  (b) of the anions  $\text{O}^{2-}$  plotted against the molar fraction of  $\text{Cu}^{2+}$  in the  $\text{Cu}_x\text{Zn}_{2-x}\text{TiO}_4$  spinel solid solution. Model 1 shows the Rietveld refinement results in table 3.6 while model 2 presents the results in table 3.7.

parameter  $u$  from 0.2604(1) for  $x=0$  to 0.2610(1) for  $x=0.86(5)$ . According to equation 1.1<sup>[2]</sup>, without changing  $a$  the increase of  $u$  means an expansion of the tetrahedra at the expense of the octahedra, while it is the opposite if  $a$  increases and  $u$  keeps stable in the meantime. Then both the decrease of  $a$  and increase of  $u$  indicated a contraction of the octahedra or an expansion of the tetrahedra or both together.

The oxygen  $U_{\text{iso}}$  increased by  $\sim 0.006 \text{ \AA}^2$  due to the incorporation of  $\text{Cu}^{2+}$ , which is consistent with the literature data based on XRD data<sup>[113]</sup>. However, the ND results were around  $0.01 \text{ \AA}^2$  smaller than the XRD results<sup>[113]</sup>. In other oxide spinel solid solutions like  $\text{MgAl}_2\text{O}_4\text{-MgMn}_2\text{O}_4$ <sup>[152]</sup> and  $\text{MgAl}_2\text{O}_4\text{-CuAl}_2\text{O}_4$ <sup>[153]</sup>, the increase of  $U_{\text{iso}}$  for the anions caused by cation substitutions was also observed. Recently, oxygen  $U_{\text{iso}}$  was

reported to be unchanged in the  $(\text{Cu},\text{Mn})\text{WO}_4$  spinel system<sup>[154]</sup>. It was probably due to the very limited solid solution range where only 0.25  $\text{Mn}^{2+}$  was replaced by  $\text{Cu}^{2+}$  at maximum in the molar fraction<sup>[154]</sup>.

Figure 3.9 shows the mean tetrahedral bond lengths  $d_{T-O}$  and the mean octahedral bond lengths  $d_{M-O}$  of the  $\text{Cu}_x\text{Zn}_{2-x}\text{TiO}_4$  spinels. The values of  $d_{T-O}$  for  $0 \leq x < 1$  and  $d_{M-O}$  for  $0 \leq x \leq 0.6$  were fitted by a line. With the increase of  $\text{Cu}^{2+}$  concentration from 0 to 0.86(5) in the solid solution, no change of  $d_{T-O}$  was observed ( $d_{T-O} = 1.986 \pm 0.002 \text{ \AA}$ ) whereas  $d_{M-O}$  decreased from 2.034(2)  $\text{\AA}$  to 2.022(2)  $\text{\AA}$ . The relation of  $d_{M-O}$  with  $x$  in  $\text{Cu}_x\text{Zn}_{2-x}\text{TiO}_4$  was  $d_{M-O} = 2.034(2) - 0.011(3)x$  ( $0 \leq x \leq 0.6$ ). Therefore, the decrease of  $a$  (figure 3.7) and the increase of  $u$  (figure 3.8) were due to the stable  $d_{T-O}$  and the reduction of  $d_{M-O}$ .

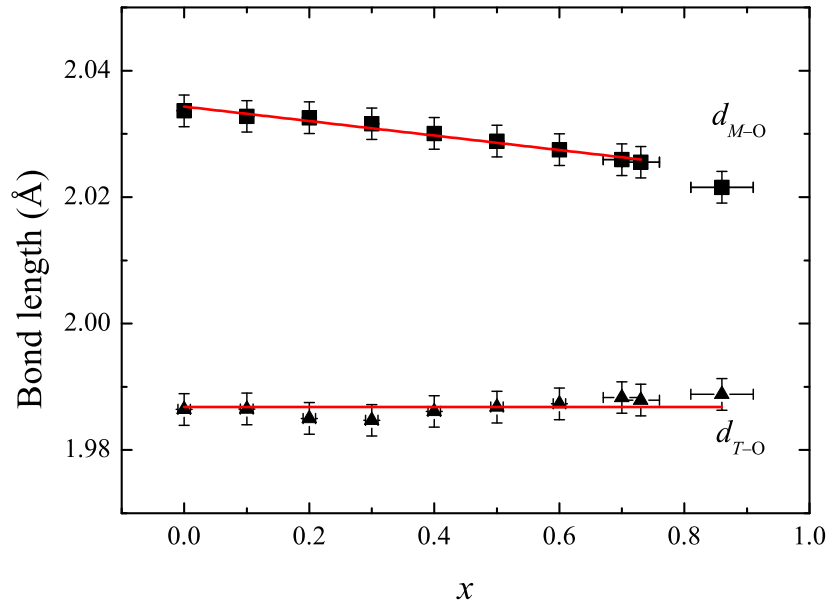


Figure 3.9: Mean tetrahedral bond lengths  $d_{T-O}$  and mean octahedral bond lengths  $d_{M-O}$  with the molar fraction of  $\text{Cu}^{2+}$  in the  $\text{Cu}_x\text{Zn}_{2-x}\text{TiO}_4$  spinels. The solid lines are linear fittings of the data.

The decrease of  $d_{M-O}$  is attributed to the replacement of  $\text{Zn}^{2+}$  by  $\text{Cu}^{2+}$  in the octahedral sites. In a regular octahedron of the cubic spinel structure, the average bond length  $d_{\text{Zn-O}}$  was determined to be 2.10  $\text{\AA}$  based on DFT calculations<sup>[155]</sup>, whereas a value of 2.08  $\text{\AA}$  was reported for the average bond length  $d_{\text{Cu-O}}$  from the experiments<sup>[153]</sup>. Consequently, the decreases of  $d_{M-O}$  by 0.012(3)  $\text{\AA}$  in  $\text{Cu}_x\text{Zn}_{2-x}\text{TiO}_4$  spinels can be ascribed to the cation substitution.

### 3.3.6 Physical properties of the bulk sample with $x = 0.4$

In order to evaluate the effect of structural changes on physical properties, UV-vis optical absorption, thermal expansion and elastic properties of the  $\text{Cu}_x\text{Zn}_{2-x}\text{TiO}_4$  solid solution were investigated.

Due to the  $d$ -orbital splitting, the transition metal ion  $\text{Cu}^{2+}$  ( $3d^9$ ) suffers the Jahn-Teller effect and typically induces local tetragonal distortion of the regular oxygen octahedra  $\text{CuO}_6$  via stretching two  $\text{Cu-O}$  bonds and contracting the other four perpendicular to them<sup>[156]</sup>. The electronic  $d-d$  transition of  $\text{Cu}^{2+}$  allows an absorption band in the UV-vis spectrum. The  $\text{Cu}_x\text{Zn}_{1-x}\text{Al}_2\text{O}_4$  spinels have a maximum absorption at 750 nm for the octahedrally coordinated  $\text{Cu}^{2+}$  and at 1550 nm for the tetrahedrally coordinated  $\text{Cu}^{2+}$ <sup>[149]</sup>. In another spinel solid solution  $\text{Cu}_x\text{Mg}_{1-x}\text{Al}_2\text{O}_4$ ,  $\text{Cu}^{2+}$  in the octahedral and tetrahedral sites led to the absorption bands at  $\sim 740$  nm and 1430 nm, respectively<sup>[153]</sup>. Therefore, an absorption band in visible light region (around 750 nm) is expected for  $\text{Cu}_x\text{Zn}_{2-x}\text{TiO}_4$  spinels. Figure 3.10 shows UV-vis absorption spectrum of the the sample with  $x = 0.4$ . No absorption peak was observed.

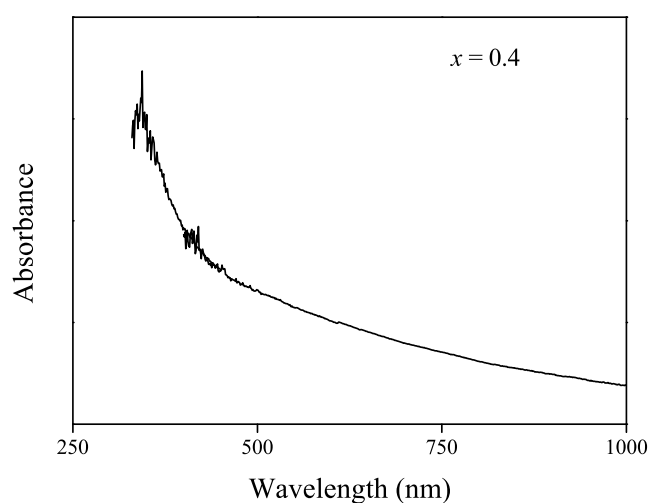


Figure 3.10: UV-vis absorption spectrum of  $\text{Cu}_x\text{Zn}_{2-x}\text{TiO}_4$  with  $x = 0.4$ .

The bulk sample with  $x = 0.4$  had a buoyancy density of 90%. Figure 3.11 shows SEM images of the sample. It reveals an inhomogeneous microstructure with a large porosity.

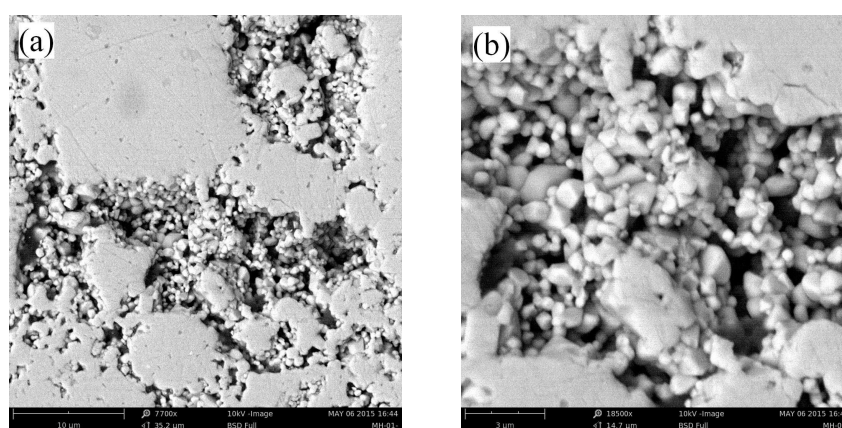


Figure 3.11: SEM images of the bulk sample  $\text{Cu}_x\text{Zn}_{2-x}\text{TiO}_4$  with  $x = 0.4$ .

The 4-2 inverse oxide spinels have similar thermal expansion coefficients with  $\text{Zn}_2\text{TiO}_4$ , which was  $11.7(4) \times 10^{-6} \text{ K}^{-1}$  [71]. Figure 3.12 (a) shows thermal expansion properties of the bulk sample with  $x = 0.4$ . A linear thermal expansion coefficient of  $1.05(3) \times 10^{-6} \text{ K}^{-1}$  was obtained by fitting the experimental data in 297–1067 K with a second-order polynomial. The value was much smaller than that of  $\text{Zn}_2\text{TiO}_4$  in the temperature range of 293–1298 K, which was investigated by *in situ* high-temperature X-ray diffraction [71]. The coefficient of linear thermal expansion varies significantly with the relative density and microstructure of the bulk sample [157,158]. It normally decreases with the porosity. A porosity of 10% leads to 10% of the expected thermal expansion coefficient.

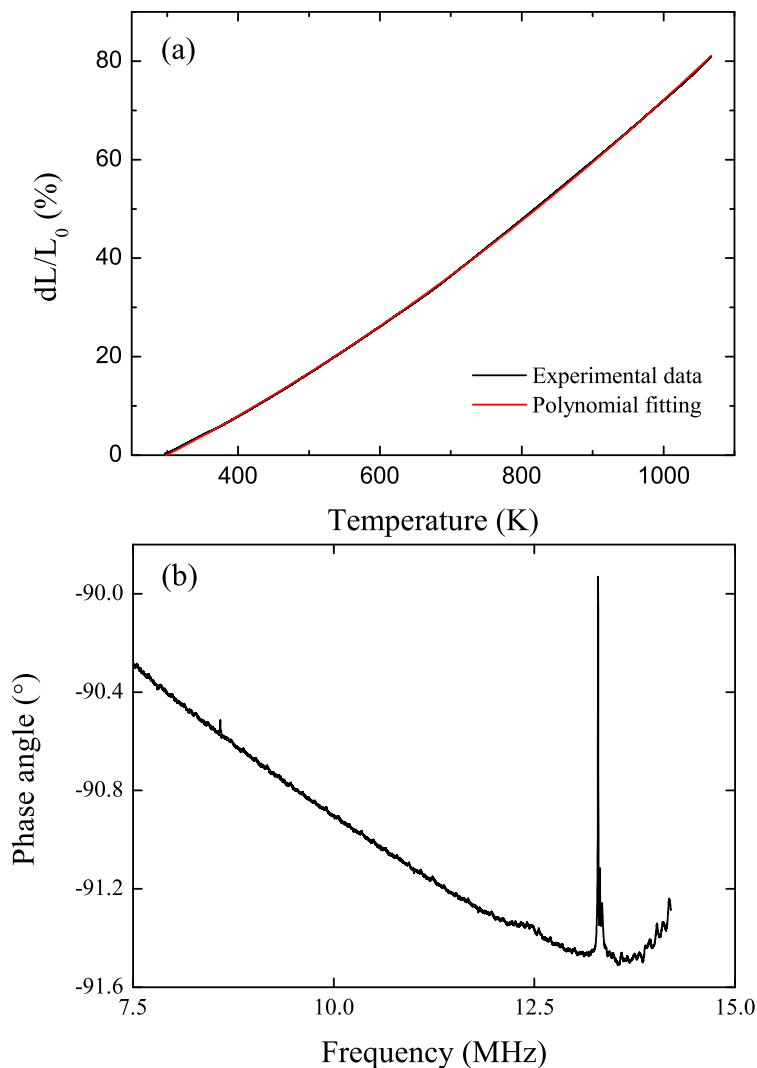


Figure 3.12: Thermal expansion property (a) and plane wave ultrasound spectrum (b) of the bulk sample  $\text{Cu}_x\text{Zn}_{2-x}\text{TiO}_4$  with  $x = 0.4$ .

Figure 3.12 (b) gives the plane wave ultrasound spectrum of the bulk sample with  $x = 0.4$ . The propagation velocity of the longitudinal wave depends on the sample den-

sity<sup>[143]</sup>. The wave velocity and the elastic coefficient decrease with decreasing density. A relative density of 90% is too low to measure the elastic property of the sample.

### 3.4 Conclusion

Spinel solid solution  $\text{Cu}_x\text{Zn}_{2-x}\text{TiO}_4$ ,  $0.0 \leq x \leq 0.86(5)$ , with high purities were synthesised from the binary oxides by the mechanochemical activation assisted solid state synthesis using tungsten carbide milling bowls instead of agate ones and an additional soaking treatment with acetic acid solution. Rietveld refinements of neutron diffraction data indicated the structural changes due to the substitution of  $\text{Zn}^{2+}$  by  $\text{Cu}^{2+}$ . The results showed nonambiguously an increase of positional parameter  $u$  with an increasing incorporation of  $\text{Cu}^{2+}$ . In addition, despite local tetragonal Jahn-Teller distortions around  $\text{Cu}^{2+}$  were not strong enough to lower the cubic symmetry of the spinels, they led to a significant contraction of the average octahedral bond length while not changing the average tetrahedral bond length. Due to the electronic  $d-d$  transition of octahedral  $\text{Cu}^{2+}$ , an absorption band in visible light region (around 750 nm) is expected but could not be measured for  $\text{Cu}_x\text{Zn}_{2-x}\text{TiO}_4$  cubic spinel solid solution. The coefficient of linear thermal expansion for the bulk sample with  $x = 0.4$  indicated 10% of the expected value due to the inhomogeneous microstructure and 90% of the theoretical density.





## 4 MgTi<sub>2</sub>O<sub>5</sub>

### 4.1 Introduction

A low bulk thermal expansion coefficient<sup>[107,109]</sup>, a high refractive index<sup>[103]</sup>, the ability to host transition metal ions<sup>[74,159,160]</sup>, a one-dimensional channel structure<sup>[161]</sup>, and a wide bandgap of 3.4 eV<sup>[162]</sup> make MgTi<sub>2</sub>O<sub>5</sub> (karrooite) attractive for multiple applications, such as ceramic pigments<sup>[101,103]</sup>, filters<sup>[163]</sup>, UV photocatalysts<sup>[104]</sup>, and as anode materials for batteries<sup>[161,164,165]</sup>. According to the MgO–TiO<sub>2</sub> equilibrium phase diagram in air at atmospheric pressure<sup>[110,166,167]</sup>, MgTi<sub>2</sub>O<sub>5</sub> is only stable over the temperature range of 403–1953 K in equilibrium. It melts at around 1953 K and decomposes to MgTiO<sub>3</sub> (geikielite) and TiO<sub>2</sub> at temperatures below around 403 K<sup>[100]</sup>. However, the large positive entropy at high temperatures<sup>[83,87,92,93]</sup> and the slow kinetic of the Mg/Ti interchange at low temperatures (below 973 K)<sup>[87,89,93,110]</sup> allow the metastable MgTi<sub>2</sub>O<sub>5</sub> with an orthorhombic pseudobrookite structure and various Mg/Ti disorder to be formed and employed in a wide temperature range<sup>[82,87,88]</sup>. Synthesis, structural characterisation and thermodynamic stability of the endmember MgTi<sub>2</sub>O<sub>5</sub> are of fundamental importance for understanding the structures and properties of the isostructural pseudobrookite-type solid solutions.

MgTi<sub>2</sub>O<sub>5</sub> exhibits anisotropic physical and mechanical properties. The thermal expansion anisotropy and elastic modulus anisotropy for MgTi<sub>2</sub>O<sub>5</sub> are found to show an opposite trend. Bayer<sup>[22]</sup> observed that the largest thermal expansion occurs in the [001] direction and the smallest expansion occurs in the [100] direction. It is due to the fact that the coefficient of thermal expansion for Ti–O bonds ( $\sim 6 \times 10^{-6} \text{ K}^{-1}$ ) is half that for Mg–O ( $\sim 14 \pm 2 \times 10^{-6} \text{ K}^{-1}$ )<sup>[92]</sup>. Hazen and Yang<sup>[97]</sup> investigated the dependence of bulk moduli on the Mg/Ti order by studying the high pressure compressibility of MgTi<sub>2</sub>O<sub>5</sub> single crystals in the range of 0–8 GPa in diamond anvil cells. The result showed the [100] direction of MgTi<sub>2</sub>O<sub>5</sub> to be the most compressible and [001] the least<sup>[97]</sup>, which can be explained by the different bulk moduli of MgO<sub>6</sub> octahedra (170 GPa) and TiO<sub>6</sub> octahedra (250 GPa)<sup>[19]</sup>. However, up to now, the elastic stiffness coefficients of MgTi<sub>2</sub>O<sub>5</sub> have not been investigated theoretically or experimentally. In order to probe the elasticity of fully ordered MgTi<sub>2</sub>O<sub>5</sub>, lattice dynamical calculations are carried out based on density functional theory.

Cation distribution affects the structural and vibrational properties of MgTi<sub>2</sub>O<sub>5</sub><sup>[100]</sup>. Lennie et al.<sup>[92]</sup> systematically investigated the dependence of lattice parameters and octahedral parameters on Mg/Ti disorder. However, effect of Mg/Ti disorder on the vibrational properties has not been determined. According to group theory, the orthorhombic pseudobrookite-type MgTi<sub>2</sub>O<sub>5</sub> has 24 Raman modes ( $8A_g + 5B_{1g} + 3B_{2g} + 8B_{3g}$ ), 21 infrared modes, of which 18 are optic ( $7B_{1u} + 7B_{2u} + 4B_{3u}$ ) and 3 are acoustic ( $B_{1u} + B_{2u} + B_{3u}$ ), as well as 3 silent modes ( $3A_u$ ). There have been several Raman and infrared spectroscopy studies on MgTi<sub>2</sub>O<sub>5</sub> observing Raman spectra that expand up

to around  $1500\text{ cm}^{-1}$ <sup>[162,168]</sup> and reporting 3 discernible infrared peaks in the range of  $400\text{--}1000\text{ cm}^{-1}$ <sup>[162,169,170]</sup>. Theoretical methods are capable of providing an analogous assignment of the vibrational modes, which allows to establish a direct relationship between cation ordering and vibrational properties. Therefore, experimental measurements and DFT calculations are employed to correlate optic properties of  $\text{MgTi}_2\text{O}_5$  with Mg/Ti disorder.

The Mg/Ti disorder contributes to the heat capacity of  $\text{MgTi}_2\text{O}_5$  and thermodynamic models have been proposed<sup>[83,87,92,93]</sup>. The molar Gibbs free energy of  $\text{MgTi}_2\text{O}_5$  consists of a configurational contribution as well as a lattice vibrational contribution<sup>[93]</sup>. The simple configurational component can be described as  $-TS_{\text{config}}$ , where the configurational entropy  $S_{\text{config}}$  is a function of the cation disorder parameter  $X$  ( $X$  is defined in page 8)<sup>[87,93]</sup>. The vibrational component is represented by model parameters, which are estimated from the measured high-temperature relative enthalpies<sup>[83,92,93]</sup>. Only very few experimentally determined data for vibrational enthalpy and entropy of  $\text{MgTi}_2\text{O}_5$  have been reported, which demands a low-temperature heat capacity measurement. The heat capacities of  $\text{MgTi}_2\text{O}_5$  powder (197 g, purity  $\geq 99.5\%$ ) between 50 K and 298 K was measured using a quasi-adiabatic low-temperature calorimeter, from which the vibrational entropy of  $\text{MgTi}_2\text{O}_5$  at ambient temperature was estimated to be  $127.2(8)\text{ J K}^{-1}$ <sup>[171,172]</sup>. Though the sample was probably disordered  $\text{MgTi}_2\text{O}_5$ <sup>[93]</sup>, no detailed structural information of the sample including the cation distribution was reported in the study<sup>[171]</sup>. Here, we have measured the low-temperature heat capacities of  $\text{MgTi}_2\text{O}_5$  with different Mg/Ti disorder parameters and calculated the vibrational entropies and enthalpies of  $\text{MgTi}_2\text{O}_5$ .

## 4.2 Experimental and computational approaches

### 4.2.1 Sample preparation

Powder samples of MgO and  $\text{TiO}_2$  anatase (purity 99%, Merck, Germany) were used. The MgO was pre-calcined at 1073 K for 2 h. A mixture of the oxides with a stoichiometric molar ratio of 1 : 2 were first ball milled at 300 rpm for 3 h using a planetary ball mill (Fritsch P7). Tungsten carbide milling balls (diameter 10 mm) were used and the mass ratio of balls to powder was 20 : 1. Then the mixture was pressed into cylinders (diameter 5 mm, height 10 mm), followed by heat treatments at 1073–1473 K in air for 4–96 h. Finally, the samples were cooled down by turning off the furnace and were ground into fine powders for further characterisation. As a reference, the stoichiometric mixture without ball milling was ground, pressed, heat treated at 1273–1473 K in air and then cooled within the furnace.

Two small pellets with dimensions  $2 \times 2 \times 0.5\text{ mm}$  were cut from the sample milled for 3 h and sintered at 1473 K. One pellet was measured without further treatment while the other one was enclosed in a Pt foil and annealed at 873 K for 60 days in order to increase the Mg/Ti order.

Figure 4.1 shows photographs of the  $\text{MgTi}_2\text{O}_5$  cylinders and pellets under different synthesis conditions.  $\text{MgTi}_2\text{O}_5$  with a synthesis temperature of 1173 K is white in colour. The colour of  $\text{MgTi}_2\text{O}_5$  quenched at 1473 K is dark grey.

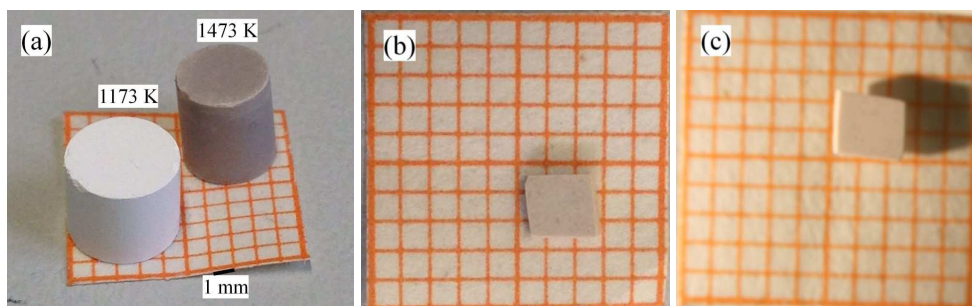


Figure 4.1: Photographs of  $\text{MgTi}_2\text{O}_5$  cylinders and the pellets for low temperature heat capacity measurements. (a) The  $\text{MgTi}_2\text{O}_5$  cylinders were synthesised at 1173 K and 1473 K, respectively. (b) The  $\text{MgTi}_2\text{O}_5$  pellet was synthesised at 1473 K. (c) The  $\text{MgTi}_2\text{O}_5$  pellet was annealed at 873 K.

### 4.2.2 X-ray diffraction

Powder X-ray diffraction data were collected on a X'pert X-ray diffractometer (PANalytical) with Bragg-Brentano geometry over a  $2\theta$  range of  $10\text{--}140^\circ$  using  $\text{CuK}\alpha_1$  radiation ( $\lambda = 1.5406 \text{ \AA}$ , 40 kV, 30 mA) at ambient conditions. In the incident beam path, a curved Ge 110 monochromator,  $0.5^\circ$  divergence slit and 15 mm brass mask were mounted. Around 20 wt.% silicon powder was added as an internal standard for a long measurement with collecting time of around 17 h, using a step size of  $0.002^\circ$  and 200 s per step.

Rietveld refinements of the XRD data with pseudo-Voigt profile functions were carried out using the GSAS programme<sup>[122]</sup> and the EXPGUI interface<sup>[123]</sup>. Initial cell and atomic parameters of  $\text{MgTi}_2\text{O}_5$  and  $\text{TiO}_2$  (rutile) were taken from the literature<sup>[92,173]</sup>. The background was fitted by a Chebyshev polynomial with 8 terms. All atoms were regarded as having isotropic thermal displacement parameters and chemical compositions of  $\text{MgTi}_2\text{O}_5$  were treated as stoichiometric. Due to the small difference in scattering power between the  $\text{Mg}^{2+}$  ion and the  $\text{Ti}^{4+}$  ion for this energy of X-rays, the site occupancy was not refined but calculated from the ambient-temperature lattice parameter  $b$  using the linear relation mentioned in section 1.2.1 (page 8)<sup>[92]</sup>.

### 4.2.3 Raman spectroscopy

Raman spectra of powders were collected in backscattering configuration at ambient conditions with a micro-Raman spectrometer (Renishaw) using the 532 nm line of an Nd:YAG laser (Lightwave). The spectral region ranged from  $100 \text{ cm}^{-1}$  to  $1500 \text{ cm}^{-1}$ . In order to avoid sample degradation, the laser power was kept at 20 mW and the sample was exposed for 10 s. A  $1800 \text{ groove mm}^{-1}$  grating was used and the Rayleigh line filtered with an edge filter. The spectral resolution was  $2 \text{ cm}^{-1}$ . The measurements were done by Dr. Igor Alencar, Dr. Javier Ruiz-Fuertes and Dr. Lkhamsuren Bayarjargal.

#### 4.2.4 Low-temperature heat capacity

Low-temperature heat capacity of the two pellets was measured in the range of 2 K to 325 K using PPMS (Quantum Design). At each temperature, the response to a heat pulse was measured three times. The heat capacities of the empty holder containing Apiezon N grease, with which the sample was thermally coupled to the sample holder, was measured and subtracted from the data obtained for the samples. The data were collected by Dr. Johannes Bauer. The enthalpies and entropies of  $MgTi_2O_5$  were calculated after fitting the measured heat capacity data by high-order polynomials for different temperature ranges.

#### 4.2.5 Density functional theory

DFT calculations were performed by Prof. Dr. Björn Winkler with commercial and academic versions of the CASTEP programme using the generalised gradient approximation (GGA) formalised by Perdew-Burke-Ernzerhof (PBE) with a plane wave basis set and normconserving pseudopotentials<sup>[140,141]</sup>. A fully ordered  $MgTi_2O_5$  model with lattice parameters of  $a = 3.7317 \text{ \AA}$ ,  $b = 9.7919 \text{ \AA}$  and  $c = 10.1112 \text{ \AA}$  was constructed. The maximum cutoff energy of the plane waves was 990 eV. A  $8 \times 8 \times 4$  Monkhorst-Pack grid was employed to compute phonon frequencies and eigenvectors, corresponding to a  $k$ -point separation less than  $0.36 \text{ \AA}^{-1}$ . Lattice dynamical properties of fully ordered  $MgTi_2O_5$ , such as the vibrational frequencies and intensities, the elastic stiffness coefficients and the low-temperature heat capacities were obtained, assuming the validity of both the harmonic and adiabatic approximation<sup>[174]</sup>.

### 4.3 Results and discussion

#### 4.3.1 Mg/Ti disorder

After 3 h of ball milling, no reaction occurred and the average crystallite sizes of the starting materials ( $TiO_2$  anatase and MgO) were decreased to around 500 nm, as estimated by applying the Scherrer equation<sup>[175,176]</sup>. Pure  $MgTi_2O_5$  was obtained after a heat treatment at 1173 K. Figure 4.2 shows the Rietveld refinement results of XRD data of pure  $MgTi_2O_5$  synthesised at 1173 K.

Table 4.1 summarises the synthesis conditions and Rietveld refinement results of  $MgTi_2O_5$ . The required synthesis temperature decreased from 1373 K to 1173 K after 3 h of ball milling. The unannealed  $MgTi_2O_5$  had a Mg/Ti disorder parameter varying from 0.30(1) to 0.37(1), which was drastically reduced to 0.14(1) after annealing at 873 K. Mg/Ti disorder of  $MgTi_2O_5$  was retained from the high-temperature cation configuration. With the increase of disorder, the average M1–O1 bond length decreased while the M2–O1 bond length increased, which is in accordance with the literature<sup>[89,92]</sup>.

The dependence of the disorder parameter  $X$  of  $MgTi_2O_5$  on the synthesis conditions is depicted in figure 4.3. It shows that ball milling prior to the heat treatment causes an increase of the Mg/Ti disorder in  $MgTi_2O_5$ .

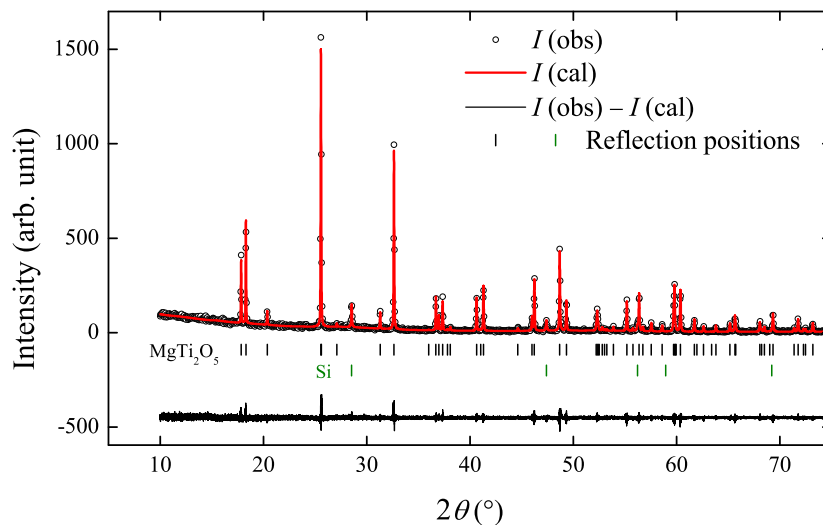


Figure 4.2: Rietveld refinement results of XRD data of the pure MgTi<sub>2</sub>O<sub>5</sub> synthesised at 1173 K. 10 wt.% silicon powder was added to MgTi<sub>2</sub>O<sub>5</sub> as an internal standard. The bottom black curve represents the difference between the observed data (black circles) and the calculated (continuous red curve) data. The bottom tickmarks indicate reflections of the crystalline phases.

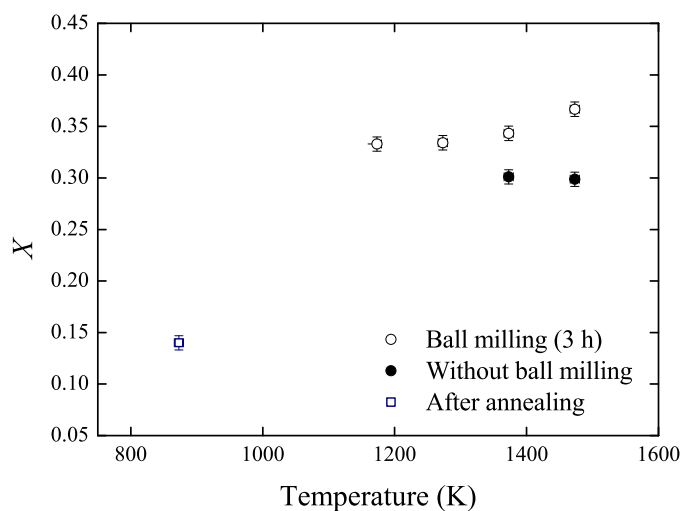


Figure 4.3: Dependence of the Mg/Ti disorder parameter  $X$  on the synthesis condition.

Table 4.1: Synthesis condition and Rietveld refinement results of XRD for  $\text{MgTi}_2\text{O}_5$  with space group  $Cmcm$  and  $Z=4$ . Thermal displacement parameters were fixed to reasonable values:  $U_{\text{iso}}(M1) = U_{\text{iso}}(M2) = 0.006 \text{ \AA}^2$ , oxygen  $U_{\text{iso}} = 0.01 \text{ \AA}^2$ . Estimated standard deviation (esd) in the last decimal digit is indicated with parentheses.

Milling time [h]	0	0	3	3	3	3	3
Sintering temp. [K]	1373	1473	1173	1273	1373	1473	1473
Sintering time [h]	4	4	15	4	4	4	4
Annealing temp. [K]							873
Annealing time [h]							1500
Purity [wt.%]	98(1)	99(1)	100	100	100	100	100
$a$ [ $\text{\AA}$ ]	3.7439(1)	3.7433(1)	3.7448(1)	3.7437(1)	3.7444(1)	3.7456(1)	3.7386(1)
$b$ [ $\text{\AA}$ ]	9.7384(1)	9.7381(1)	9.7422(1)	9.7422(1)	9.7432(1)	9.7463(1)	9.7192(1)
$c$ [ $\text{\AA}$ ]	9.9956(1)	10.0012(1)	9.9958(1)	9.9989(1)	9.9960(1)	9.9939(1)	10.0160(1)
$V$ [ $\text{\AA}^3$ ]	364.44(1)	364.57(1)	364.67(1)	364.67(1)	364.71(1)	364.84(1)	363.95(1)
M1 (4c) sites							
$x$	0.1937(4)	0.1939(3)	0.1931(1)	0.1935(1)	0.1939(4)	0.1954(2)	0.1921(2)
M2 (8f) sites							
$x$	0.1353(2)	0.1352(2)	0.1354(1)	0.1350(1)	0.1357(2)	0.1391(1)	0.1332(1)
$y$	0.5650(2)	0.5649(2)	0.5643(1)	0.5645(1)	0.5644(2)	0.5636(1)	0.5656(2)
O1 (4c)							
$x$	0.7698(9)	0.7734(8)	0.7718(3)	0.7732(3)	0.7728(4)	0.7595(5)	0.7850(5)
O2 (8f)							
$x$	0.0488(7)	0.0467(6)	0.0465(2)	0.0452(2)	0.0475(3)	0.0626(3)	0.0494(3)
$y$	0.1135(6)	0.1131(5)	0.1133(2)	0.1126(2)	0.1120(3)	0.1070(3)	0.1096(4)
O3 (8f)							
$x$	0.3114(6)	0.3122(5)	0.3126(2)	0.3129(2)	0.3131(2)	0.3136(3)	0.3083(4)
$y$	0.0664(7)	0.0654(5)	0.0669(2)	0.0665(2)	0.0648(2)	0.0617(3)	0.0637(5)
M1–O1 length [ $\text{\AA}$ ]	2.014(1)	2.025(3)	2.023(1)	2.026(1)	2.017(1)	1.975(2)	2.076(2)
M2–O1 length [ $\text{\AA}$ ]	2.067(1)	2.054(4)	2.065(1)	2.059(1)	2.075(1)	2.109(2)	2.011(2)
O1–M1–O1 angle [ $^\circ$ ]	136.8(1)	135.1(4)	135.4(2)	134.9(1)	135.5(4)	143.1(3)	128.4(2)
$R_{\text{wp}}$ [%]	26.4	20.8	22.2	21.7	20.5	24.9	25.8
$R_{\text{wpb}}$ [%]	34.2	36.6	38.2	31.0	33.5	40.1	44.2
$\chi^2$	1.10	1.09	0.98	1.04	1.01	1.15	1.15
$X$ †	0.30(1)	0.30(1)	0.33(1)	0.33(1)	0.34(1)	0.37(1)	0.14(1)

† The Mg/Ti disorder parameters  $X$  are calculated values:  $X = 8.6909b - 84.334$ <sup>[92]</sup>.

For all refinements,  $R_{wp}$  factors are relatively high and  $\chi^2$  are less than 1. The possible reason is the relative low intensity of the Bragg reflections with respect to the background in the current experimental settings<sup>[177,178]</sup>. However, the refinements converged quite satisfactorily, as indicated by figure 4.2.

### 4.3.2 Vibrational properties

Raman spectra of the  $MgTi_2O_5$  samples are shown in figure 4.4. The spectra were normalised to the most intense band in the sample with the smallest disorder parameter of  $X = 0.14(1)$  to facilitate a comparison. Due to the significant broadening present in all samples, only 12 Raman modes were unambiguously identified. For the samples with a larger  $X$  value, only 9 bands could be identified. As the Mg/Ti disorder increases, the mode at  $640(2) \text{ cm}^{-1}$  shows the most apparent blueshift within the resolution of our Raman spectrometer ( $\pm 2 \text{ cm}^{-1}$ ).

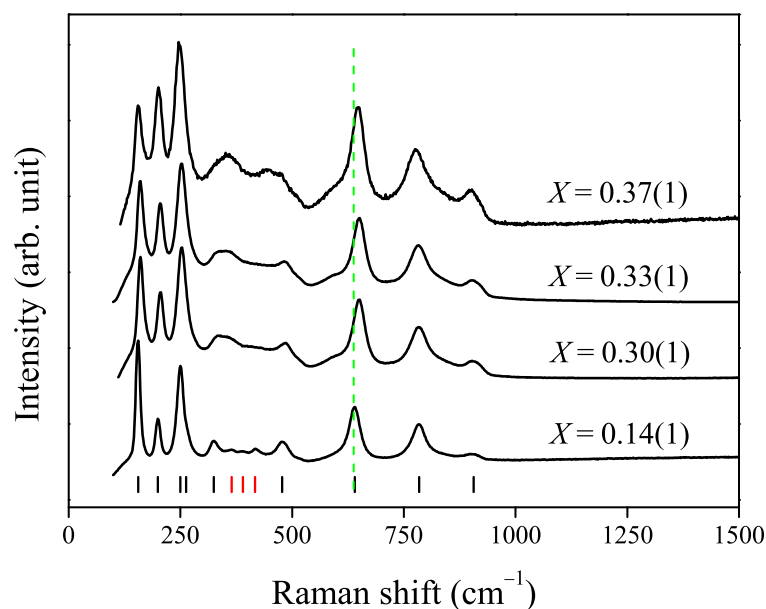


Figure 4.4: Raman spectra of  $MgTi_2O_5$  which are distinguished by the disorder parameter  $X$ . The dashed line is a guide to the eye highlighting the Raman shift. The short vertical bars show the observed Raman band positions where the three in red colour are only valid for  $X = 0.14(1)$ .

Figure 4.5 (a) shows a comparison of the theoretical Raman spectrum of fully ordered  $MgTi_2O_5$  to the measured Raman spectrum of  $MgTi_2O_5$  with  $X = 0.14(1)$ . The agreement of the computed maximum intensities with experimentally determined intensities is outstanding. Figure 4.5 (b) gives a plot of the theoretical Raman shifts of  $MgTi_2O_5$  against the experimentally determined values. The agreement of the frequency is very good except for the mode at  $640(2) \text{ cm}^{-1}$ , as indicated by the circle area.

This mode is assigned to be the  $B_{1g}(5)$  Raman mode according to the calculation. Frequencies of the  $B_{1g}(5)$  mode for the disordered  $\text{MgTi}_2\text{O}_5$  are higher than that for fully ordered  $\text{MgTi}_2\text{O}_5$ . The  $B_{1g}(5)$  Raman mode is a very sensitive indicator for cation disorder of  $\text{MgTi}_2\text{O}_5$ .

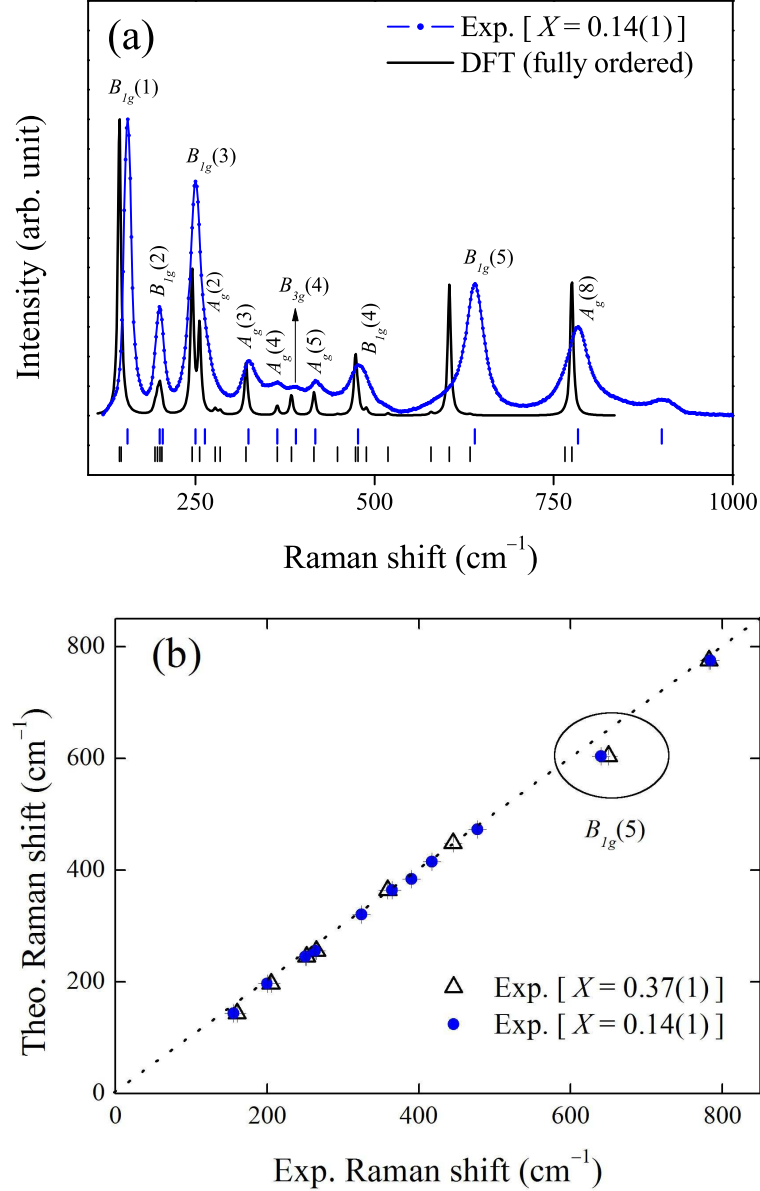


Figure 4.5: (a) The theoretical Raman spectrum with band assignments of fully ordered  $\text{MgTi}_2\text{O}_5$ , compared to the measured Raman spectrum of  $\text{MgTi}_2\text{O}_5$  with  $X = 0.14(1)$ . (b) The theoretical Raman shifts of  $\text{MgTi}_2\text{O}_5$  against the experimental determined values.

Table 4.2 shows the frequencies and assignment of our calculated and observed Raman modes, as well as those previously reported in the literature<sup>[162,168]</sup>. The assign-



ment was based on the frequency and the intensity of the Raman modes. Some Raman modes overlap in frequency and might lead to questionable assignments, e.g.  $A_g(1)$  and  $B_{2g}(2)$  Raman modes.

The simulated Raman spectrum of fully ordered  $MgTi_2O_5$  distributed in the range of  $100\text{--}800\text{ cm}^{-1}$ , a much limited frequency range than previously reported by Liermann et al.<sup>[168]</sup> who assigned Raman modes up to  $1500\text{ cm}^{-1}$ . Only one higher frequency mode was observed in our experiments at around  $905(2)\text{ cm}^{-1}$  which was assigned to an overtone due to the combination of the  $B_{1g}(3)$  Raman mode at  $251(2)\text{ cm}^{-1}$  and  $B_{1g}(5)$  Raman mode at  $650(2)\text{ cm}^{-1}$ . The origin of this band is very likely identical to the previously reported Raman bands at  $915\text{ cm}^{-1}$  and  $913\text{ cm}^{-1}$ <sup>[162,168]</sup>. The experimental Raman modes with frequencies higher than  $800\text{ cm}^{-1}$  in the literature<sup>[168]</sup> are probably overtones or combination bands.

Table 4.2: Theoretical and experimental Raman vibrational modes  $\Gamma$  of  $MgTi_2O_5$  from this study as well as experimental values from the literature<sup>[162,168]</sup>, with esd of the least-significant unit in parentheses. DFT calculation of Raman frequency ( $\text{cm}^{-1}$ ) and Raman activity  $\gamma$  was based on fully ordered  $MgTi_2O_5$  ( $X=0$ ).

$\Gamma$	Theory		Experimental results				
	$X=0$	$\gamma$	$X=0.14(1)$	$X=0.37(1)$	$X=0.070$ <sup>[168]</sup>	$X=0.485$ <sup>[168]</sup>	$X$ unknown <sup>[162]</sup>
$B_{1g}(1)$	144	201	155	160	165.3(3)	168(1)	165
$B_{2g}(1)$	146	7					
$B_{3g}(1)$	193	9					
$A_g(1)$	197	17					
$B_{1g}(2)$	200	28	200	205	206.8(3)	198(1)	207
$B_{2g}(2)$	203	10					
$B_{1g}(3)$	245	243	250	252		260.7(5)	259
$A_g(2)$	256	153	263	265	270.34(3)	274(2)	
$B_{3g}(2)$	278	11					
$B_{3g}(3)$	284	8					
$A_g(3)$	321	135	324		329.1(1)	323.8(8)	
$A_g(4)$	364	29	364	359	369.9(1)	356(1)	
$B_{3g}(4)$	384	66	390				
$A_g(5)$	415	85	417		421.9(1)	448(2)	
$B_{3g}(5)$	448	4					
$B_{1g}(4)$	473	249	477	484	499(13)		491
$A_g(6)$	477	61					
$B_{3g}(6)$	488	27					
$A_g(7)$	519	11			522(1)		
$B_{2g}(3)$	579	14				593(3)	
$B_{1g}(5)$	604	790	640	650	632(1)	653(3)	654
$B_{3g}(7)$	633	7					
$B_{3g}(8)$	766	8					
$A_g(8)$	775	1137	784	782	789.92(1)	779.2(1)	798
Overtone			901	902	913.0(2)	908.7(4)	915

Assuming the experimental data from this study and the literature<sup>[168]</sup> are in an equal weight, Raman frequencies of the  $B_{1g}(5)$  mode for  $\text{MgTi}_2\text{O}_5$  have a linear dependence on the Mg/Ti disorder parameter  $X$ :  $\Gamma = 629(1) + 60(5) X \text{ cm}^{-1}$ , as indicated in figure 4.6. The extrapolated  $\Gamma$  for fully ordered ( $X=0$ ) and fully disordered ( $X=0.67$ ) is  $629 \text{ cm}^{-1}$  and  $669 \text{ cm}^{-1}$ , respectively. The theoretical frequency of  $B_{1g}(5)$  mode is  $25 \text{ cm}^{-1}$  lower than the extrapolated value. Nevertheless, the linear relation provides a convenient way for the rapid detection of the Mg/Ti ordering state of  $\text{MgTi}_2\text{O}_5$ .

In order to understand the high sensitivity of the  $B_{1g}(5)$  Raman mode on  $X$ , we have calculated its eigenvector. A sketch is shown in figure 4.7. This mode has an unusual displacement pattern. It corresponds to a displacement of oxygens O1 parallel to around [001], while all other atoms essentially remain stationary. The  $B_{1g}(5)$  Raman mode is related to two O1–M1–O1 bending movements and an anti-phase stretching movement of two M2–O1 bonds, where the two M1 octahedra and two M2 octahedra share a same corner O1. The bending and stretching motions compete to increase the frequency of the  $B_{1g}(5)$  Raman mode with the increase of the Mg/Ti disorder.

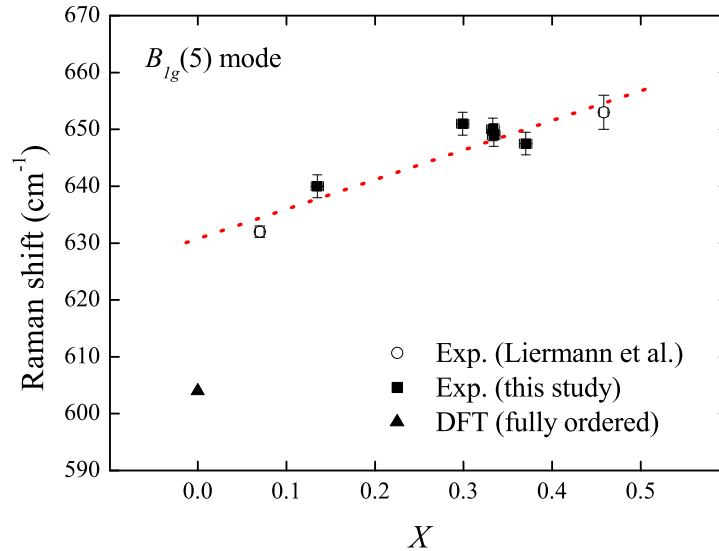


Figure 4.6: Frequencies of the  $B_{1g}(5)$  Raman mode for  $\text{MgTi}_2\text{O}_5$  against the Mg/Ti disorder parameter  $X$ . The filled squares are experimental data from this study, while the open circles presents data from the literature<sup>[168]</sup>. The dashed line is the linear fit of these two data sets which are assumed to carry equal weight. As a comparison, the calculated value from the DFT calculation is plotted in the filled triangle.

The computed infrared absorption of fully ordered  $\text{MgTi}_2\text{O}_5$  is depicted in figure 4.8. Wavenumbers and assignments of the 18 infrared-active modes are tabulated in table 4.3, excluding the three acoustic modes with  $B_{1u}$ ,  $B_{2u}$  and  $B_{3u}$  symmetry. Concerning both the wavenumbers and the intensities, the experimentally determined infrared

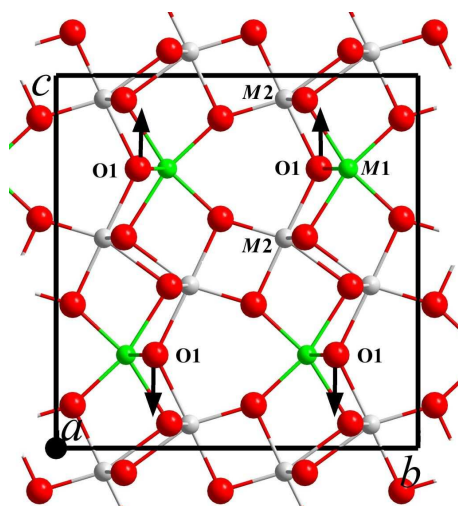


Figure 4.7: Oxygen O1 motions corresponding to the  $B_{1g}(5)$  Raman mode of fully ordered  $\text{MgTi}_2\text{O}_5$  in (100) plane. The red, green and gray spheres denote oxygen atoms, M1 sites and M2 sites, respectively. Bonds between the Mg/Ti cations and the oxygen anions are shown.

modes of disordered  $\text{MgTi}_2\text{O}_5$  at around  $426\text{ cm}^{-1}$ ,  $505\text{ cm}^{-1}$  and  $648\text{ cm}^{-1}$  [169,170] were assigned to  $B_{3u}(3)$ ,  $B_{3u}(4)$  and  $B_{2u}(6)$  modes, respectively. There is a 5–9% deviation between our theoretical infrared absorption bands and the reported experimental values. The quality of the spectra in the literature [169,170] is too poor to be used to evaluate the effect of Mg/Ti disorder on IR frequencies of  $\text{MgTi}_2\text{O}_5$ .

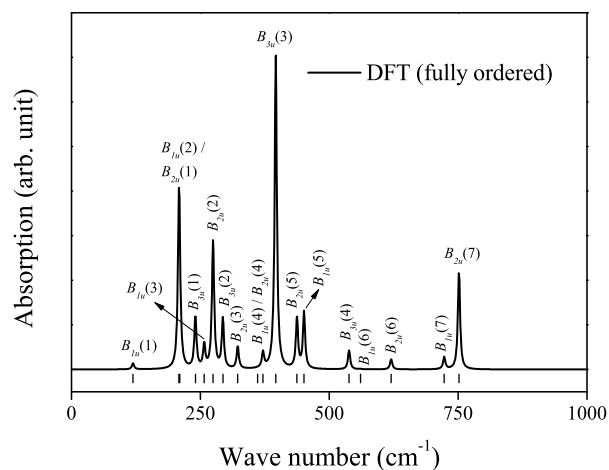


Figure 4.8: Computed infrared absorption spectrum of fully ordered  $\text{MgTi}_2\text{O}_5$ .

Table 4.3: Theoretical infrared vibrational modes  $\Gamma$  and IR activity  $\gamma$  of fully ordered  $MgTi_2O_5$  from DFT calculation and experimental IR frequencies in the literature<sup>[169,170]</sup>. The three acoustic modes are not included.

$\Gamma$	Theory		Experimental results	
	$X=0$	$\gamma$	$X=0.11$ <sup>[169]</sup>	$X=0.34$ <sup>[170]</sup>
$B_{1u}(1)$	119	3		
$B_{1u}(2)$	208	94		
$B_{2u}(1)$	210	4		
$B_{3u}(1)$	240	27		
$B_{1u}(3)$	257	12		
$B_{2u}(2)$	275	68		
$B_{3u}(2)$	294	26		
$B_{2u}(3)$	322	12		
$B_{1u}(4)$	361	0.1		
$B_{2u}(4)$	371	8		
$B_{3u}(3)$	396	166		425.99
$B_{2u}(5)$	437	27		
$B_{1u}(5)$	451	30		
$B_{3u}(4)$	538	10	509.8	505.30
$B_{1u}(6)$	561	0.2		
$B_{2u}(6)$	620	6	641.2	648.03
$B_{1u}(7)$	723	6		
$B_{2u}(7)$	752	52		

### 4.3.3 Elasticity

Table 4.4 lists the 9 independent elastic stiffness coefficients  $c_{ij}$  of fully ordered  $MgTi_2O_5$  derived from DFT calculations. The compression coefficients ( $c_{11}$ ,  $c_{22}$  and  $c_{33}$ ) as well as the shear coefficients ( $c_{44}$ ,  $c_{55}$  and  $c_{66}$ ) show some anisotropy. The compressibility is smallest along the [100] direction and largest along the [001] direction, which shows a same trend with the thermal expansion properties<sup>[22]</sup>. Because the  $TiO_6$  octahedron is more compressible than the  $MgO_6$  octahedron<sup>[19]</sup>, a decreasing elastic anisotropy is expected during the structural transition of  $MgTi_2O_5$  from fully ordered to fully disordered, where  $c_{11}$  tends to decrease while  $c_{33}$  increases. Our elastic parameter calculations yielded a bulk modulus of 161(1) GPa for fully ordered  $MgTi_2O_5$ , which is close to the reported value of 167(1) GPa<sup>[97]</sup>.

Table 4.4: Elastic stiffness coefficients  $c_{ij}$  of fully ordered  $MgTi_2O_5$  from theory in GPa.

$c_{11}$	$c_{22}$	$c_{33}$	$c_{44}$	$c_{55}$	$c_{66}$	$c_{12}$	$c_{13}$	$c_{23}$
300(1)	269(1)	244(1)	76(1)	85(1)	53(1)	145(1)	105(1)	87(1)

Figure 4.9 is the representation surface of the longitudinal stiffness based on fully ordered  $MgTi_2O_5$  structure. No strong anisotropy is visible.

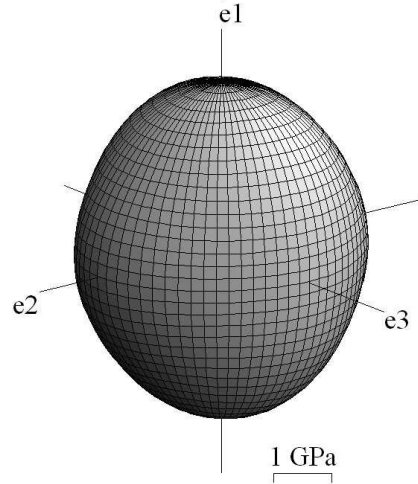


Figure 4.9: Representation surface of the longitudinal elastic stiffness of fully ordered  $\text{MgTi}_2\text{O}_5$ .

#### 4.3.4 Low-temperature thermodynamic properties

Figure 4.10 depicts the theoretical and the experimental low-temperature heat capacities  $C_p$  of  $\text{MgTi}_2\text{O}_5$ . The theoretical values obtained from DFT calculations of fully ordered  $\text{MgTi}_2\text{O}_5$  are in reasonable agreement with our measured  $C_p$  and the reported experimental  $C_p$  [171] of disordered  $\text{MgTi}_2\text{O}_5$ .

For disordered  $\text{MgTi}_2\text{O}_5$  with  $X = 0.14(1)$  and  $X = 0.37(1)$ , the measured  $C_p$  in the range 2–325 K were fitted by high-order polynomials in three temperature ranges, respectively. The fittings are shown in figure B.1. Then the fitted values were used to calculate the standard enthalpy  $H^0$  and entropy  $S^0$  of disordered  $\text{MgTi}_2\text{O}_5$  at 298 K using equations 2.6 and 2.7. The results are tabulated in table 4.5 and compared with the literature [171].  $H^0$  and  $S^0$  of  $\text{MgTi}_2\text{O}_5$  increased by  $4.6(2) \text{ J K}^{-1}$  and  $0.66(5) \times 10^3 \text{ J}$  with the increase of Mg/Ti disorder from  $X = 0.14(1)$  to  $X = 0.37(1)$ , respectively.

The standard entropy  $S^0$  is a sum of the lattice vibrational contribution and the configurational contribution. By assuming an equilibrium and random Mg/Ti distribution in each set of the octahedral sites, the standard configurational entropy  $S_{\text{config}}^0$  of  $\text{MgTi}_2\text{O}_5$  at 298 K was associated with the disorder parameter  $X$  by equation 4.1 [87,93,179]. Figure 4.11 plots  $S_{\text{config}}^0$  of  $\text{MgTi}_2\text{O}_5$  against the disorder parameter. As tabulated in table 4.5,  $S_{\text{config}}^0$  of  $\text{MgTi}_2\text{O}_5$  with a fully ordered structure,  $X = 0.14(1)$  and  $X = 0.37(1)$  were  $0, 7.6(4)$  and  $13.4(2) \text{ J K}^{-1}$ , respectively. With an increase of the disorder parameter from  $0.14(1)$  to  $0.37(1)$ , the excess configurational entropy was  $5.9(6) \text{ J K}^{-1}$ .

$$S_{\text{config}}^0 = -R[X \ln X + (1 - X) \ln(1 - X) + X \ln(X/2) + (2 - X) \ln(1 - X/2)] \quad (4.1)$$

The standard lattice vibrational entropy  $S_{\text{vibra}}^0$  at 298 K was calculated by  $S^0 - S_{\text{config}}^0$ ,

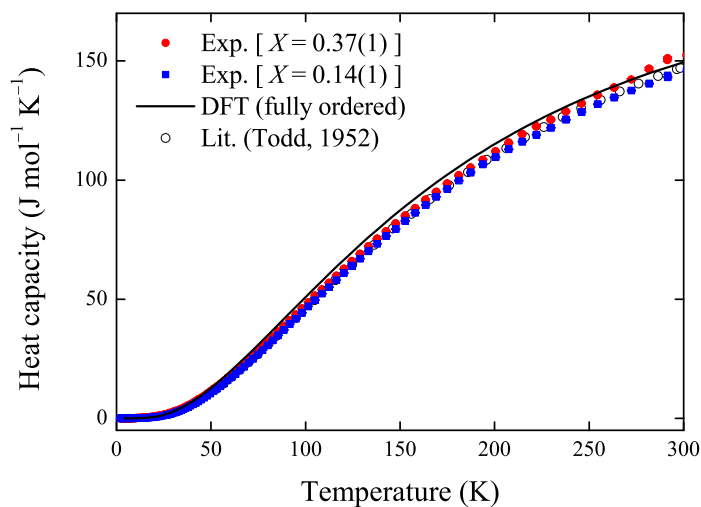


Figure 4.10: Low-temperature heat capacities  $C_p$  of  $\text{MgTi}_2\text{O}_5$ . The continuous black curve are the theoretical data of fully ordered  $\text{MgTi}_2\text{O}_5$  from DFT calculations. The filled blue squares and the filled red circles show the measured data of  $\text{MgTi}_2\text{O}_5$  with  $X = 0.14(1)$  and  $0.37(1)$  from this study, respectively. The open squares are the reported experimental data of  $\text{MgTi}_2\text{O}_5$  with an unknown  $X$  in the temperature range 50–298 K<sup>[171]</sup>.

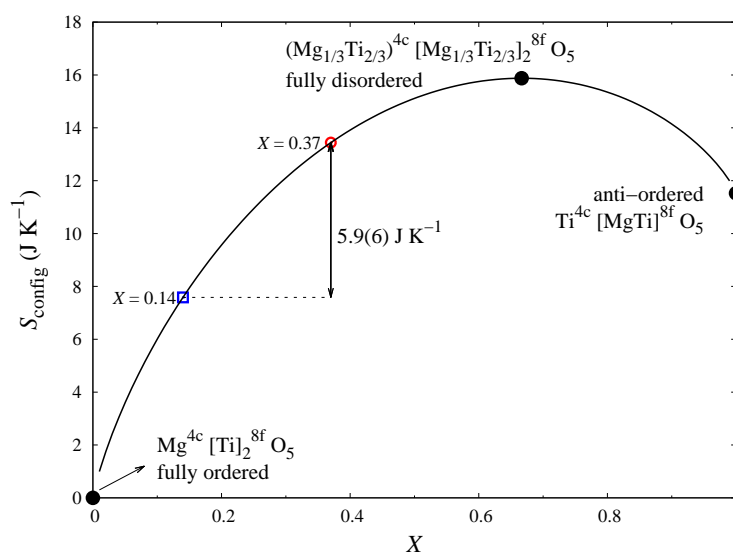


Figure 4.11: Evolution of the standard configurational entropy  $S_{\text{config}}^0$  of  $\text{MgTi}_2\text{O}_5$  with the disorder parameter  $X$ . With the increase of  $X$  from 0.14(1) (the blue square) to 0.37(1) (the red circle),  $S_{\text{config}}^0$  increased by  $5.9(6) \text{ J K}^{-1}$ .

as shown in table 4.5. The value of  $S_{\text{vibra}}^0$  for  $\text{MgTi}_2\text{O}_5$  with  $X=0.14(1)$  and  $0.37(1)$  was  $117.2(4)$  and  $116.0(2)\text{J K}^{-1}$ , respectively. They were smaller than the values of  $134.24\text{J K}^{-1}$  from DFT calculation in this study and  $149.55\text{J K}^{-1}$  from thermodynamic modeling in the literature<sup>[83]</sup>.

Table 4.5: Standard enthalpies ( $\times 10^3\text{J}$ ) and entropies ( $\text{J K}^{-1}$ ) of  $\text{MgTi}_2\text{O}_5$  at 298 K. Values shown in parentheses are esd's in the last decimal place.

	X = 0 (DFT)	X = 0.14(1) (exp.)	X = 0.37(1) (exp.)	X = 0 (cal.) <sup>[83]</sup>	X unknown (exp.) <sup>[171]</sup>
$H^0$	23.43	22.12(3)	22.78(3)		
$S^0$		124.8(1)	129.4(1)		127.2(8)
$S_{\text{config}}^0$		7.6(4)	13.4(2)		
$S_{\text{vibra}}^0$	134.24	117.2(4)	116.0(2)	149.55	

The experimental  $C_p$  of  $\text{MgTi}_2\text{O}_5$  with  $X=0.37(1)$  was higher than  $\text{MgTi}_2\text{O}_5$  with  $X=0.14(1)$  in the temperature range of 0–298 K. The differences,  $\Delta C_p$ , increased with increasing temperature. The differences of enthalpies and entropies between the two disordered samples of  $\text{MgTi}_2\text{O}_5$  at low temperatures were calculated by integrating  $\Delta C_p$  and  $\frac{C_p}{T}$  over temperature. Figure 4.12 plots  $\Delta H$  and  $\Delta S$  with temperature.

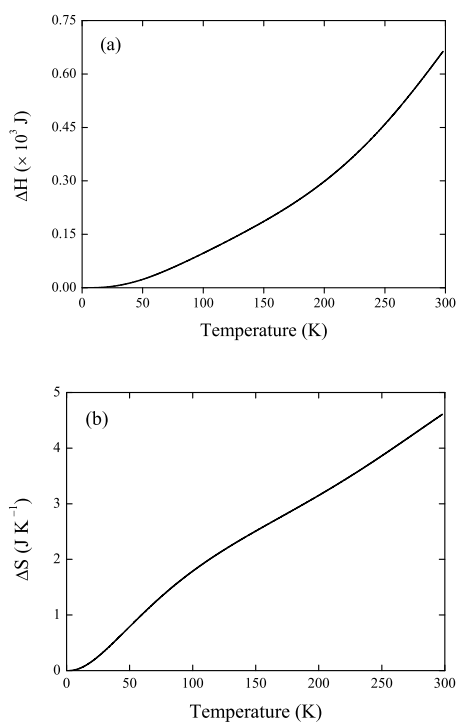


Figure 4.12: Low-temperature vibrational enthalpies  $\Delta H$  (a) and entropies  $\Delta S$  (b) between the two disordered  $\text{MgTi}_2\text{O}_5$  with  $X=0.37(1)$  and  $X=0.14(1)$ .

## 4.4 Conclusion

Solid state synthesis of pseudobrookite-type compound  $MgTi_2O_5$  was facilitated by a mechanochemical activation process, as evidenced by the reduced synthesis temperature of 1173 K compared to 1373 K without ball milling treatment. The Mg/Ti disorder of  $MgTi_2O_5$  at ambient conditions varied from 0.14(1) to 0.37(1) and depended on the synthesis conditions. For example, the mechanochemical activation process led to a more disordered structure. Reliable predictions of the vibrational, elastic and thermodynamic properties were achieved by DFT calculations based on fully ordered  $MgTi_2O_5$ , which were in accordance with the experiments. A comparison between experimental and theoretical Raman and IR spectra showed that the vibrational properties of  $MgTi_2O_5$  were sensitive to the Mg/Ti disorder. In particular, the  $B_{1g}(5)$  Raman mode blueshifted significantly with the increase of the Mg/Ti disorder and its frequency correlated with the Mg/Ti disorder parameter by a linear relation, which allowed a rapid detection of the ordering state of  $MgTi_2O_5$ . According to the calculation, a total standard entropy of  $134.24 \text{ J K}^{-1}$  and a bulk modulus of 161(1) GPa were estimated for fully ordered  $MgTi_2O_5$ .



## 5 $\text{Zn}_x\text{Mg}_{1-x}\text{Ti}_2\text{O}_5$ ( $0 \leq x \leq 1$ ) and $\text{Cu}_x\text{Mg}_{1-x}\text{Ti}_2\text{O}_5$ ( $0 \leq x \leq 0.5$ )

### 5.1 Introduction

The synthetic compound  $\text{MgTi}_2\text{O}_5$  and  $\text{MgTi}_2\text{O}_5$ -based solid solutions have attracted much attention due to the pseudobrookite-type structure which bears distinct octahedral  $M1$  ( $4c$ ) and  $M2$  ( $8f$ ) sites and can host di- and trivalent transition metal ions<sup>[100]</sup>.  $\text{Al}_2\text{TiO}_5$ - $\text{MgTi}_2\text{O}_5$  solid solution improves the thermal stability and mechanical properties of the isostructural compound  $\text{Al}_2\text{TiO}_5$ <sup>[108]</sup>. Investigations of  $\text{FeTi}_2\text{O}_5$ - $\text{MgTi}_2\text{O}_5$  solid solution are valuable in understanding the intermediate member of armalcolite mineral ( $\text{Fe}_{0.5}\text{Mg}_{0.5}\text{Ti}_2\text{O}_5$ ) which is found in natural rocks, such as terrestrial igneous and lunar basalt<sup>[79,180,181]</sup>. Replacement of the element Mg in  $\text{MgTi}_2\text{O}_5$  by the divalent element Zn, Co, Ni, Mn or Ca can enhance its practical application as microwave dielectric ceramics<sup>[102,169]</sup> and pigments<sup>[101,103]</sup>.

Because of the high thermodynamic instability of the pseudobrookite-type structure under ambient conditions, many endmember compounds have not been obtained, which blocks the studies of  $\text{MgTi}_2\text{O}_5$ -based solid solutions<sup>[100,182]</sup>. Effect of cation substitution on crystal structure and properties of  $\text{MgTi}_2\text{O}_5$  were rarely investigated<sup>[103,161]</sup>. The normal substitution fractions of  $\text{Mg}^{2+}$  by other divalent cations were reported in the molar ratio range of 5–20%<sup>[100,102,169]</sup>. In addition, the limitation of  $\text{Ni}^{2+}$  in the  $\text{NiTi}_2\text{O}_5$ - $\text{MgTi}_2\text{O}_5$  solid solution was only extended to 60% in molar ratio and the compound  $\text{NiTi}_2\text{O}_5$  was not discovered<sup>[103]</sup>. As  $\text{Ni}^{2+}$  possesses a special preference for the octahedral site,  $\text{Zn}^{2+}$  which strongly prefers the tetrahedral site was chosen as a comparison.  $\text{Cu}^{2+}$ , which has a comparable Shannon radius with  $\text{Mg}^{2+}$  and  $\text{Zn}^{2+}$ , was also employed to replace  $\text{Mg}^{2+}$ .

Limited research has been reported on  $\text{ZnTi}_2\text{O}_5$ - $\text{MgTi}_2\text{O}_5$  solid solution, among which only 5–10%  $\text{Mg}^{2+}$  was substituted by  $\text{Zn}^{2+}$ <sup>[102,169]</sup>. Huang and Shen<sup>[102]</sup> found that replacing 5%  $\text{Mg}^{2+}$  by  $\text{Zn}^{2+}$  led to an increase of the unit cell volume of  $\text{MgTi}_2\text{O}_5$ . However, Karande et al.<sup>[169]</sup> observed that the unit cell volume of the intermediate compound  $\text{Zn}_{0.1}\text{Mg}_{0.9}\text{Ti}_2\text{O}_5$  was smaller than that of  $\text{MgTi}_2\text{O}_5$ . The evolution of the unit cell dimensions due to substituting  $\text{Mg}^{2+}$  by  $\text{Zn}^{2+}$  needs to be systematically investigated. Besides, Kapoor et al.<sup>[104]</sup> attempted to synthesise the endmember compound  $\text{ZnTi}_2\text{O}_5$  using an aerogel process but only obtained a composite of  $\text{ZnTiO}_3$  and  $\text{TiO}_2$ . Here, mechanochemical activation assisted solid state synthesis with a subsequent quenching and self-propagating high-temperature synthesis were employed to explore synthesis and crystal structures of the substitutional solid solutions  $\text{ZnTi}_2\text{O}_5$ - $\text{MgTi}_2\text{O}_5$  and  $\text{CuTi}_2\text{O}_5$ - $\text{MgTi}_2\text{O}_5$  at ambient pressure.

## 5.2 Experimental section

### 5.2.1 Sample preparation

The samples with compositions of  $Zn_xMg_{1-x}Ti_2O_5$  ( $0 \leq x \leq 1$ ) were prepared from the binary oxides (purity 99%, Merck) ZnO, MgO and  $TiO_2$  (anatase) in stoichiometric amounts. The interval of  $x$  was 0.1. MgO was calcined at 1073 K for 2 h. The mixture of the oxides was ball milled at 300 rpm for 3 h using a planetary ball mill (Fritsch P7). The material of the grinding bowls/balls was hard metal tungsten carbide and the mass ratio of balls to powder was 10:1. Then the well-blended mixture was pressed into small cylinders (diameter 5 mm, height 10 mm). The cylinders were heat treated at 1473–1573 K for 2–4 h in air, followed by a process of quenching the cylinders from the synthesis temperature into a mixture of ice and water. Finally, the cylinders were ground into powders using an agate mortar.

Some additional approaches were employed to synthesise the endmember compound  $ZnTi_2O_5$ . In the first method, a stoichiometric composition of  $ZnO:TiO_2 = 1:2$  in molar ratio was used. The mixture was first ball milled at 750 rpm for 600 min and then pelletised. Some of the pellets were sintered at 1473–1573 K for 4 h with a muffle furnace in air while the other pellets were ignited using our SHS set-up (page 15) under Ar atmosphere. In another method, a starting composition of  $ZnO:TiO_2$  (anatase): $\alpha$ -Ti = 1:1.5:0.5 in molar ratio was used. The mixture was first milled at 750 rpm for 330 min under Ar atmosphere and then pelleted, and the pellet was ignited using the SHS set-up under Ar atmosphere.

The samples  $Cu_xMg_{1-x}Ti_2O_5$  ( $0 \leq x \leq 0.5$ ) were prepared starting from the binary oxides (purity 99%, Merck) CuO, MgO and  $TiO_2$  (anatase) in stoichiometric amounts. MgO was calcined at 1073 K for 2 h. The mixture of the oxides was ball milled at 300 rpm for 3 h using a planetary ball mill (Fritsch P7). The material of the grinding bowls/balls was hard metal tungsten carbide and the mass ratio of balls to powder was 10:1. Then the well-blended mixture was pressed into small cylinders (diameter 5 mm, height 10 mm). The cylinders were heat treated at 1273 K for 4 h in air, followed by a process of quenching the cylinders directly into a mixture of ice and water. Finally, the quenched cylinders were ground into powders using an agate mortar.

Fig 5.1 shows photographs of  $Cu_xMg_{1-x}Ti_2O_5$  and  $Zn_xMg_{1-x}Ti_2O_5$ . Cation substitutions led to changes of  $MgTi_2O_5$  in colour.  $Cu_xMg_{1-x}Ti_2O_5$  are dark brown and black while  $Zn_xMg_{1-x}Ti_2O_5$  vary from light grey to dark grey.

### 5.2.2 X-ray diffraction

Powder X-ray diffraction data were collected on a X'pert diffractometer (PANalytical) with Bragg-Brentano geometry over a  $2\theta$  range of 10–140° using  $CuK\alpha_1$  radiation ( $\lambda = 1.5406 \text{ \AA}$ , 40 kV, 30 mA) at ambient conditions. In the incident beam path, a curved Ge 110 monochromator, a 0.5° divergence slit and a 15 mm brass mask were mounted. An external method was employed to calibrate the diffractometer using silicon powder. The collecting time of the samples was around 17 h, using a step size of 0.002° and 200 s per step.

Rietveld refinements of the XRD data for  $Zn_xMg_{1-x}Ti_2O_5$  were carried out using

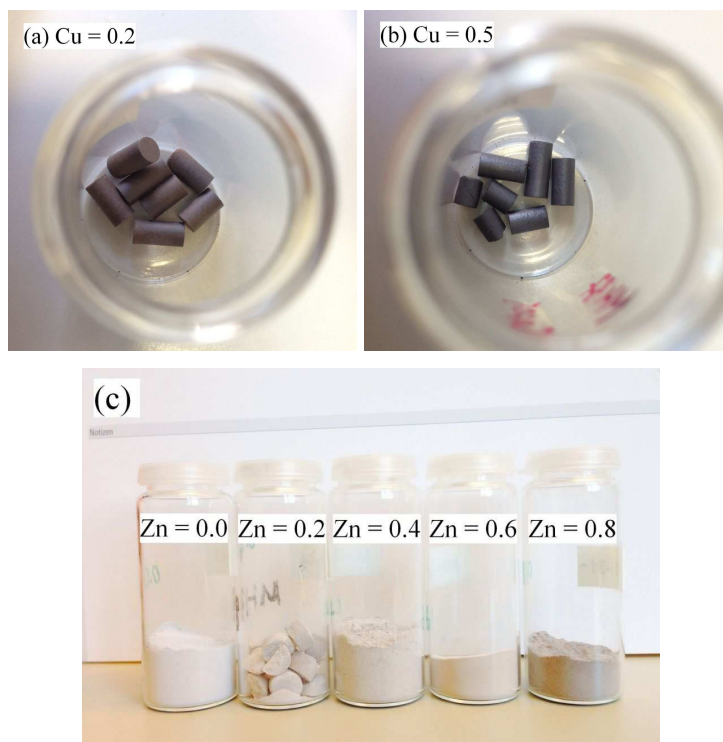


Figure 5.1: (a)  $\text{Cu}_x\text{Mg}_{1-x}\text{Ti}_2\text{O}_5$  with  $x = 0.2$ , (b)  $\text{Cu}_x\text{Mg}_{1-x}\text{Ti}_2\text{O}_5$  with  $x = 0.5$ , (c)  $\text{Zn}_x\text{Mg}_{1-x}\text{Ti}_2\text{O}_5$  with  $x = 0, 0.2, 0.4, 0.6$  and  $0.8$ .

the GSAS programme<sup>[122]</sup> and the EXPGUI interface<sup>[123]</sup>. The peak shapes were described by pseudo-Voigt profile functions. Initial cell and atomic parameters of  $\text{MgTi}_2\text{O}_5$  and  $\text{TiO}_2$  (rutile) were taken from the literature<sup>[92,173]</sup>. The background was fitted by a Chebyshev polynomial with 8 terms. Thermal displacements of all atoms were regarded as isotropic. The positional parameters and  $U_{\text{iso}}$  of the cations in the same set of sites was constrained to be the same. Meanwhile, each site was constrained to be fully occupied. Absorption correction, lattice parameters, positional parameters,  $U_{\text{iso}}$ , profile parameters (GU, GV, GW, LX, LY) and the scale factor were refined.

Le Bail refinements of the XRD data for  $\text{Cu}_x\text{Mg}_{1-x}\text{Ti}_2\text{O}_5$  with pseudo-Voigt profile functions were carried out using the GSAS programme<sup>[122]</sup> and the EXPGUI interface<sup>[123]</sup>. The lattice parameters and atomic parameters of  $\text{MgTi}_2\text{O}_5$ <sup>[92]</sup> were used as starting structural models for  $\text{Cu}_x\text{Mg}_{1-x}\text{Ti}_2\text{O}_5$ . The background was described by a Chebyshev polynomial with 8 terms. Besides, zero shift, lattice parameters and profile parameters (GU, GV, GW, LX, LY) were refined.

### 5.2.3 Neutron diffraction

High-resolution powder neutron diffraction data for  $\text{Zn}_x\text{Mg}_{1-x}\text{Ti}_2\text{O}_5$  were collected at ambient conditions on the D2B diffractometer of the Institut Laue-Langevin (ILL). Two samples ( $x = 0.0$  and  $0.8$ ) were measured with a typical sample mass of 5 g. The incident beam Ge 335 monochromator was mounted to produce a neutron beam with

a monochromatic wavelength of 1.5946 Å. The primary neutron beam was focused by putting a collimator with vertical divergence of  $1/6^\circ$  and a horizontal slit of 30 mm between the monochromator and the samples. Neutron intensities were collected in the  $2\theta$  range of 0–160° with a step size of 0.05°. The diffractometer was equipped with 128 detectors which were spaced at 1.25° intervals. In order to improve statistics, each scan was repeated 10 times. The time for one measurement was around 4 h.

Rietveld refinement was employed to analyse the crystal structures of  $Zn_xMg_{1-x}Ti_2O_5$  with  $x=0.0$  and 0.8. The profile of the reflections was refined with a pseudo-Voigt profile function and the background was fitted using a Chebyshev polynomial with 8 terms. Thermal displacements of all atoms were regarded as isotropic. The positional parameters and  $U_{iso}$  of cations in the same set of sites were constrained to be the same. Each site was constrained to be fully occupied.

#### 5.2.4 Raman spectroscopy

Raman spectra of the products were collected in the range of 100–2000  $cm^{-1}$  using a Renishaw Raman spectrometer (RM-100) equipped with a Leica DMLM optical microscope at ambient conditions. For excitation, the 532 nm line of a Nd:YAG laser with an exposure time of 10–30 s was used. The power was 2 mW for  $Zn_xMg_{1-x}Ti_2O_5$  and 20 mW for  $Cu_xMg_{1-x}Ti_2O_5$ . A quasi-backscattering geometry and a 1800 groove  $mm^{-1}$  grating was employed. The data were collected by Dr. Lkhamsuren Bayarjargal.

## 5.3 Results and discussion

### 5.3.1 Phase compositions

According to the XRD data,  $\text{Zn}_x\text{Mg}_{1-x}\text{Ti}_2\text{O}_5$  with  $0 \leq x \leq 0.9$  and  $\text{Cu}_x\text{Mg}_{1-x}\text{Ti}_2\text{O}_5$  with  $0 \leq x \leq 0.5$  were synthesised by mechanochemical activation assisted solid state synthesis. The solid solutions crystallised in an orthorhombic pseudobrookite-type structure with space group  $Cmcm$ . Solid state synthesis of the endmember  $\text{ZnTi}_2\text{O}_5$  from binary oxides yielded a composite of  $\alpha\text{-Zn}_2\text{TiO}_4$  and  $\text{TiO}_2$  (rutile). Though no propagation occurred in the SHS reactions, high temperature was achieved to generate the endmember  $\text{ZnTi}_2\text{O}_5$  in the SHS product by using  $\alpha\text{-Ti}$  in the starting materials.

Table 5.1 summarises the synthesis conditions and purities of the  $\text{Zn}_x\text{Mg}_{1-x}\text{Ti}_2\text{O}_5$  and  $\text{Cu}_x\text{Mg}_{1-x}\text{Ti}_2\text{O}_5$  solid solution. The purity of  $\text{Zn}_x\text{Mg}_{1-x}\text{Ti}_2\text{O}_5$  depended on the synthesis temperature. For  $0 \leq x \leq 0.6$ , 99(1) wt.% purities were achieved at 1473 K. At the same temperature, the purity slightly decreased to 96(1) wt.% when the molar fraction of zinc increased to 70%. Therefore, the synthesis temperature of  $\text{Zn}_x\text{Mg}_{1-x}\text{Ti}_2\text{O}_5$  with  $x > 0.7$  was increased to 1573 K. The sample with  $x = 0.8$  had a purity of 96(1) wt.% while for  $x = 0.9$  the purity decreased dramatically to  $\sim 30$  wt.%. During the Rietveld refinement, the chemical compositions of  $\text{Zn}_x\text{Mg}_{1-x}\text{Ti}_2\text{O}_5$  with  $x \leq 0.8$  were treated as stoichiometric. The synthesis temperature of  $\text{Cu}_x\text{Mg}_{1-x}\text{Ti}_2\text{O}_5$  was 1273 K. Since reflections of the impurity phase  $\text{TiO}_2$  (rutile) were at the background level, chemical compositions of  $\text{Cu}_x\text{Mg}_{1-x}\text{Ti}_2\text{O}_5$  were treated as stoichiometric for the sake of simplicity.

Table 5.1: Synthesis conditions and purities of  $\text{Zn}_x\text{Mg}_{1-x}\text{Ti}_2\text{O}_5$  with  $0 \leq x \leq 1$  and  $\text{Cu}_x\text{Mg}_{1-x}\text{Ti}_2\text{O}_5$  with  $0 \leq x \leq 0.5$ .

Method	$\text{Zn}_x\text{Mg}_{1-x}\text{Ti}_2\text{O}_5$				$\text{ZnTi}_2\text{O}_5$	$\text{Cu}_x\text{Mg}_{1-x}\text{Ti}_2\text{O}_5$
	Solid state synthesis				SHS set-up	Solid state
Chemical composition	$0 \leq x \leq 0.6$	$x = 0.7$	$x = 0.8$	$x = 0.9$	$\text{ZnTi}_2\text{O}_5$	$0 \leq x \leq 0.5$
Speed of milling [rpm]	300	300	300	300	750	300
Time of milling [h]	3	3	3	3	3	3
Temperature [K]	1473	1473	1573	1573		1273
Holding time [h]	2	2	4	4		4
Purity [wt.%]	99(1)	96(1)	96(1)	$\sim 30$	19	minor CuO

Figure 5.2 shows a picture of the cylinder by employing SHS reaction of  $\text{ZnO}$ ,  $\text{TiO}_2$  and  $\alpha\text{-Ti}$ . The reaction occurred at the top part of the cylinder which was the origin of the ignition. The XRD pattern of the product (the top part of the cylinder) indicates a new crystalline phase, which could not be identified by any known compound in the  $\text{ZnO}\text{-TiO}_2$  binary system<sup>[30,183]</sup>. Le Bail refinement result shows an orthorhombic symmetry with lattice parameters of 3.7188(25) Å for  $a$ , 9.7886(25) Å for  $b$  and 10.1205(25) Å for  $c$ . These values are comparable with lattice parameters of  $\text{MgTi}_2\text{O}_5$ .

A Rietveld refinement of XRD for the SHS product was carried out by assuming the new crystalline phase as an orthorhombic pseudobrookite-type  $\text{ZnTi}_2\text{O}_5$  phase. The positional parameters and  $U_{\text{iso}}$  of the atoms for  $\text{ZnTi}_2\text{O}_5$  were based on  $\text{MgTi}_2\text{O}_5$ . Figure 5.3 presents the Rietveld refinement result. The reaction yielded 19 wt.%  $\text{ZnTi}_2\text{O}_5$  and the impurities included  $\text{TiO}_2$  (rutile),  $\text{Zn}_2\text{TiO}_4$  (spinel) and  $\text{ZnTiO}_3$ . The formation

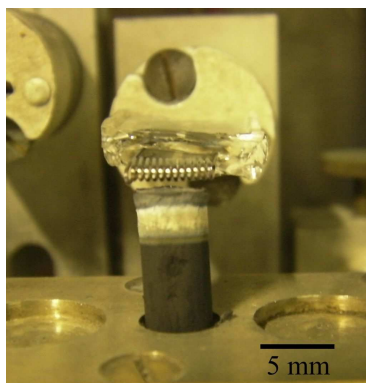


Figure 5.2: The product for the synthesis of  $ZnTi_2O_5$  starting from  $ZnO$ ,  $TiO_2$  and  $\alpha$ -Ti using the SHS set-up. The reaction occurred at the ignition point of the cylinder (top part).

of  $ZnTi_2O_5$  by employing the SHS set-up is attributed to an extremely high ignition temperature and the high thermal conductivity of  $\alpha$ -Ti metal ( $21.9 \text{ W m}^{-1} \text{ K}^{-1}$ ) with respect to oxides. In addition, the starting composition and the super-fast cooling rate of the reaction are responsible for stabilising  $ZnTi_2O_5$  at ambient conditions.

### 5.3.2 Rietveld refinements for $MgTi_2O_5$

Structural parameters of the endmember  $MgTi_2O_5$  were obtained by refining the X-ray diffraction and neutron diffraction data for the samples with a synthesis temperature of 1273 K and 1473 K. The Mg/Ti disorder parameter  $X$  was calculated from the linear relation with lattice parameter  $b$  (page 8), which was 0.38 for  $MgTi_2O_5$  synthesised at 1273 K and 0.4 for 1473 K.

The XRD data were refined by using fixed values for the site occupancy and the thermal displacement parameter. The thermal displacement parameter  $U_{iso}$  of cations and anions was constrained to be  $0.005 \text{ \AA}^2$  and  $0.01 \text{ \AA}^2$ , respectively. The zero shift, scale factor, backgrounds, lattice parameters, atomic positional parameters and profile parameters were refined simultaneously to achieve convergence.

The site occupancy and the thermal displacement parameter were refined for the ND data. Constraints were added to have a full occupation of the  $M1$  and  $M2$  sites. The value of  $U_{iso}$  ( $M2$ ) was fixed to be  $0.005 \text{ \AA}^2$  due to the unphysically small value in the refinement. In the final Rietveld refinement results, convergence was achieved by refining the zero shift, scale factor, backgrounds, lattice parameters, atomic positional parameters, thermal displacement parameter, site occupancies and profile parameters simultaneously.

Table 5.2 lists the Rietveld refinement results for  $MgTi_2O_5$ . Figure 5.4 shows Rietveld refinements of neutron diffraction for  $MgTi_2O_5$  with  $X = 0.4$ . As inferred from the stoichiometric atomic fraction and  $R_{wp}$  value, the ND results are reasonable. The XRD and ND results of this sample agree well with each other. They show very small differences with the single crystal XRD data of  $MgTi_2O_5$  with  $X = 0.404(5)$ <sup>[89]</sup>.

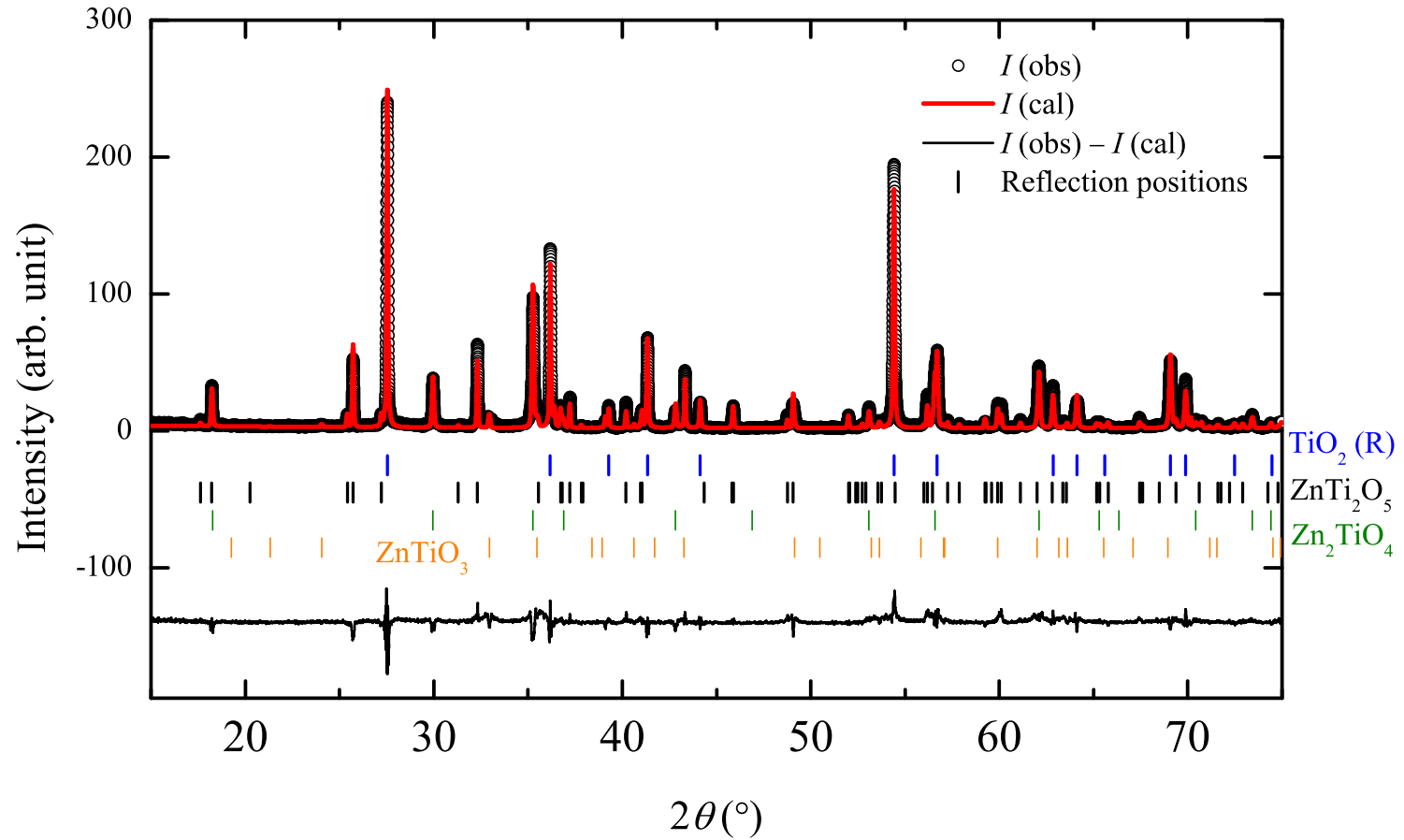


Figure 5.3: Rietveld refinement result of XRD for the SHS product. The bottom black curve represents the difference between the observed data (black circles) and the calculated (continuous red curve) data. The tickmarks indicate reflections from crystalline phases including  $\text{ZnTi}_2\text{O}_5$ ,  $\text{TiO}_2$  (rutile),  $\text{Zn}_2\text{TiO}_4$  (spinel) and  $\text{ZnTiO}_3$ .

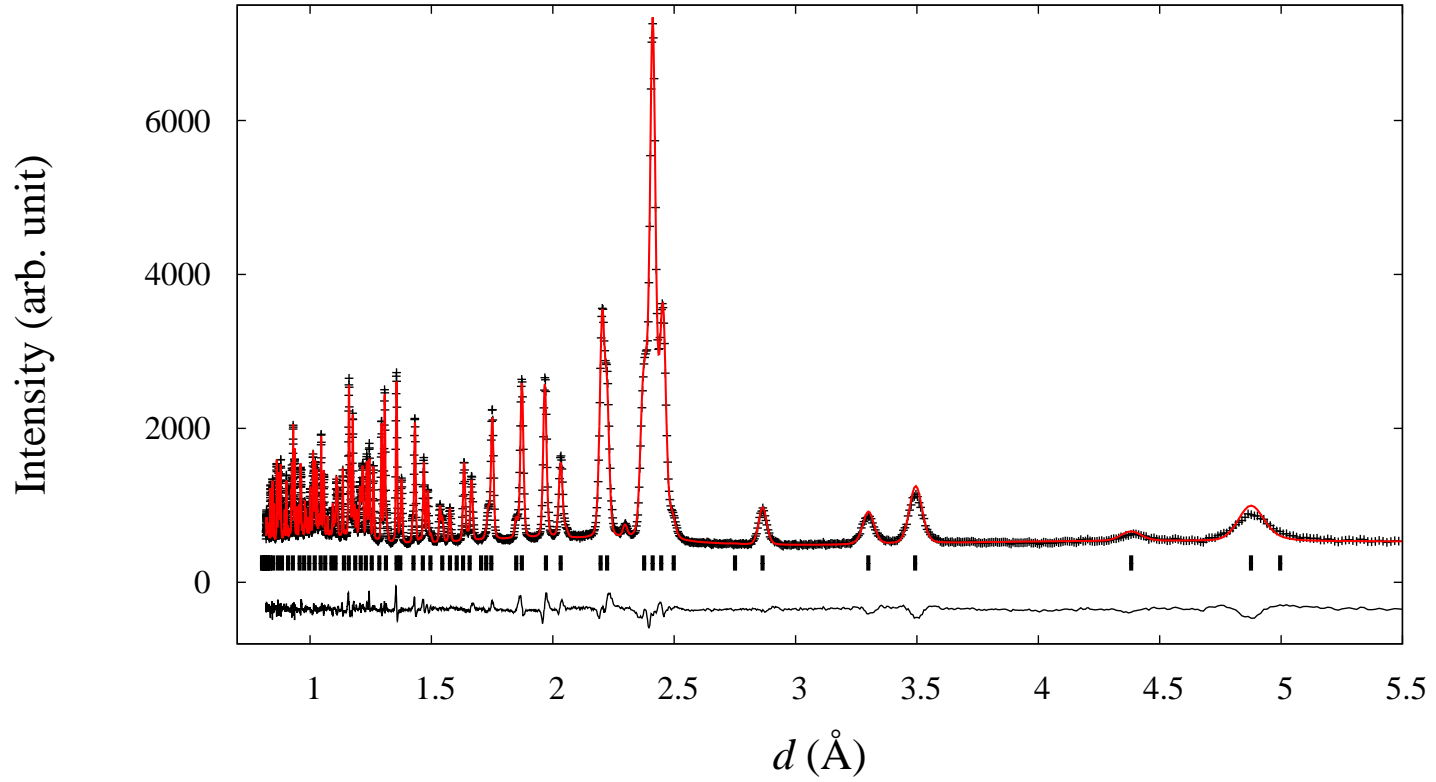


Figure 5.4: Rietveld refinement results of neutron diffraction for the endmember  $\text{MgTi}_2\text{O}_5$ . The bottom black curve represents the difference between the observed data (black circles) and the calculated (continuous red curve) data. The tickmarks indicate positions of the reflections.



Table 5.2: Rietveld refinement results of X-ray diffraction and neutron diffraction for the orthorhombic pseudobrookite-type endmember  $\text{MgTi}_2\text{O}_5$  with space group  $Cmcm$ . The thermal displacement parameter  $U_{\text{iso}}$  has a unit of  $\times 0.01 \text{ \AA}^2$ . The values without error bars have been fixed in the refinement. The results are compared with single crystal XRD data from the literature<sup>[89]</sup>.

	X = 0.38 (XRD)	X = 0.4 (XRD)	X = 0.4 (ND)	X = 0.4 (Lit. <sup>[89]</sup> )
Unit cell				
$a$ [ $\text{\AA}$ ]	3.74509(5)	3.74643(2)	3.74445(5)	3.7464(4)
$b$ [ $\text{\AA}$ ]	9.7488(2)	9.75128(6)	9.75223(13)	9.7461(6)
$c$ [ $\text{\AA}$ ]	9.9909(2)	9.98896(6)	9.99307(13)	9.9875(4)
$V$ [ $\text{\AA}^3$ ]	364.768(7)	364.922(5)	364.914(6)	364.67(4)
$\rho$ [ $\text{g cm}^{-3}$ ]	3.644	3.642	3.636	3.644
X	0.38	0.4	0.392(3)	0.404(5)
M1 (4c) sites				
$x$	0.1927(4)	0.1921(2)	0.1906(5)	0.19241(7)
$U_{\text{iso}}$	0.5	0.5	0.71(12)	0.71(4)
$\text{Mg}^{2+}$	0.62	0.6	0.610(3)	0.596(5)
$\text{Ti}^{4+}$	0.38	0.4	0.390(3)	0.404(5)
M2 (8f) sites				
$x$	0.1353(2)	0.1353(1)	0.1349(3)	0.13523(4)
$y$	0.5644(2)	0.5636(1)	0.5602(3)	0.56386(4)
$U_{\text{iso}}$	0.5	0.5	0.5	0.62(3)
$\text{Mg}^{2+}$	0.19	0.2	0.192(3)	0.202(5)
$\text{Ti}^{4+}$	0.81	0.8	0.808(3)	0.798(5)
O1 (4c)				
$x$	0.7669(8)	0.7672(4)	0.7687(1)	0.76906(23)
$U_{\text{iso}}$	1.0	1.0	0.85(3)	1.13(6)
O2 (8f)				
$x$	0.0468(6)	0.0471(3)	0.0469(1)	0.04670(15)
$y$	0.1137(5)	0.1164(3)	0.1155(1)	0.11550(17)
$U_{\text{iso}}$	1.0	1.0	0.81(2)	1.10(4)
O3 (8f)				
$x$	0.3110(6)	0.3132(3)	0.3113(1)	0.31197(16)
$y$	0.0690(6)	0.0688(3)	0.0684(1)	0.06764(16)
$U_{\text{iso}}$	1.0	1.0	0.70(2)	0.98(5)
Atomic fraction				
Total $\text{Mg}^{2+}$	1	1	0.995	1.00
Total $\text{Ti}^{4+}$	2	2	2.005	2.00
Rietveld agreement factors				
$R_{\text{wp}}$ [%]	23.7	39.1	3.9	2.3
$R_{\text{wpb}}$ [%]	33.5	49.5	4.4	
$\chi^2$	1.1	0.9	6.5	

### 5.3.3 Rietveld refinement results for $\text{Zn}_x\text{Mg}_{1-x}\text{Ti}_2\text{O}_5$

Rietveld refinements of XRD for  $\text{Zn}_x\text{Mg}_{1-x}\text{Ti}_2\text{O}_5$  were carried out by fixing the site occupancies and thermal displacement parameters due to the excessive structural parameters, including 3 lattice parameters, 8 atomic positional parameters, 5  $U_{\text{iso}}$  parameters, 6 cationic site occupancies and 5 profile parameters.

For  $x \leq 0.6$ , the structural model is built by setting 80%  $Ti^{4+}$  and 20%  $Zn^{2+}$  in the  $M2$  octahedral sites. The  $M1$  octahedral sites were occupied by  $Zn^{2+}$ ,  $Mg^{2+}$  and 40%  $Ti^{4+}$ . The thermal displacement parameters  $U_{iso}$  for cations and oxygen were fixed at 0.5 and  $1 \times 10^{-2} \text{ \AA}^2$ , respectively. Convergent refinements were achieved and the difference curves between the observed and calculated X-ray reflection intensities were narrow, indicating reasonable structural models. Figure 5.5 shows Rietveld refinement results of  $Zn_xMg_{1-x}Ti_2O_5$  with  $x = 0.4$  in a short  $2\theta$  range of  $15\text{--}65^\circ$ .

Table 5.3 summarises Rietveld refinement results of XRD for the  $Zn_xMg_{1-x}Ti_2O_5$  solid solutions with  $0 \leq x \leq 0.6$ . A full site occupancy for each set of sites was constrained. With the increase of  $x$ , the unit cell volume and density of the solid solutions both increased. The goodness of fit was smaller than 1.0 and  $R_{wp}$  factors were high. One reason is that too much data points were collected<sup>[184]</sup>. As the samples were quenched from 1473–1573 K, texture could exist. Another reason is because of the inaccurate site occupancies and  $U_{iso}$  values. The small deviation of chemical compositions of the solid solution from their ideal composition would also lead to an increase of the gap between the calculated and observed values.

For  $Zn_xMg_{1-x}Ti_2O_5$  with  $x = 0.7$  and  $0.8$ , Rietveld refinements of XRD were carried out by setting several different site occupancies of the cations. The refinement strategies and results are tabulated in table 5.4. Thermal displacement parameters  $U_{iso}$  of the cations and oxygen anions were fixed at 0.5 and  $1 \times 10^{-2} \text{ \AA}^2$ , respectively. For both samples, the models of incorporating 60%  $Zn^{2+}$  into the  $M1$  (4c) sites generally achieved better results than those having 70%  $Zn^{2+}$  in the  $M1$  (4c) sites. The best site occupancies was 60%  $Zn^{2+}$ , 10%  $Mg^{2+}$  and 30%  $Ti^{4+}$  in the  $M1$  (4c) sites and the Rietveld refinement results are shown in figure 5.6.

Rietveld refinement of neutron diffraction for  $x = 0.8$  was employed by fixing  $U_{iso}$  of the cations in the  $M2$  sites to be  $5 \times 10^{-3} \text{ \AA}^2$ . Two constraints were added to keep a full site occupancy of the  $M1$  (4c) sites and the  $M2$  (8f) sites. The site occupancy of  $Ti^{4+}$  in each set of sites was divided into two parts. One part was constrained with  $Zn^{2+}$  in the same sites and the other part was constrained with  $Mg^{2+}$  in the same sites. Convergence was achieved by refining zero shift, background, scale factor, lattice parameters, atomic positional parameters,  $U_{iso}$  parameters, cationic site occupancies and profile parameters simultaneously. The results are tabulated in table 5.4 and plotted in figure 5.7. The refined atomic fraction of cations agreed well with the stoichiometric chemical composition, indicating reliable site occupancies.

The result of neutron diffraction for  $x = 0.8$  is tabulated in table 5.4. It shows 58.5(3)%  $Zn^{2+}$  occupying the  $M1$  (4c) sites, which is consistent with the structural model of setting 60%  $Zn^{2+}$  in  $M1$  in the XRD data. Site occupancies of  $Zn_xMg_{1-x}Ti_2O_5$  with  $x = 0.8$  are almost the same with the XRD results of strategy 2 in table 5.4. It confirms a reasonable structural model of the XRD data.

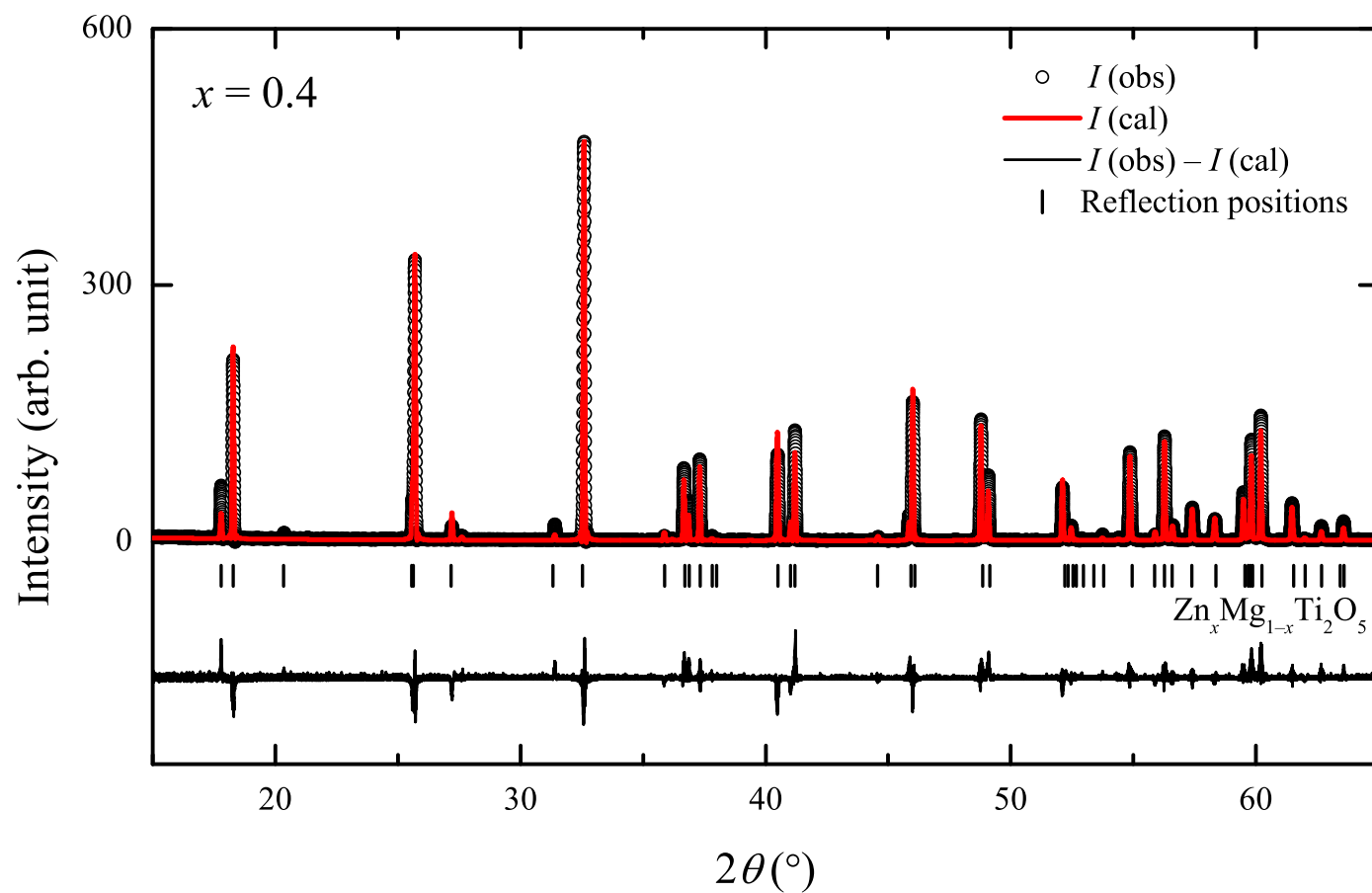


Figure 5.5: Rietveld refinement results of X-ray diffraction for  $\text{Zn}_x\text{Mg}_{1-x}\text{Ti}_2\text{O}_5$  with  $x = 0.4$ . The black dots represent the observed data, while the red curves show the calculated data. A black curve in the bottom shows the difference between them. The tickmarks indicate  $2\theta$  positions of the reflections from crystalline phases.

Table 5.3: Rietveld refinement results of XRD for  $\text{Zn}_x\text{Mg}_{1-x}\text{Ti}_2\text{O}_5$  with  $0 \leq x \leq 0.6$  using fixed values for site occupancies and thermal displacement parameters. The solid solution was refined using an orthorhombic pseudobrookite-type structure with space group  $Cmcm$ . The thermal displacement parameter  $U_{\text{iso}}$  has a unit of  $\times 0.01 \text{ \AA}^2$ .

	$x=0.0$	$x=0.1$	$x=0.2$	$x=0.3$	$x=0.4$	$x=0.5$	$x=0.6$
Unit cell							
$a$ [Å]	3.74643(2)	3.74386(2)	3.74083(2)	3.73828(2)	3.73542(2)	3.73169(1)	3.72841(1)
$b$ [Å]	9.75128(6)	9.75812(5)	9.76247(5)	9.76747(4)	9.77258(4)	9.77567(4)	9.78154(5)
$c$ [Å]	9.98896(6)	10.00192(5)	10.01304(5)	10.02488(4)	10.03825(4)	10.05195(4)	10.06418(5)
$V$ [Å <sup>3</sup> ]	364.922(5)	365.401(3)	365.674(2)	366.044(2)	366.443(2)	366.692(2)	367.037(2)
$\rho$ [g cm <sup>-3</sup> ]	3.642	3.712	3.784	3.855	3.925	3.997	4.067
Site occupancy							
$\text{Zn}^{2+}$ (4c/8f)	0/0	0.1/0	0.2/0	0.3/0	0.4/0	0.5/0	0.6/0
$\text{Mg}^{2+}$ (4c/8f)	0.6/0.2	0.5/0.2	0.4/0.2	0.3/0.2	0.2/0.2	0.1/0.2	0/0.2
M1 (4c) sites							
$x$	0.1921(2)	0.1921(2)	0.1910(1)	0.1900(1)	0.1896(1)	0.1888(1)	0.1884(1)
$U_{\text{iso}}$	0.5	0.5	0.5	0.5	0.5	0.5	0.5
M2 (8f) sites							
$x$	0.1354(1)	0.1355(1)	0.1353(1)	0.1352(1)	0.1347(1)	0.1346(1)	0.1343(1)
$y$	0.5636(1)	0.5637(1)	0.5639(1)	0.5643(1)	0.5643(1)	0.5649(1)	0.5649(1)
$U_{\text{iso}}$	0.5	0.5	0.5	0.5	0.5	0.5	0.5
O1 (4c)							
$x$	0.7669(4)	0.7668(4)	0.7667(4)	0.7651(5)	0.7642(5)	0.7635(4)	0.7600(7)
$U_{\text{iso}}$	1.0	1.0	1.0	1.0	1.0	1.0	1.0
O2 (8f)							
$x$	0.0470(3)	0.0495(3)	0.0461(3)	0.0448(3)	0.0447(3)	0.0429(3)	0.0435(4)
$y$	0.1162(3)	0.1135(3)	0.1144(3)	0.1155(3)	0.1165(3)	0.1179(3)	0.1155(4)
$U_{\text{iso}}$	1.0	1.0	1.0	1.0	1.0	1.0	1.0
O3 (8f)							
$x$	0.3130(3)	0.3120(3)	0.3127(3)	0.3146(3)	0.3140(3)	0.3174(3)	0.3174(4)
$y$	0.0688(3)	0.0669(3)	0.0662(3)	0.0651(3)	0.0637(2)	0.0629(2)	0.0662(4)
$U_{\text{iso}}$	1.0	1.0	1.0	1.0	1.0	1.0	1.0
Rietveld agreement factors							
$R_{\text{wp}}$ [%]	39.1	39.1	39.0	38.8	38.6	39.7	41.2
$R_{\text{wpb}}$ [%]	49.5	45.8	48.4	47.4	41.6	45.7	46.1
$\chi^2$	0.9	0.9	0.9	0.9	1.0	1.0	1.1

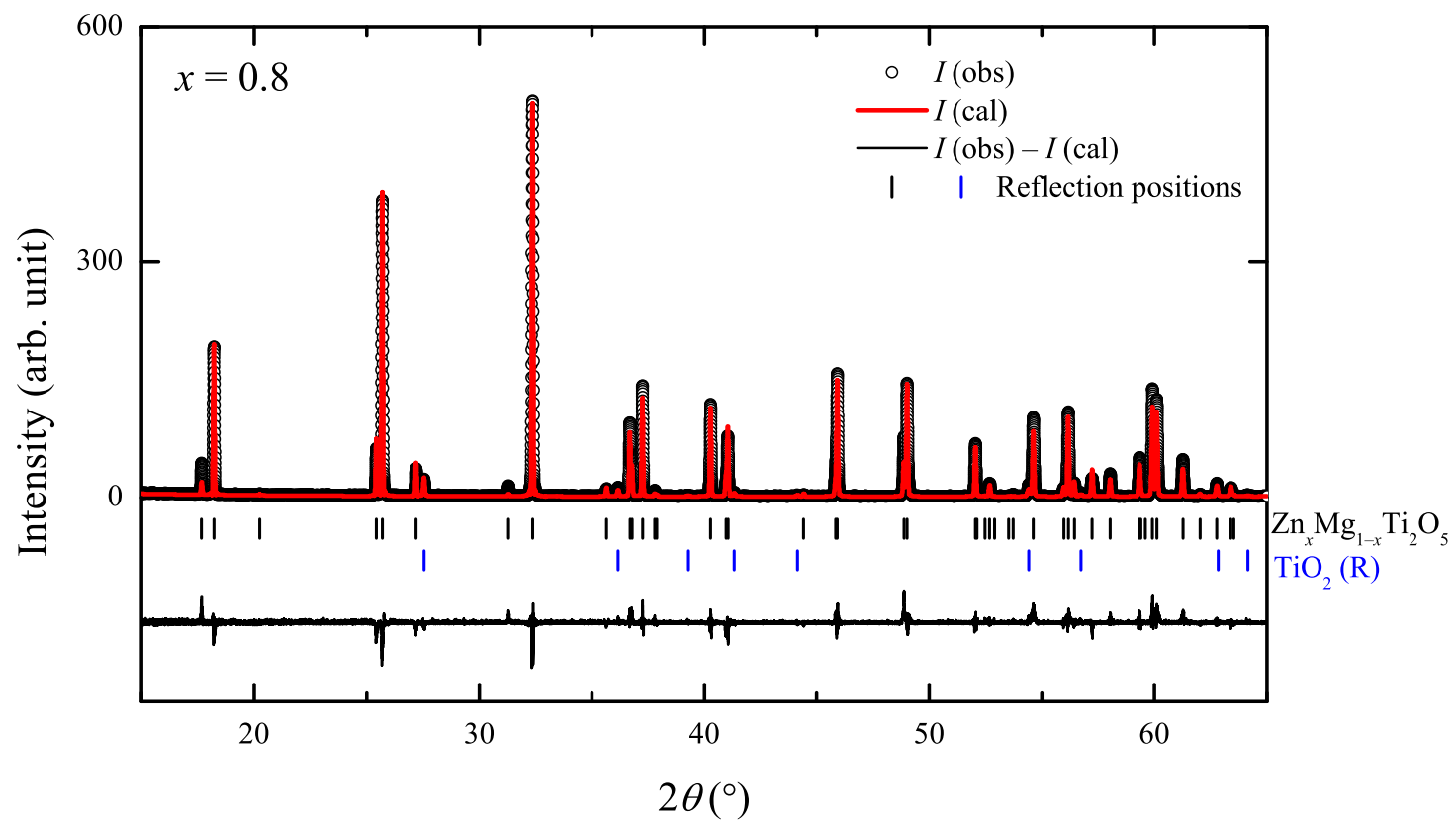


Figure 5.6: Rietveld refinement results of X-ray diffraction for  $\text{Zn}_x\text{Mg}_{1-x}\text{Ti}_2\text{O}_5$  with  $x = 0.8$ . The black dots represent the observed data, while the red curves show the calculated data. A black curve in the bottom shows the difference between them. The tickmarks indicate  $2\theta$  positions of the reflections from crystalline phases.

Table 5.4: Rietveld refinement strategies and results of X-ray diffraction and neutron diffraction for  $\text{Zn}_x\text{Mg}_{1-x}\text{Ti}_2\text{O}_5$  with  $x = 0.7$  and 0.8. Thermal displacement parameters  $U_{\text{iso}}$  have a unit of  $\times 10^{-2} \text{ \AA}^2$ . The values without error bar have been fixed in the refinement.

	$x = 0.7$ (XRD)				$x = 0.8$ (XRD)			$x = 0.8$ (ND)
$a$ [Å]	3.72536(2)				3.72135(2)			3.72134(4)
$b$ [Å]	9.78700(5)				9.79117(6)			9.78623(12)
$c$ [Å]	10.07842(5)				10.09127(6)			10.09588(13)
$\rho$ [ $\text{g cm}^{-3}$ ]	4.137				4.208			4.216
M1 (4c) sites								
$\text{Zn}^{2+}$	0.6	0.6	0.7	0.7	0.6	0.6	0.8	0.585(3)
$\text{Mg}^{2+}$		0.1	0.1			0.1		0.119(3)
$\text{Ti}^{4+}$	0.4	0.3	0.2	0.3	0.4	0.3	0.2	0.296(3)
$x$	0.1870(1)	0.1873(1)	0.1869(1)	0.1862(1)	0.1870(1)	0.1874(1)	0.1865(1)	0.1872(3)
$U_{\text{iso}}$	0.5	0.5	0.5	0.5	0.5	0.5	0.5	0.38(7)
M2 (8f) sites								
$\text{Zn}^{2+}$	0.05	0.05			0.1	0.1		0.101(5)
$\text{Mg}^{2+}$	0.15	0.1	0.1	0.15	0.1	0.05	0.1	0.034(5)
$\text{Ti}^{4+}$	0.8	0.85	0.9	0.85	0.8	0.85	0.9	0.865(5)
$x$	0.1337(1)	0.1336(1)	0.1337(1)	0.1345(1)	0.1348(1)	0.1347(1)	0.1352(1)	0.1365(2)
$y$	0.5657(1)	0.5655(1)	0.5657(1)	0.5684(1)	0.5654(1)	0.5653(1)	0.5659(1)	0.5600(3)
$U_{\text{iso}}$	0.5	0.5	0.5	0.5	0.5	0.5	0.5	0.5
O1 (4c)								
$x$	0.7668(5)	0.7680(5)	0.7666(5)	0.7634(5)	0.7682(5)	0.7690(5)	0.7682(5)	0.7736(1)
$U_{\text{iso}}$	1.0	1.0	1.0	1.0	1.0	1.0	1.0	1.02(4)
O2 (8f)								
$x$	0.0386(4)	0.0392(4)	0.0386(4)	0.0298(4)	0.0453(3)	0.0417(3)	0.0393(3)	0.0464(1)
$y$	0.1179(3)	0.1166(3)	0.1181(3)	0.1347(4)	0.1151(3)	0.1150(3)	0.1179(3)	0.1141(1)
$U_{\text{iso}}$	1.0	1.0	1.0	1.0	1.0	1.0	1.0	0.90(3)
O3 (8f)								
$x$	0.3210(3)	0.3202(3)	0.3207(3)	0.3258(4)	0.3173(3)	0.3170(3)	0.3182(3)	0.3128(1)
$y$	0.0624(3)	0.0628(3)	0.0625(3)	0.0654(3)	0.0626(3)	0.0635(3)	0.0623(3)	0.0648(1)
$U_{\text{iso}}$	1.0	1.0	1.0	1.0	1.0	1.0	1.0	0.99(3)
$R_{\text{wp}}$ [%]	41.0	39.41	40.28	46.19	36.2	35.67	37.65	2.7
$R_{\text{wpb}}$ [%]	46.5	44.78	45.83	52.14	37.2	36.18	38.53	3.5
$\chi^2$	1.0	0.97	1.01	1.33	0.9	0.83	0.92	4.4

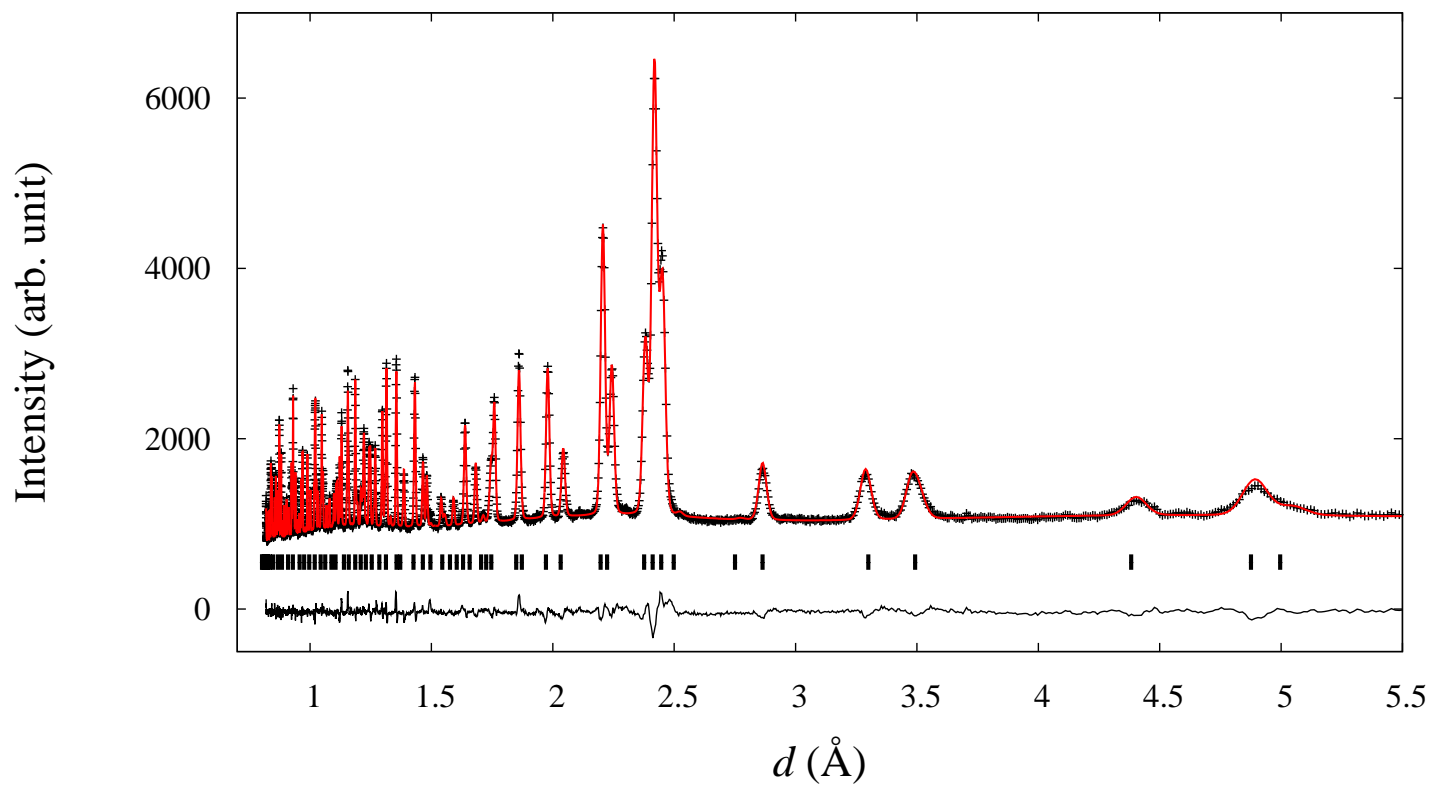


Figure 5.7: Rietveld refinement results of neutron diffraction for  $\text{Zn}_x\text{Mg}_{1-x}\text{Ti}_2\text{O}_5$  with  $x = 0.8$ . The bottom black curve represents the difference between the observed data (black circles) and the calculated (continuous red curve) data. The tickmarks indicate positions of the reflections.

### 5.3.4 Structural changes in the $Zn_xMg_{1-x}Ti_2O_5$ solid solution

Lattice parameters of the  $Zn_xMg_{1-x}Ti_2O_5$  solid solution with  $0 \leq x \leq 1$  were plotted against the composition, as shown in figure 5.8. The complete solid solution system  $ZnTi_2O_5$ – $MgTi_2O_5$  obeyed Vegard's law. A similar linear correlation has been reported for  $Zn_xCu_{1-x}Fe_2O_4$ <sup>[185]</sup> and  $Zn_xNi_{1-x}Fe_2O_4$  spinels<sup>[148]</sup>. Extrapolating the line to  $x = 1.0$  gave  $a = 3.7158(26)$  Å,  $b = 9.7997(33)$  Å,  $c = 10.1159(26)$  Å and  $V = 368.37(31)$  Å<sup>3</sup> for end-member  $ZnTi_2O_5$ . The experimentally determined lattice parameters of  $ZnTi_2O_5$  deviated only slightly ( $\pm 0.11\%$ ) from the extrapolated values, which confirmed the formation of pseudobrookite-type  $ZnTi_2O_5$  by using the SHS set-up. The unit cell volume increased with increasing  $Zn^{2+}$ . However, the results are different with the values in the literature<sup>[102,169]</sup>.

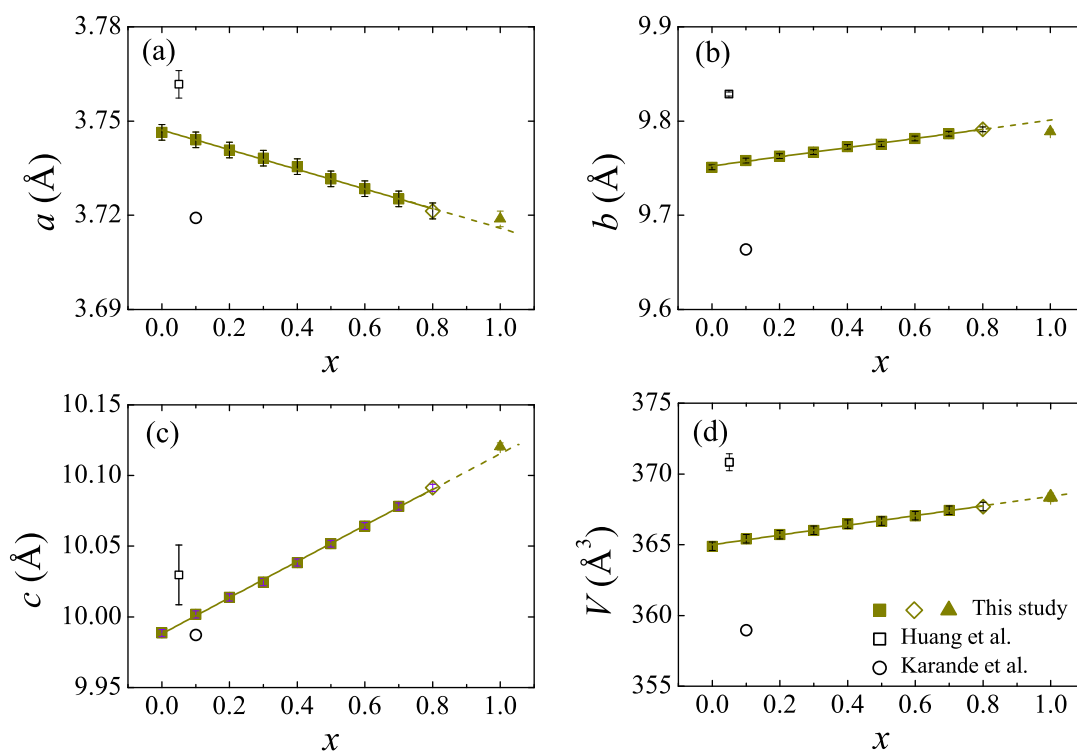


Figure 5.8: Lattice parameters of the solid solution  $Zn_xMg_{1-x}Ti_2O_5$  with  $0 \leq x \leq 1$ . The filled squares represent the samples quenched at 1473 K, which are fitted linearly. The open diamonds denote the sample quenched at 1573 K, while the open squares show the SHS product of  $ZnTi_2O_5$ . The open squares and circles are data in the literature<sup>[102,169]</sup>.

Cation distribution in the  $M1$  ( $4c$ ) sites of the  $Zn_xMg_{1-x}Ti_2O_5$  solid solution is demonstrated in figure 5.9. Both XRD results and neutron diffraction results are shown. The endmember  $MgTi_2O_5$  has 40%  $Ti^{4+}$  and 60%  $Mg^{2+}$  in the  $M1$  ( $4c$ ) sites. With the increasing incorporation of  $Zn^{2+}$  up to 60%,  $Mg^{2+}$  in the  $M1$  sites was gradually replaced by  $Zn^{2+}$ .  $Zn^{2+}$  preferably incorporated into the larger  $M1$  octahedra. When more than



60%  $\text{Mg}^{2+}$  was substituted by  $\text{Zn}^{2+}$ , 60%  $\text{Zn}^{2+}$  occupied the M1 octahedra and the extra part of  $\text{Zn}^{2+}$  was forced into the M2 octahedra. Meanwhile,  $\text{Ti}^{4+}$  in the M2 sites exchanged with  $\text{Mg}^{2+}$  in the M1 sites.

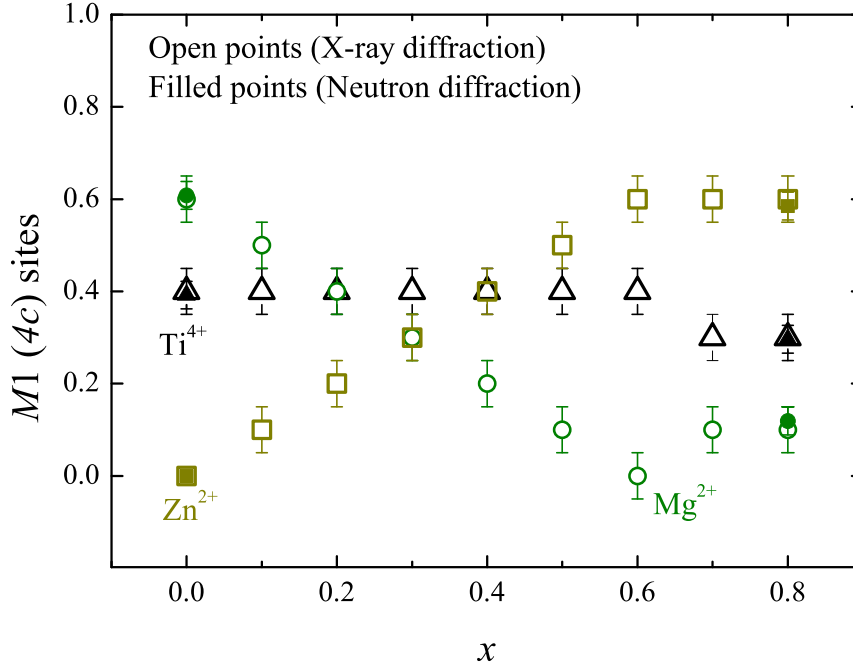


Figure 5.9: Site occupancy in M1 (4c) of the solid solution  $\text{Zn}_x\text{Mg}_{1-x}\text{Ti}_2\text{O}_5$  with  $0 \leq x \leq 0.8$ . The open symbols show XRD results while the filled symbols show neutron diffraction results.

Figure 5.10 presents the  $M$ -O bond lengths of the  $\text{Zn}_x\text{Mg}_{1-x}\text{Ti}_2\text{O}_5$  solid solution.  $M1\text{-O}3$ , the largest of  $M1\text{-O}$  bond lengths, increased significantly with the substitution of  $\text{Mg}^{2+}$  by  $\text{Zn}^{2+}$ . Meanwhile,  $M1\text{-O}2$ , the smallest of  $M1\text{-O}$  bond lengths, decreased moderately. Changes of the  $M1\text{-O}$  bond lengths show that incorporation of  $\text{Zn}^{2+}$  in  $\text{Zn}_x\text{Mg}_{1-x}\text{Ti}_2\text{O}_5$  led to an increased distortion of the M1 octahedra. Among the  $M2\text{-O}$  bond lengths, with increasing  $\text{Zn}^{2+}$  only  $M2\text{-O}2'$  and  $M2\text{-O}3$  shortened while the others expanded. The distortion of the M2 octahedra increased with increasing  $\text{Zn}^{2+}$ . Variation of the  $M\text{-O}$  bond lengths is summarised in table 5.5.

Table 5.5: Variation of the  $M\text{-O}$  bond lengths of  $\text{Zn}_x\text{Mg}_{1-x}\text{Ti}_2\text{O}_5$  with increasing amount of  $\text{Zn}^{2+}$  from 0 to 0.8.

	M1-O1	M1-O2	M1-O3	M2-O1	M2-O2	M2-O2'	M2-O3	M2-O3'
$\Delta$	-0.62%	-1.11%	7.98%	1.62%	5.73%	-3.80%	-1.58%	4.48%

Table 5.6 tabulates the  $M1\text{-M}2$  and  $M2\text{-M}2$  bond lengths of the  $\text{Zn}_x\text{Mg}_{1-x}\text{Ti}_2\text{O}_5$  solid solution. With the replacement of  $\text{Mg}^{2+}$  by  $\text{Zn}^{2+}$ , the  $M1\text{-M}2$  bond lengths increased. The  $M2\text{-M}2$  bond length, between two M2 octahedra which share the  $\text{O}2\text{-O}2$

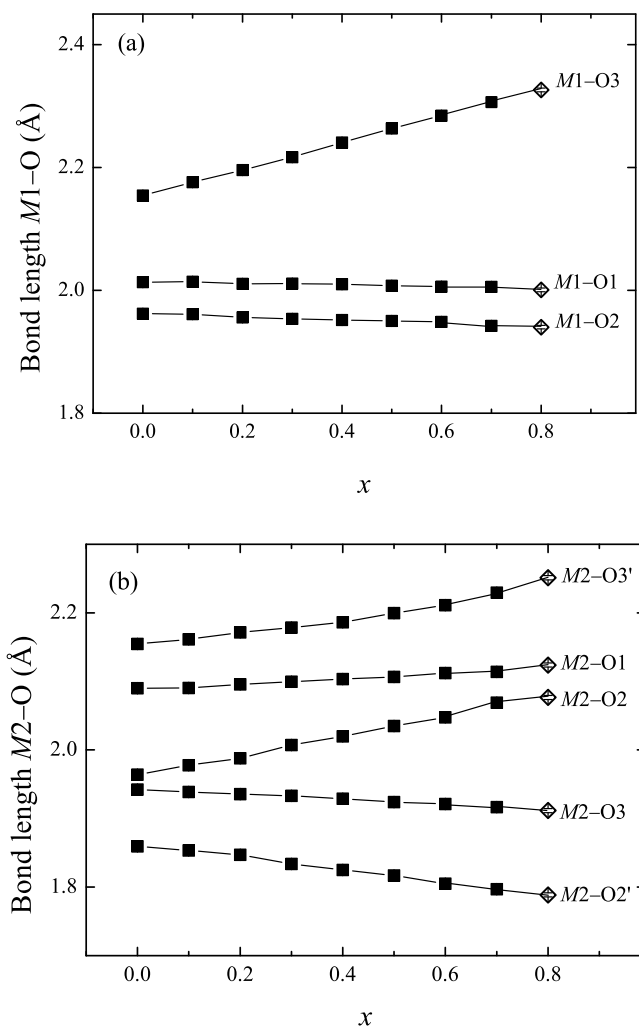


Figure 5.10: The M1–O and M2–O bond lengths of the  $Zn_xMg_{1-x}Ti_2O_5$  solid solution with  $0 \leq x \leq 0.8$ . Filled squares represent the samples quenched at 1473 K while open diamonds denote the sample quenched at 1573 K. The lines are guides for the eye.

edges, remained a constant value of 2.94(1) Å. The other M2–M2 bond lengths, between two M2 octahedra which share the O3–O3' edges, increased by 2.24%.

Table 5.6: Bond lengths of M–M (Å) in the  $Zn_xMg_{1-x}Ti_2O_5$  solid solution with  $0 \leq x \leq 0.8$  based on Rietveld refinements of XRD data.

$x$	0	0.1	0.2	0.3	0.4	0.5	0.6	0.7	0.8
M1–M2	3.181(3)	3.186(1)	3.190(1)	3.196(1)	3.200(1)	3.209(1)	3.213(1)	3.222(1)	3.224(1)
	3.132(3)	3.131(1)	3.138(1)	3.143(1)	3.148(1)	3.150(1)	3.155(1)	3.162(1)	3.158(1)
M2–M2	2.930(2)	2.935(2)	2.935(2)	2.939(2)	2.933(2)	2.939(2)	2.935(2)	2.930(2)	2.949(2)
	3.182(2)	3.181(2)	3.187(2)	3.192(1)	3.198(2)	3.204(1)	3.210(1)	3.225(2)	3.209(2)

Figure 5.11 shows the evolution of the  $M2-O1-M2$  and  $M2-O1-M1$  bond angles of  $Zn_xMg_{1-x}Ti_2O_5$  ( $0 \leq x \leq 0.8$ ). With the increase of  $Zn^{2+}$ ,  $M2-O1-M2$  drastically decreased ( $-3.37\%$  at maximum) while  $M2-O1-M1$  slightly increased ( $+0.82\%$  at maximum). It shows a decreasing kinking angle between the  $M2$  octahedra which share the corner atom O1.

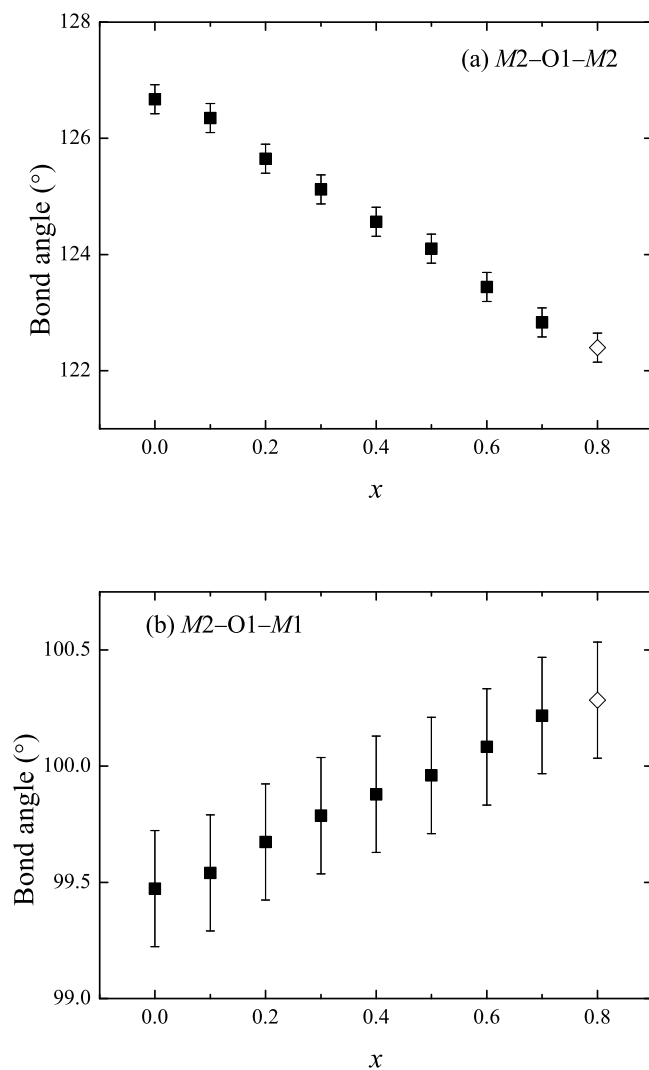


Figure 5.11: Bond angles of  $M2-O1-M2$  (a) and  $M2-O1-M1$  (b) in the solid solution  $Zn_xMg_{1-x}Ti_2O_5$  with  $0 \leq x \leq 0.8$ . Filled squares represent the samples synthesised at 1473 K while open diamonds denote the sample synthesised at 1573 K.

### 5.3.5 Raman spectra of $Zn_xMg_{1-x}Ti_2O_5$

Figure 5.12 shows Raman spectra of  $Zn_xMg_{1-x}Ti_2O_5$  with  $0 \leq x \leq 0.8$  which were normalised to the band with the smallest wavenumber. Raman bands of  $Zn_xMg_{1-x}Ti_2O_5$  are distributed in the range of  $100\text{--}1000\text{ cm}^{-1}$ , which is similar to the isostructural end-member  $MgTi_2O_5$  (figure 4.4). Line broadening of the Raman spectra was observed and the Raman bands overlapped. Based on the previous DFT calculations of fully ordered  $MgTi_2O_5$ , some of the Raman bands were identified unambiguously.

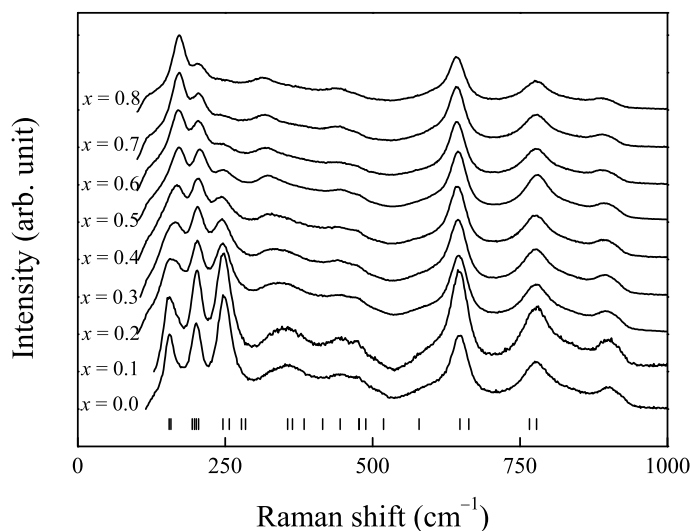


Figure 5.12: Raman spectra of the  $Zn_xMg_{1-x}Ti_2O_5$  solid solution which were normalised to the band with the smallest wavenumber. The bottom tickmarks show theoretical Raman frequencies of fully ordered  $MgTi_2O_5$ .

$Zn_xMg_{1-x}Ti_2O_5$  with  $x = 0.9$  and the endmember  $ZnTi_2O_5$  were also characterised by Raman spectroscopy. The results are shown in figure 5.13. The most intense Raman bands were indexed to the  $TiO_2$  (rutile) phase<sup>[186]</sup>. Due to the broadening of Raman bands, only one band at  $175(2)\text{ cm}^{-1}$  was recognized for  $Zn_xMg_{1-x}Ti_2O_5$  with  $x = 0.9$ , which was assigned to be the  $B_{1g}(1)$  Raman mode. No Raman mode was observed for  $ZnTi_2O_5$ .

Figure 5.14 shows the most obvious Raman shifts in the  $Zn_xMg_{1-x}Ti_2O_5$  solid solution. Substitution of  $Mg^{2+}$  by  $Zn^{2+}$  led to a significant blueshift of the  $B_{1g}(1)$  Raman mode, a strong redshift of the  $A_g(3)$  Raman mode, and slight redshifts of the  $B_{1g}(3)$  and  $B_{1g}(5)$  Raman modes. As known from figure 4.7, the  $B_{1g}(5)$  Raman mode of  $MgTi_2O_5$  corresponded to the displacement of the cornersharing atoms O1 parallel to  $[001]$ . With increasing  $Zn^{2+}$  in  $Zn_xMg_{1-x}Ti_2O_5$ , the  $M1\text{--}O1$  bond length shortened by  $-0.62\%$  and the  $M2\text{--}O1$  bond length elongated by  $1.62\%$ . Consequently, the energy for  $O1\text{--}M1\text{--}O1$  bending and  $M2\text{--}O1$  stretching along  $c$  direction increased and decreased, respectively. Raman frequency of the  $B_{1g}(5)$  Raman mode was influenced by both motions.

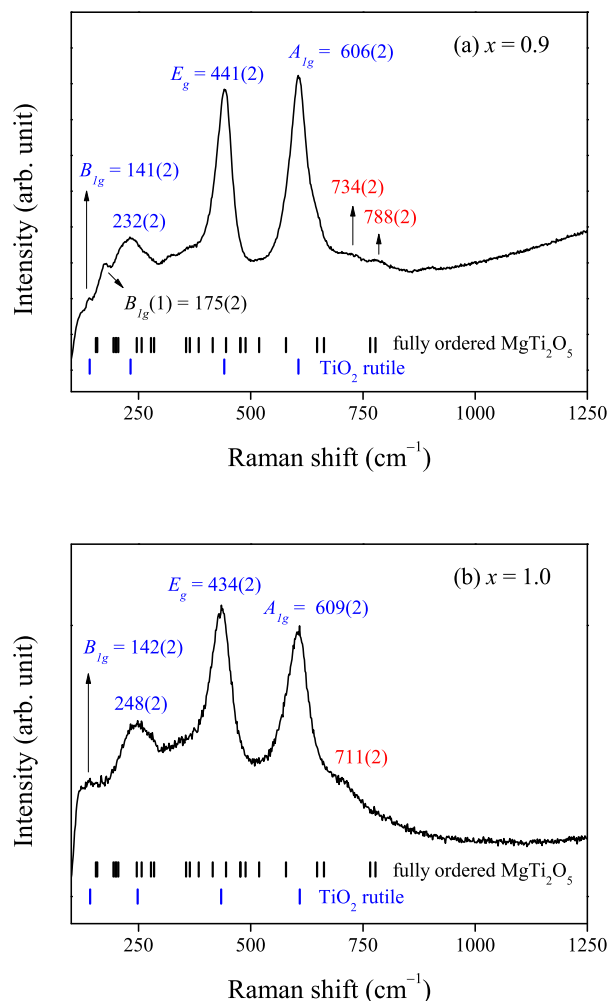


Figure 5.13: Raman spectra of  $\text{Zn}_x\text{Mg}_{1-x}\text{Ti}_2\text{O}_5$  with  $x=0.9$  and  $\text{ZnTi}_2\text{O}_5$ . Fraction of  $\text{Zn}_x\text{Mg}_{1-x}\text{Ti}_2\text{O}_5$  is  $\sim 30$  wt.% for  $x=0.9$  while 19 wt.% for  $\text{ZnTi}_2\text{O}_5$ . The blue tickmarks show the first and second order Raman scattering of the  $\text{TiO}_2$  rutile phase<sup>[186]</sup>. The black tickmarks indicate theoretical Raman frequencies of fully ordered  $\text{MgTi}_2\text{O}_5$ . Several weak Raman modes could not be indexed and are marked with red texts.

As a comparison, replacing  $\text{Mg}^{2+}$  by  $\text{Zn}^{2+}$  and exchanging  $\text{Mg}^{2+}$  (4c) with  $\text{Ti}^{4+}$  (8f) both led to a reduction of the bond length  $M1\text{-O}1$  and an increase of the bond length  $M2\text{-O}1$ . However, the  $B_{1g}(5)$  mode shifted towards a lower wavenumber due to the  $\text{Zn}^{2+}$  replacement while moved to a higher wavenumber due to the  $\text{Ti}^{4+}$  exchange. Reason for the contrary trend of Raman shift of  $B_{1g}(5)$  mode was probably that the  $M1\text{-O}1$  bending stiffness was smaller than the  $M2\text{-O}1$  stretching stiffness for the former case while larger than the stretching stiffness for the latter. In the solid solution  $\text{Zn}_x\text{Mg}_{1-x}\text{Ti}_2\text{O}_5$ , substitution of  $\text{Mg}^{2+}$  in the  $M1$  (4c) sites by  $\text{Zn}^{2+}$  caused weakening

of the M1–O1 bending motion along [001] direction.

The  $B_{1g}(3)$  Raman mode corresponded to displacements of the cornersharing O1 along [010] direction. The O1 motion comprised of a bending vibration of the M1–O1 bond and a stretching vibration of the M2–O1 bond. The intensity of this mode decreased gradually with the increase of  $Zn^{2+}$  and disappeared at  $x = 0.6$ . It was due to the increasing cation substitution in the M1 (4c) sites. Thus replacing of  $Mg^{2+}$  by  $Zn^{2+}$  in the  $Zn_xMg_{1-x}Ti_2O_5$  solid solution not only caused a redshift in frequency of the  $B_{1g}(3)$  Raman mode but also resulted in a disappearance of the intensity.

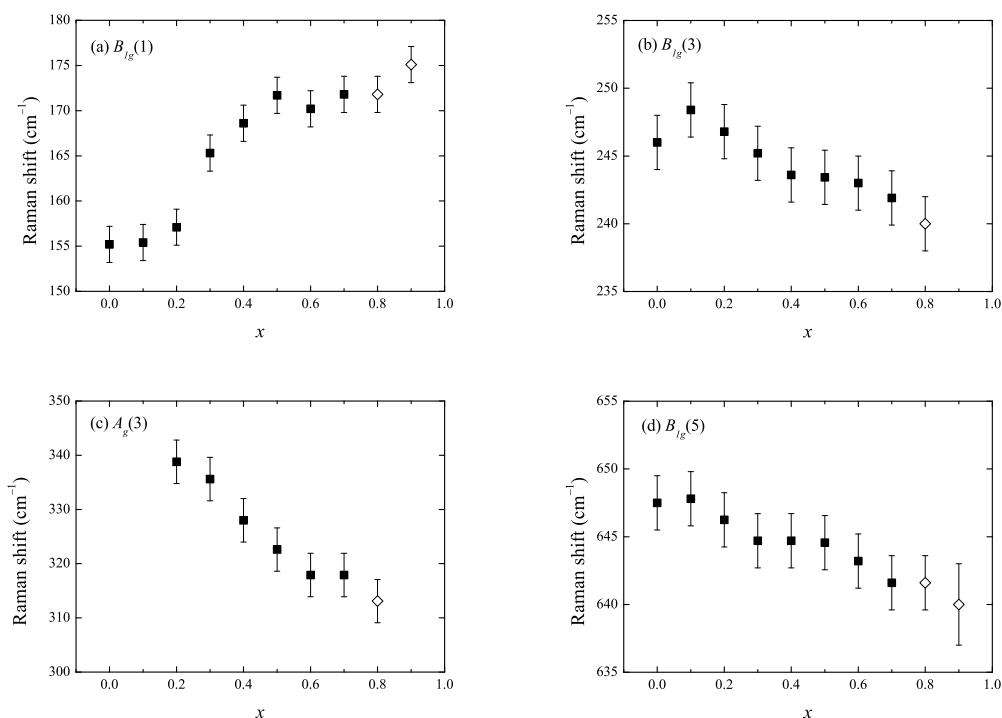


Figure 5.14: Raman shifts of the Raman modes for the  $Zn_xMg_{1-x}Ti_2O_5$  solid solution. (a)  $B_{1g}(1)$  Raman mode, (b)  $B_{1g}(3)$  Raman mode, (c)  $A_g(3)$  Raman mode and (d)  $B_{1g}(5)$  Raman mode.

The overtone at around  $900\text{ cm}^{-1}$ , which was experimentally observed in the disordered  $MgTi_2O_5$ , appeared in Raman spectra of the  $Zn_xMg_{1-x}Ti_2O_5$  solid solution. The Raman frequency of the overtone redshifted with the increase of zinc concentration, as shown in figure 5.15. As the overtone was interpreted to be a combination of  $B_{1g}(3)$  and  $B_{1g}(5)$  Raman modes, a sum of the two modes was calculated and compared with the experimental frequencies. The calculated values are slightly smaller than the observed values. The redshift of the overtone was ascribed to redshifts of  $B_{1g}(3)$  and  $B_{1g}(5)$  Raman modes (figure 5.14).

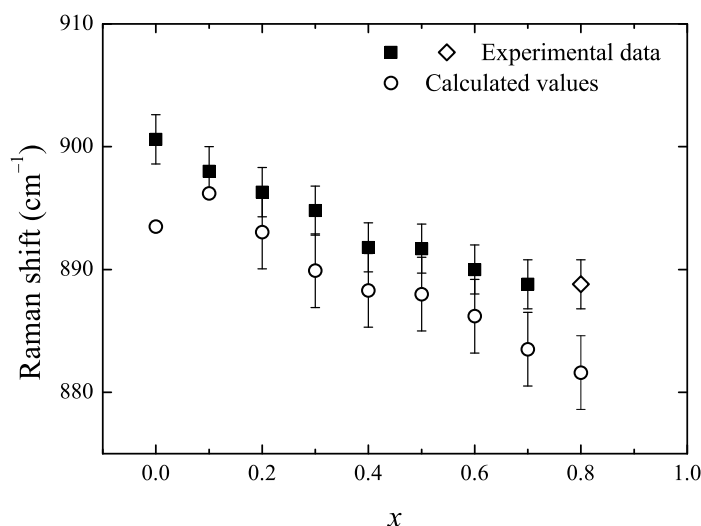


Figure 5.15: Raman shift of the overtone at around  $900\text{ cm}^{-1}$  for  $\text{Zn}_x\text{Mg}_{1-x}\text{Ti}_2\text{O}_5$ . Filled squares represent the samples synthesised at 1473 K while open diamonds denote the sample synthesised at 1573 K. Open circles indicate the sum of  $B_{1g}(3)$  and  $B_{1g}(5)$  Raman modes.

### 5.3.6 Le Bail refinement results for $\text{Cu}_x\text{Mg}_{1-x}\text{Ti}_2\text{O}_5$

The XRD data of  $\text{Cu}_x\text{Mg}_{1-x}\text{Ti}_2\text{O}_5$  with  $0 \leq x \leq 0.5$  were analysed by Le Bail refinements. The zero shift, background parameters, lattice parameters and profile parameters were refined. Table 5.7 lists the Le Bail refinement results for  $\text{Cu}_x\text{Mg}_{1-x}\text{Ti}_2\text{O}_5$ . Figure 5.16 gives a typical Le Bail refinement result for  $x = 0.5$ .

Figure 5.17 presents the variation of lattice parameters and unit cell volume  $V$  with molar fraction of copper in  $\text{Cu}_x\text{Mg}_{1-x}\text{Ti}_2\text{O}_5$ . The change of  $a$  was very small while  $b$  increased slightly. With the increase of  $\text{Cu}^{2+}$ ,  $c$  remained unchanged at a low copper concentration and slightly decreased at  $x \geq 0.5$ . As a result,  $V$  held a constant value of  $364.99(6)\text{ \AA}^3$ .

As a comparison, the complete replacement of  $\text{Mg}^{2+}$  by  $\text{Zn}^{2+}$  led to a volume increase of 0.9%, as shown in figure 5.8. Though Shannon ionic radii of the octahedrally coordinated  $\text{Mg}^{2+}$  ( $r = 0.72\text{ \AA}$ ),  $\text{Cu}^{2+}$  ( $r = 0.73\text{ \AA}$ ) and  $\text{Zn}^{2+}$  ( $r = 0.74\text{ \AA}$ ) are close, unit cell dimensions of the  $\text{Zn}_x\text{Mg}_{1-x}\text{Ti}_2\text{O}_5$  and  $\text{Cu}_x\text{Mg}_{1-x}\text{Ti}_2\text{O}_5$  solid solutions are different from each other. The possible reason is that the cations have different crystal field splitting energies and electronegativity.

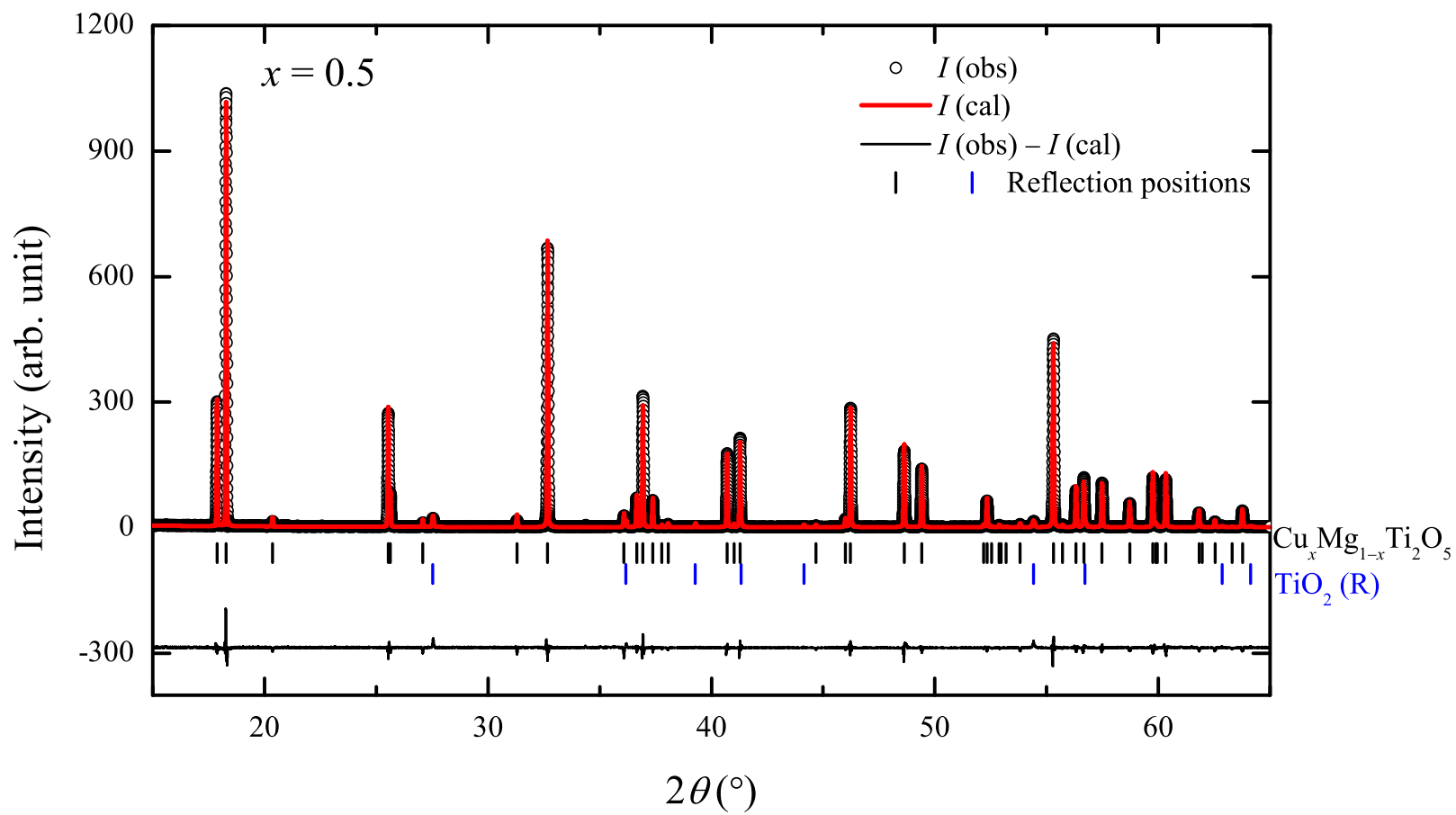


Figure 5.16: Le Bail refinement result of XRD for  $\text{Cu}_x\text{Mg}_{1-x}\text{Ti}_2\text{O}_5$  with  $x = 0.5$ . The bottom black curve represents the difference between the observed data (black circles) and the calculated (continuous red curve) data. The tickmarks indicate reflections from the crystalline phases.



Table 5.7: Le Bail refinement results of XRD for  $\text{Cu}_x\text{Mg}_{1-x}\text{Ti}_2\text{O}_5$  with  $0 < x \leq 0.5$ . The solid solution was refined using an orthorhombic pseudobrookite-type structure with space group  $Cmcm$ .

	$x=0.1$	$x=0.2$	$x=0.3$	$x=0.4$	$x=0.5$
Unit cell					
$a$ [Å]	3.74537(1)	3.74504(4)	3.74910(1)	3.74985(1)	3.75022(1)
$b$ [Å]	9.7496(2)	9.7527(2)	9.7525(2)	9.7519(2)	9.7560(2)
$c$ [Å]	9.9941(2)	9.9926(2)	9.9835(2)	9.9827(2)	9.9774(2)
$V$ [Å <sup>3</sup> ]	364.944(1)	364.973(1)	365.031(1)	365.048(1)	365.047(1)
Profile parameters					
GU	66.2(2)	259(3)	22.6(2)	18.1(2)	3.7(2)
GV	-20.9(9)	-109(2)	-8.6(1)	-7.9(1)	-0.6(1)
GW	6.6(2)	13.8(2)	1.33(1)	1.07(2)	1.13(2)
LX	3.07(4)	4.29(6)	0.45(1)	0.50(1)	0.37(2)
LY	0.76(7)	2.08(1)	0.84(2)	1.28(3)	1.86(2)
Rietveld agreement factors					
$R_{\text{wp}}$ [%]	43.2	42.3	29.6	37.0	37.4
$R_{\text{wpb}}$ [%]	47.6	48.0	31.5	37.2	50.0
$\chi^2$	1.1	1.1	1.1	1.1	1.0

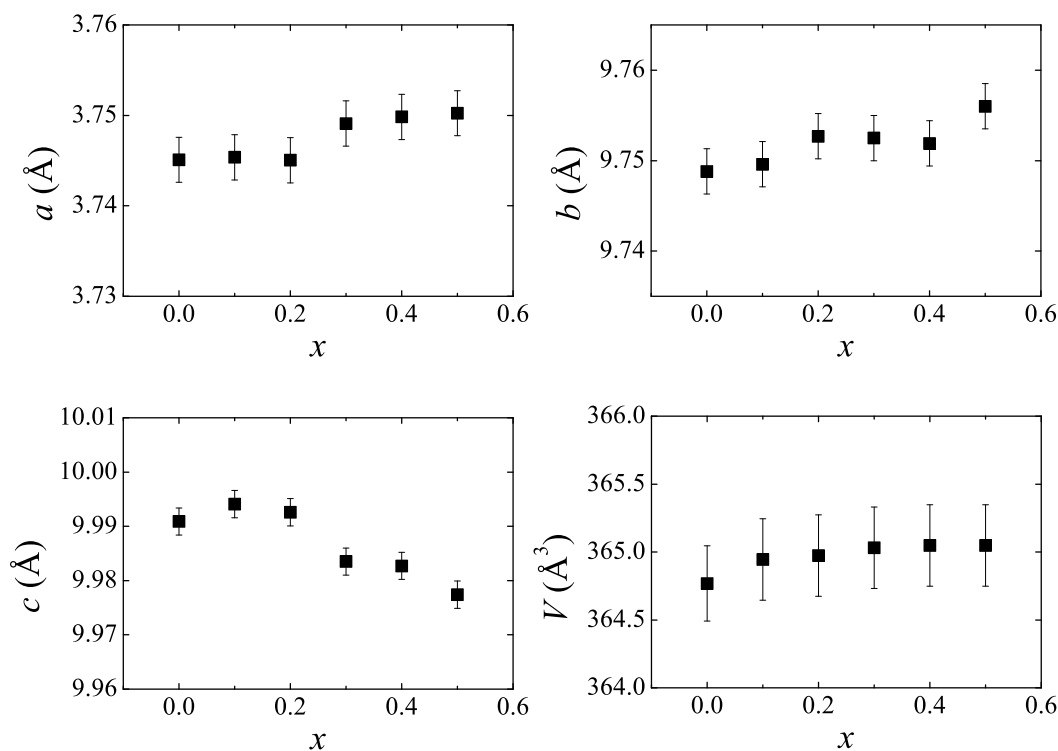


Figure 5.17: Lattice parameters of the samples  $\text{Cu}_x\text{Mg}_{1-x}\text{Ti}_2\text{O}_5$  which have an orthorhombic pseudobrookite-type structure with space group  $Cmcm$ .

### 5.3.7 Raman spectra of $Cu_xMg_{1-x}Ti_2O_5$

Raman spectra of the  $Cu_xMg_{1-x}Ti_2O_5$  solid solution with  $0 \leq x \leq 0.5$  were normalised to the intensity of the first band, as plotted in figure 5.18. Only a few Raman modes were identified unambiguously due to serious broadening of the Raman modes. Assignments of the Raman modes for  $Cu_xMg_{1-x}Ti_2O_5$  are based on the theoretical Raman frequencies and intensities of fully ordered  $MgTi_2O_5$  (see figure 4.5 and table 4.2).

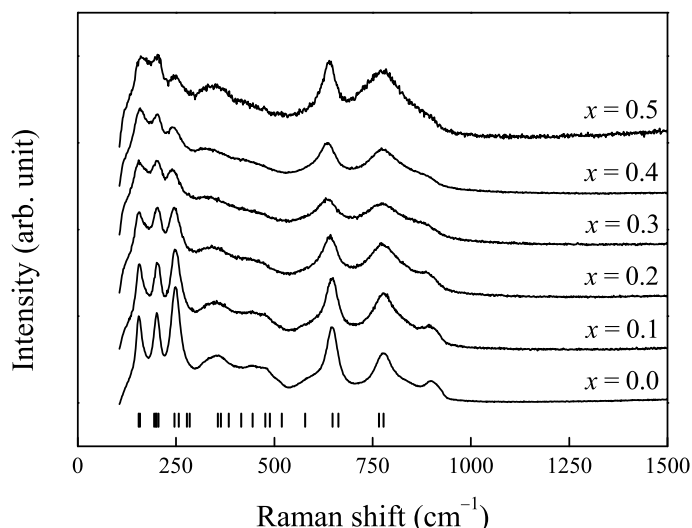


Figure 5.18: Raman spectra of  $Cu_xMg_{1-x}Ti_2O_5$  normalised to the intensity of the first band.

Frequencies of the Raman modes for  $Cu_xMg_{1-x}Ti_2O_5$  are tabulated in table 5.8. Almost no shift was observed for the  $B_{1g}(2)$  mode with a frequency of  $202(3) \text{ cm}^{-1}$  while the overtone at around  $900 \text{ cm}^{-1}$  was too broad to be identified for  $x \geq 0.3$ .

Table 5.8: Assignment of Raman modes  $\Gamma$  for the pseudobrookite-type  $Cu_xMg_{1-x}Ti_2O_5$  solid solution with  $0 \leq x \leq 0.5$  based on the theoretical Raman frequencies and intensities of fully ordered  $MgTi_2O_5$  (figure 4.5 and table 4.2).

$\Gamma$	$x=0.0$	$x=0.1$	$x=0.2$	$x=0.3$	$x=0.4$	$x=0.5$
$B_{1g}(1)$	155(2)	157(2)	157(2)	155(2)	158(2)	160(2)
$B_{1g}(2)$	201(2)	201(2)	201(2)	201(2)	203(2)	203(2)
$B_{1g}(3)$	248(3)	247(3)	245(3)	242(3)	243(3)	245(3)
$B_{1g}(5)$	648(2)	646(2)	643(2)	635(2)	637(2)	640(2)
$A_g(8)$	777(2)	778(2)	772(2)	777(2)	772(2)	777(2)
Overtone	901(3)	898(3)	892(3)			

Figure 5.19 shows Raman shifts of the  $B_{1g}(1)$ ,  $B_{1g}(3)$ ,  $B_{1g}(5)$  and  $A_g(8)$  Raman modes with the molar fraction of  $Cu^{2+}$  in  $Cu_xMg_{1-x}Ti_2O_5$ . The  $B_{1g}(1)$  Raman mode had a

stable frequency of  $155(2) \text{ cm}^{-1}$  for  $x$  below 0.3 and shifted slightly towards higher frequencies at a higher content of copper. In addition, the frequency of the  $B_{1g}(3)$  Raman mode decreased from  $248(2) \text{ cm}^{-1}$  to  $242(2) \text{ cm}^{-1}$  with the increase of  $x$  from 0.0 to 0.3, and then increased slightly to  $245(2) \text{ cm}^{-1}$  for  $x = 0.5$ . A similar trend was observed for the frequency of the  $B_{1g}(5)$  Raman mode, which decreased from  $x = 0$  to 0.3 and then increased at  $0.3 \leq x \leq 0.5$ . For  $x$  below 0.3, the redshifts of the  $B_{1g}(3)$  and  $B_{1g}(5)$  Raman modes are consistent with the redshift of the overtone at around  $900 \text{ cm}^{-1}$ .  $A_g(8)$  Raman mode fluctuated in the employed range of solid solution and was positioned at around  $775(3) \text{ cm}^{-1}$ .

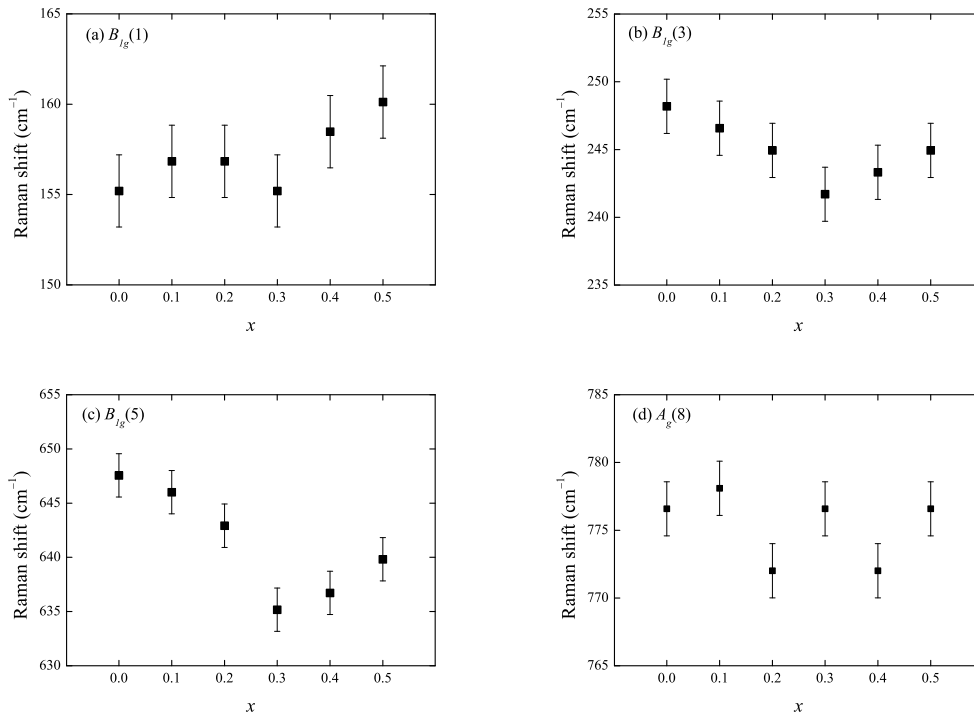


Figure 5.19: Raman shifts of the  $B_{1g}(1)$ ,  $B_{1g}(3)$ ,  $B_{1g}(5)$  and  $A_g(8)$  Raman modes for the solid solution  $\text{Cu}_x\text{Mg}_{1-x}\text{Ti}_2\text{O}_5$ .

In order to evaluate the cation distribution, Raman spectra of the  $\text{Cu}_x\text{Mg}_{1-x}\text{Ti}_2\text{O}_5$  solid solution were compared with those of  $\text{Zn}_x\text{Mg}_{1-x}\text{Ti}_2\text{O}_5$ . The frequency of the  $B_{1g}(3)$  Raman mode lowered by  $7(2) \text{ cm}^{-1}$  due to the incorporation of 30%  $\text{Cu}^{2+}$ , which was close to the decrease of  $6(2) \text{ cm}^{-1}$  due to the incorporation of 80%  $\text{Zn}^{2+}$ . However, replacement of 30%  $\text{Mg}^{2+}$  by  $\text{Cu}^{2+}$  led to a reduction of  $13(2) \text{ cm}^{-1}$  in frequency of the  $B_{1g}(5)$  Raman mode, which was nearly double of the frequency reduction of  $6(2) \text{ cm}^{-1}$  caused by the substitution of 90%  $\text{Mg}^{2+}$  by  $\text{Zn}^{2+}$ . The blueshifts of the  $B_{1g}(3)$  and  $B_{1g}(5)$  Raman modes for  $_x\text{Mg}_{1-x}\text{Ti}_2\text{O}_5$  at  $x \geq 0.3$  indicate a movement of  $\text{Ti}^{4+}$  from the M2 to M1 octahedral sites.

In both solid solutions, the relative intensity of  $B_{1g}(3)$  mode to  $B_{1g}(5)$  mode decreased with increasing replacements of  $\text{Mg}^{2+}$  by  $\text{Cu}^{2+}/\text{Zn}^{2+}$ . However, the relative

intensity of  $B_{1g}(2)$  to  $B_{1g}(1)$  decreased in  $Zn_xMg_{1-x}Ti_2O_5$  while kept at around 1 in  $Cu_xMg_{1-x}Ti_2O_5$ . Changes in the Raman frequencies and intensities of the solid solutions are ascribed to different site occupancies of the cations.

## 5.4 Conclusion

The complete solid solution  $Zn_xMg_{1-x}Ti_2O_5$  was synthesised by mechanochemical activation assisted solid state synthesis and by employing the self-propagating high-temperature synthesis set-up. It crystallised in the orthorhombic pseudobrookite-type structure with space group  $Cmcm$ . Vegard's Law was obeyed in the complete solid solution. With increasing substitution of  $Mg^{2+}$  by  $Zn^{2+}$ , the lattice parameter  $a$  decreased while  $b$  and  $c$  increased, which resulted in around 1% increase of the unit cell volume.

Structural parameters of  $Zn_xMg_{1-x}Ti_2O_5$  with  $0 \leq x \leq 0.8$  were refined by using X-ray and neutron diffraction data.  $Zn^{2+}$  preferred to replace  $Mg^{2+}$  in the  $M1$  sites up to an atomic fraction of 60%. At  $x \geq 0.6$ , 60%  $Zn^{2+}$  occupied the  $M1$  sites and the extra part of  $Zn^{2+}$  incorporated into the  $M2$  sites. Meanwhile, almost an equivalent amount of  $Ti^{4+}$  moved from the  $M1$  to  $M2$  sites to exchange with  $Mg^{2+}$  in the  $M2$  sites. Variation of the  $M-O$  bond lengths and  $M-O-M$  bond angles indicated a decreasing kinking angle between the cornersharing  $M2$  octahedra with the increase of zinc concentration.

Raman modes of  $Zn_xMg_{1-x}Ti_2O_5$  were assigned based on Raman frequencies and intensities of fully ordered  $MgTi_2O_5$ . Due to the replacement of  $Mg^{2+}$  by  $Zn^{2+}$  in the  $M1$  sites,  $B_{1g}(1)$  Raman mode blueshifted while  $A_g(3)$ ,  $B_{1g}(3)$  and  $B_{1g}(5)$  Raman modes redshifted. Moreover, the intensity ratio of  $B_{1g}(2)$  to  $B_{1g}(1)$  mode and that of  $B_{1g}(3)$  to  $B_{1g}(5)$  mode both decreased, which was caused by the increasing cation disorder in the  $M1$  sites.

By a combination of mechanochemical activation and solid state synthesis, the  $Cu_xMg_{1-x}Ti_2O_5$  solid solution with  $0 \leq x \leq 0.5$  was synthesised at a temperature of 1273 K. The replacement of  $Mg^{2+}$  by  $Cu^{2+}$  led to no change of the orthorhombic symmetry of  $MgTi_2O_5$ . Though lattice parameters varied slightly, the unit cell volume of  $Cu_xMg_{1-x}Ti_2O_5$  remained  $364.99(6) \text{ \AA}^3$ . Due to substituting  $Mg^{2+}$  by  $Cu^{2+}$ , frequencies of both  $B_{1g}(3)$  and  $B_{1g}(5)$  Raman modes slightly redshifted for copper below 30% and blueshifted at a higher content of copper. Meanwhile, the relative intensity of the  $B_{1g}(3)$  mode to the  $B_{1g}(5)$  mode decreased while the  $B_{1g}(2)$  Raman mode had the same intensity as the  $B_{1g}(1)$  Raman mode. It was deduced that incorporation of more than 30%  $Cu^{2+}$  led to the movement of  $Ti^{4+}$  from the  $M2$  ( $8f$ ) to  $M1$  ( $4c$ ) sites.

## 6 $\text{Ti}_5\text{Si}_3\text{Z}_x$ with $Z = \text{B}$ or $\text{O}$

### 6.1 Introduction

Self-propagating high-temperature synthesis (SHS) has been shown to be an effective technique to synthesise endmember  $\text{Zn}_2\text{TiO}_5$  in the  $\text{Zn}_x\text{Mg}_{1-x}\text{Ti}_2\text{O}_5$  solid solution, and thus was employed to investigate interstitial solid solutions based on  $\text{Ti}_5\text{Si}_3$ .

The intermetallic compound  $\text{Ti}_5\text{Si}_3$  with  $\text{Mn}_5\text{Si}_3$ -type structure, as described in hexagonal symmetry with space group  $P6_3/mcm$  (no. 193), has a high melting point of 2403 K and a high enthalpy of formation of  $-579$  kJ/mol from the elements<sup>[187]</sup>.  $\text{Ti}_5\text{Si}_3$  has been synthesised by various methods including chemical/physical vapour deposition, rapid thermal processing, casting or powder metallurgical processes and self-propagating high-temperature synthesis<sup>[188,189]</sup>. Figure 6.1 shows the crystal structure of  $\text{Ti}_5\text{Si}_3$ <sup>[190]</sup>. Ti1 (4d) atoms are in distorted octahedral coordination by Si and form a linear chain parallel to [001]<sup>[190,191]</sup>. Ti2 (6g) atoms constitute the shared triangular faces of a trigonal antiprismatic chain extending along the [001] direction<sup>[190,191]</sup>. Each Ti2 atom is linked to Si atoms, which builds connections between the octahedra and trigonal antiprisms and globally results in a hexagonal structure<sup>[190,191]</sup>.

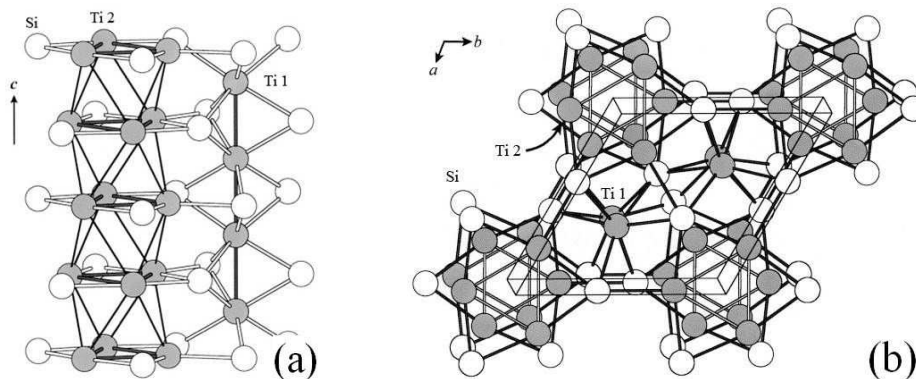


Figure 6.1: Crystal structure<sup>[190]</sup> of  $\text{Ti}_5\text{Si}_3$  with hexagonal symmetry and space group  $P6_3/mcm$ : (a) view parallel [110] and (b) view parallel close to [001].

Solid solutions of  $\text{Ti}_5\text{Si}_3\text{Z}_x$  ( $Z = \text{B}, \text{C}, \text{N}, \text{O}$  and  $x \leq 1.0$ ) retained the same structure as endmember  $\text{Ti}_5\text{Si}_3$  and the interstitial atoms  $Z$  occupied the centre of the trigonal antiprisms<sup>[191,192]</sup>. Lattice parameters of  $\text{Ti}_5\text{Si}_3$  varied with the type and content of interstitial atoms<sup>[191-193]</sup>. Here, self-propagating high-temperature synthesis was employed to synthesise the interstitial solid solutions  $\text{Ti}_5\text{Si}_3\text{Z}_x$  by using  $\alpha$ -Ti, Si and  $\text{NaBH}_4$  as starting materials.  $\text{NaBH}_4$  has a low melting temperature and decomposes in the reaction. It serves as a boron source.

## 6.2 Experimental details

### 6.2.1 Sample preparation

Firstly, self-propagating high-temperature synthesis of  $Ti_5Si_3$  was revisited. A mixture with a molar ratio of  $Ti:Si = 5:3$  was prepared by fully grinding titanium (purity 99%,  $\sim 40 \mu m$ , sigma-Aldrich) and silicon (purity  $> 99\%$ ,  $\sim 40 \mu m$ , sigma-Aldrich) powders using a mortar. Then the mixture was pressed into cylinders with a green density of 60% (diameter 6 mm, height 15 mm), under an axial force of 80 bar for 20 s. After that, the cylinders were ignited by a tungsten coil in the solid flame set-up under argon flow and then cooled down to ambient temperature in argon atmosphere. Finally, the products were crushed and ground into powders.

Additionally,  $Ti_5Si_3$  product a fraction of 5–40 wt.% was added to the stoichiometric starting materials as a retardant. Then self-propagating high-temperature synthesis was carried out on the mixture in the same conditions as demonstrated previously. Consequently, a series of diluted samples were prepared and ground into powders.

At last, 1–4 wt.%  $NaBH_4$  ( $\sim 40 \mu m$ , sigma-Aldrich) was added to the stoichiometric starting materials. The mixture was pressed into cylinders with green densities of 85–95% under axial forces of 30–120 bar for 20 s. Solid flame reactions were conducted on the cylinders and the obtained samples were ground into powders.

### 6.2.2 X-ray diffraction

Around 10 wt.% silicon powder was added to each sample as internal standard. X-ray diffraction data were collected on a PANalytical X'Pert Pro X-ray diffractometer equipped with a  $CuK_{\alpha 1}$  radiation source (Ge 110 monochromator,  $\lambda = 1.5406 \text{ \AA}$ , 45 kV, 35 mA). The measurements were carried out in Bragg-Brentano geometry and spinning mode (2 revolutions per second) over a  $2\theta$  range of  $10\text{--}110^\circ$  with a step size of  $0.0016^\circ$ . One measurement took around 14 hours.

Rietveld refinement of the XRD data was employed to determine lattice parameters, positional and isotropic thermal displacement parameters of atoms and the fraction of the crystalline phases using the GSAS<sup>[122]</sup> and EXPGUI<sup>[123]</sup> packages. The initial structure models were taken from the literature<sup>[194,195]</sup>. The background was refined by a Chebyshev polynomial with 8 terms while the profile parameters were refined using a pseudo-Voigt function.

## 6.3 Results and discussion

Revisiting of self-propagating high-temperature synthesis of  $Ti_5Si_3$  yielded a pure  $Ti_5Si_3$  phase (space group  $P6_3/mcm$ ), which was in accordance with the literature<sup>[189,196–198]</sup>. As observed by Yeh and Hsu<sup>[197]</sup>, a mechanochemical activation procedure of the starting materials ( $Ti:Si = 5:3$  in molar ratio) for 10 h led to the formation of a second phase  $Ti_5Si_4$  in the self-propagating high-temperature synthesis of  $Ti_5Si_3$ . Hence, mechanochemical activation was not employed in the experiments.

Table 6.1 tabulates the phase composition of the samples with 0–40 wt.% dilution and the Rietveld refinement results using the XRD data. Crystalline phase of the products remained  $\text{Ti}_5\text{Si}_3$  when the dilution was less than 10 wt.%. With further increase of the dilution, impurities emerged. The main one was  $\text{Ti}_5\text{Si}_4$ , along with  $\text{TiSi}_2$ ,  $\text{TiSi}$  and some unknown reflections that were hard to index because of the weak reflection intensity.

Table 6.1: Phase composition of the samples with 0–40 wt.% dilution obtained by self-propagating high-temperature synthesis and Rietveld refinement results using the XRD data.

Dilution [wt.%]	Si [wt.%]	Products	Reduced $\chi^2$	$R_{\text{wp}}$
0	15.4(2)	$\text{Ti}_5\text{Si}_3$	1.12	20.87%
5	13.5(3)	$\text{Ti}_5\text{Si}_3$	1.12	21.40%
10	17.7(3)	$\text{Ti}_5\text{Si}_3$	1.30	23.31%
15	17.9(3)	$\text{Ti}_5\text{Si}_3$ , $\text{Ti}_5\text{Si}_4$	1.67	23.99%
20	21.8(2)	$\text{Ti}_5\text{Si}_3$ , $\text{Ti}_5\text{Si}_4$ , $\text{TiSi}_2$	1.43	22.48%
25	21.9(2)	$\text{Ti}_5\text{Si}_3$ , $\text{Ti}_5\text{Si}_4$ , $\text{TiSi}_2$	1.35	21.65%
30	17.0(7)	$\text{Ti}_5\text{Si}_3$ , $\text{Ti}_5\text{Si}_4$ , $\text{TiSi}$	1.30	23.03%
35	17.4(5)	$\text{Ti}_5\text{Si}_3$ , $\text{Ti}_5\text{Si}_4$ , $\text{TiSi}$	1.35	23.68%
40	17.2(2)	$\text{Ti}_5\text{Si}_3$ , $\text{Ti}_5\text{Si}_4$ , $\text{TiSi}$	1.37	19.42%

In the X-ray diffraction patterns obvious splitting of the reflections was observed for  $\text{Ti}_5\text{Si}_3$  in the whole  $2\theta$  range, indicating two  $\text{Ti}_5\text{Si}_3$  phases with different unit cells. Though refining the data with one  $\text{Ti}_5\text{Si}_3$  phase or two  $\text{Ti}_5\text{Si}_3$  phases both achieved convergence, results with two phases were better than with one phase, as shown in figure 6.2. Hence all samples were refined using two  $\text{Ti}_5\text{Si}_3$  phases. Figure 6.3 presents the Rietveld refinement results for the samples with no dilution and 20 wt.% dilution.

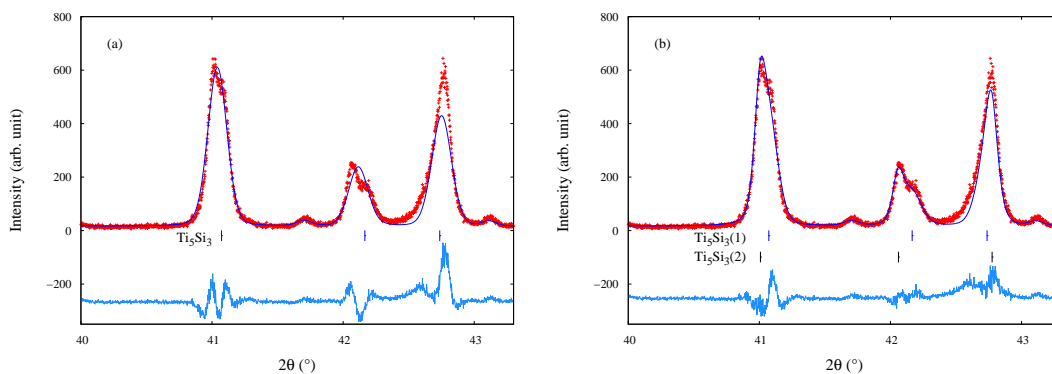


Figure 6.2: Rietveld refinement results in the selected  $2\theta$  range for the sample with a dilution of 30 wt.% using one  $\text{Ti}_5\text{Si}_3$  unit cell (a) and using two  $\text{Ti}_5\text{Si}_3$  unit cells (b).

Figure 6.4 shows the evolution of lattice parameters of  $\text{Ti}_5\text{Si}_3$  with the increase of dilution by refining using two unit cells.  $a$  and  $c$  values of the  $\text{Ti}_5\text{Si}_3(1)$  phase were stable

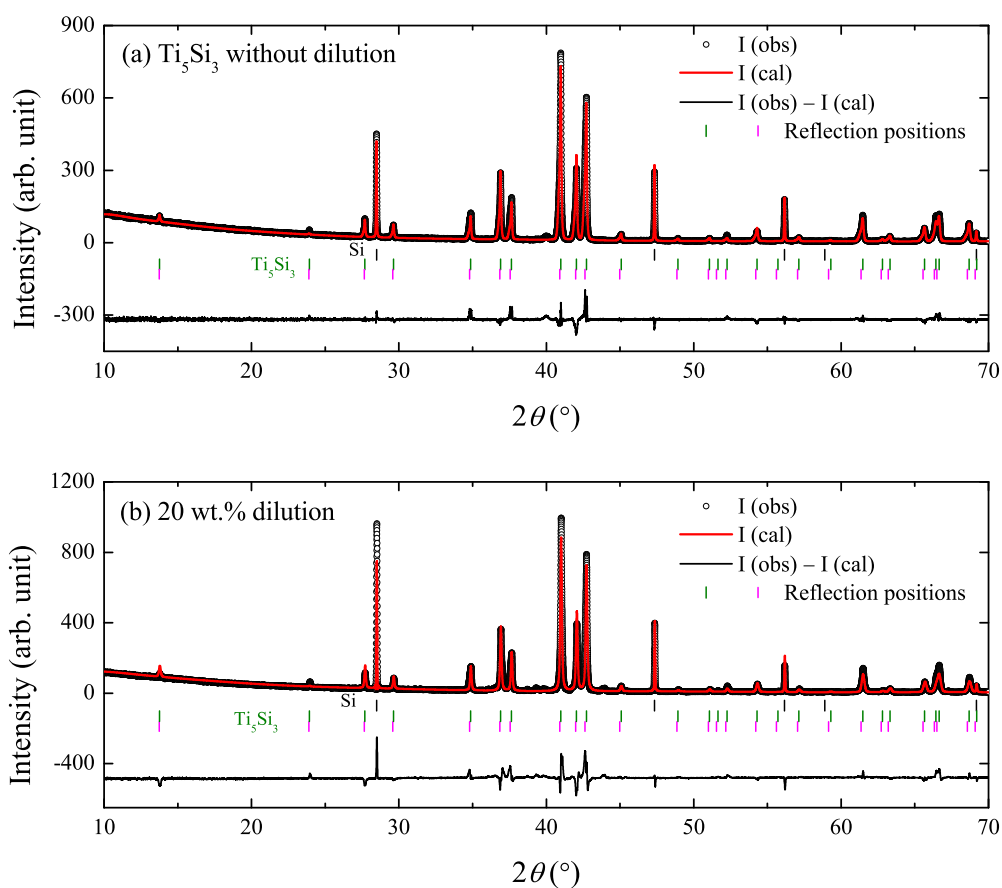


Figure 6.3: Rietveld refinement results in  $2\theta = 10\text{--}70^\circ$  of the samples with different dilutions by using two  $Ti_5Si_3$  phases. (a) the sample without dilution and (b) the sample with a dilution of 20 wt.%.

for all dilutions, while for the  $Ti_5Si_3(2)$  phase  $a$  decreased at high dilutions ( $\geq 20$  wt.%) and  $c$  kept constant.

For the  $Ti_5Si_3(1)$  phase,  $a = 7.446(1)$  Å was smaller than  $a = 7.459(1)$  Å of the pure  $Ti_5Si_3$  while  $c = 5.143(2)$  Å was also smaller than  $c = 5.152(1)$  Å of the pure  $Ti_5Si_3$  [191]. It probably contained an interstitial atom oxygen, which was introduced due to porosity of the cylinders and came from the starting materials. As estimated from lattice parameters of  $Ti_5Si_3O_x$  in the literature [191,192], the  $Ti_5Si_3(1)$  phase had a formula of  $Ti_5Si_3O_x$  with  $x$  around 0.3. The  $Ti_5Si_3(2)$  phase disappeared at a high dilution of 40 wt.%. Considering the formation of impurities at high dilutions, the  $Ti_5Si_3(2)$  phase indicated  $Ti_5Si_3$  with an increasing silicon deficiency.

Table 6.2 tabulates the synthesis condition, phase composition and Le Bail refinement results of the samples containing 1–4 wt.%  $NaBH_4$  obtained by self-propagating high-temperature synthesis. An impurity of  $Ti_5Si_4$  phase emerged when fraction of  $NaBH_4$  was above 2 wt.%.

In the XRD data splitting of the reflections from  $Ti_5Si_3$  was much more obvious



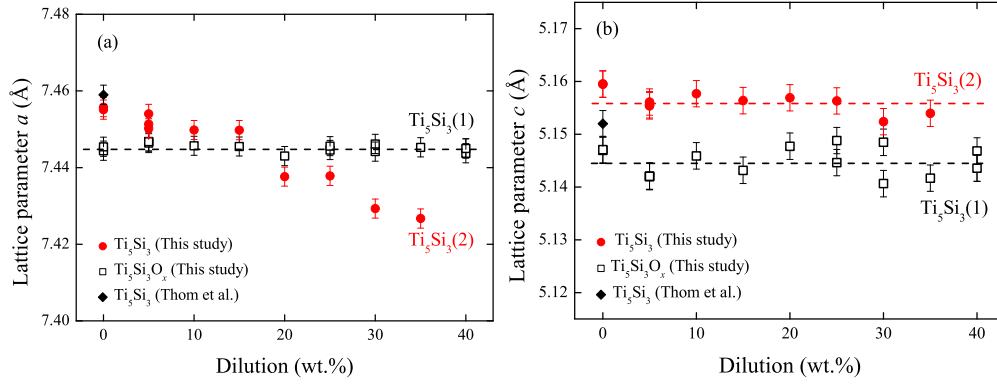


Figure 6.4: Evolution of lattice parameters of  $\text{Ti}_5\text{Si}_3$  with increasing dilution by refining using two unit cells. The results were compared with pure  $\text{Ti}_5\text{Si}_3$  phase in the literature<sup>[191]</sup>.

Table 6.2: Synthesis conditions, phase composition and Le Bail refinement results of the samples containing 1–4 wt.%  $\text{NaBH}_4$  by using self-propagating high-temperature synthesis.

$\text{NaBH}_4$ [wt.%]	Density	Press	Products	Reduced $\chi^2$	$R_{\text{wp}}$
1	85%	30 bar	$\text{Ti}_5\text{Si}_3$	1.20	22.69%
2	85%	30 bar	$\text{Ti}_5\text{Si}_3$	1.17	22.66%
3	95%	30 bar	$\text{Ti}_5\text{Si}_3, \text{Ti}_5\text{Si}_4$	0.97	20.40%
3	95%	60 bar	$\text{Ti}_5\text{Si}_3, \text{Ti}_5\text{Si}_4$	1.14	22.03%
3	95%	120 bar	$\text{Ti}_5\text{Si}_3, \text{Ti}_5\text{Si}_4$	0.96	20.76%
3	90%	60 bar	$\text{Ti}_5\text{Si}_3, \text{Ti}_5\text{Si}_4$	0.95	20.28%
3	90%	80 bar	$\text{Ti}_5\text{Si}_3, \text{Ti}_5\text{Si}_4$	1.24	22.11%
3	90%	90 bar	$\text{Ti}_5\text{Si}_3, \text{Ti}_5\text{Si}_4$	1.36	24.59%
3	80%	60 bar	$\text{Ti}_5\text{Si}_3, \text{Ti}_5\text{Si}_4$	1.05	20.31%
4	85%	30 bar	$\text{Ti}_5\text{Si}_3, \text{Ti}_5\text{Si}_4$	1.21	23.29%
4	85%	120 bar	$\text{Ti}_5\text{Si}_3, \text{Ti}_5\text{Si}_4$	0.94	20.10%

than the samples with 0–40 wt.% dilution. However, only Le Bail and no Rietveld refinement was performed on the X-ray diffraction data of the samples containing  $\text{NaBH}_4$  because the interstitial atoms could not be detected by powder X-ray diffraction. Figure 6.5 shows Le Bail refinement result of the sample containing 3 wt.%  $\text{NaBH}_4$  in the range of  $2\theta = 40\text{--}43^\circ$ , which clearly indicated two  $\text{Ti}_5\text{Si}_3$  phases in the sample. Some interstitial atoms were incorporated into  $\text{Ti}_5\text{Si}_3$  forming  $\text{Ti}_5\text{Si}_3\text{Z}_x$ .

Figure 6.6 shows the evolution of lattice parameters of  $\text{Ti}_5\text{Si}_3\text{Z}_x$  in the samples containing 1–4 wt.%  $\text{NaBH}_4$  based on Le Bail refinement results. The phase  $\text{Ti}_5\text{Si}_3(1)$  had a contracted unit cell and the interstitial atoms might be oxygen/sodium. In the other phase, both  $a$  and  $c$  expanded as compared to pure  $\text{Ti}_5\text{Si}_3$  phase, increasing from  $a = 7.459(1) \text{ \AA}$ ,  $c = 5.152(1) \text{ \AA}$ <sup>[191]</sup> to  $a = 7.468 \text{ \AA}$ ,  $c = 5.172 \text{ \AA}$ . The lattice parameters were very close to those of  $\text{Ti}_5\text{Si}_3\text{B}_x$  with  $x = 0.5$ :  $a = 7.478 \text{ \AA}$  and  $c = 5.179 \text{ \AA}$ <sup>[192]</sup>. Therefore, this phase was determined to be  $\text{Ti}_5\text{Si}_3\text{B}_x$  with  $x$  around 0.5.

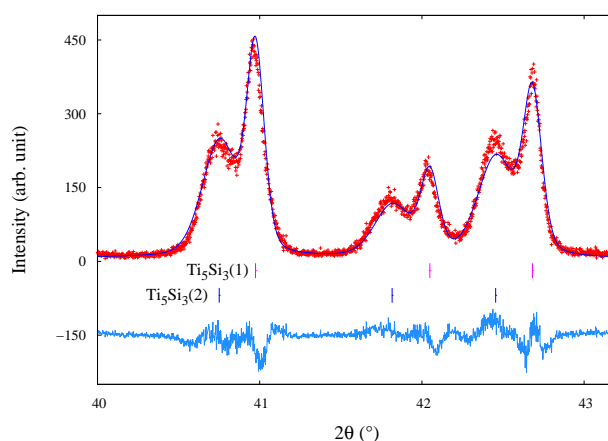


Figure 6.5: Le Bail refinement result in  $2\theta = 40\text{--}43^\circ$  of the sample containing 3 wt.%  $NaBH_4$  by refining using two  $Ti_5Si_3$  unit cells.

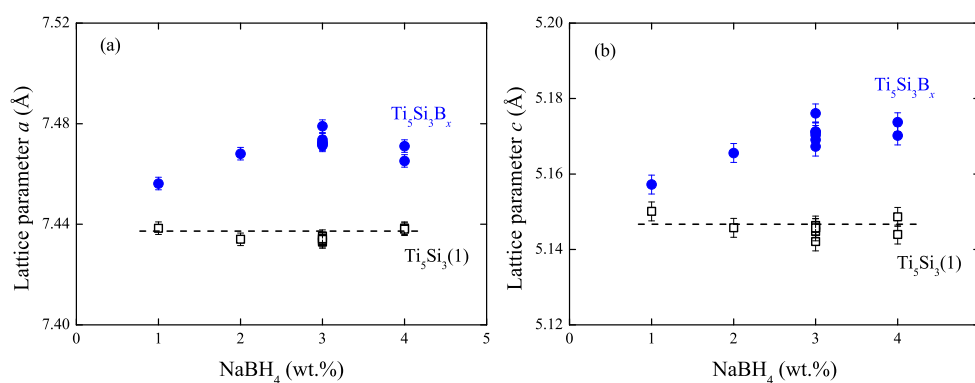


Figure 6.6: Lattice parameters of  $Ti_5Si_3Z_x$  in the samples containing 1–4 wt.%  $NaBH_4$  where  $Z$  refers to oxygen/sodium in one phase and denotes boron in the other phase.

## 6.4 Conclusion

Self-propagating high-temperature synthesis of  $Ti_5Si_3$  with a dilution of 0–40 wt.% from the stoichiometric elements yielded  $Ti_5Si_3$  and  $Ti_5Si_3O_x$  ( $x$  around 0.3). With a dilution above around 20 wt.%,  $Ti_5Si_3$  phase had an increasing silicon deficiency as indicated by the decrease of lattice parameter  $a$ . When 1–4 wt.%  $NaBH_4$  was added into the stoichiometric mixture of Ti and Si, obvious splitting of reflections were observed in the XRD patterns of the samples. It was due to the formation of  $Ti_5Si_3B_x$  and  $Ti_5Si_3Z_x$  ( $Z = \text{oxygen/sodium}$ ), which led to an expansion and contraction of the unit cell, respectively.

## 7 Summary and outlook

A series of  $\text{Ti}^{4+}$ -containing solid solutions have been synthesised. The synthesis approaches include: (i) conventional solid state synthesis of  $\text{MgTi}_2\text{O}_5$  from oxides, (ii) mechanochemical activation assisted solid state synthesis of the spinel-type  $\text{Cu}_x\text{Zn}_{2-x}\text{TiO}_4$ , the pseudobrookite-type  $\text{Zn}_x\text{Mg}_{1-x}\text{Ti}_2\text{O}_5$  and  $\text{Cu}_x\text{Mg}_{1-x}\text{Ti}_2\text{O}_5$  from oxides, (iii) mechanochemical activation assisted self-propagating high-temperature synthesis of end-member  $\text{ZnTi}_2\text{O}_5$  from oxides and a metal, and (iiii) self-propagating high-temperature synthesis of the  $\text{Mn}_5\text{Si}_3$ -type  $\text{Ti}_5\text{Si}_3\text{Z}_x$  ( $Z = \text{B/O}$ ) from elements and a hydride. The impurities of  $\text{ZnO}$  and  $\text{CuO}$  in  $\text{Cu}_x\text{Zn}_{2-x}\text{TiO}_4$  solid solution with  $0 \leq x \leq 0.7$  were removed by soaking the samples in the acetic acid solution. For  $\text{Cu}_x\text{Zn}_{2-x}\text{TiO}_4$  with  $x$  around 0.75 and 0.86, a minor amount of  $\text{CuO}$  co-existed with the spinel phase. Moreover, the disordered  $\text{MgTi}_2\text{O}_5$  was annealed at 873 K for a long time in order to improve the  $\text{Mg/Ti}$  order. Meanwhile, a quenching process was employed for  $\text{MgTi}_2\text{O}_5$  and its solid solutions in order to retain their high-temperature structures. Purities of  $\text{Zn}_x\text{Mg}_{1-x}\text{Ti}_2\text{O}_5$  with  $0 \leq x \leq 0.8$  and  $\text{Cu}_x\text{Mg}_{1-x}\text{Ti}_2\text{O}_5$  were above 96 wt.%. Purity of  $\text{Zn}_x\text{Mg}_{1-x}\text{Ti}_2\text{O}_5$  with  $x = 0.9$  and  $\text{ZnTi}_2\text{O}_5$  was 30 wt.% and 19 wt.%, respectively. Two  $\text{Ti}_5\text{Si}_3\text{Z}_x$  phases were generated for the self-propagating high-temperature synthesis of  $\text{Ti}_5\text{Si}_3$  with additions.

Rietveld refinements of  $\text{Cu}_x\text{Zn}_{2-x}\text{TiO}_4$  cubic spinels using neutron diffraction data were carried out with several strategies. When variable thermal displacement parameters of the cations were allowed,  $\text{Zn}^{2+}$ , less than 0.01  $\text{Cu}^{2+}$  and no more than 0.02  $\text{Ti}^{4+}$  in molar fraction occupied the tetrahedral  $8a$  sites. When thermal displacement parameter of the cations was fixed to be  $U_{\text{iso}} = 0.005 \text{ \AA}^2$ , at maximum 0.04  $\text{Cu}^{2+}$  and 0.04  $\text{Ti}^{4+}$  incorporated into the tetrahedral  $8a$  sites. With increasing incorporation of  $\text{Cu}^{2+}$ , the lattice parameter decreased linearly for  $x \leq 0.6$  and contracted more strongly with higher copper contents. The positional parameter and isotropic thermal displacement parameter of the anions increased with increasing copper in the solid solution range of  $0.0 \leq x \leq 0.86(5)$ . The average octahedral bond length increased while the average tetrahedral bond length held the same value. The structural changes as well as incomplete solubility of the  $\text{Cu}_x\text{Zn}_{2-x}\text{TiO}_4$  solid solution were ascribed to local Jahn-Teller distortions around  $\text{Cu}^{2+}$ .

The pseudobrookite group with an orthorhombic symmetry, another dense oxide, has been much less studied than spinels. Both experimental and theoretical approaches were employed to investigate the endmember  $\text{MgTi}_2\text{O}_5$ . Structural changes and vibrational properties of the pseudobrookite-type solid solutions  $\text{Zn}_x\text{Mg}_{1-x}\text{Ti}_2\text{O}_5$  and  $\text{Cu}_x\text{Mg}_{1-x}\text{Ti}_2\text{O}_5$  were compared. The synthesis temperature of  $\text{MgTi}_2\text{O}_5$  was reduced to 1173 K due to the mechanochemical activation process. With increasing exchange of  $\text{Ti}^{4+}$  in the  $M2$  ( $8f$ ) sites with  $\text{Mg}^{2+}$  in the  $M1$  ( $4c$ ) sites, the  $B_{1g}(5)$  Raman modes blueshifted linearly. Vibrational properties and low-temperature thermodynamic properties of  $\text{MgTi}_2\text{O}_5$  varied with the  $\text{Mg/Ti}$  disorder.

A new endmember  $\text{ZnTi}_2\text{O}_5$  was discovered by employing the self-propagating high-temperature synthesis set-up and using the mechanical activated mixture of Ti metal,  $\text{TiO}_2$  (anatase) and ZnO, showing a high crystallisation temperature of  $\text{ZnTi}_2\text{O}_5$ .  $\text{Zn}_x\text{Mg}_{1-x}\text{Ti}_2\text{O}_5$  with  $0 \leq x \leq 0.8$  were synthesised at temperatures of 1473–1573 K whereas  $\text{Cu}_x\text{Mg}_{1-x}\text{Ti}_2\text{O}_5$  with  $0 \leq x \leq 0.5$  was obtained at 1273 K. Rietveld refinements of the X-ray and neutron diffraction data for  $\text{Zn}_x\text{Mg}_{1-x}\text{Ti}_2\text{O}_5$  solid solution showed that  $\text{Zn}^{2+}$  preferably substituted  $\text{Mg}^{2+}$  in the  $M1$  sites at  $x \leq 0.6$ . At a higher content of zinc, 0.6  $\text{Zn}^{2+}$  occupied the  $M1$  sites while the other part of  $\text{Zn}^{2+}$  incorporated into the  $M2$  sites.  $\text{Zn}^{2+}$  in the  $M2$  sites forced a migration of  $\text{Ti}^{4+}$  from the  $M2$  to  $M1$  sites to exchange with  $\text{Mg}^{2+}$  in the  $M1$  sites.

The structural and vibrational properties of  $\text{Zn}_x\text{Mg}_{1-x}\text{Ti}_2\text{O}_5$  and  $\text{Cu}_x\text{Mg}_{1-x}\text{Ti}_2\text{O}_5$  solid solutions depended on the type and site occupancy of the cations. The unit cell of  $\text{MgTi}_2\text{O}_5$  expanded significantly and linearly due to the replacement of  $\text{Mg}^{2+}$  by  $\text{Zn}^{2+}$  while no obvious change was observed with the substitution of  $\text{Mg}^{2+}$  by  $\text{Cu}^{2+}$ . Zinc induced a linear increase of  $b$  and a decreasing kinking angle of the edgesharing chain of the  $M2$  octahedra. With the increase of  $x$ , the  $B_{1g}(5)$  Raman mode redshifted in  $\text{Zn}_x\text{Mg}_{1-x}\text{Ti}_2\text{O}_5$  whereas the mode first redshifted and then blueshifted in  $\text{Cu}_x\text{Mg}_{1-x}\text{Ti}_2\text{O}_5$ . This indicated different site occupancies of the two solid solutions. Neutron diffraction data are capable to reveal the accurate cation distributions. A systematic investigation of structural changes using *in situ* time-of-flight neutron diffraction under high ( $p$ ,  $T$ ) conditions can provide thermodynamics of cation exchange in the pseudobrookite-type structure.

The attempt to synthesise hexagonal  $\text{Ti}_5\text{Si}_3$  with small interstitial atoms by using self-propagating high-temperature synthesis is successful. More efforts could be made for synthesis of pure interstitial solid solutions by SHS.

## A $\text{Cu}_x\text{Zn}_{2-x}\text{TiO}_4$ cubic spinels

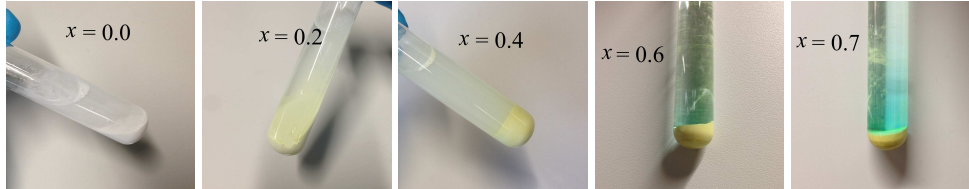


Figure A.1: Picture of the samples being soaked in the acetic acid solution (25 vol.%  $\text{CH}_3\text{COOH}$  and 75 vol.%  $\text{H}_2\text{O}$ ) by using glass tubes. The samples have nominal compositions of  $\text{Cu}_x\text{Zn}_{2-x}\text{TiO}_4$  before the soaking treatments.

Table A.1: Structural parameters of the co-existing  $\text{CuO}$  in the sample  $\text{Cu}_x\text{Zn}_{2-x}\text{TiO}_4$  with  $x = 0.86(5)$  as compared with literature values of the pure phase  $\text{CuO}$  and their differences  $\Delta$  [199,200].

	This study	Lit. [199,200]	$\Delta$
Space group	C2/c (no. 15)	C2/c (no. 15)	
Z	4	4	
$a$ [ $\text{\AA}$ ]	4.6912(3)	4.6837(5)	-0.16%
$b$ [ $\text{\AA}$ ]	3.4177(2)	3.4226(5)	+0.14%
$c$ [ $\text{\AA}$ ]	5.1350(4)	5.1288(6)	-0.12%
$\beta$ [ $^\circ$ ]	99.40(2)	99.54	+0.14%
$\text{O}_y$	0.41805(8)	0.4184(13)	+0.08%
$U_{\text{iso}}(\text{Cu}) [\times 0.01 \text{\AA}^2]$	0.76(3)		
$U_{\text{iso}}(\text{O}) [\times 0.01 \text{\AA}^2]$	0.62(5)		
$\text{Cu}(2)\text{-O-Cu}(3)$ [ $^\circ$ ]	145.94(3)	145.82	-0.08%
$\text{Cu}(1)\text{-O-Cu}(4)$ [ $^\circ$ ]	109.02(3)	108.85	-0.16%
$\text{Cu}(2)\text{-O-Cu}(4)$ [ $^\circ$ ]	103.96(3)	104.03	+0.07%
$\text{Cu}(2)\text{-O-Cu}(5)$ [ $^\circ$ ]	95.68(3)	95.72	+0.05%

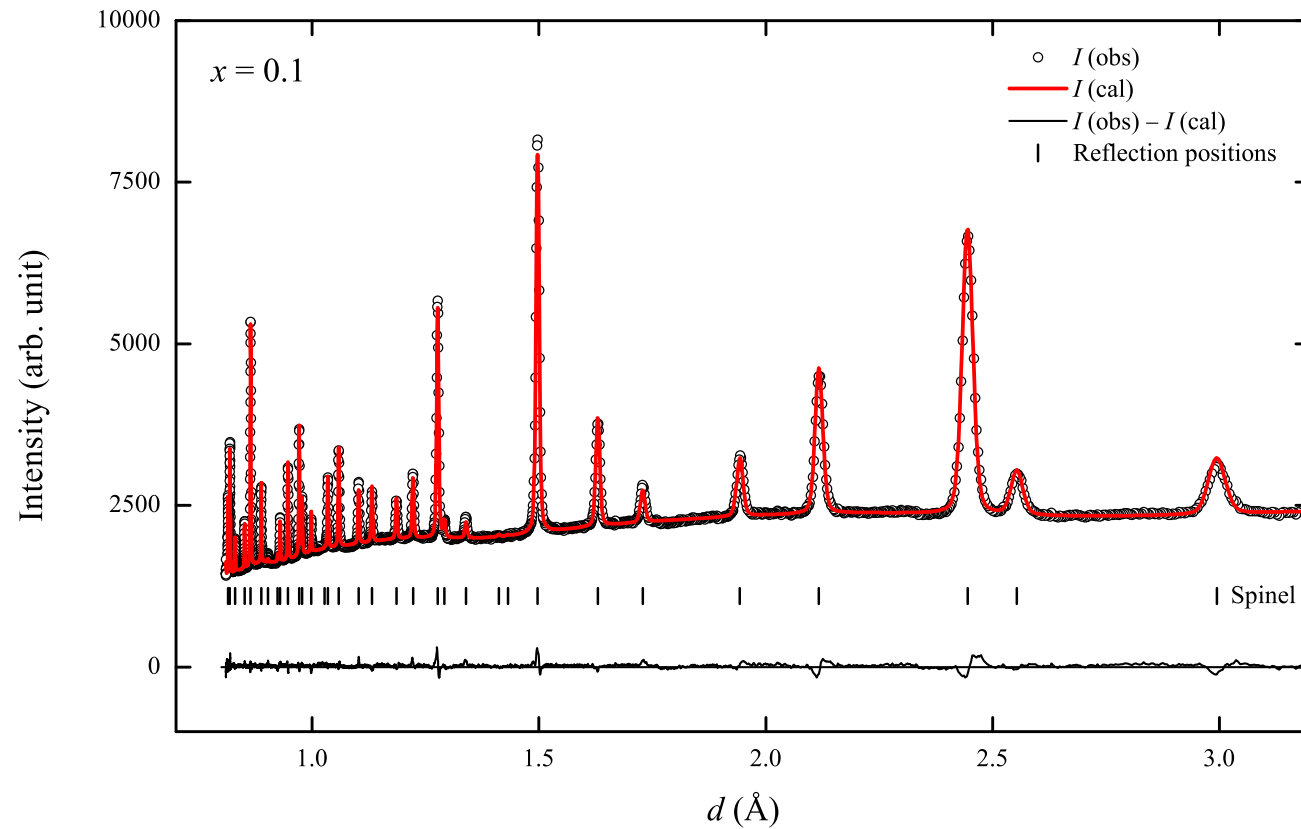


Figure A.2: Rietveld refinement results of neutron diffraction for the sample  $\text{Cu}_x\text{Zn}_{2-x}\text{TiO}_4$  with  $x = 0.1$  assuming  $\text{Zn}^{2+}$ ,  $\text{Cu}^{2+}$  and  $\text{Ti}^{4+}$  in the tetrahedral sites (strategy 4). Observed (circles) and calculated data (red curve), a difference curve (bottom black curve) and reflection positions of the spinel (black tickmarks) are shown.

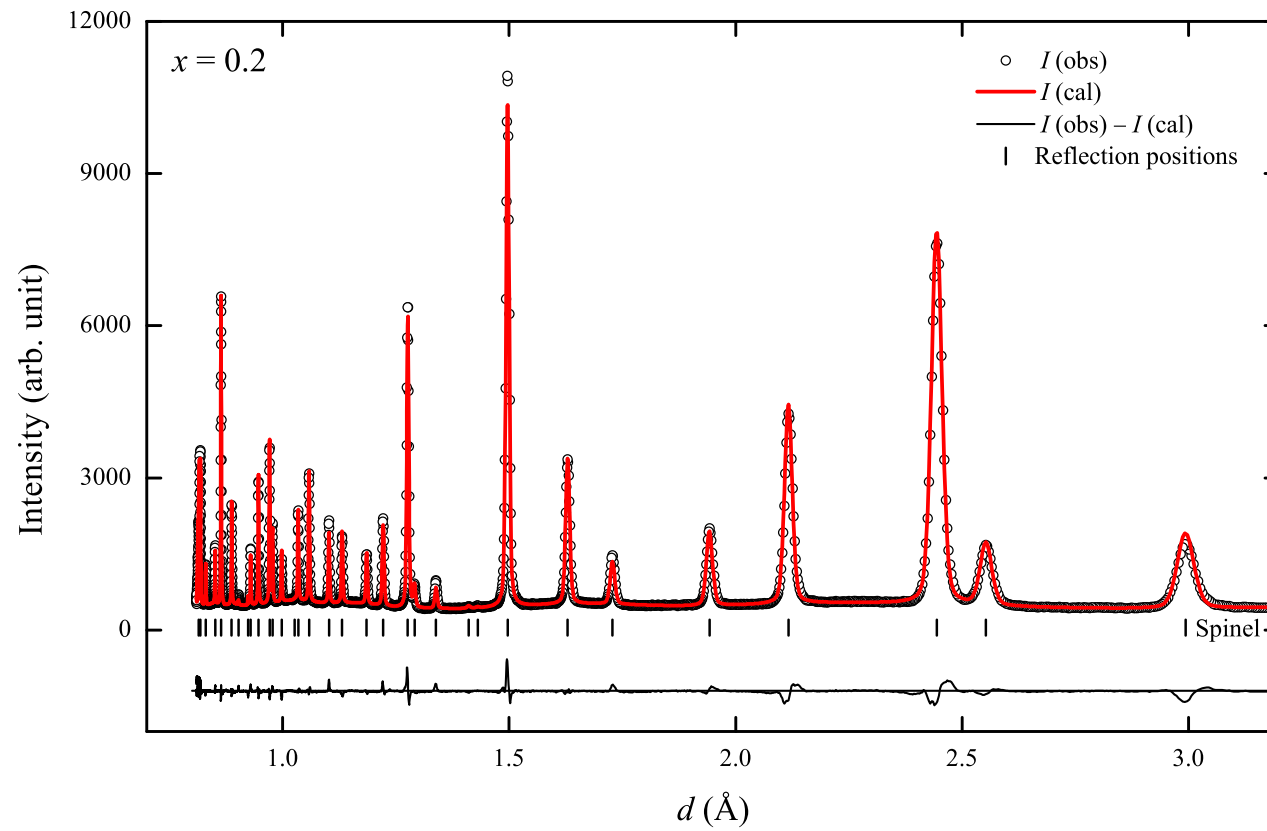


Figure A.3: Rietveld refinement results of neutron diffraction for the sample  $\text{Cu}_x\text{Zn}_{2-x}\text{TiO}_4$  with  $x = 0.2$  assuming  $\text{Zn}^{2+}$ ,  $\text{Cu}^{2+}$  and  $\text{Ti}^{4+}$  in the tetrahedral sites (strategy 4). Observed (circles) and calculated data (red curve), a difference curve (bottom black curve) and reflection positions of the spinel (black tickmarks) are shown.

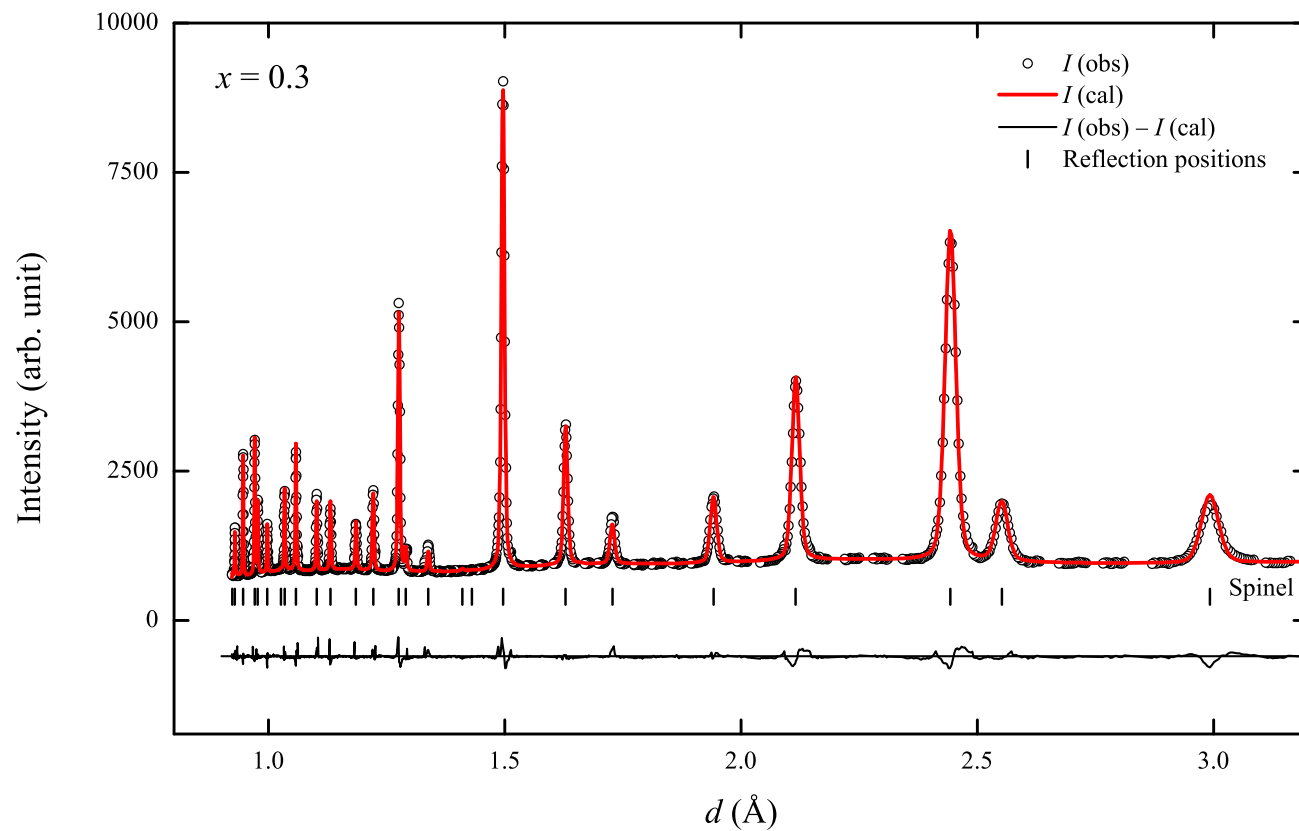


Figure A.4: Rietveld refinement results of neutron diffraction for the sample  $\text{Cu}_x\text{Zn}_{2-x}\text{TiO}_4$  with  $x = 0.3$  assuming  $\text{Zn}^{2+}$ ,  $\text{Cu}^{2+}$  and  $\text{Ti}^{4+}$  in the tetrahedral sites (strategy 4). Observed (circles) and calculated data (red curve), a difference curve (bottom black curve) and reflection positions of the spinel (black tickmarks) are shown.



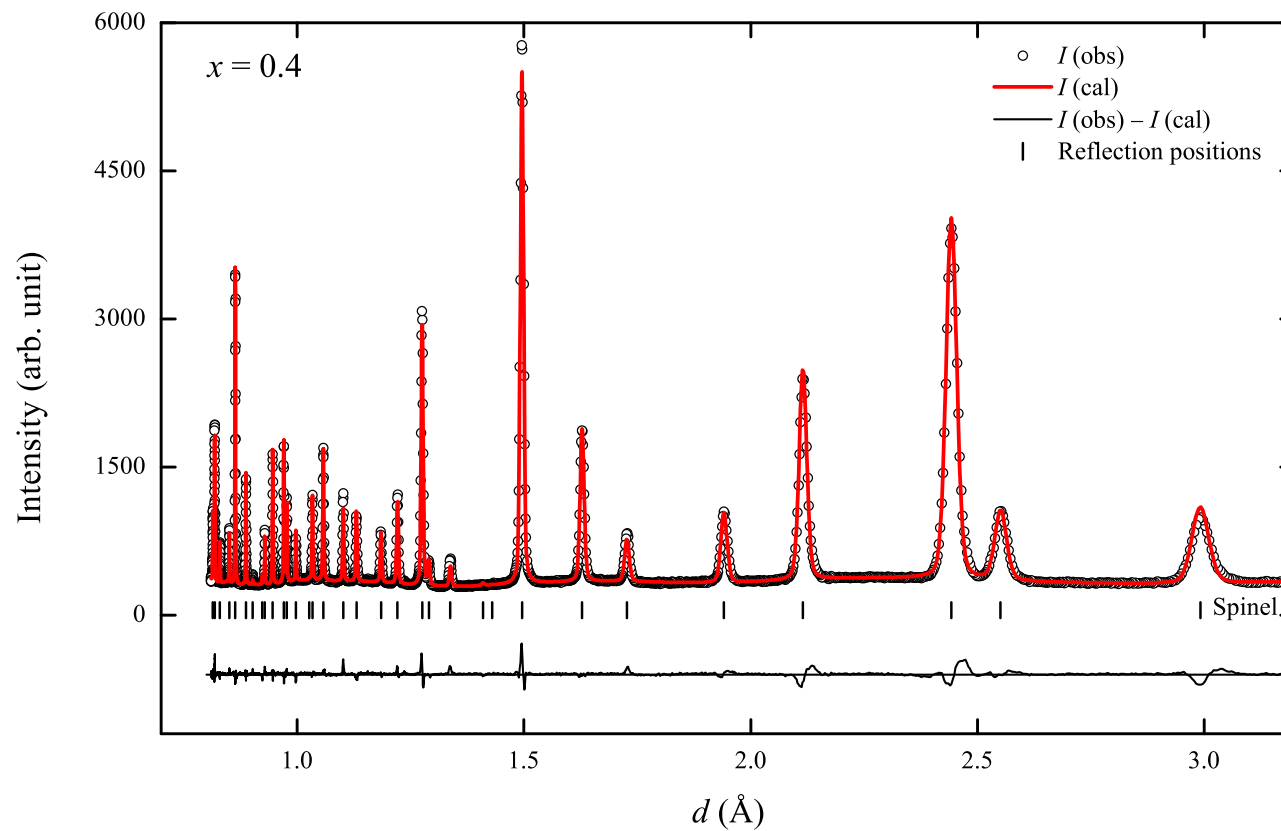


Figure A.5: Rietveld refinement results of neutron diffraction for the sample  $\text{Cu}_x\text{Zn}_{2-x}\text{TiO}_4$  with  $x = 0.4$  assuming  $\text{Zn}^{2+}$ ,  $\text{Cu}^{2+}$  and  $\text{Ti}^{4+}$  in the tetrahedral sites (strategy 4). Observed (circles) and calculated data (red curve), a difference curve (bottom black curve) and reflection positions of the spinel (black tickmarks) are shown.

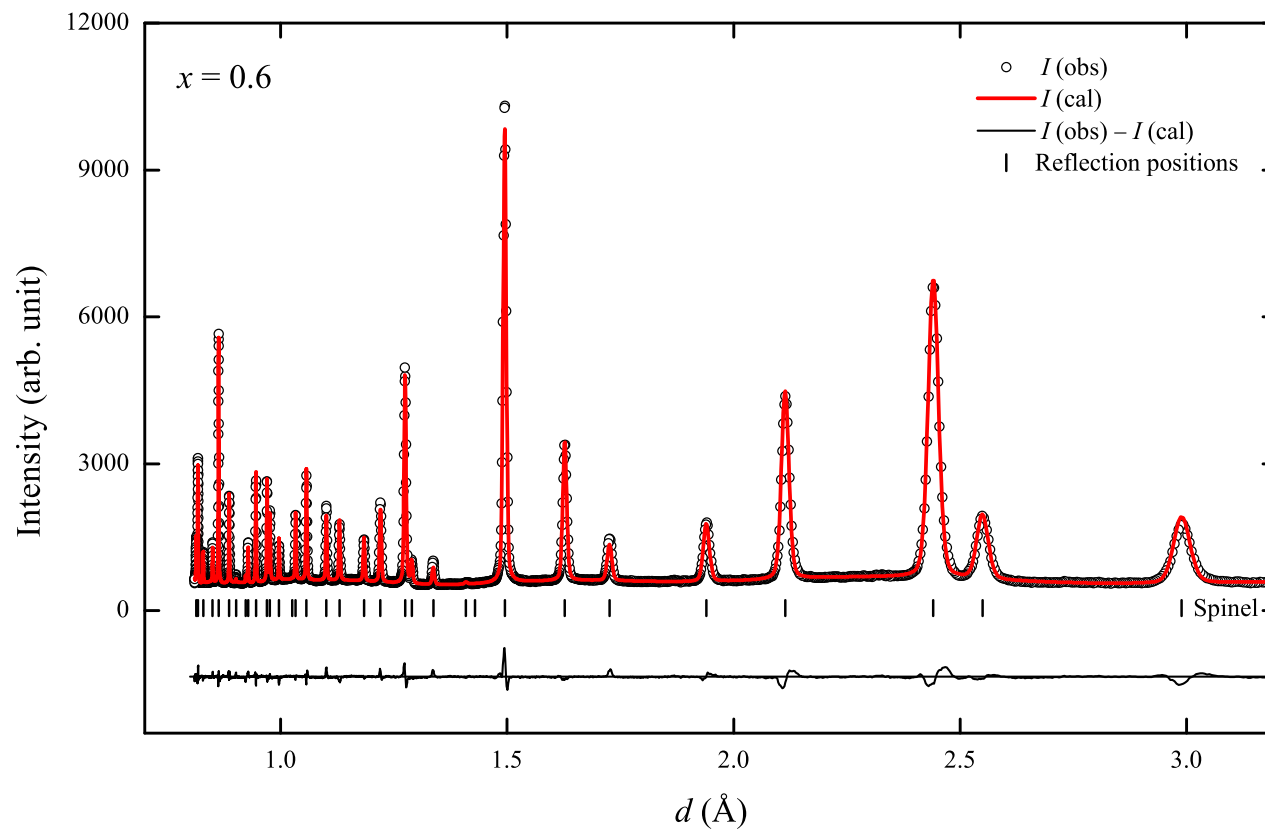


Figure A.6: Rietveld refinement results of neutron diffraction for the sample  $\text{Cu}_x\text{Zn}_{2-x}\text{TiO}_4$  with  $x = 0.6$  assuming  $\text{Zn}^{2+}$ ,  $\text{Cu}^{2+}$  and  $\text{Ti}^{4+}$  in the tetrahedral sites (strategy 4). Observed (circles) and calculated data (red curve), a difference curve (bottom black curve) and reflection positions of the spinel (black tickmarks) are shown.

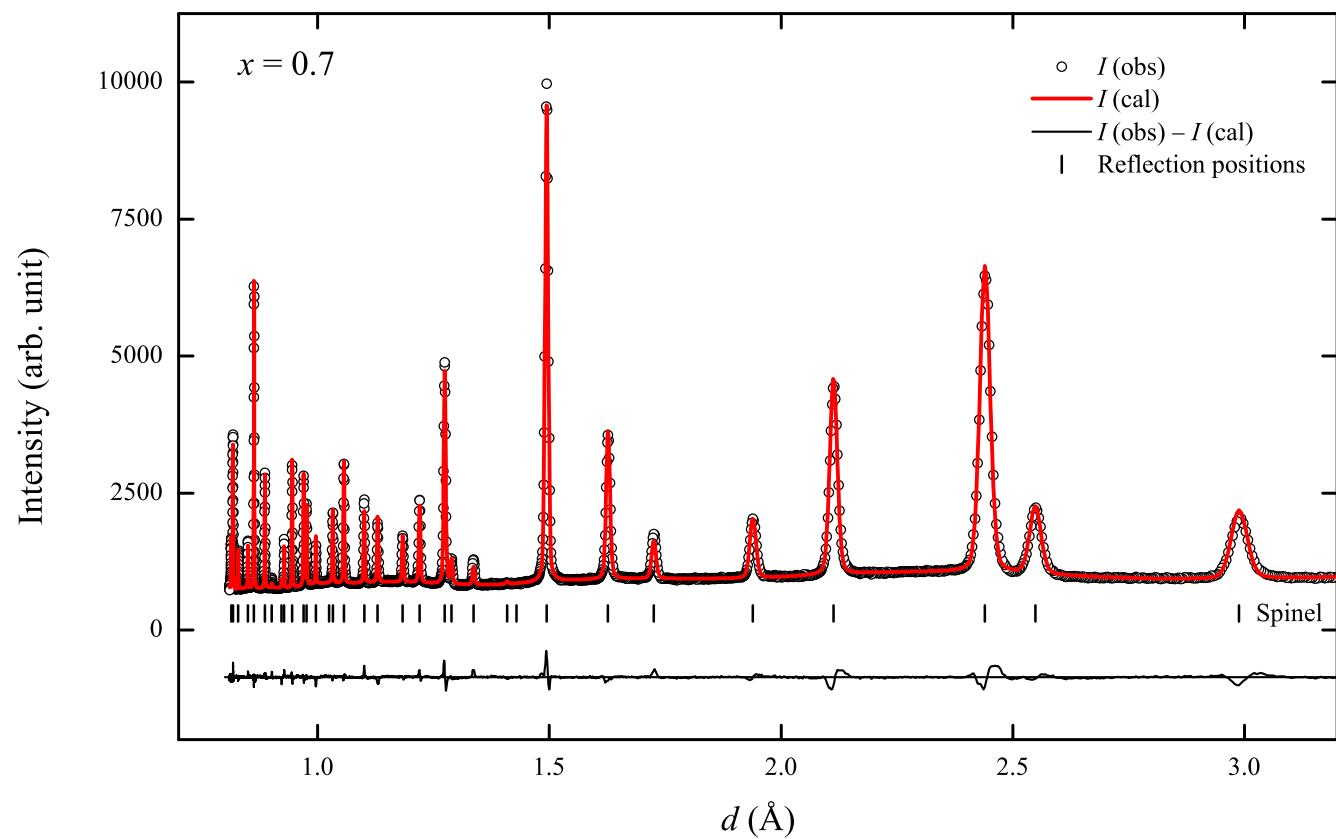


Figure A.7: Rietveld refinement results of neutron diffraction for the sample  $\text{Cu}_x\text{Zn}_{2-x}\text{TiO}_4$  with  $x = 0.7$  assuming  $\text{Zn}^{2+}$ ,  $\text{Cu}^{2+}$  and  $\text{Ti}^{4+}$  in the tetrahedral sites (strategy 4). Observed (circles) and calculated data (red curve), a difference curve (bottom black curve) and reflection positions of the spinel (black tickmarks) are shown.

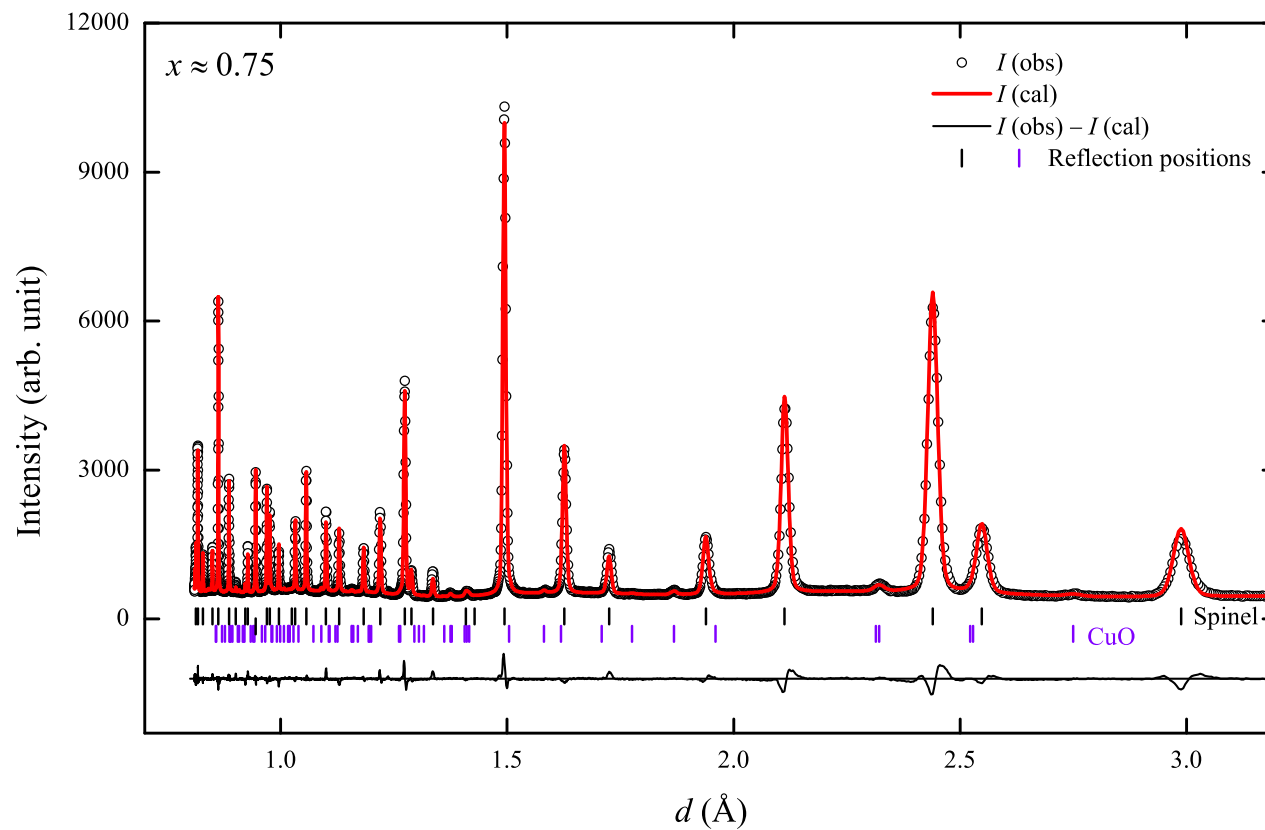


Figure A.8: Rietveld refinement results of neutron diffraction for the sample  $\text{Cu}_x\text{Zn}_{2-x}\text{TiO}_4$  with  $x \approx 0.75$  assuming  $\text{Zn}^{2+}$ ,  $\text{Cu}^{2+}$  and  $\text{Ti}^{4+}$  in the tetrahedral sites (strategy 4). Observed (circles) and calculated data (red curve), a difference curve (bottom black curve) and reflection positions of the crystalline phases (tickmarks) are shown.

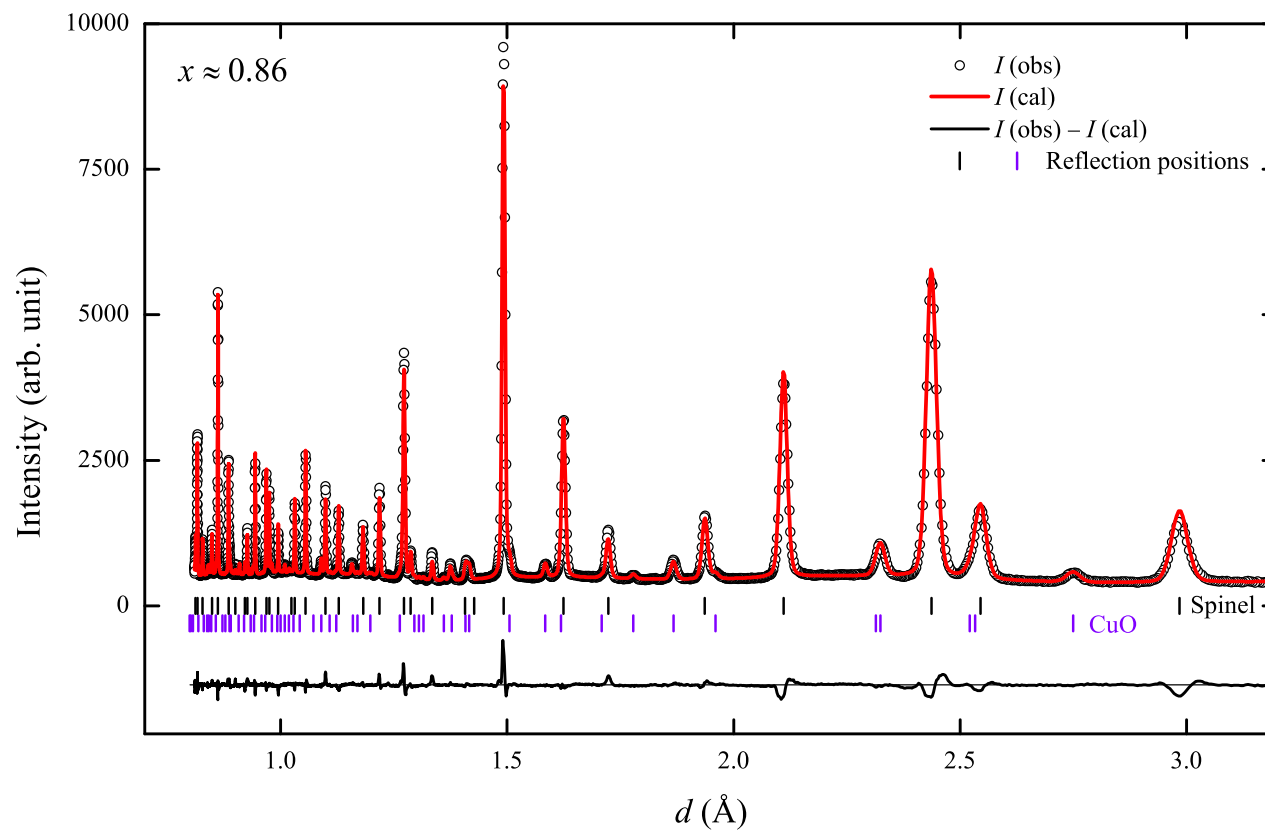


Figure A.9: Rietveld refinement results of neutron diffraction for the sample  $\text{Cu}_x\text{Zn}_{2-x}\text{TiO}_4$  with  $x \approx 0.86$  assuming  $\text{Zn}^{2+}$ ,  $\text{Cu}^{2+}$  and  $\text{Ti}^{4+}$  in the tetrahedral sites (strategy 4). Observed (circles) and calculated data (red curve), a difference curve (bottom black curve) and reflection positions of the crystalline phases (tickmarks) are shown.



## B Pseudobrookite-type $\text{MgTi}_2\text{O}_5$

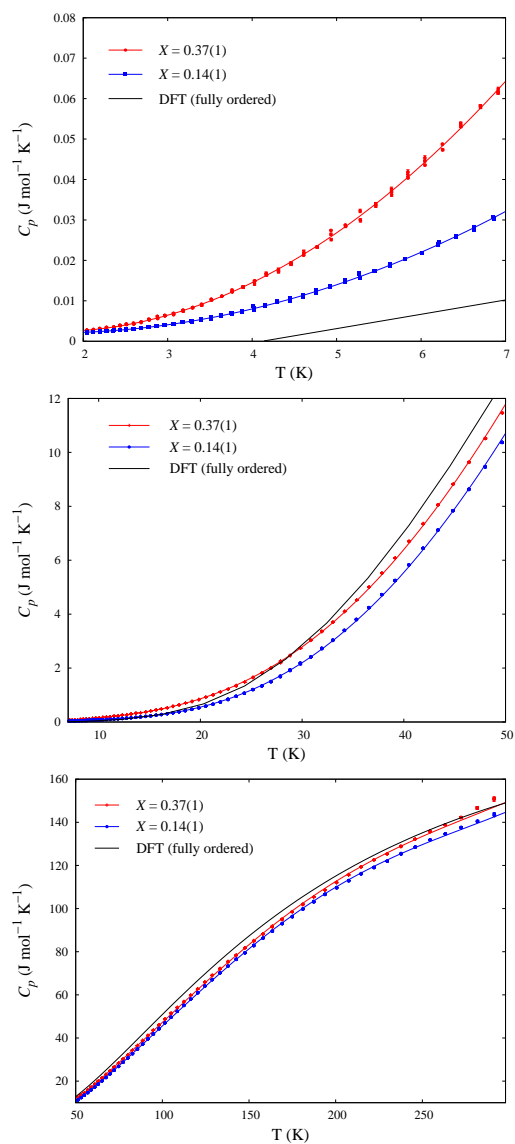


Figure B.1: Polynomial fits of the measured low-temperature heat capacities of  $\text{MgTi}_2\text{O}_5$  with  $X = 0.14(1)$  and  $0.37(1)$  in three temperature ranges, as compared with the DFT calculated curve of fully ordered  $\text{MgTi}_2\text{O}_5$ .

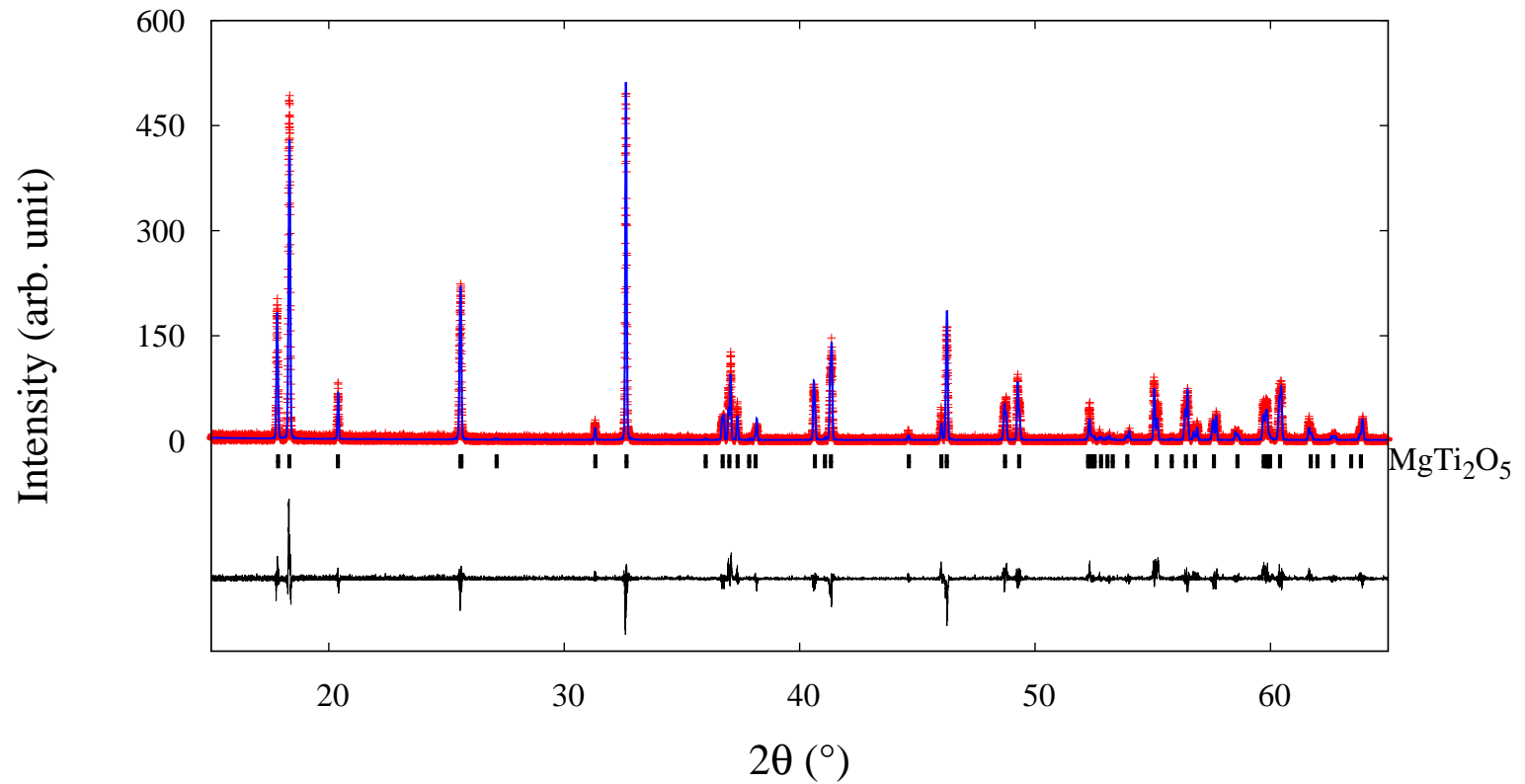


Figure B.2: Rietveld refinement results of X-ray diffraction for  $\text{MgTi}_2\text{O}_5$  with  $X = 0.14(1)$ , which was annealed at a temperature of 873 K. Observed (red crosses) and calculated data (blue curve), a difference curve (bottom black curve) and reflection positions of the crystalline phase (black tickmarks) are shown.



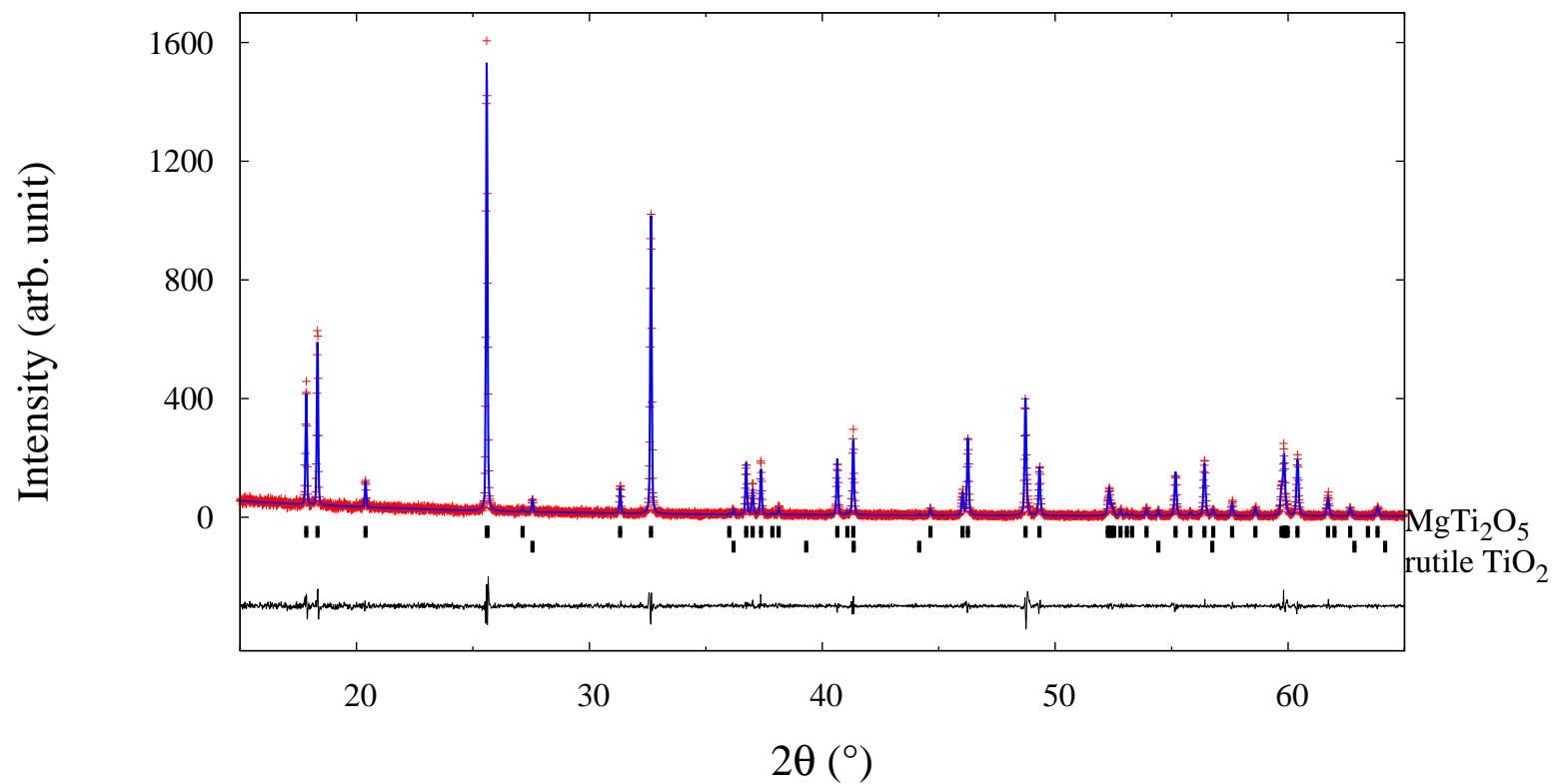


Figure B.3: Rietveld refinement results of X-ray diffraction for MgTi<sub>2</sub>O<sub>5</sub> with  $X = 0.30(1)$ , which was not ball milled and had a synthesis temperature of 1473 K. Observed (red crosses) and calculated data (blue curve), a difference curve (bottom black curve) and reflection positions of the crystalline phases (black tickmarks) are shown.

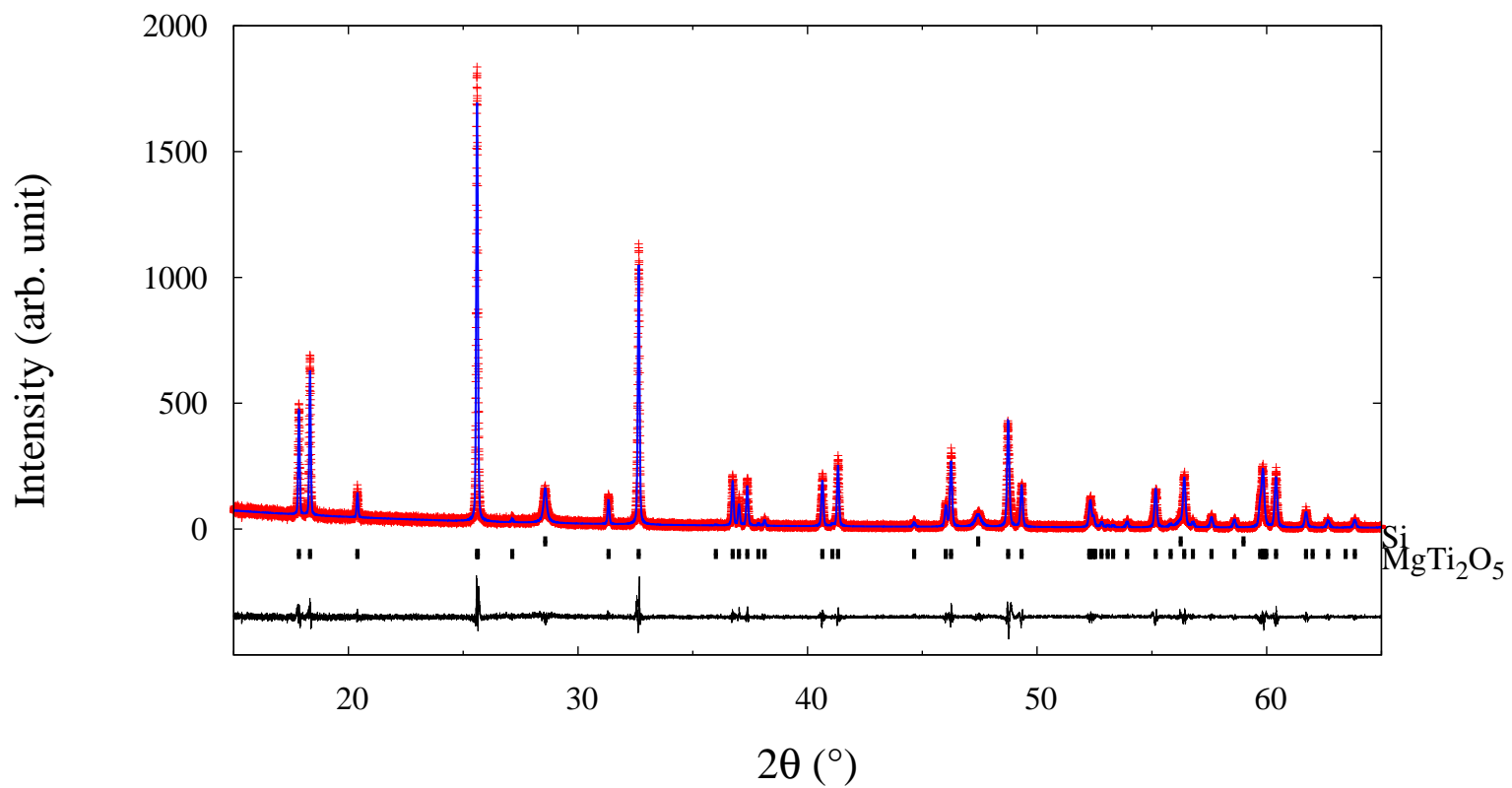


Figure B.4: Rietveld refinement results of X-ray diffraction for  $\text{MgTi}_2\text{O}_5$  with  $X = 0.33(1)$ , which was ball milled and had a synthesis temperature of 1273 K. Observed (red crosses) and calculated data (blue curve), a difference curve (bottom black curve) and reflection positions of the crystalline phases (black tickmarks) are shown.

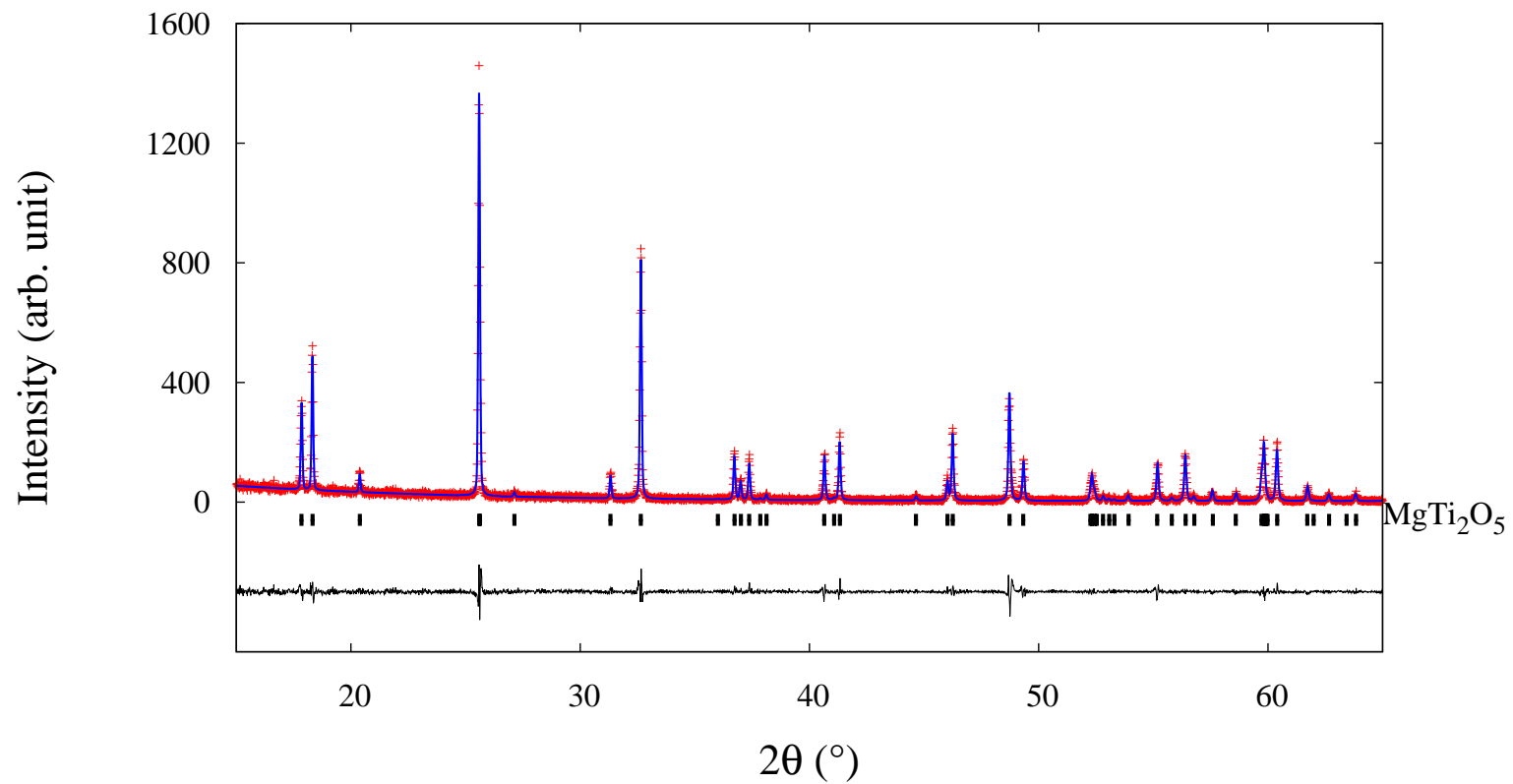


Figure B.5: Rietveld refinement results of X-ray diffraction for MgTi<sub>2</sub>O<sub>5</sub> with  $X = 0.34(1)$ , which was ball milled and had a synthesis temperature of 1373 K. Observed (red crosses) and calculated data (blue curve), a difference curve (bottom black curve) and reflection positions of the crystalline phase (black tickmarks) are shown.

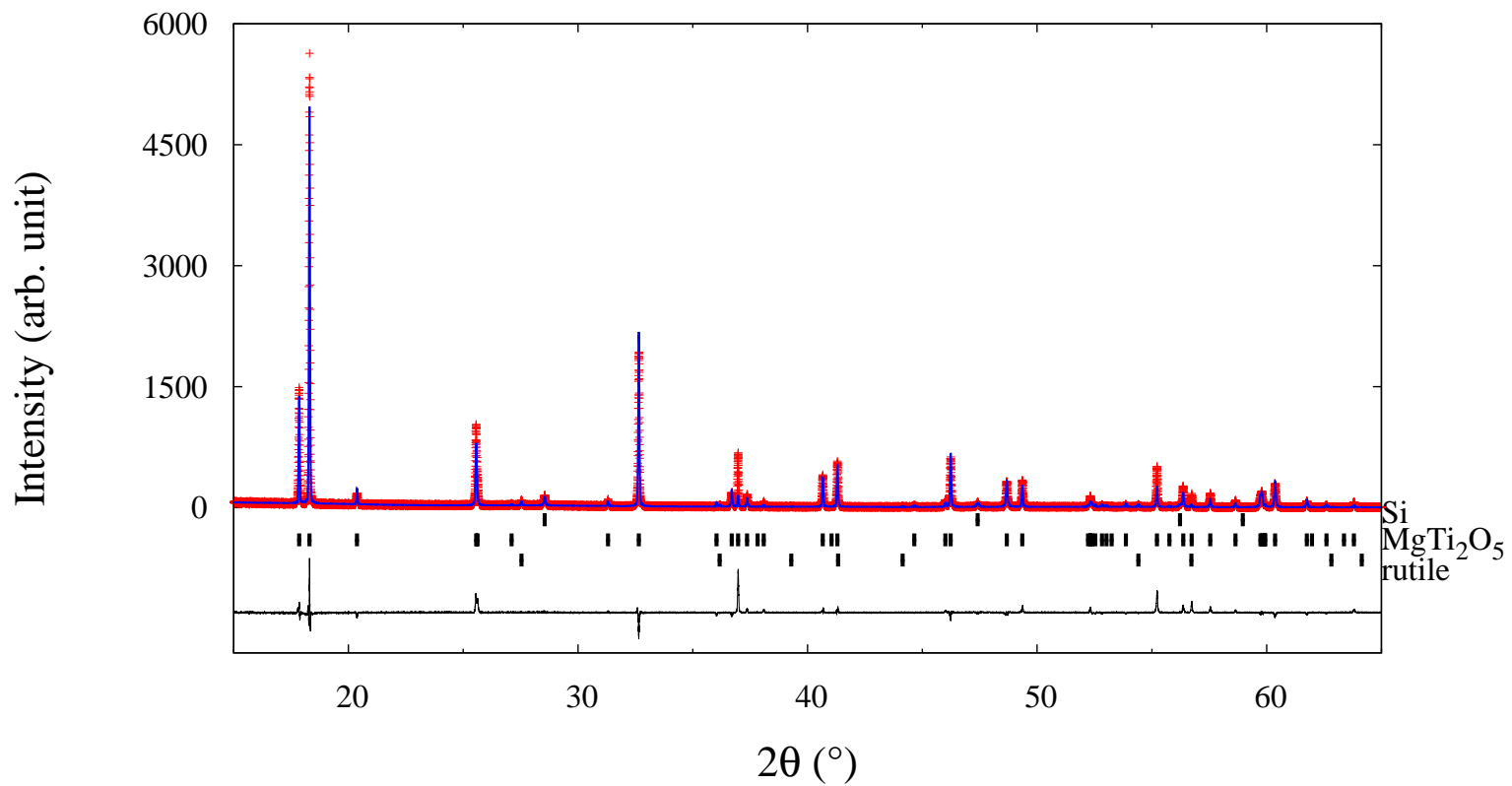


Figure B.6: Rietveld refinement results of X-ray diffraction for  $\text{MgTi}_2\text{O}_5$  with  $X = 0.37(1)$ , which was ball milled and had a synthesis temperature of 1473 K. Observed (red crosses) and calculated data (blue curve), a difference curve (bottom black curve) and reflection positions of the crystalline phases (black tickmarks) are shown.

## C Pseudobrookite-type $\text{Zn}_x\text{Mg}_{1-x}\text{Ti}_2\text{O}_5$ and $\text{Cu}_x\text{Mg}_{1-x}\text{Ti}_2\text{O}_5$

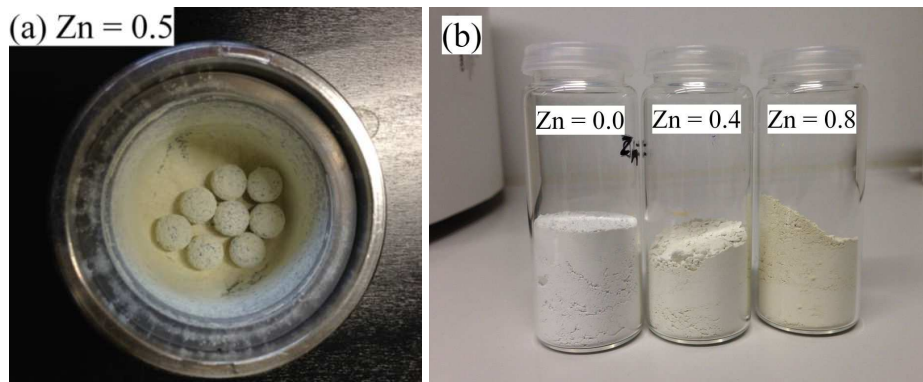


Figure C.1: Mixtures of  $\text{Zn}_x\text{Mg}_{1-x}\text{Ti}_2\text{O}_5$  after ball milling: (a)  $x = 0.5$  and (b)  $x = 0.0, 0.4$  and  $0.8$ .

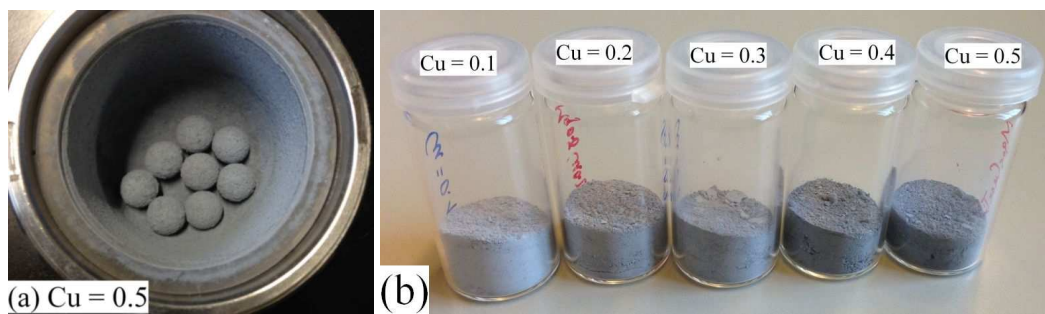


Figure C.2: Mixtures of  $\text{Cu}_x\text{Mg}_{1-x}\text{Ti}_2\text{O}_5$  after ball milling: (a)  $x = 0.5$  and (b)  $x = 0.1, 0.2, 0.3, 0.4$  and  $0.5$ .

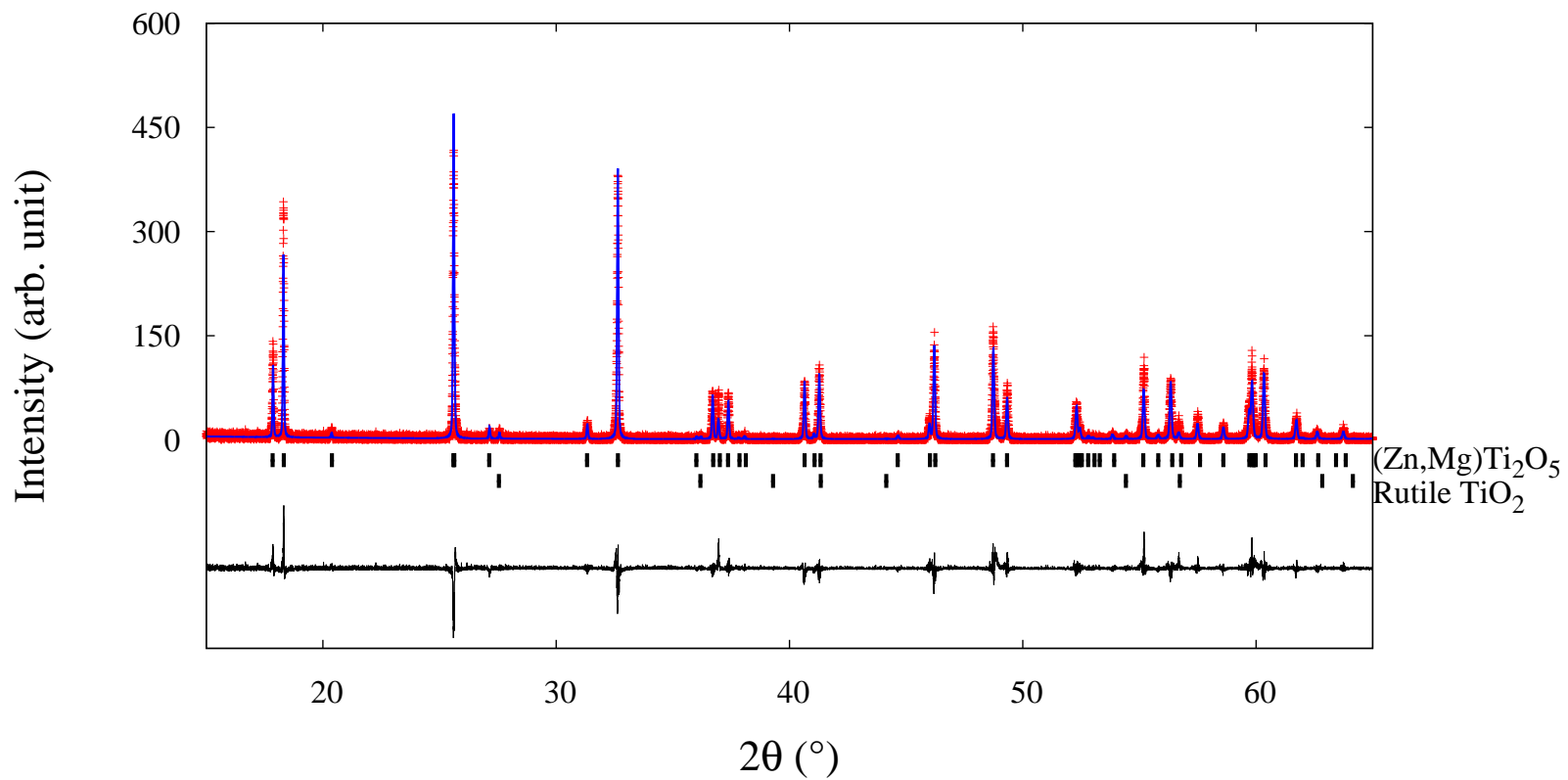


Figure C.3: Rietveld refinement results of X-ray diffraction for  $\text{Zn}_x\text{Mg}_{1-x}\text{Ti}_2\text{O}_5$  with  $x = 0.1$ , which had a synthesis temperature of 1473 K. Observed (red crosses) and calculated data (blue curve), a difference curve (bottom black curve) and reflection positions of the crystalline phases (black tickmarks) are shown.

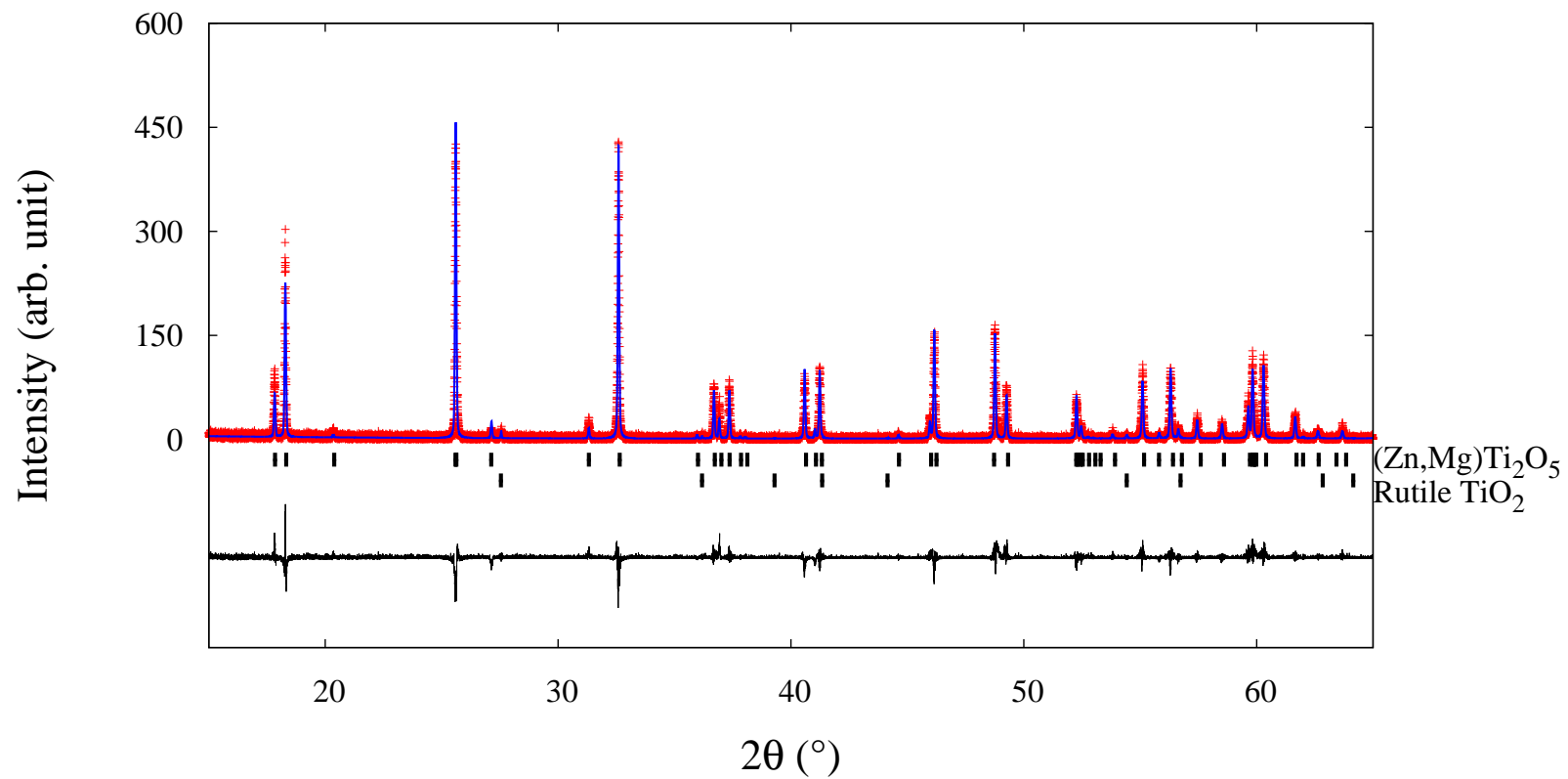


Figure C.4: Rietveld refinement results of X-ray diffraction for  $\text{Zn}_x\text{Mg}_{1-x}\text{Ti}_2\text{O}_5$  with  $x = 0.2$ , which had a synthesis temperature of 1473 K. Observed (red crosses) and calculated data (blue curve), a difference curve (bottom black curve) and reflection positions of the crystalline phases (black tickmarks) are shown.

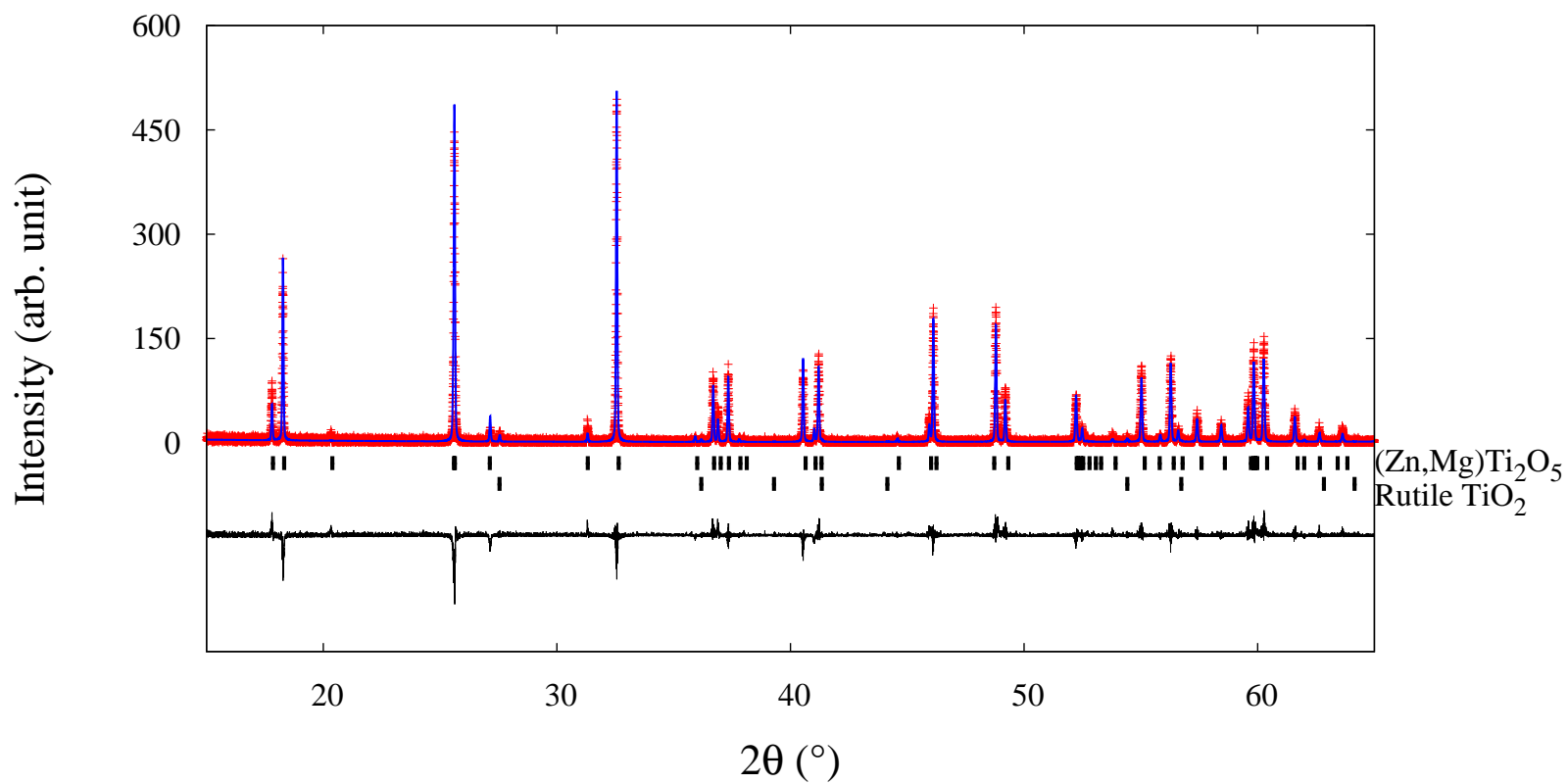


Figure C.5: Rietveld refinement results of X-ray diffraction for  $\text{Zn}_x\text{Mg}_{1-x}\text{Ti}_2\text{O}_5$  with  $x = 0.3$ , which had a synthesis temperature of 1473 K. Observed (red crosses) and calculated data (blue curve), a difference curve (bottom black curve) and reflection positions of the crystalline phases (black tickmarks) are shown.



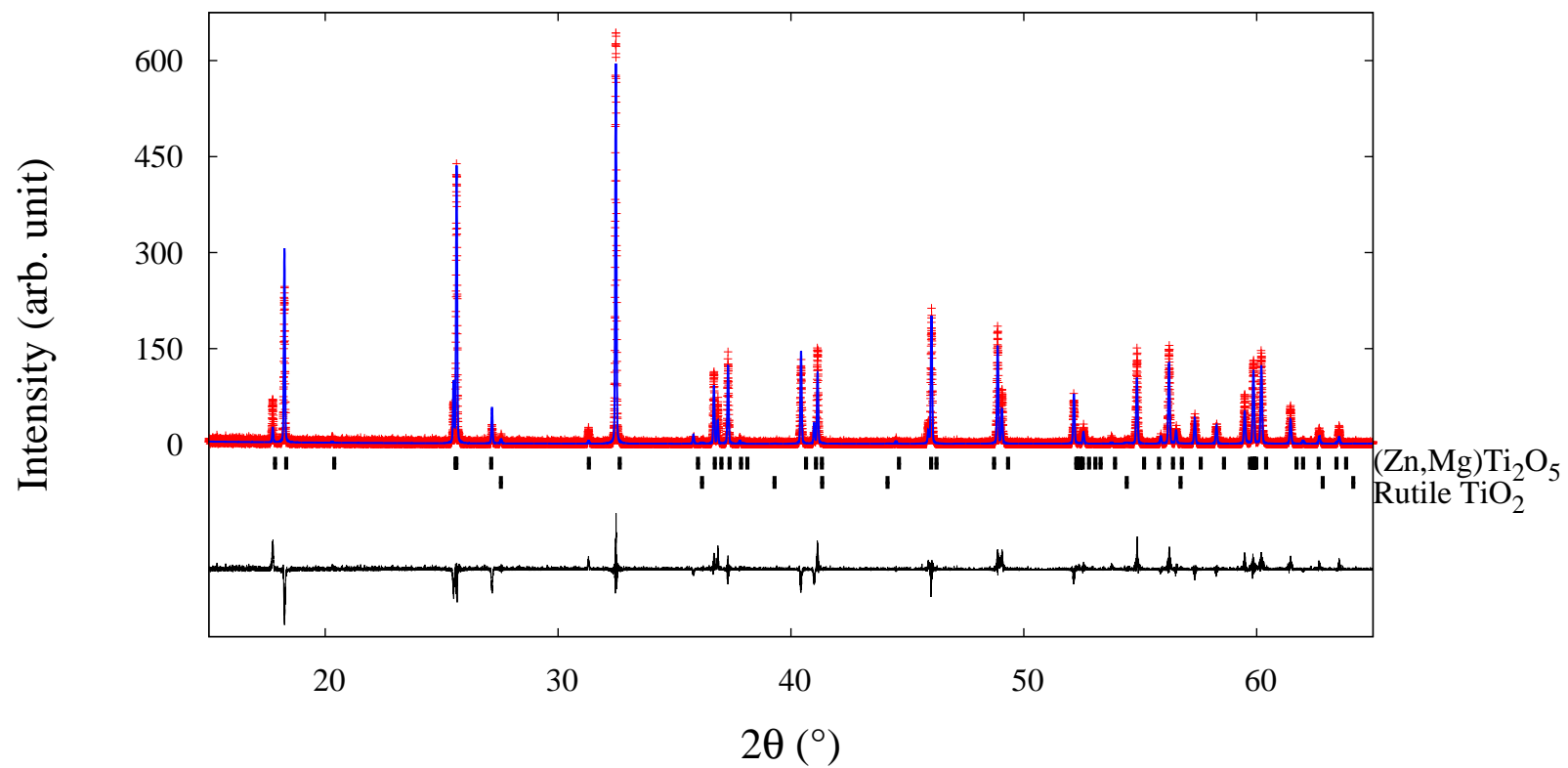


Figure C.6: Rietveld refinement results of X-ray diffraction for  $\text{Zn}_x\text{Mg}_{1-x}\text{Ti}_2\text{O}_5$  with  $x = 0.5$ , which had a synthesis temperature of 1473 K. Observed (red crosses) and calculated data (blue curve), a difference curve (bottom black curve) and reflection positions of the crystalline phases (black tickmarks) are shown.

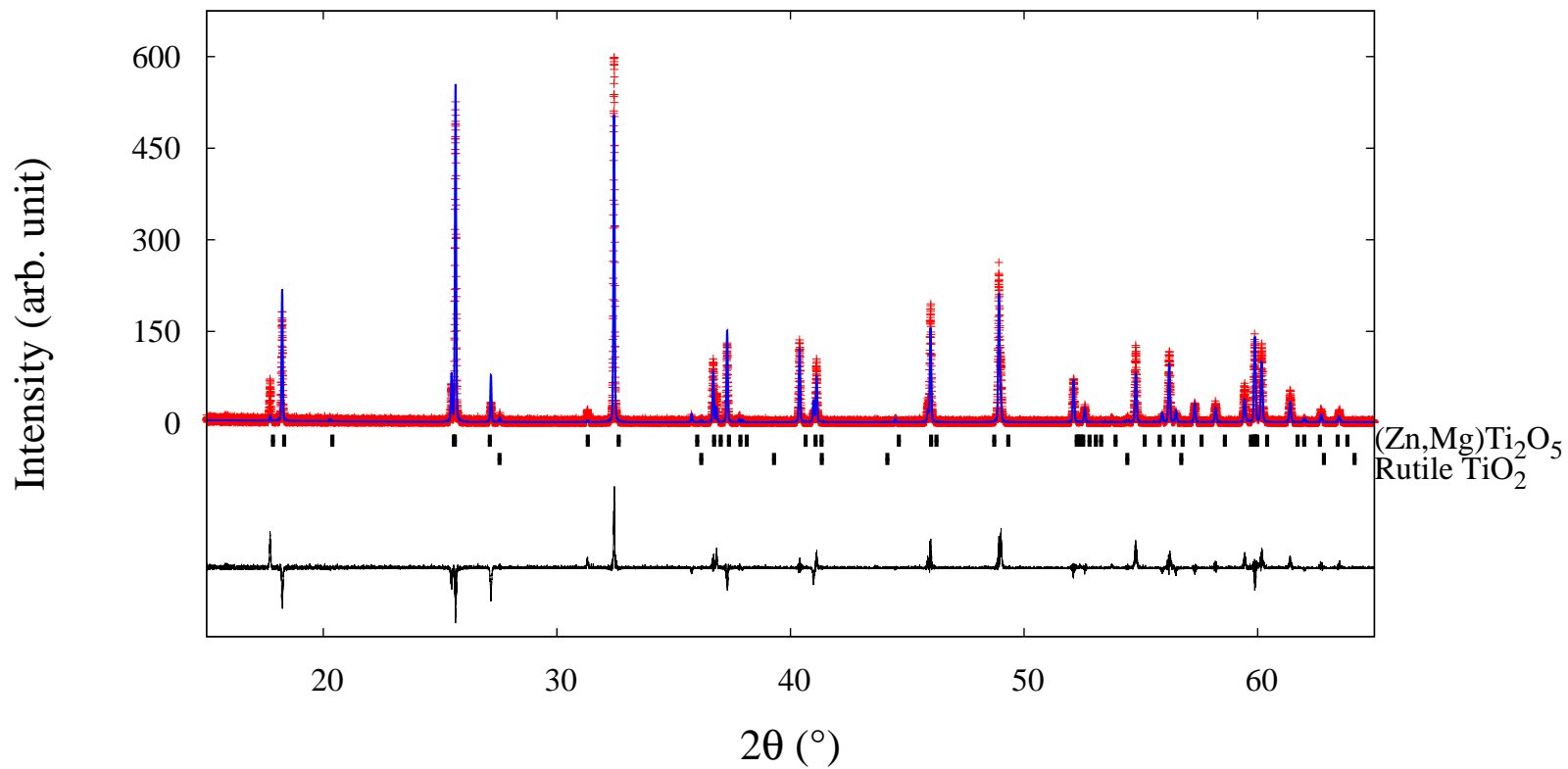


Figure C.7: Rietveld refinement results of X-ray diffraction for  $\text{Zn}_x\text{Mg}_{1-x}\text{Ti}_2\text{O}_5$  with  $x = 0.6$ , which had a synthesis temperature of 1473 K. Observed (red crosses) and calculated data (blue curve), a difference curve (bottom black curve) and reflection positions of the crystalline phases (black tickmarks) are shown.

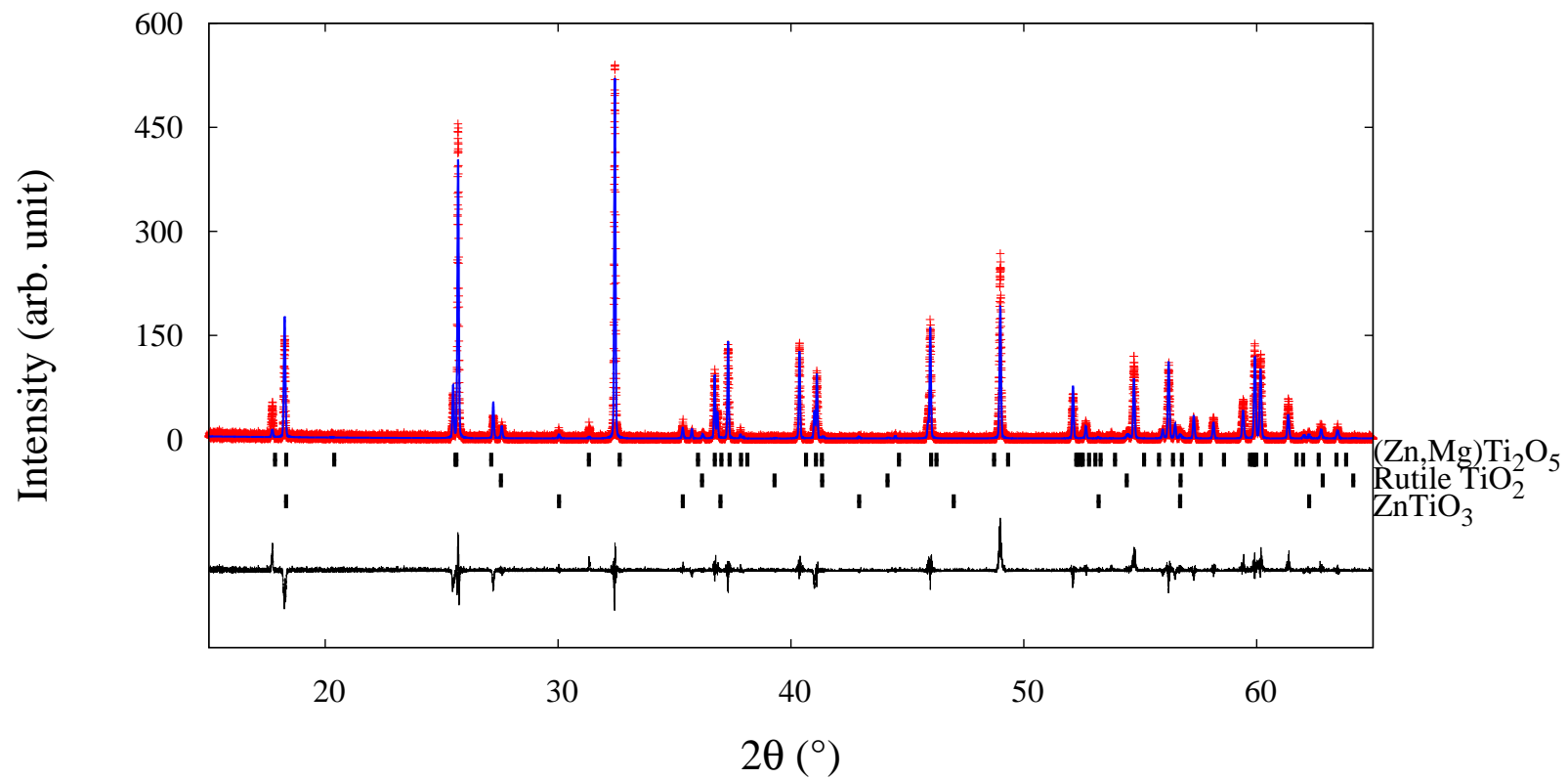


Figure C.8: Rietveld refinement results of X-ray diffraction for  $\text{Zn}_x\text{Mg}_{1-x}\text{Ti}_2\text{O}_5$  with  $x = 0.7$ , which had a synthesis temperature of 1473 K. Observed (red crosses) and calculated data (blue curve), a difference curve (bottom black curve) and reflection positions of the crystalline phases (black tickmarks) are shown.

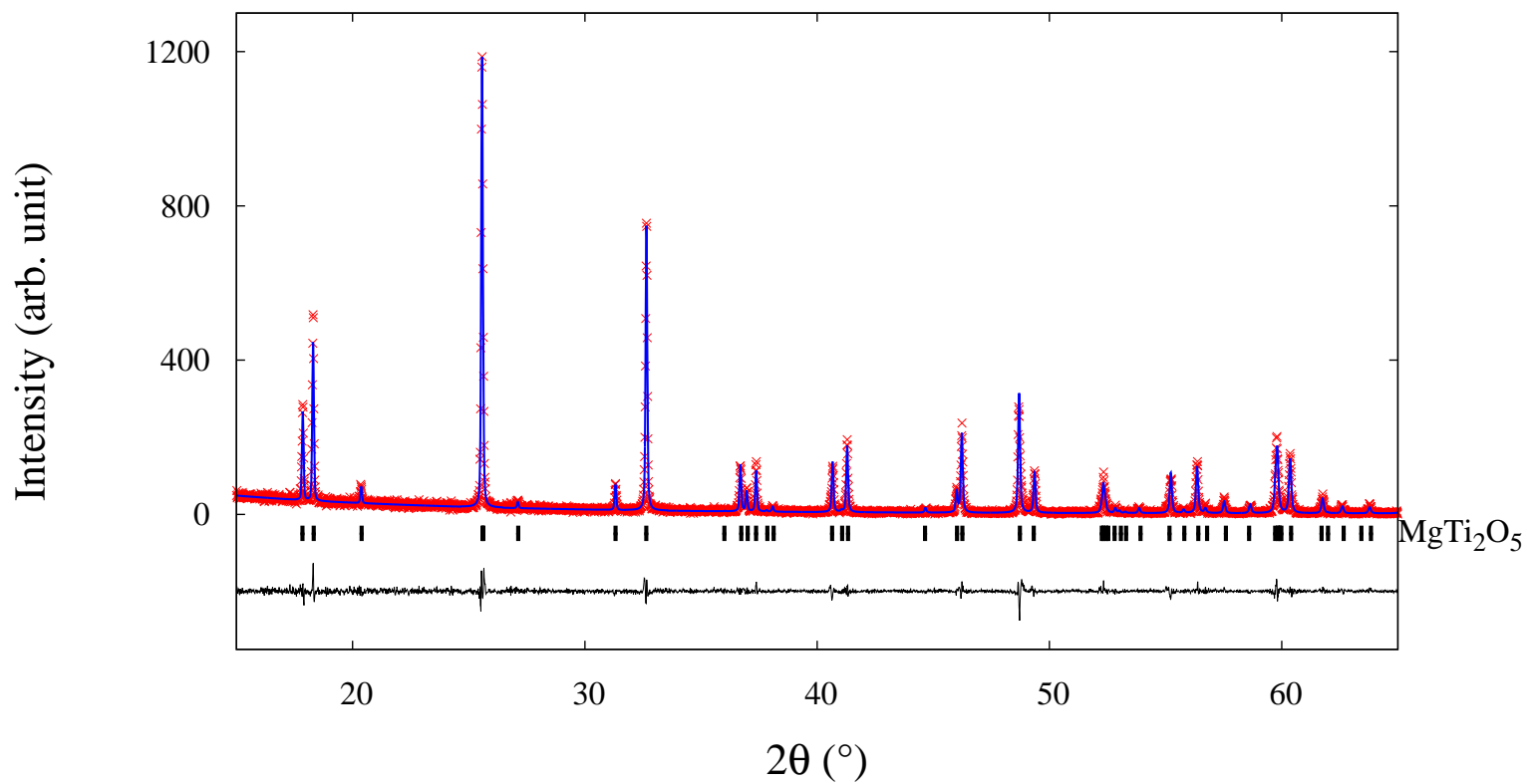


Figure C.9: Rietveld refinement results of X-ray diffraction for  $\text{Cu}_x\text{Mg}_{1-x}\text{Ti}_2\text{O}_5$  with  $x=0$ , which had a synthesis temperature of 1273 K. Observed (red crosses) and calculated data (blue curve), a difference curve (bottom black curve) and reflection positions of the crystalline phase (black tickmarks) are shown.

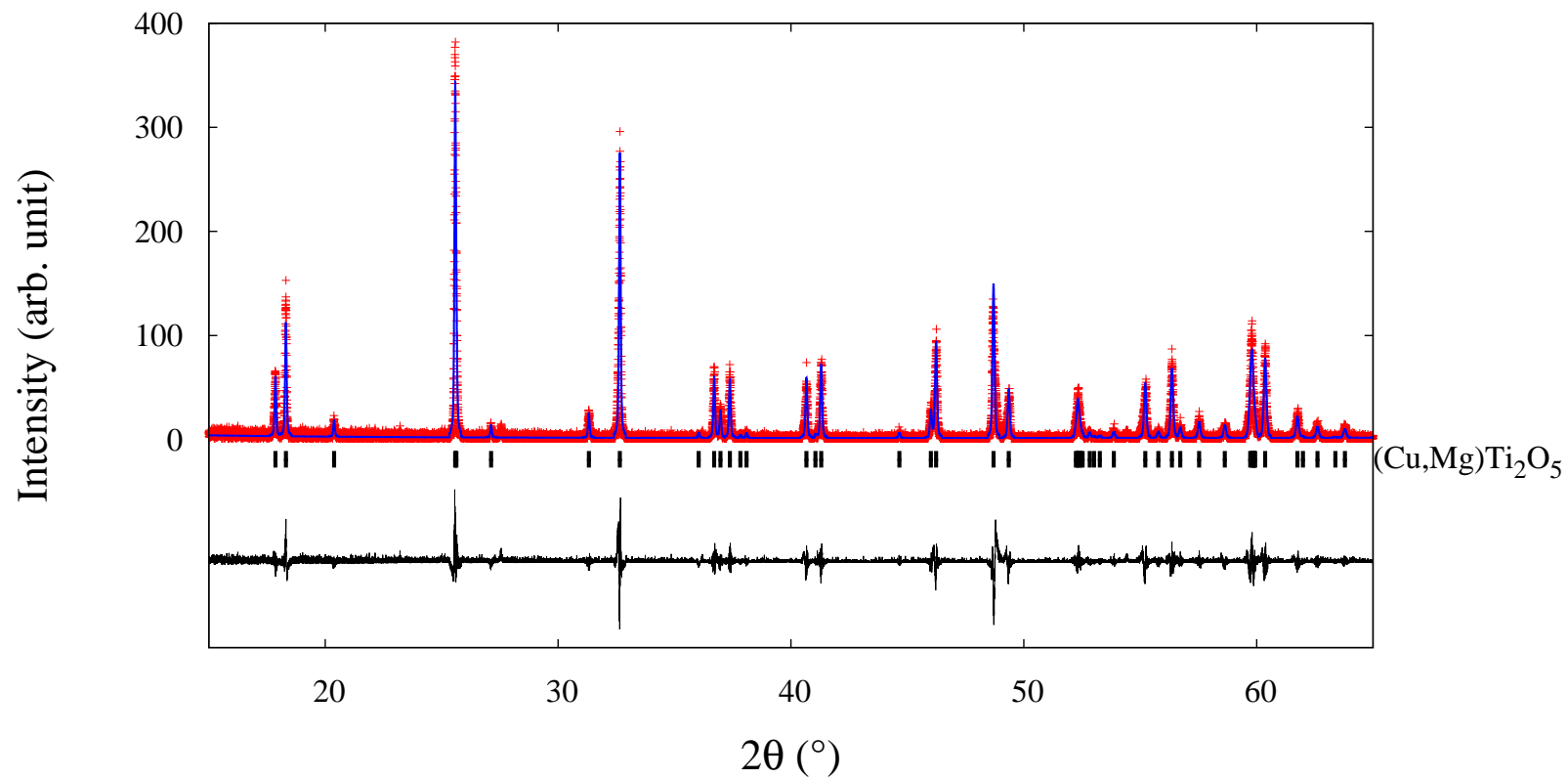


Figure C.10: Le Bail refinement results of X-ray diffraction for  $\text{Cu}_x\text{Mg}_{1-x}\text{Ti}_2\text{O}_5$  with  $x = 0.1$ , which had a synthesis temperature of 1273 K. Observed (red crosses) and calculated data (blue curve), a difference curve (bottom black curve) and reflection positions of the crystalline phase (black tickmarks) are shown.

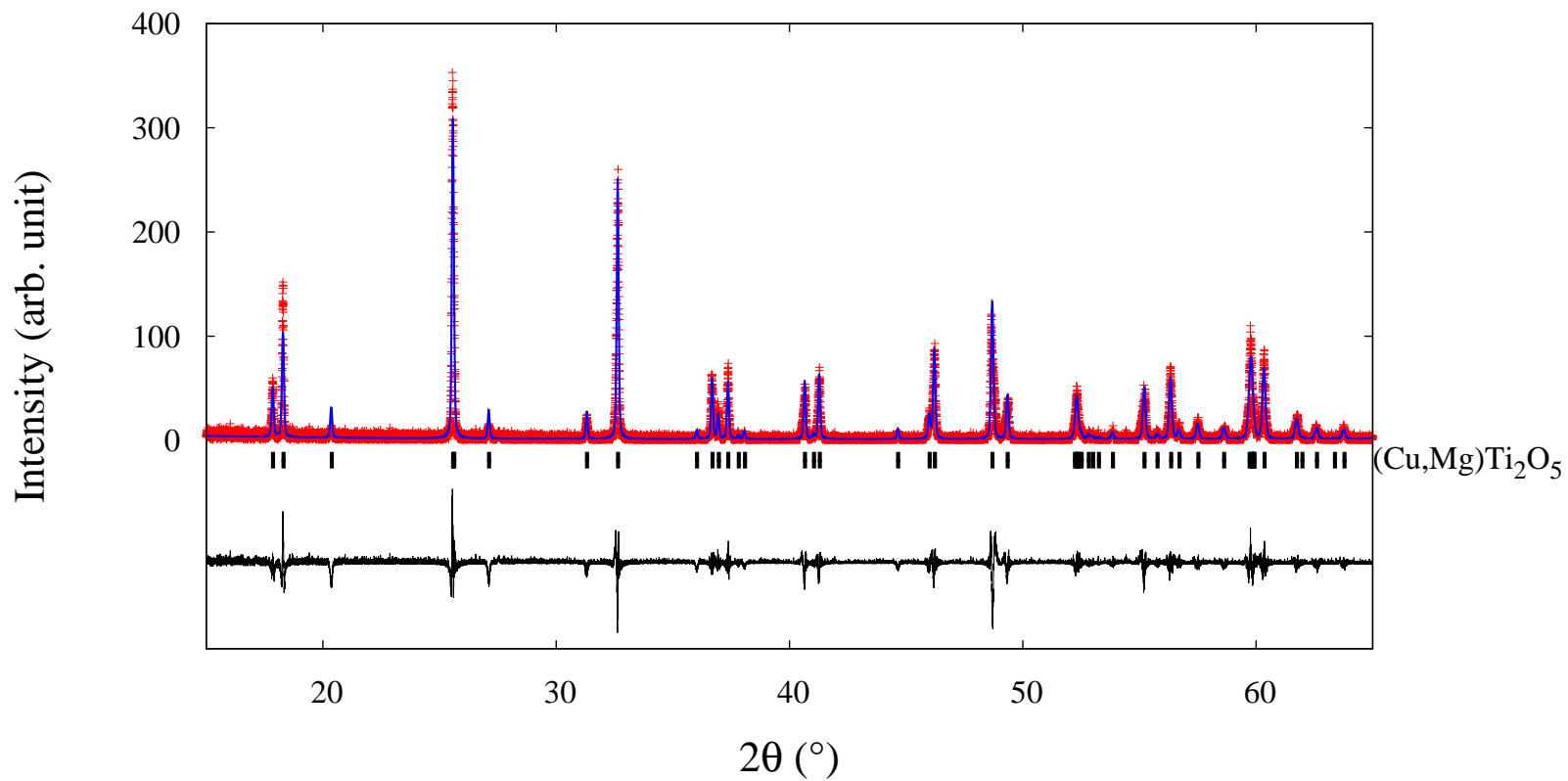


Figure C.11: Le Bail refinement results of X-ray diffraction for  $\text{Cu}_x\text{Mg}_{1-x}\text{Ti}_2\text{O}_5$  with  $x = 0.2$ , which had a synthesis temperature of 1273 K. Observed (red crosses) and calculated data (blue curve), a difference curve (bottom black curve) and reflection positions of the crystalline phase (black tickmarks) are shown.

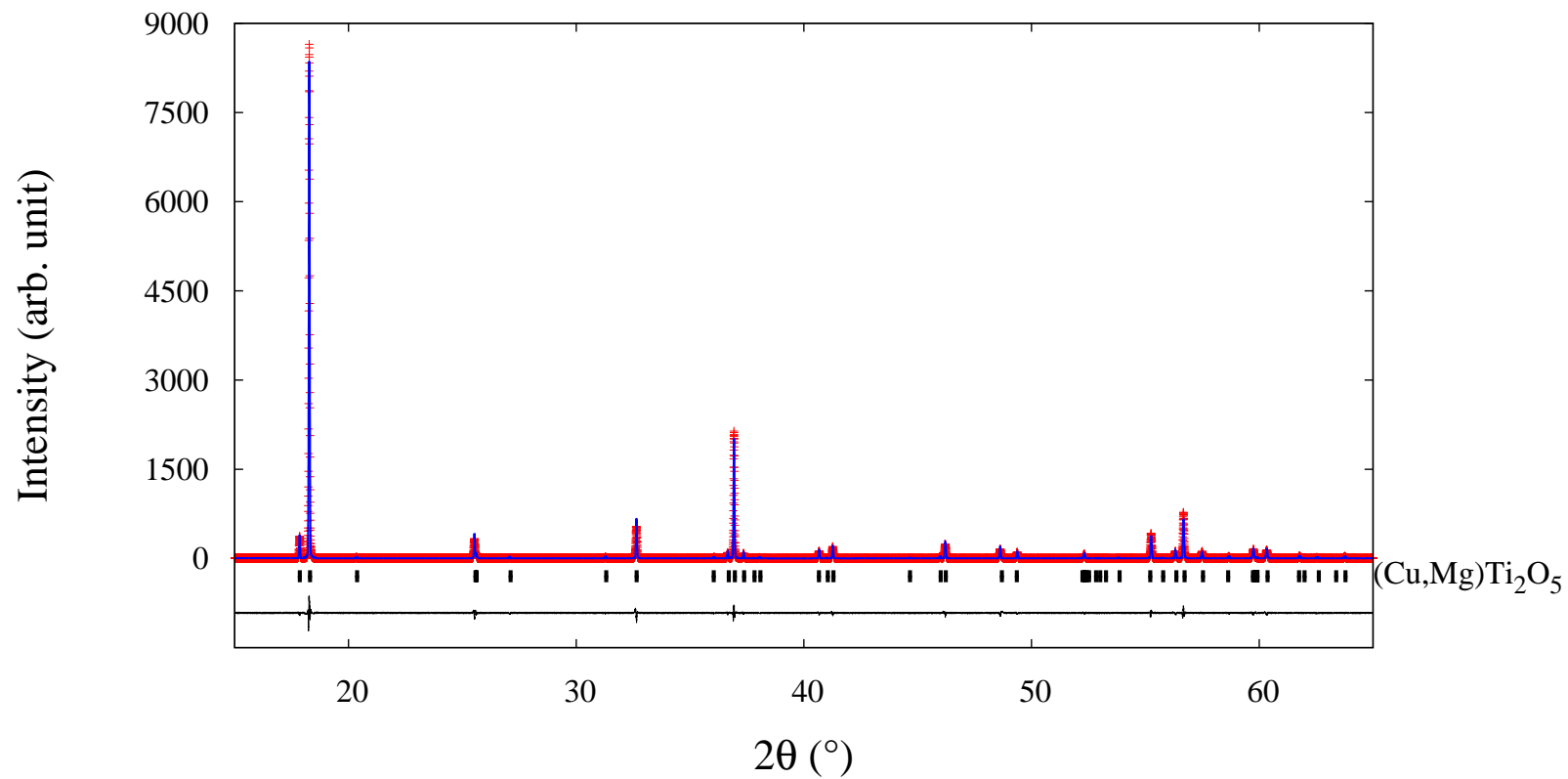


Figure C.12: Le Bail refinement results of X-ray diffraction for  $\text{Cu}_x\text{Mg}_{1-x}\text{Ti}_2\text{O}_5$  with  $x = 0.3$ , which had a synthesis temperature of 1273 K. Observed (red crosses) and calculated data (blue curve), a difference curve (bottom black curve) and reflection positions of the crystalline phase (black tickmarks) are shown.

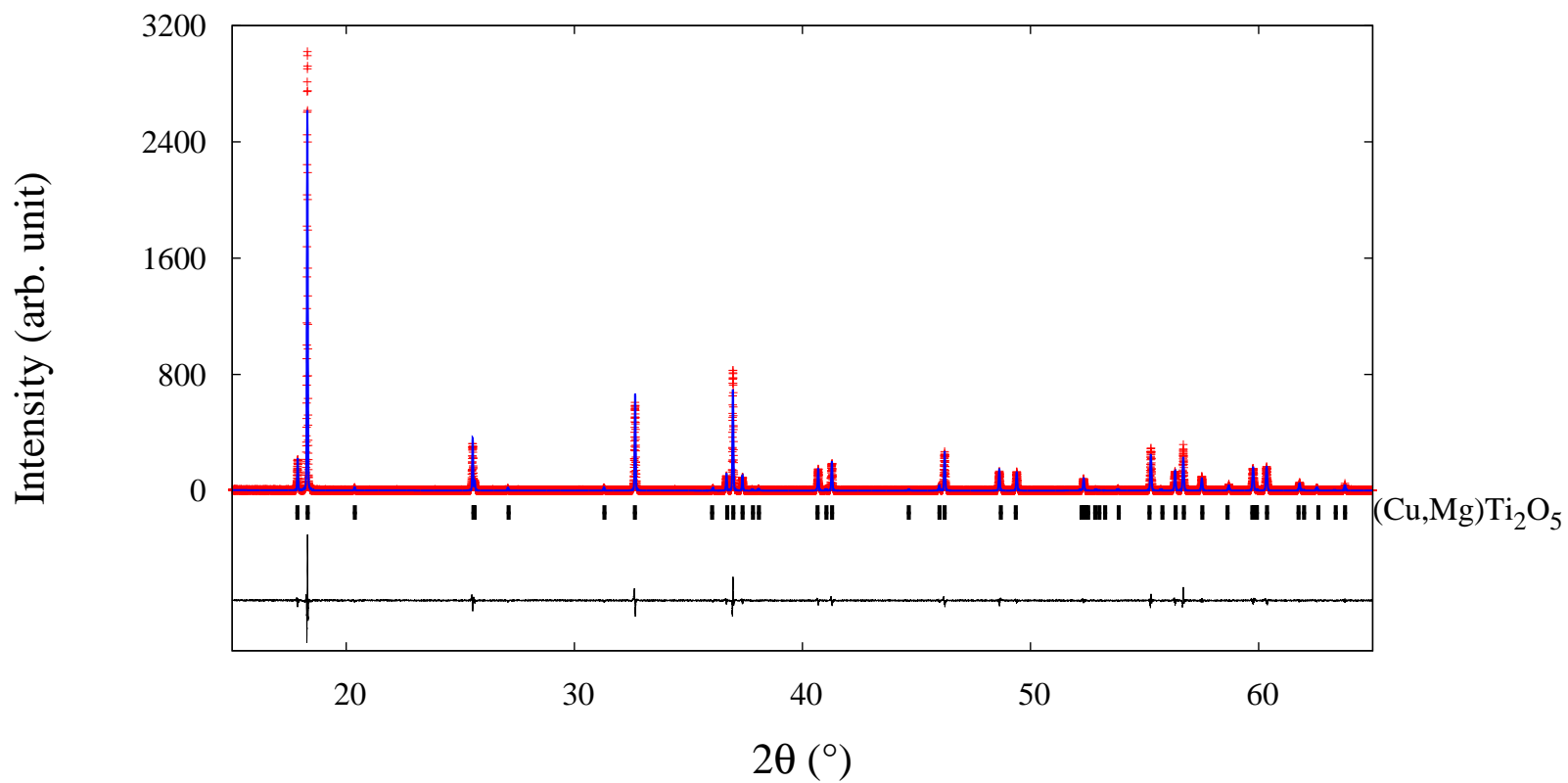


Figure C.13: Le Bail refinement results of X-ray diffraction for  $\text{Cu}_x\text{Mg}_{1-x}\text{Ti}_2\text{O}_5$  with  $x=0.4$ , which had a synthesis temperature of 1273 K. Observed (red crosses) and calculated data (blue curve), a difference curve (bottom black curve) and reflection positions of the crystalline phase (black tickmarks) are shown.



## References

- [1] R. J. Hill, J. R. Craig, and G. V. Gibbs. Systematics of the spinel structure type. *Physics and Chemistry of Minerals*, 4(4):317–339, 1979.
- [2] K. E. Sickafus, J. M. Wills, and N. W. Grimes. Structure of spinel. *Journal of the American Ceramic Society*, 82(12):3279–3292, 1999.
- [3] X.-W. Zhang and A. Zunger. Diagrammatic separation of different crystal structures of  $A_2BX_4$  compounds without energy minimization: A pseudopotential orbital radii approach. *Advanced Functional Materials*, 20(12):1944–1952, 2010.
- [4] C. Biagioni and M. Pasero. The systematics of the spinel-type minerals: An overview. *American Mineralogist*, 99(7):1254–1264, 2014.
- [5] H. D. Lutz and H.-J. Steiner. Phase diagrams of the systems  $\text{Li}_2\text{ZnCl}_4$ – $\text{Na}_2\text{ZnCl}_4$  and  $\text{Li}_2\text{ZnCl}_4$ – $\text{Li}_2\text{MnCl}_4$ . The spinel-olivine phase transition of  $\text{Li}_2\text{ZnCl}_4$ . *Thermochimica Acta*, 211:189–197, 1992.
- [6] I. Solinas and H. D. Lutz. Nonceramic preparation techniques for ternary halides  $AB_2X_4$  with  $A = \text{Mg, Mn, Zn}$ ;  $B = \text{Li, Na}$ ;  $X = \text{Cl, Br}$ . *Journal of Solid State Chemistry*, 117(1):34–38, 1995.
- [7] J. Kohl, S. Nakhal, N. Ferro, P. Bottke, M. Wilkening, T. Bredow, P. Heitjans, and M. Lerch. Low-temperature synthesis, characterization, and stability of spinel-type  $\text{Li}_2\text{NiF}_4$  and solid-solutions  $\text{Li}_2\text{Ni}_{1-x}\text{Co}_x\text{F}_4$ . *Zeitschrift für anorganische und allgemeine Chemie*, 639(2):326–333, 2013.
- [8] I. Lindqvist. Crystal structure studies on anhydrous sodium molybdates and tungstates. *Acta Chemica Scandinavica*, 4:1066–1074, 1950.
- [9] A. D. Fortes. Crystal structures of spinel-type  $\text{Na}_2\text{MoO}_4$  and  $\text{Na}_2\text{WO}_4$  revisited using neutron powder diffraction. *Acta Crystallographica Section E*, 71(6):592–596, 2015.
- [10] H. St. C. O'Neill and A. Navrotsky. Simple spinels: crystallographic parameters, cation radii, lattice energies, and cation distribution. *American Mineralogist*, 68(1–2):181–194, 1983.
- [11] I. N. S. Jackson, R. C. Liebermann, and A. E. Ringwood. Disproportionation of spinels to mixed oxides: significance of cation configuration and implications for the mantle. *Earth and Planetary Science Letters*, 24(2):203–208, 1974.
- [12] J. Gittins, J. J. Fawcett, J. C. Rucklidge, and C. K. Brooks. An occurrence of the spinel end-member  $\text{Mg}_2\text{TiO}_4$  and related spinel solid solutions. *Mineralogical Magazine*, 45(337):135–137, 1982.

- [13] R. M. Hazen. Comparative compressibilities of silicate spinels: Anomalous behavior of  $(\text{Mg,Fe})_2\text{SiO}_4$ . *Science*, 259(5092):206–209, 1993.
- [14] R. M. Hazen, R. T. Downs, L. W. Finger, and J.-D. Ko. Crystal chemistry of ferromagnesian silicate spinels: evidence for Mg-Si disorder. *American Mineralogist*, 78(11–12):1320–1323, 1993.
- [15] Y.-G. Yu, V. L. Vinograd, B. Winkler, and R. M. Wentzcovitch. Phase equilibria of  $(\text{Mg,Fe})_2\text{SiO}_4$  at the earth's upper mantle conditions from first-principles studies. *Physics of the Earth and Planetary Interiors*, 217:36–47, 2013.
- [16] B. A. Wechsler and R. B. Von Dreele. Structure refinements of  $\text{Mg}_2\text{TiO}_4$ ,  $\text{MgTiO}_3$  and  $\text{MgTi}_2\text{O}_5$  by time-of-flight neutron powder diffraction. *Acta Crystallographica Section B*, 45(6):542–549, 1989.
- [17] H. St. C. O'Neill, S. A. T. Redfern, S. Kesson, and S. Short. An in situ neutron diffraction study of cation disordering in synthetic qandilite  $\text{Mg}_2\text{TiO}_4$  at high temperatures. *American Mineralogist*, 88(5–6):860–865, 2003.
- [18] R. M. Hazen and H.-X. Yang. Effects of cation substitution and order-disorder on  $P - V - T$  equations of state of cubic spinels. *American Mineralogist*, 84(11–12):1956–1960, 1999.
- [19] J. R. Smyth, S. D. Jacobsen, and R. M. Hazen. Comparative crystal chemistry of dense oxide minerals. In R. M. Hazen and R. T. Downs, editors, *High-temperature and high-pressure crystal chemistry*, volume 41, chapter 6, pages 157–186. 2000.
- [20] R. W. Grimes, A. B. Anderson, and A. H. Heuer. Predictions of cation distributions in  $AB_2O_4$  spinels from normalized ion energies. *Journal of the American Chemical Society*, 111(1):1–7, 1989.
- [21] A. Navrotsky and O. J. Kleppa. Thermodynamics of formation of simple spinels. *Journal of Inorganic and Nuclear Chemistry*, 30:479–498, 1968.
- [22] G. Bayer. Thermal expansion characteristics and stability of pseudobrookite-type compounds,  $\text{Me}_3\text{O}_5$ . *Journal of the Less Common Metals*, 24(2):129–138, 1971.
- [23] A. M. Pendás, A. Costales, M. A. Blanco, J. M. Recio, and V. Luaña. Local compressibilities in crystals. *Physical Review B*, 62:13970–13978, 2000.
- [24] L. W. Finger, R. M. Hazen, and A. M. Hofmeister. High-pressure crystal chemistry of spinel ( $\text{MgAl}_2\text{O}_4$ ) and magnetite ( $\text{Fe}_3\text{O}_4$ ): Comparisons with silicate spinels. *Physics and Chemistry of Minerals*, 13(4):215–220, 1986.
- [25] I. K. Sedler, A. Feenstra, and T. Peters. An X-ray powder diffraction study of synthetic  $(\text{Fe,Mn})_2\text{TiO}_4$  spinel. *European Journal of Mineralogy*, 6(6):873–886, 11 1994.
- [26] Y. Ishikawa, S. Sato, and Y. Syono. Neutron and magnetic studies of a single crystal of  $\text{Fe}_2\text{TiO}_4$ . *Journal of the Physical Society of Japan*, 31(2):452–460, 1971.

- [27] S. Ogawa and S. Waki. Specific heat of  $\text{Co}_2\text{TiO}_4$  and its anomaly associated with magnetic transition. *Journal of the Physical Society of Japan*, 20(4):540–545, 1965.
- [28] J. Hubsch and G. Gavoille. Semi-spin-glass behavior in the  $\text{Co}_2\text{TiO}_4$  compound. *Physical Review B*, 26:3815–3823, 1982.
- [29] W. Schäfer, E. Jansen, and G. Will. Angle-dispersive time-of-flight diffraction in a pulsed beam: an efficient technology to exploit the thermal-neutron spectrum – design of a JULIOS diffractometer and experimental tests. *Journal of Applied Crystallography*, 26(5):660–669, 1993.
- [30] U. Steinike and B. Wallis. Formation and structure of Ti-Zn-oxides. *Crystal Research and Technology*, 32(1):187–193, 1997.
- [31] R. B. Von Dreele, A. Navrotsky, and A. L. Bowman. Refinement of the crystal structure of  $\text{Mg}_2\text{GeO}_4$  spinel. *Acta Crystallographica Section B*, 33(7):2287–2288, 1977.
- [32] M. D. Welch, M. A. Cooper, and F. C. Hawthorne. The crystal structure of brunoegerite,  $\text{Fe}_2\text{GeO}_4$  spinel. *Mineralogical Magazine*, 65(3):441–444, 2001.
- [33] H. Satomura, K. Tsushima, and K. Uematsu. Crystal growth of cobalt germanate  $\text{Co}_2\text{GeO}_4$ . *Journal of Crystal Growth*, 39(2):241–242, 1977.
- [34] K. Hirota, T. Inoue, N. Mochida, and A. Ohtsuka. Study of germanium spinels (part 3). *Journal of the Ceramic Society of Japan*, 98(1141), 1990.
- [35] J. K. Srivastava, J. A. Kulkarni, S. Ramakrishnan, S. Singh, V. R. Marathe, G. Chandra, V. S. Darshane, and R. Vijayaraghavan. The spin glass behaviour of disordered spinel ferrite  $\text{Co}_2\text{TiO}_4$ . *Journal of Physics C: Solid State Physics*, 20(14):2139, 1987.
- [36] J. K. Burdett, G. D. Price, and S. L. Price. Role of the crystal-field theory in determining the structures of spinels. *Journal of the American Chemical Society*, 104(1): 92–95, 1982.
- [37] A. N. Cormack, G. V. Lewis, S. C. Parker, and C. R. A. Catlow. On the cation distribution of spinels. *Journal of Physics and Chemistry of Solids*, 49(1):53–57, 1988.
- [38] V. Šepelák, A. Düvel, M. Wilkening, K.-D. Becker, and P. Heitjans. Mechanochemical reactions and syntheses of oxides. *Chemical Society Reviews*, 42:7507–7520, 2013.
- [39] S. K. Manik, P. Bose, and S. K. Pradhan. Microstructure characterization and phase transformation kinetics of ball-milled prepared nanocrystalline  $\text{Zn}_2\text{TiO}_4$  by Rietveld method. *Materials Chemistry and Physics*, 82(3):837–847, 2003.
- [40] T. P. Yadav, N. K. Mukhopadhyay, R. S. Tiwari, and O. N. Srivastava. Synthesis of nanocrystalline  $(\text{Co},\text{Ni})\text{Al}_2\text{O}_4$  spinel powder by mechanical milling of quasicrystalline materials. *Journal of Nanoscience and Nanotechnology*, 7:575–579, 2007.

- [41] T. P. Yadav, N. K. Mukhopadhyay, R. S. Tiwari, and O. N. Srivastava. Low-temperature synthesis of nanocrystalline spinel by mechanical milling and annealing of Al–Ni–Fe decagonal quasicrystals. *Philosophical Magazine*, 88:2227–2236, 2008.
- [42] J. M. Robertson and A. J. Pointon. The cation distribution in nickel ferrite. *Solid State Communications*, 4(6):257–259, 1966.
- [43] K. N. Subramanyam and L. R. Khare. The effect of heat treatment on the lattice parameter of nickel ferrite. *Acta Crystallographica Section B*, 35(1):269, 1979.
- [44] M. Shimada, F. Kanamaru, M. Koizumi, and N. Yamamoto. Preparation of a new Cu-substituted cobaltite spinel:  $\text{CuCo}_2\text{O}_4$ . *Materials Research Bulletin*, 10(7):733–736, 1975.
- [45] M. P. Tare, R. R. Tripathi, S. Sampath, and S. M. Tare. Structural and electrical study of  $\text{ZnCuTiO}_4$ ,  $\text{ZnCuSnO}_4$  and  $\text{ZnCuGeO}_4$  synthesised using metallic copper. *Bulletin of Materials Science*, 13(3):191–195, 1990.
- [46] I. Ganesh. A review on magnesium aluminate ( $\text{MgAl}_2\text{O}_4$ ) spinel: synthesis, processing and applications. *International Materials Reviews*, 58(2):63–112, 2013.
- [47] M. Inagaki, Y. Masuda, C. Shibata, and S. Naka.  $\text{Co}_2\text{TiO}_4$  spinel prepared by alkoxide hydrolysis in an ammonium complex of  $\text{Co}^{2+}$ . *Journal of Inorganic and Nuclear Chemistry*, 36(11):2623–2624, 1974.
- [48] F. Meyer, R. Hempelmann, S. Mathur, and M. Veith. Microemulsion mediated sol-gel synthesis of nano-scaled  $\text{MAl}_2\text{O}_4$  ( $M = \text{Co}, \text{Ni}, \text{Cu}$ ) spinels from single-source heterobimetallic alkoxide precursors. *Journal of Materials Chemistry*, 9:1755–1763, 1999.
- [49] S. Ferdov. Low temperature and autogenous pressure synthesis of spinel-type  $\text{Cu}_2\text{GeO}_4$ . *Materials Letters*, 138:13–15, 2015.
- [50] I. Reimanis and H.-J. Kleebe. A review on the sintering and microstructure development of transparent spinel ( $\text{MgAl}_2\text{O}_4$ ). *Journal of the American Ceramic Society*, 92(7):1472–1480, 2009.
- [51] K. Morita, B.-N. Kim, K. Hiraga, and H. Yoshida. Fabrication of transparent  $\text{MgAl}_2\text{O}_4$  spinel polycrystal by spark plasma sintering processing. *Scripta Materialia*, 58(12):1114–1117, 2008.
- [52] C. F. Windisch Jr., G. J. Exarhos, K. F. Ferris, M. H. Engelhard, and D. C. Stewart. Infrared transparent spinel films with p-type conductivity. *Thin Solid Films*, 398–399:45–52, 2001.
- [53] M. Dekkers, G. Rijnders, and D. H. A. Blank.  $\text{ZnIr}_2\text{O}_4$ , a p-type transparent oxide semiconductor in the class of spinel zinc-d<sup>6</sup>-transition metal oxide. *Applied Physics Letters*, 90(021903), 2007.

- [54] M. Y. Nassar, I. S. Ahmed, and I. Samir. A novel synthetic route for magnesium aluminate ( $\text{MgAl}_2\text{O}_4$ ) nanoparticles using sol-gel auto combustion method and their photocatalytic properties. *Spectrochimica Acta Part A: Molecular and Biomolecular Spectroscopy*, 131:329–334, 2014.
- [55] J. S. Sanghera, G. Villalobos, W. Kim, S. Bayya, and I. D. Aggarwal. Transparent spinel ceramic. *NRL Review*, pages 215–217, 2009.
- [56] H. Mizoguchi, M. Hirano, S. Fujitsu, T. Takeuchi, K. Ueda, and H. Hosono.  $\text{ZnRh}_2\text{O}_4$ : A  $p$ -type semiconducting oxide with a valence band composed of a low spin state of  $\text{Rh}^{3+}$  in a  $4d^6$  configuration. *Applied Physics Letters*, 80(7):1207–1209, 2002.
- [57] H. J. Kim, I. Ch. Song, J. H. Sim, H. Kim, D. Kim, Y. E. Ihm, and W. K. Choo. Electrical and magnetic properties of spinel-type magnetic semiconductor  $\text{ZnCo}_2\text{O}_4$  grown by reactive magnetron sputtering. *Journal of Applied Physics*, 95(11):7387–7389, 2004.
- [58] D. O. Scanlon and G. W. Watson. Band gap anomalies of the  $(\text{ZnM}_2\text{O}_4)$ -O-III ( $M$ -III = Co, Rh, Ir) spinels. *Physical Chemistry Chemical Physics*, 13(20):9667–9675, 2011.
- [59] N. H. Van Maaren, G. M. Schaeffer, and F. K. Lotgering. Superconductivity in sulpho- and selenospinel. *Physics Letters A*, 25(3):238–239, 1967.
- [60] D. C. Johnston, H. Prakash, W. H. Zachariassen, and R. Viswanathan. High temperature superconductivity in the Li-Ti-O ternary system. *Materials Research Bulletin*, 8(7):777–784, 1973.
- [61] E. G. Moshopoulou. Superconductivity in the spinel compound  $\text{LiTi}_2\text{O}_4$ . *Journal of the American Ceramic Society*, 82(12):3317–3320, 1999.
- [62] K. Jin, G. He, X. Zhang, S. Maruyama, S. Yasui, R. Suchoski, J. Shin, Y. Jiang, H.-S. Yu, J. Yuan, L. Shan, F. V. Kusmartsev, R. L. Greene, and I. Takeuchi. Anomalous magnetoresistance in the spinel superconductor  $\text{LiTi}_2\text{O}_4$ . *Nature Communications*, 6:7183, 2015.
- [63] R. N. Shelton, D. C. Johnston, and H. Adrian. Measurement of the pressure dependence of  $T_c$  for superconducting spinel compounds. *Solid State Communications*, 20(11):1077–1080, 1976.
- [64] M. A. Green, M. Dalton, K. Prassides, P. Day, and D. A. Neumann. Lattice vibrations of the superconducting oxide spinels  $(\text{Li,Mg})_{1+x}\text{Ti}_{2-x}\text{O}_4$ . *Journal of Physics: Condensed Matter*, 9(49):10855, 1997.
- [65] G.-H. Cao, H. Kitazawa, H. Suzuki, T. Furubayashi, K. Hirata, and T. Matsumoto. Superconductivity in Zn-doped  $\text{CuIr}_2\text{S}_4$ . *Physica C: Superconductivity*, 341–348(2): 735–736, 2000.

- [66] H.-X. Luo, T. Klimczuk, L. MÜchler, L. Schoop, D. Hirai, M. K. Fuccillo, C. Felser, and R. J. Cava. Superconductivity in the  $\text{Cu}(\text{Ir}_{1-x}\text{Pt}_x)_2\text{Se}_4$  spinel. *Physical Review B*, 87(21):214510, 2013.
- [67] G. Blasse. *Crystal chemistry and some magnetic properties of mixed metal oxides with spinel structure*. Philips Research Laboratory, 1964. Philips Research Reports Supplements Nr. 3.
- [68] S. Thota and M. S. Seehra. Co-existence of ferrimagnetism and spin-glass state in the spinel  $\text{Co}_2\text{SnO}_4$ . *Journal of Applied Physics*, 113(20):203905, 2013.
- [69] S. Thota, V. Narang, S. Nayak, S. Sambasivam, B. C. Choi, T. Sarkar, M. S. Andersson, R. Mathieu, and M. S. Seehra. On the nature of magnetic state in the spinel  $\text{Co}_2\text{SnO}_4$ . *Journal of Physics: Condensed Matter*, 27(16):166001, 2015.
- [70] In Y. Waseda, editor, *Anomalous X-Ray Scattering for Materials Characterization: Atomic-Scale Structure Determination (Springer Tracts in Modern Physics)*. Springer, Berlin, 2002.
- [71] G. Bayer. Thermal expansion of oxide compounds with spinel structure. *Thermochimica Acta*, 3(6):421–426, 1972.
- [72] D. Errandonea.  $\text{AB}_2\text{O}_4$  compounds at high pressures. In F. J. Manjón, I. Tiginyanu, and V. Ursaki, editors, *Pressure-induced phase transitions in  $\text{AB}_2\text{X}_4$  chalcogenide compounds*, volume 189, chapter 2, pages 53–73. 2014.
- [73] F. Nestola, T. Balić-Žunić, M. Koch-Müller, L. Secco, F. Princivalle, F. Parisi, and A. Dal Negro. High-pressure crystal structure investigation of synthetic  $\text{Fe}_2\text{SiO}_4$  spinel. *Mineralogical Magazine*, 75(5):2649–2655, 2011.
- [74] J. F. W. Bowles. Definition and range of composition of naturally occurring minerals with the pseudobrookite structure. *American Mineralogist*, 73:1377–1383, 1988.
- [75] H.-P. Bojar and F. Walter. Fluoro-magnesiostastingsite from Dealul Uroi (Hunedoara county, Romania): Mineral data and crystal structure of a new amphibole end-member. *European Journal of Mineralogy*, 18(4):503–508, 2006.
- [76] V. Stähle and M. Koch. Primary and secondary pseudobrookite minerals in volcanic rocks from the Katzenbuckel Alkaline Complex, southwestern Germany. *Swiss Bulletin of Mineralogy and Petrology*, 83(2):145–158, 2003.
- [77] L. Pauling. The crystal structure of pseudobrookite. *Zeitschrift für Kristallographie*, 73(1–6):97–112, 1930.
- [78] A. T. Anderson, F. R. Boyd, T. E. Bunch, E. N. Cameron, A. El Goresy, L. W. Finger, S. E. Haggerty, O. B. James, K. Keil, M. Prinz, and P. Ramdohr. Armalcolite: A new mineral from the apollo 11 samples. In A. A. Levinson, editor, *Proceedings of the Apollo 11 Lunar Science Conference*, volume 1 of *Geochimica et Cosmochimica Acta Supplement*, pages 55–63. Pergamon Press, 1970.

- [79] D. H. Lindsley, S. E. Kesson, M. J. Hartzman, and M. K. Cushman. The stability of armalcolite: Experimental studies in the system MgO-Fe-Ti-O. In *Lunar and Planetary Science Conference Proceedings*, volume 5, pages 521–534, 1974.
- [80] I. J. Kim. Thermal stability of Al<sub>2</sub>TiO<sub>5</sub> ceramics for new diesel particulate filter applications—a literature review. *Journal of Ceramic Processing Research*, 11(4):411–418, 2010.
- [81] M. Dondi, T. S. Lyubenova, J. B. Carda, and M. Ocaña. M-doped Al<sub>2</sub>TiO<sub>5</sub> (M = Cr, Mn, Co) solid solutions and their use as ceramic pigments. *Journal of the American Ceramic Society*, 92(9):1972–1980, 2009.
- [82] A. Navrotsky. Thermodynamics of formation of some compounds with the pseudobrookite structure and of the FeTi<sub>2</sub>O<sub>5</sub>-Ti<sub>3</sub>O<sub>5</sub> solid solution series. *American Mineralogist*, 60:249–256, 1975.
- [83] D. Xirouchakis, A. Smirnov, K. Woody, D. H. Lindsley, and D. J. Andersen. Thermodynamics and stability of pseudobrookite-type MgTi<sub>2</sub>O<sub>5</sub> (karrooite). *American Mineralogist*, 87(5–6):658–667, 2002.
- [84] R. G. Teller, M. R. Antonio, A. E. Grau, M. Gueguin, and E. Kostiner. Structural analysis of metastable pseudobrookite ferrous titanium oxides with neutron diffraction and mossbauer spectroscopy. *Journal of Solid State Chemistry*, 88(2):334–350, 1990.
- [85] D. M. Xirouchakis. Pseudobrookite-group oxide solutions and basaltic melts. *Lithos*, 95(1–2):1–9, 2007. The role of accessory minerals in rocks: Petrogenetic indicators of metamorphic and igneous processes theme, session VGP8 of the annual European Geosciences Union General Assembly.
- [86] H. Müller-Buschbaum and M. Waburg. Pseudobrookite mit weitgehend geordneter Metallverteilung: CoTi<sub>2</sub>O<sub>5</sub>, MgTi<sub>2</sub>O<sub>5</sub> und FeTi<sub>2</sub>O<sub>5</sub>. *Monatshefte für Chemie / Chemical Monthly*, 114(1):21–25, 1983.
- [87] N. E. Brown and A. Navrotsky. Structural, thermodynamic, and kinetic aspects of disordering in the pseudobrookite-type compound karrooite, MgTi<sub>2</sub>O<sub>5</sub>. *American Mineralogist*, 74:902–912, 1989.
- [88] M. D. Lind and R. M. Housley. Crystallization studies of lunar igneous rocks: crystal structure of synthetic armalcolite. *Science*, 175:521–523, 1972.
- [89] H.-X. Yang and R. M. Hazen. Crystal chemistry of cation order-disorder in pseudobrookite-type MgTi<sub>2</sub>O<sub>5</sub>. *Journal of Solid State Chemistry*, 138(2):238–244, 1998.
- [90] I. E. Grey and J. Ward. An X-ray and Mössbauer study of the FeTi<sub>2</sub>O<sub>5</sub>-Ti<sub>3</sub>O<sub>5</sub>. *Journal of Solid State Chemistry*, 7(3):300–307, 1973.
- [91] I. E. Grey, C. Li, and I. C. Madsen. Phase equilibria and structural studies on the solid solution MgTi<sub>2</sub>O<sub>5</sub>-Ti<sub>3</sub>O<sub>5</sub>. *Journal of Solid State Chemistry*, 113(1):62–73, 1994.

- [92] A. R. Lennie, K. S. Knight, and C. M. B. Henderson. Cation ordering in  $\text{MgTi}_2\text{O}_5$  (karrooite): probing temperature dependent effects with neutrons. *American Mineralogist*, 92:1165–1180, 2007.
- [93] M. S. Ghiorso, H.-X. Yang, and R. M. Hazen. Thermodynamics of cation ordering in karrooite  $\text{MgTi}_2\text{O}_5$ . *American Mineralogist*, 84:1370–1374, 1999.
- [94] R. D. Shannon. Revised effective ionic radii and systematic studies of interatomic distances in halides and chalcogenides. *Acta Crystallographica*, A32:751–767, 1976.
- [95] R. M. Hazen and A. Navrotsky. Effects of pressure on order-disorder reactions. *American Mineralogist*, 81:1021–1035, 1996.
- [96] W.-Q. Guo, S. Malus, D.-H. Ryan, and Z. Altounian. Crystal structure and cation distributions in the  $\text{FeTi}_2\text{O}_5$ – $\text{Fe}_2\text{TiO}_5$  solid solution series. *Journal of Physics: Condensed Matter*, 11(33):6337, 1999.
- [97] R. M. Hazen and H.-X. Yang. Increased compressibility of pseudobrookite-type  $\text{MgTi}_2\text{O}_5$  caused by cation disorder. *Science*, 277(5334):1965–1967, 1997.
- [98] H.-X. Yang and R. M. Hazen. Comparative high-pressure crystal chemistry of karrooite,  $\text{MgTi}_2\text{O}_5$ , with different ordering states. *American Mineralogist*, 84(1–2):130–137, 1999.
- [99] Y. Suzuki and M. Morimoto. Uniformly porous  $\text{MgTi}_2\text{O}_5$  with narrow pore-size distribution: in situ processing, microstructure and thermal expansion behavior. *Journal of the Ceramic Society of Japan*, 118(1384):1212–1216, 2010.
- [100] Y. Suzuki and Y. Shinoda. Magnesium dititanate ( $\text{MgTi}_2\text{O}_5$ ) with pseudobrookite structure: a review. *Science and Technology of Advanced Materials*, 12(3):034301, 2011.
- [101] F. Matteucci, G. Cruciani, M. Dondi, G. Gasparotto, and D. M. Tobaldi. Crystal structure, optical properties and colouring performance of karrooite  $\text{MgTi}_2\text{O}_5$  ceramic pigments. *Journal of Solid State Chemistry*, 180(11):3196–3210, 2007.
- [102] C.-L. Huang and C.-H. Shen. Phase evolution and dielectric properties of  $(\text{Mg}_{0.95}\text{M}_{0.05}^{2+})\text{Ti}_2\text{O}_5$  ( $\text{M}^{2+} = \text{Co}, \text{Ni}, \text{and Zn}$ ) ceramics at microwave frequencies. *Journal of the American Ceramic Society*, 92(2):384–388, 2009.
- [103] M. Llusar, E. Garcia, M. T. Garcia, C. Gargori, J. A. Badenes, and G. Monros. Synthesis, stability and coloring properties of yellow-orange pigments based on Ni-doped karrooite. *Journal of the European Ceramic Society*, 35(1):357–376, 2015.
- [104] P. N. Kapoor, S. Uma, S. Rodriguez, and K. J. Klabunde. Aerogel processing of  $\text{MTi}_2\text{O}_5$  ( $\text{M} = \text{Mg}, \text{Mn}, \text{Fe}, \text{Co}, \text{Zn}, \text{Sn}$ ) compositions using single source precursors: synthesis, characterization and photocatalytic behavior. *Journal of Molecular Catalysis A: Chemical*, 229(1–2):145–150, 2005.



- [105] M. Onoda. Phase transitions of  $\text{Ti}_3\text{O}_5$ . *Journal of Solid State Chemistry*, 136(1): 67–73, 1998.
- [106] G. Hyett, M. A. Green, and I. P. Parkin. The use of combinatorial chemical vapor deposition in the synthesis of  $\text{Ti}_{3-\delta}\text{O}_4\text{N}$  with  $0.06 < \delta < 0.25$ : A titanium oxynitride phase isostructural to Anosovite. *Journal of the American Chemical Society*, 129(50):15541–15548, 2007.
- [107] J. A. Kuszyk and R. C. Brast. Influence of grain size on effects of thermal expansion anisotropy in  $\text{MgTi}_2\text{O}_5$ . *Journal of the American Ceramic Society*, 56(8):420–423, 1973.
- [108] V. Buscaglia, G. Battilana, M. Leoni, and P. Nanni. Decomposition of  $\text{Al}_2\text{TiO}_5$ - $\text{MgTi}_2\text{O}_5$  solid solutions: a thermodynamic approach. *Journal of Materials Science*, 31:5009–5016, 1996.
- [109] H. J. Siebeneck, D. P. H. Hasselman, J. J. Cleveland, and R. C. Bradt. Effects of grain size and microcracking on the thermal diffusivity of  $\text{MgTi}_2\text{O}_5$ . *Journal of the American Ceramic Society*, 60:336–338, 1977.
- [110] B. A. Wechsler and A. Navrotsky. Thermodynamics and structural chemistry of compounds in the system  $\text{MgO-TiO}_2$ . *Journal of Solid State Chemistry*, 55(2):165–180, 1984.
- [111] I. B. De Arenas. Reactive sintering of aluminum titanate. In A. Lakshmanan, editor, *Sintering of Ceramics – New Emerging Techniques*, pages 501–526. 2012.
- [112] M. Dondi, F. Matteucci, G. Cruciani, G. Gasparotto, and D. M. Tobaldi. Pseudobrookite ceramic pigments: Crystal structural, optical and technological properties. *Solid State Sciences*, 9(5):362–369, 2007.
- [113] J. Ruiz-Fuertes, T. Bernert, M. He, B. Winkler, V. L. Vinograd, and V. Milman. Local structure of  $\text{Cu}_x\text{Zn}_{2-x}\text{TiO}_4$  inverse spinel. *Applied Physics Letters*, 105(7): 071911, 2014.
- [114] M. Sopicka-Lizer. *High-energy ball milling: Mechanochemical processing of nanopowders*. Woodhead publishing limited, 2010.
- [115] In C. H. Bamford and C. F. H. Tipper, editors, *Reactions in the Solid State*, volume 22 of *Comprehensive Chemical Kinetics*, pages 1–340. Elsevier, 1980.
- [116] J. Subrahmanyam and M. Vijayakumar. Self-propagating high-temperature synthesis. *Journal of Materials Science*, 27(23):6249–6273, 1992.
- [117] A. G. Merzhanov. 40 Years of SHS: A lucky star of a scientific discovery. Bentham Science Publishers, 2012.
- [118] A. G. Merzhanov. Solid flames: Discoveries, concepts, and horizons of cognition. *Combustion Science and Technology*, 98:307–336, 1994.

- [119] X.-L. Su, F. Fu, Y.-G. Yan, G. Zheng, T. Liang, Q. Zhang, X. Cheng, D.-W. Yang, H. Chi, X.-F. Tang, Q.-J. Zhang, and C. Uher. Self-propagating high-temperature synthesis for compound thermoelectrics and new criterion for combustion processing. *Nature Communications*, 5(4908), 2014.
- [120] H. M. Rietveld. Line profiles of neutron powder-diffraction peaks for structure refinement. *Acta Crystallographica*, 22:151–152, 1967.
- [121] H. M. Rietveld. A profile refinement method for nuclear and magnetic structures. *Journal of Applied Crystallography*, 2(2):65–71, 1969.
- [122] A. Larson and R. B. Von Dreele. GSAS, 2004.
- [123] B. H. Toby. EXPGUI, a graphical user interface for GSAS. *Journal of Applied Crystallography*, 34:210–213, 2001.
- [124] S. C. Vogel. gsaslanguage: a GSAS script language for automated Rietveld refinements of diffraction data. *Journal of Applied Crystallography*, 44:873–877, 2011.
- [125] W. L. Bragg. The diffraction of short electromagnetic waves by a crystal. In *Proceedings of the Cambridge Philosophical Society*, volume 17, pages 43–57, 1913.
- [126] M. Hoelzel and A. Senyshyn. High-resolution powder diffractometer. In T. Brückel, G. Heger, D. Richter, G. Roth, and R. Zorn, editors, *Neutron Scattering: Experiment Manuals of the JCNS Laboratory Course*. Forschungszentrum Jülich, 2014.
- [127] P. J. Brown, A. G. Fox, E. N. Maslen, M. A. O’Keefe, and B. T. M. Willis. Intensity of diffracted intensities. In *International Tables for Crystallography*, volume C of *Lunar and Planetary Science Conference Proceedings*, pages 554–595, 2006.
- [128] V. F. Sears. Neutron scattering lengths and cross sections. *Neutron News*, 3(3): 26–37, 1992.
- [129] E. Suard and L. Gendrin. Description of the D2B – High-resolution two-axis diffractometer. <http://www.ill.eu/instruments-support/instruments-groups/instruments/d2b>.
- [130] In R. A. Young, editor, *The Rietveld Method*. Oxford University Press, New York, 1993.
- [131] A. Le Bail, H. Duroy, and J. L. Fourquet. Ab-initio structure determination of  $\text{LiSbWO}_6$  by X-ray powder diffraction. *Materials Research Bulletin*, 23(3):447–452, 1988.
- [132] C. V. Raman and K. S. Krishnan. A new type of secondary radiation. *Nature*, 121: 501–502, 1928.
- [133] J. R. Ferraro, K. Nakamoto, and C. W. Brown. Basic theory. In *Introductory Raman Spectroscopy*, chapter 1, pages 1–94. Academic Press, San Diego, second edition edition, 2003.

- [134] J. R. Ferraro, K. Nakamoto, and C. W. Brown. In *Introductory Raman Spectroscopy*. Academic Press, San Diego, second edition edition, 2003.
- [135] N. Colthup, L. H. Daly, and S. E. Wiberley. In *Introduction to Infrared and Raman Spectroscopy*. Academic Press, San Diego, second edition edition, 1975.
- [136] T. Tsuji. *Heat capacity of solids*, chapter 5. John Wiley and Sons, Ltd, 2010.
- [137] Quantum Design. <http://www.qdusa.com/>.
- [138] K. Capelle. A bird's-eye view of density-functional theory. *Brazilian Journal of Physics*, 36:1318–1343, 2006.
- [139] B. Winkler and V. Milman. Density functional theory based calculations for high pressure research. *Zeitschrift für Kristallographie*, 229(2):112–122, 2014.
- [140] S. J. Clark, M. D. Segall, C. J. Pickard, P. J. Hasnip, M. J. Probert, K. Refson, and M. C. Payne. First principles methods using CASTEP. *Zeitschrift für Kristallographie*, 220:567–570, 2005.
- [141] J. P. Perdew, K. Burke, and M. Ernzerhof. Generalized gradient approximation made simple. *Physical Review Letters*, 77:3865–3868, 1996.
- [142] D. Arbeck, E. Haussühl, L. Bayarjagal, B. Winkler, N. Paulsen, S. Haussühl, and V. Milman. Piezoelectric properties of retgersite determined by ultrasonic measurements. *The European Physical Journal B*, 73(2):167–175, 2010.
- [143] A. Thust, Y. Arinicheva, E. Haussühl, J. Ruiz-Fuertes, L. Bayarjagal, S. C. Vogel, S. Neumeier, and B. Winkler. Physical properties of  $\text{La}_{1-x}\text{Eu}_x\text{PO}_4$ ,  $0 \leq x \leq 1$ , monazite-type ceramics. *Journal of the American Ceramic Society*, 98(12):4016–4021, 2015.
- [144] R. K. Datta and R. Roy. Stability of  $\text{Ni}_2\text{TiO}_4$ . *Zeitschrift für Kristallographie*, 121:410–417, 1965.
- [145] R.-Y. Chen, M. Knapp, M. Yavuz, S.-H. Ren, R. Witte, R. Heinzmann, H. Hahn, H. Ehrenberg, and S. Indris. Nanoscale spinel  $\text{LiFeTiO}_4$  for intercalation pseudo-capacitive  $\text{Li}^+$  storage. *Physical Chemistry Chemical Physics*, 17:1482–1488, 2015.
- [146] A. C. Chaves, S. J. G. Lima, R. C. M. U. Araújo, M. A. M. A. Maurera, E. Longo, P. S. Pizani, L. G. P. Simões, L. E. B. Soledade, A. G. Souza, and I. M. G. Dos Santos. Photoluminescence in disordered  $\text{Zn}_2\text{TiO}_4$ . *Journal of Solid State Chemistry*, 179(4):985–992, 2006.
- [147] T. Esaka, T. Ikebe, and M. Kamata. Formation of oxide ion conductive phase in the substituted oxide system based on  $\text{Zn}_2\text{TiO}_4$ . *Solid State Ionics*, 76(3–4):237–242, 1995.
- [148] A. Navrotsky and A. Muan. Phase equilibria and thermodynamic properties of solid solutions in the systems  $\text{ZnO-CoO-TiO}_2$  and  $\text{ZnO-NiO-TiO}_2$  at 1050 °C. *Journal of Inorganic and Nuclear Chemistry*, 32(11):3471–3484, 1970.

- [149] A. Le Nestour, M. Gaudon, G. Villeneuve, R. Andriessen, and A. Demourgues. Steric and electronic effects relating to the  $\text{Cu}^{2+}$  Jahn-Teller distortion in  $\text{Zn}_{1-x}\text{Cu}_x\text{Al}_2\text{O}_4$  spinels. *Inorganic Chemistry*, 46(7):2645–2658, 2007.
- [150] R. L. Millard, R. C. Peterson, and B. K. Hunter. Study of the cubic to tetragonal transition in  $\text{Mg}_2\text{TiO}_4$  and  $\text{Zn}_2\text{TiO}_4$  spinels by  $^{17}\text{O}$  MAS NMR and Rietveld refinement of X-ray diffraction data. *American Mineralogist*, 80:885–896, 1995.
- [151] Arillo, M. A. and López, M. L. and Pico, C. and Veiga, M. L. and Jiménez-López, A. and Rodríguez-Castellón, E. Surface characterisation of spinels with ti(IV) distributed in tetrahedral and octahedral sites. *Journal of Alloys and Compounds*, 317–318:160–163, 2001.
- [152] F. Bosi, U. Hålenius, G. B. Andreozzi, H. Skogby, and S. Lucchesi. Structural refinement and crystal chemistry of Mn-doped spinel: A case for tetrahedrally coordinated  $\text{Mn}^{3+}$  in an oxygen-based structure. *American Mineralogist*, 92(1): 27–33, 2007.
- [153] R. A. Fregola, F. Bosi, H. Skogby, and U. Hålenius. Cation ordering over short-range and long-range scales in the  $\text{MgAl}_2\text{O}_4$ – $\text{CuAl}_2\text{O}_4$  series. *American Mineralogist*, 97(11–12):1821–1827, 2012.
- [154] P. Patureau, M. Josse, R. Dessapt, J.-Y. Mevellec, F. Porcher, M. Maglione, P. Deniard, and C. Payen. Incorporation of Jahn-Teller  $\text{Cu}^{2+}$  ions into magnetoelectric multiferroic  $\text{MnWO}_4$ : structural, magnetic, and dielectric permittivity properties of  $\text{Mn}_{1-x}\text{Cu}_x\text{WO}_4$  ( $x \leq 0.25$ ). *Inorganic Chemistry*, 54(22):10623–10631, 2015.
- [155] M. Pavlov, Per E. M. Siegbahn, and M. Sandström. Hydration of beryllium, magnesium, calcium, and zinc ions using density functional theory. *The Journal of Physical Chemistry A*, 102(1):219–228, 1998.
- [156] Yu. V. Yablokov and T. A. Ivanova. The labile magnetic structure of JT copper and nickel complexes in the layered oxides. *Coordination Chemistry Reviews*, 190–192: 1255–1267, 1999.
- [157] S. Ghabezloo. Micromechanical analysis of the effect of porosity on the thermal expansion coefficient of heterogeneous porous materials. *International Journal of Rock Mechanics and Mining Sciences*, 55:97–101, 2012.
- [158] Q. Zeng, K. F. Li, T. Fen-Chong, and P. Dangla. Effect of porosity on thermal expansion coefficient of cement pastes and mortars. *Construction and Building Materials*, 28(1):468–475, 2012.
- [159] J. L. Hayob and E. J. Essene. Armalcolite in crustal paragneiss xenoliths, central Mexico. *American Mineralogist*, 80:810–822, 1995.
- [160] S. Klemme, D. Günther, K. Hametner, S. Prowatke, and T. Zack. The partitioning of trace elements between ilmenite, ulvospinel, armalcolite and silicate melts with implications for the early differentiation of the moon. *Chemical Geology*, 234: 251–263, 2006.

- [161] M. A. Reddy, M. S. Kishore, V. Pralong, V. Caignaert, U. V. Varadaraju, and B. Raveau. Synthesis and lithium insertion into nanophase  $\text{MgTi}_2\text{O}_5$  with pseudo-brookite structure. *Chemistry of Materials*, 20(6):2192–2197, 2008.
- [162] Y. Qu, W. Zhou, Y. Xie, L. Jiang, J.-Q. Wang, G.-H. Tian, Z.-Y. Ren, C.-G. Tian, and H.-G. Fu. A novel phase-mixed  $\text{MgTiO}_3$ - $\text{MgTi}_2\text{O}_5$  heterogeneous nanorod for high efficiency photocatalytic hydrogen production. *Chemical Communications*, 49:8510–8512, 2013.
- [163] Y. Suzuki, T. S. Suzuki, Y. Shinoda, and K. Yoshida. Uniformly porous  $\text{MgTi}_2\text{O}_5$  with narrow pore-size distribution: XAFS study, improved in situ synthesis, and new in situ surface coating. *Advanced Engineering Materials*, 14(12):1134–1138, 2012.
- [164] M. V. Reddy, G. V. Subba Rao, and B. V. R. Chowdari. Metal oxides and oxysalts as anode materials for Li ion batteries. *Chemical Reviews*, 113(7):5364–5457, 2013.
- [165] F.-X. Xie, Y.-F. Deng, Y. Xie, H.-J. Xu, and G.-H. Chen. Ultra-small nanoparticles of  $\text{MgTi}_2\text{O}_5$  embedded in carbon rods with superior rate performance for sodium ion batteries. *Chemical Communications*, 51:3545–3548, 2015.
- [166] I. Shindo. Determination of the phase diagram by the slow cooling float zone method: The system  $\text{MgO-TiO}_2$ . *Journal of Crystal Growth*, 50(4):839–851, 1980.
- [167] G. Eriksson and A. D. Pelton. Critical evaluation and optimization of the thermodynamic properties and phase diagrams of the  $\text{CaO-Al}_2\text{O}_3$ ,  $\text{Al}_2\text{O}_3\text{-SiO}_2$ , and  $\text{CaO-Al}_2\text{O}_3\text{-SiO}_2$  systems. *Metallurgical Transactions B*, 24(5):807–816, 1993.
- [168] H. P. Liermann, R. T. Downs, and H.-X. Yang. Site disorder revealed through Raman spectra from oriented single crystals: A case study on karooite ( $\text{MgTi}_2\text{O}_5$ ). *American Mineralogist*, 91(5–6):790–793, 2006.
- [169] A. H. Karande, S. Y. Shingare, S. S. Gurav, and S. V. Salvi. Influence of anatase and rutile phases on physical properties of new nanosize  $\text{MgTi}_2\text{O}_5$ . *International Journal of Chemical and Physical Sciences*, 3:17–20, 2014.
- [170] A. H. Karande, S. Y. Shingare, S. S. Gurav, and S. V. Salvi. Role of divalent substitution in dielectric behavior and pressure sensitivity of  $\text{MgTi}_2\text{O}_5$ . *International Journal of Chemical and Physical Sciences*, 3:1–9, 2014.
- [171] S. S. Todd. Low temperature heat capacities and entropies at 298.16 K of magnesium orthotitanate and magnesium dititanate. *Journal of the American Chemical Society*, 74:4669–4670, 1952.
- [172] K. K. Kelley, B. F. Naylor, and C. H. Shomate. The thermodynamic properties of manganese. *U. S. Bureau of Mines Technical Paper 686*, 1946.
- [173] C. M. B. Henderson, K. S. Knight, and A. R. Lennie. Temperature dependence of rutile ( $\text{TiO}_2$ ) and geikielite ( $\text{MgTiO}_3$ ) structures determined using neutron powder diffraction. *The Open Mineralogy Journal*, 3:1–11, 2007.

- [174] K. Refson, S. J. Clark, and P. R. Tulip. Variational density functional perturbation theory for dielectrics and lattice dynamics. *Physical Review B*, 73:155114, 2006.
- [175] P. Scherrer. Bestimmung der Größe und der inneren Struktur von Kolloidteilchen mittels Röntgenstrahlen. *Nachrichten von der Gesellschaft der Wissenschaften zu Göttingen, Mathematisch-Physikalische Klasse*, 1918:98–100, 1918.
- [176] A. Patterson. The Scherrer formula for X-ray particle size determination. *Physical Review*, 56:978–982, 1939.
- [177] E. Prince. Mathematical aspects of rietveld refinement. In R. A. Young, editor, *The Rietveld Method*, chapter 3. Oxford University Press, New York, 1993.
- [178] R. J. Hill. Data collection strategies: fitting the experiment to the need. In R. A. Young, editor, *The Rietveld Method*, chapter 5. Oxford University Press, New York, 1993.
- [179] A. Navrotsky and O. J. Kleppa. The thermodynamics of cation distributions in simple spinels. *Journal of Inorganic and Nuclear Chemistry*, 29(11):2701–2714, 1967.
- [180] J. J. Friel and R. I. Harker. Armalcolite stability as a function of pressure and oxygen fugacity. *Geochimica et Cosmochimica Acta*, 41:403–410, 1977.
- [181] M. P. Gora and A. YA. Shevko. Armalcolite (Mg,Fe)Ti<sub>2</sub>O<sub>5</sub> in the Siberian platform floodbasalts. In *Geochimica et Cosmochimica Acta. Goldschmidt 2010: Earth, Energy, and the Environment*, volume 74 of 12, page A348, Knoxville Tennessee, USA, 2010.
- [182] J. K. Burdett and J. R. Rodgers. *Structure and property maps for inorganic solids*. John Wiley and Sons, Ltd, 2006.
- [183] F. H. Dulin and D. E. Rase. Phase equilibria in the system ZnO–TiO<sub>2</sub>. *Journal of the American Ceramic Society*, 43(3):125–131, 1960.
- [184] L. B. McCusker, R. B. Von Dreele, D. E. Cox, D. Louër, and P. Scardi. Rietveld refinement guidelines. *Journal of Applied Crystallography*, 32(1):36–50, 1999.
- [185] D. Ravinder, K. Vijaya Kumar, and B. S. Boyanov. Elastic behaviour of Cu–Zn ferrites. *Materials Letters*, 38(11):22–27, 1999.
- [186] O. Frank, M. Zukalova, B. Laskova, J. Kurti, J. Koltai, and L. Kavan. Raman spectra of titanium dioxide (anatase, rutile) with identified oxygen isotopes (16, 17, 18). *Physical Chemistry Chemical Physics*, 14:14567–14572, 2012.
- [187] Q.-L. Guan, H.-Y. Wang, S.-L. Li, C. Liu, and Q.-C. Jiang. Microstructure characteristics of products in Ti–Si system via combustion synthesis reaction. *Journal of Materials Science*, 44(7):1902–1908, 2009.
- [188] J. M. Córdoba, E. Chicardi, M. A. Avilés, and F. J. Gotor. Formation of the complete range of Ti<sub>5</sub>Si<sub>3–x</sub>Ge<sub>x</sub> solid solutions via mechanically induced self-sustained reactions. *Intermetallics*, 19(11):1688–1692, 2011.

- [189] D. P. Riley, C. P. Oliver, and E. H. Kisi. In-situ neutron diffraction of titanium silicide,  $\text{Ti}_5\text{Si}_3$ , during self-propagating high-temperature synthesis (SHS). *Intermetallics*, 14(1):33–38, 2006.
- [190] P. A. Maggard, D. A. Knight, and J. D. Corbett. Substitutional chemistry in  $\text{Mn}_5\text{Si}_3$ -type scandium-main group compounds and the formation of quasibinary phases. *Journal of Alloys and Compounds*, 315(1–2):108–117, 2001.
- [191] A. J. Thom, V. G. Young, and M. Akinc. Lattice trends in  $\text{Ti}_5\text{Si}_3\text{Z}_x$  ( $Z = \text{B}, \text{C}, \text{N}, \text{O}$  and  $0 < x < 1$ ). *Journal of Alloys and Compounds*, 296(1–2):59–66, 2000.
- [192] J. J. Williams. Structure and high-temperature properties of  $\text{Ti}_5\text{Si}_3$  with interstitial additions. In *Retrospective Theses and Dissertations*, 12494, 1999.
- [193] A. J. Thom. Oxidation studies on small atom doped  $\text{Ti}_5\text{Si}_3$ . In *Retrospective Theses and Dissertations*, 10988, 1995.
- [194] C. Colinet and J. C. Tedenac. Structural stability of intermetallic phases in the Si–Ti system. Point defects and chemical potentials in  $\text{D}_{88}\text{-Si}_3\text{Ti}_5$  phase. *Intermetallics*, 18(8):1444–1454, 2010.
- [195] H. Sprenger and J. Nickl. Neues Titansilicid:  $\text{Ti}_5\text{Si}_4$ . *Naturwissenschaften*, 54(24):645–645, 1967.
- [196] C. R. Kachelmyer, I. O. Khomenko, A. S. Rogachev, and A. Varma. A time-resolved x-ray diffraction study of  $\text{Ti}_5\text{Si}_3$  product formation during combustion synthesis. *Journal of Materials Research*, null:3230–3240, 1997.
- [197] C. L. Yeh and C. C. Hsu. An experimental study on  $\text{Ti}_5\text{Si}_3$  formation by combustion synthesis in self-propagating mode. *Journal of Alloys and Compounds*, 395(1–2):53–58, 2005.
- [198] T. Bernert, B. Winkler, E. Haussühl, F. Trouw, S. C. Vogel, A. J. Hurd, L. Smilowitz, B. F. Henson, F. E. Merrill, C. L. Morris, F. G. Mariam, A. Saunders, and E. A. Juarez-Arellano. *In situ* observation of self-propagating high temperature syntheses of  $\text{Ta}_5\text{Si}_3$ ,  $\text{Ti}_5\text{Si}_3$  and  $\text{TiB}_2$  by proton and X-ray radiography. *Solid State Sciences*, 22(0):33–42, 2013.
- [199] S. Åsbrink and L.-J. Norrby. A refinement of the crystal structure of copper(II) oxide with a discussion of some exceptional e.s.d.'s. *Acta Crystallographica Section B*, 26(1):8–15, 1970.
- [200] M. Aïn, A. Menelle, B. M. Wanklyn, and E. F. Bertaut. Magnetic structure of  $\text{CuO}$  by neutron diffraction with polarization analysis. *Journal of Physics: Condensed Matter*, 4:5327–5338, 1992.





## Acknowledgements

My doctoral studies are carried out at the University of Frankfurt under the supervision of Prof. Dr. Björn Winkler in the support of China Scholarship Council. This thesis would not have been finished without the immense support from my supervisor, Prof. Dr. Björn Winkler, and the constant helps and encouragements from my colleagues, friends and family.

I would like to express my sincere gratitude to Prof. Dr. Björn Winkler for offering me the academic guidance, professional mentorship, tremendous opportunities, inspiration and care throughout my doctoral studies at the University of Frankfurt. His insight in science, dedication to work and care to the employees have impressed me deeply. He provides an open and warm working environment which allows me to explore the topics of interest with freedom. He leads me to shape the research and complete it. Whenever I encounter difficulties, he is always there to give advice, guidance and assistance, which makes me feel greatly enlightened and gives me the courage to move forward. He covers all the costs for the research and attending the conferences. He also provides some financial support for me to write up the thesis. I am indebted for the countless time he spent and all he has done to make this thesis a reality. I believe the experience in his group would benefit my life and academic career significantly.

I would like to thank Dr. N. Schrodtr for her support in the Rietveld refinement, Raman spectroscopy, LaTeX language and SEM. She provides the LaTeX template of the thesis. She has carefully read through and corrected the thesis for several times. She proofreads the thesis before I submit it. She has provided numerous helps in my daily life and the affairs of attending conferences.

I gratefully thank Dr. W. Morgenroth for providing constructive suggestions to the thesis and inspiring me. He makes the translation of summary for the thesis in German and proofreads the thesis before I submit it.

I thank Dr. L. Bayarjargal for his guidance, advice and encouragement to my research. He collects Raman spectra and guides me in the data analyses.

I gratefully thank PD Dr. Haussühl for his support. He trains me the laboratory skills, such as cutting, grinding, density, microscopy, X-ray diffractometers, the plane wave ultrasound spectroscopy and the thermal expansion. He collects the plane wave ultrasound spectra and the thermal expansion data. I appreciate the time and effort which he puts to help and encourage me.

I am extremely thankful to Dr. T. Bernert for guiding me in SHS, the Rietveld refinement, high speed ball milling and basic experimental skills. He introduces many useful tools to me, such as LaTeX, GSAS, EXPGUI, gsaslanguage, cmpr and gnuplot. He has spent a lot of time and provided valuable advices to my research. He always helps me even though I could not repay the kindness, which is impressive.

I am grateful to Dr. J. D. Bauer for introducing PPMS and the microscopy. He collects low temperature heat capacities, shows me the programme WinTensor and encourages

me.

I sincerely thank Dr. J. Ruiz-Fuertes for guiding me in Raman spectroscopy. He supports in preparing the poster, the oral presentation and writing a manuscript. He can share the career experiences and comfort me.

I sincerely thank Dr. I. Vellame for collecting Raman spectra and the warm encouragement.

I thank Dr. A. Friedrich for her support and warm encouragement to my research and the care to my life. She guides me in Rietveld refinement and performs the UV-vis measurements.

I thank Dr. A. Thust and A. Hirsch for sample preparations, the isostatic pressing, SEM, the valuable discussions and kind care.

I thank M. David for his support in building the SHS and ball milling equipments, operating the X-ray diffractometer and glove box, and solving the computer problems.

I thank R. Luchitskaia for ordering chemicals, introducing me to the chemical laboratory, showing me the basic skills of sample preparations and equipment operations. She cheers me up when I want to give up and provides warm helps when I encounter difficulties in my daily life. I gratefully thank PD Dr. V. Vinograd and R. Luchitskaia for their kind words and sharing.

I thank the colleagues for the helps to my research: M. Herrmann, X. Liu, D. Zimmer, C. Neun, C.-J. Fruhner, M. Stekiel, T. Wittmaack, S. Frischkorn, Tamara Koch. It is my great honor to work with all of you.

I thank our former secretary H. Apelt-Celebi for all her support in settling down, registration, receiving posts, preparing the birthday gifts, managing the coffee room, information and so on. Thank our new secretary S. Schickling-Herzog for information, receiving posts and helps.

I thank the workshop for their kind helps and concerning.

I thank Dr. E. Suard and her group in Institut Laue-Langevin for their assistance in the neutron diffraction measurements.

I thank Zhengzhou University, China Scholarship Council and the Chinese Embassy in Germany for their assistance in extending the Ph.D. study duration. I thank the kind care from Prof. Dr. Hongxia Lu and Jingyi Du. Thank the accompany of my husband, Xiujun Yu, and my friends in Frankfurt am Main.

Finally, I must express my special thanks to my grandfather, my parents, my parents in law, my sister and my brother. Thank their love and supports.

# Curriculum Vitae

Man He

## Personal Information

Date and place of birth: 08. 08. 1988, Henan, P.R. China

Gender: Female

Nationality: Chinese



## Education

09. 2012 – 10. 2016 (**Ph.D. Candidate**): Department of Geosciences/Geography, University of Frankfurt

Supervisor: Prof. Dr. Björn Winkler

"Mechanochemical activation assisted solid state synthesis, self-propagating high-temperature synthesis, and characterisation of Ti-containing solid solutions with spinel-, pseudobrookite- and  $Mn_5Si_3$ -type structures"

09. 2009 – 06. 2012 (**Master of Engineering**): School of Materials Science and Engineering, Zhengzhou University

"Synthesis and crystallisation behaviours of the glass-ceramic glazes"

Supervisor: Prof. Dr. Hong-xia Lu

09. 2005 – 06. 2009 (**Bachelor of Engineering**): School of Materials Science and Engineering, Zhengzhou University

"Preparation of the DMSO/kaolinite intercalation compound"

Supervisor: Prof. Dr. Hong-liang Xu



## **Declaration**

*I hereby declare that this submission is my own work and that, to the best of my knowledge and belief, it contains no material previously published or written by another person nor material which has been accepted for the award of any other degree or diploma of the university or other institute of higher learning, except where due acknowledgment has been made in the text.*

---

**Man He**

**Frankfurt am Main**

**19.07.2016**